



Doctoral Dissertation
Doctoral Program in Materials Science and Technology (33rd Cycle)

# Conventional and Innovative Titanium Alloys Produced Using Different Additive Manufacturing Technologies

**Alessandro Carrozza**

* * * * * *

**Supervisors:**
Prof. P. Fino, Supervisor
Prof. S. Biamino, Co-Supervisor
Prof. M. Lombardi, Co-Supervisor

**Doctoral Examination Committee:**
Prof. R. Lupoi, Referee, Trinity College Dublin
Prof. L. Nyborg, Referee, Chalmers University of Technology
Prof. S. Mayer , Referee, Montanuniversität Leoben
Prof. M. Terner , Referee, Changwon University

Politecnico di Torino
2021

# Declaration



I hereby declare that, the contents and organisation of this dissertation constitute my own original work and does not compromise in any way the rights of third parties, including those relating to the security of personal data.

…….....

Alessandro Carrozza

2021

# Summary

Titanium alloys are a class of metallic materials widely used in several industrial fields, such as automotive, aerospace and biomedical. Their main advantages lie in excellent corrosion resistance, high specific strength and low density. Among these alloys, Ti-6Al-4V shines as the “workhorse” material, covering almost 50% of the total titanium products market.

The conventional industrial sectors in which this class of materials is employed are ideal for Additive Manufacturing (AM) implementation, as the components typically produced are already characterized by a high level of complexity and the production lots are limited in number. These are typical manufacturing scenarios where modern AM technologies are highly advantageous. Moreover, AM technologies grant a lower degree of material usage and higher levels of customizability, with respect to other techniques.

Among all the titanium alloys conventionally available, only a limited number were optimized for their processing by AM. The Ti-6Al-4V alloy was one of the first materials to be processed in general and it is now well-established for being manufactured via Laser Powder Bed Fusion (LPBF). Oppositely, the Ti-6Al-2Sn-4Zr-6Mo alloy, a substitute of Ti-6Al-4V with higher strength for some niche applications, was never processed before using this technology. Ti-6Al-4V is also well suited to be produced by Electron Beam Melting (EBM) and Directed Energy Deposition (DED).

The goal of this thesis was to analyse the microstructure, the mechanical properties and their relationship for the Ti-6Al-4V alloy produced by EBM and DED. Moreover, the LPBF produced Ti-6Al-4V samples were compared with Ti-6Al-2Sn-4Zr-6Mo specimens produced for the first time using the same system.

Initially, the optimal process parameters to manufacture the Ti-6Al-4V samples by DED were assessed using the single scan approach. This step was necessary as these were the first specimens produced using this system. The microstructure of the 3D samples was carefully analysed and correlated with the environmental factors and thermal history of the process. Consequently, the mechanical properties were determined. These analyses were also conducted on samples that underwent different post-processing heat treatments, in which the cooling means were varied.

In the case of the EBM produced samples, standard process parameters were used, and the analysis of the heat treatments focused on the significance and effect of a post-annealing ageing step.

The heat treatments performed on DED and EBM produced specimens were specifically tailored in order to be comparable. Moreover, the annealing temperature was set high enough to allow a complete recrystallization of the initial microstructure. By doing so, the comparative analysis did not result biased by the significantly different microstructures typically produced using these two manufacturing technologies.

The innovative Ti-6Al-2Sn-4Zr-6Mo alloy was processed by means of LPBF. Since no prior works on the subject were found, the most suitable process window had to be determined. After that, a microstructural and mechanical characterization of the samples was conducted. Since the industrial relevance of this alloy is related to its superior mechanical properties with respect to Ti-6Al-4V, the same investigation was performed on LPBF produced Ti-6Al-4V samples with the aim to assess whether this feature was maintained when switching to LPBF as a manufacturing technology or not.

# Acknowledgment

I would like to express my gratitude and appreciation to my supervisor Prof. Paolo Fino for the opportunity to work in such an interesting, promising and advanced field. I would also like to thank Prof. Sara Biamino and Prof. Mariangela Lombardi, my co-supervisors, for their continuous support and motivation. They will always have my gratefulness for introducing me to the world of Additive Manufacturing for the first time. Their guidance, support, patience and effort will not be forgotten.

Besides my supervisors, I would also like to acknowledge a special thanks to Dr. Alberta Aversa, Dr. Giulio Marchese, Dr. Abdollah Saboori and Dr. Luca Lavagna for their help and support throughout these three years. My path would have been much rougher without their wise advices and the stimulating discussions. I would also like to thank my other co-workers, who certainly made the rougher days less unpleasant.

My sincerest gratitude goes to Prof. Anna Valente and Dr. Federico Mazzucato from SUPSI for their help and support during the collaboration between our two universities.

I would also like to thank all the people I collaborated with as part of the 4D HYBRID and MANUELA European projects. I am honoured to have had the chance to work in such a stimulating environment, in direct contact with so many professionally prepared people.

A final thanks goes to my family, my friends and Simone. I would be nothing without them and I feel privileged to have them all as part of my life.

# Contents

# List of Tables

# List of Figures

# Chapter 1

# Introduction

## 1.1 Titanium Alloys

Titanium is the 22nd element of the periodic table, ranking among the 10 most abundant elements on the Earth's crust [1]. It shares the 0.3%-0.5% of the overall crust weight composition [2,3]. This metal was firstly isolated in reasonable quantities by Prof. Hunter (Rensselaer Polytechnic Institute, Troy, NY) in 1910. He developed a system to reduce $TiCl_4$ (titanium tetrachloride), obtained from ores, using Na. Although just in 1932 Wilhelm Justin Kroll developed a more affordable process, named after himself, using Ca instead of Na as a reducing agent. The Kroll process is the most commonly used method to obtain high-purity Ti even today [4]. Before World War II, titanium was a rare metal to be found in industry. Although, from the 1950s, large scale titanium production started. This family of alloys resulted particularly appealing for aerospace applications (e.g. jet engines, aircrafts). Since then, titanium has been employed in several industrial sectors, ranging from nautical, chemical and automotive to medical, deploying some titanium alloys biocompatibility [5].

Pure titanium is characterized by a hexagonal close packed (hcp) crystal structure at room temperature, defined as α-Ti. Although, as many other metals, titanium is polymorphous and at ~880 °C it changes its crystal structure from hcp to body cubic centred (bcc), becoming β-Ti, characterized by a lower Young's modulus (E). It then keeps this form until the melting temperature ($T_m$) of 1667 °C is reached. Ti is also among the most ductile hcp metals. α-Ti shows a c/a ratio of 1.587, sensibly lower than the theoretical value of 1.633, and its principal slip systems are $\{10\bar{1}0\}\langle 11\bar{2}0\rangle$, $(0001)\langle 11\bar{2}0\rangle$ and $\{10\bar{1}\bar{1}\}\langle 11\bar{2}0\rangle$ (Figure 1) [6,7].

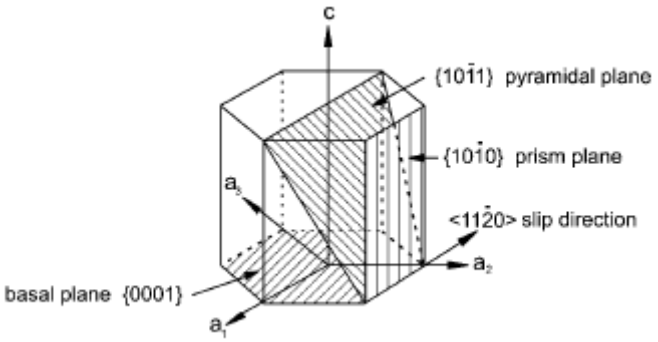


**Figure 1**: Principal slip system in hcp titanium [4].

Titanium is sometimes referenced as the "prima donna" of metals, as it can achieve exceptional combinations of interesting properties, from an engineering point of view. Although these combinations also result in a material quite difficult to handle, as it is very demanding when it comes to refinement and fabrication [5]. The physical properties of unalloyed titanium, reported in Figure 2, show how this material behaves when compared with other metals, in particular aluminium and iron, which are the most commonly used material for structural applications. The key properties of titanium are its low density, relatively high melting point and high cost.

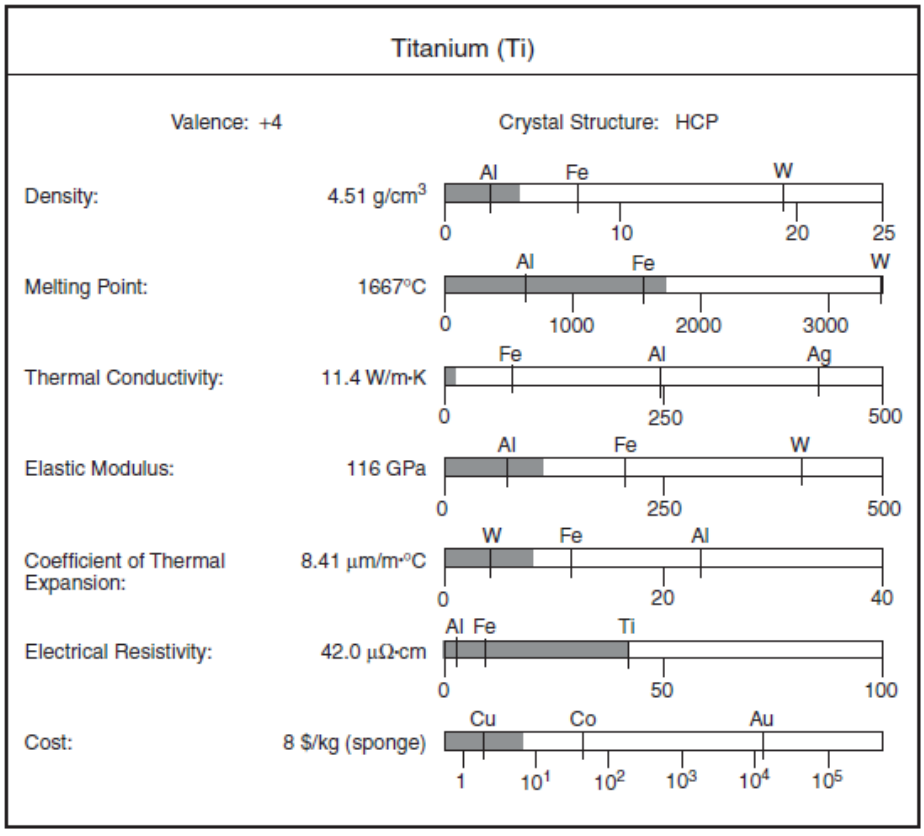


**Figure 2**: Main physical properties of pure titanium [5].

Titanium and its alloys result particularly appealing due to some specific properties this class of materials can provide. The most important are the remarkable strength-to-weight ratio and the exceptional corrosion resistance [4,7].

Even if the yield strength of titanium alloys is not exceptional, their strength-to-weight ratio, critical in field where weight reduction is very important, such as the aerospace industry, is very high, mainly due to the low density. In terms of specific strength, titanium alloys are comparable with the strongest steels [5]. As visible in Figure 3, Carbon Fibre Reinforced Plastics (CFRP) outperform titanium alloys until approximately 300 °C, from that temperature up until above 500 °C Ti alloys stand out in the aerospace sector. Even if their use at even higher temperature is challenged by their oxidation behaviour, titanium alloys grant excellent mechanical properties in a moderately high temperature range [4].

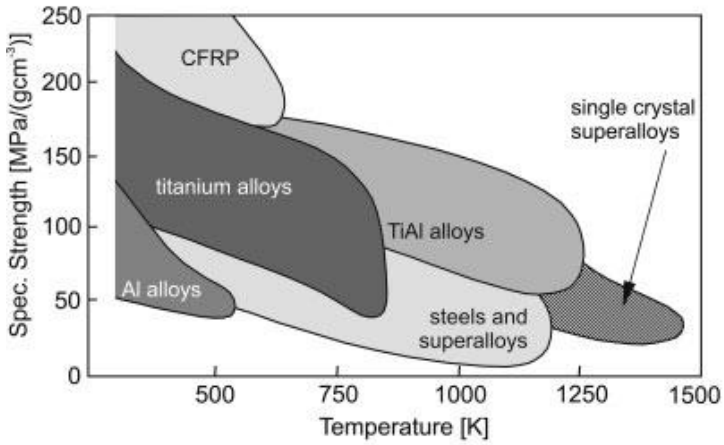


**Figure 3**: Specific strength at increasing temperature of several structural materials used in the aerospace industry [4].

Although, for specific applications, a lower Young's modulus must be taken into consideration, as in structures this leads to greater deformations. However, there are specific applications where a low E is ideal, as it leads to a high modulus of resilience, which results in a large amount of elastic strain energy stored in the material. Considering sports, tennis racquets and golf clubs are examples of objects that deploy this property.

Titanium's outstanding corrosion resistance is the result of a thin oxide layer, approximately some nanometre thick, that forms immediately on the surface of the material when exposed to air. This layer is stable throughout a wide range of pH values and it easily reforms if damaged even if O or $H_2O$ are as low as a few ppm. At higher temperatures, from approximately 200 °C [8], oxygen diffusional phenomena are favoured resulting in the oxide layer thickening. This is the result of oxygen being extremely soluble in titanium, which grants this material the ability to absorb its own oxide , which is a very favourable property when it comes to some joining technologies, such as diffusion bonding, or powder metallurgy, where otherwise the oxide would result in internal inclusions [5].

The main downside of titanium alloys surely lies in their extreme reactivity, which poses very difficult issues during processing phases and results in:

- Impossibility to use most refractory materials in contact with the molten alloy, as these are easily dissolved by liquid titanium;
- Impossibility to melt, join or process the material in presence of air, as these processes would result in oxygen/nitrogen pick-up, which severely embrittles the material. Moreover the risk of fire is a serious threat [9];
- Difficulties in machining, as titanium is characterized by a low thermal conductivity, as a result of the high bonding force between its atoms, that also causes $T_m$ to be quite high (Figure 2). This results in a scarce ability to dissipate heat and can eventually lead to a temperature rise, which causes the reactivity to increase and the base metal to dissolve the cutting tool. Hence, to process titanium, very low cutting speeds are necessary, in conjunction with highly efficient cooling fluids.

In general, the main downside of titanium alloys lies in their cost, which is quite high for a structural material. As visible in Figure 4, where the cost of different metallurgical semiproducts is compared for the three main structural alloys (steel, aluminium and titanium), titanium semiproducts appear extremely more expensive, even orders of magnitude, when compared to steel.

| Item | Material ($/pound) | | |
|---|---|---|---|
| | Steel | Aluminum | Titanium |
| Ore | 0.02 | 0.01 | 0.22 (rutile) |
| Metal | 0.10 | 1.10 | 5.44 |
| Ingot | 0.15 | 1.15 | 9.07 |
| Sheet | 0.30–0.60 | 1.00–5.00 | 15.00–50.00 |

**Figure 4**: Comparison of the cost of the three main structural metals: steel, aluminium and titanium alloys [10].

Although, even if the cost of rutile (precursor of titanium) is quite high, for example than bauxite (precursor of aluminium), such a difference in terms of final cost in not justified. In fact, as highlighted before, titanium alloys are also more difficult to be processed and are characterized by a quite low material efficiency, due to the necessity of machining. For conventional ingot metallurgy (cast and wrought), the cost of this operation is extremely high and it can account for almost half of the prize of an entire component. As an example, in Figure 5 is provided the cost breakdown for an aerospace titanium component by Boeing.

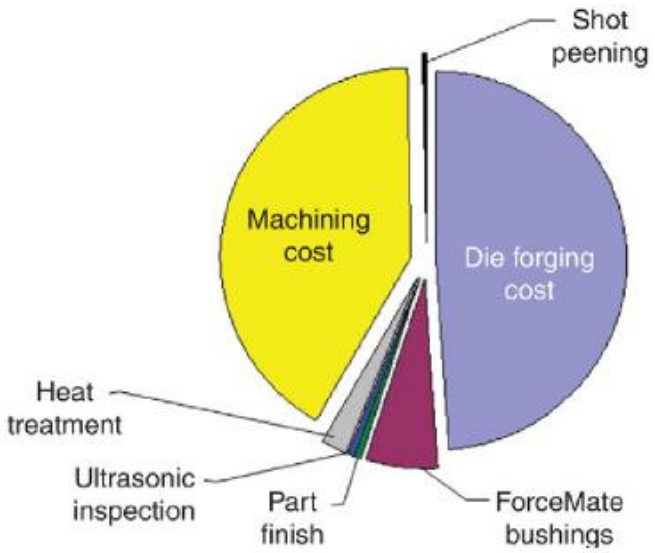


**Figure 5**: Cost breakdown of a Boeing 787 side-of-body chord made of a titanium alloy [10].

Considering the high costs of the machining operations, any technology that can grant the production of a components closer to the final form (e.g. near-net shape), without the necessity to machine it, results attractive in the field of titanium metallurgy [10]

As discussed above, the aerospace industry is certainly the most important end user of titanium alloys. In the USA, approximately 70%-80% of the overall titanium consumption is dedicated for aerospace products [11]. These alloys are particularly appreciated for weight reduction, acting as a steel replacement, and for solving issues related to space limitations, as an aluminium replacement. Overall, the possibility to operate at moderately high temperatures, their outstanding corrosion resistance in addition to their ability to reliably tolerate damages make titanium alloys even more appreciated in the aerospace industry [12,13]. On average, titanium alloys are used for 36% of engines and 7% of airframes [4]. Apart from engine parts (e.g. disks), portions of the fans systems and compressor sections, titanium alloys find usage in heavily-loaded structures, like wings and tail attachments (Figure 6). Moreover, the increasing usage of polymer matrix-carbon fibre composites (PMCs) in the aerospace industry led to a gain in popularity for titanium alloys in the same field, as PMCs are often incompatible, for electrochemical reasons, with the lighter aluminium alloys, which act as a substitute for titanium in some applications. Therefore, titanium alloys found usage even in aerospace applications without structural requirements (e.g. fasteners) [13].

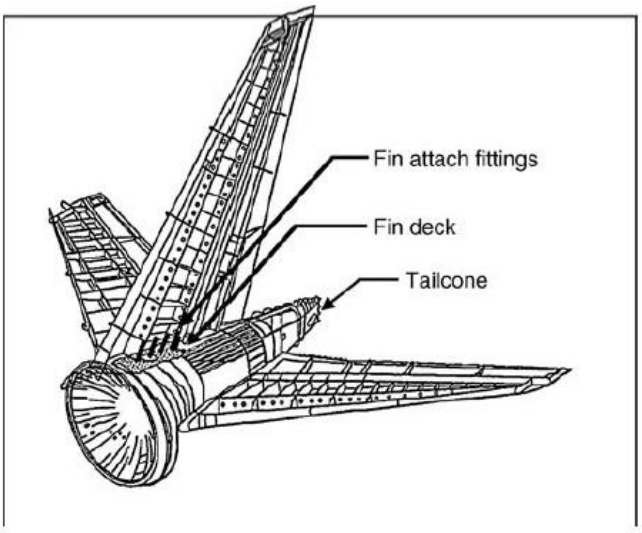


**Figure 6**: Titanium empennage attachment of a commercial aircraft, connected to PMC parts [13].

Another important industrial field is the automotive industry, in which titanium components are used for engines parts for F1 race cars since the 1980s. A widespread diffusion of this class of materials in this industrial sector is prevented by their high costs. In fact, these are used mostly for racing or special-purpose cars. However, recently titanium alloys gained popularity due to the growing attention towards fuel efficiency and performances. Nowadays most valves in cars and motorcycles are made of titanium alloys [11].

The third important field of application is the medical sector, where titanium alloys are deployed mostly due to their reduced E, elevate specific strength, outstanding biocompatibility and corrosion resistance [14]. Particularly commercial purity titanium (cp-Ti) and Ti-6Al-4V are widely used for dental/maxillofacial implants, hip/knee prostheses and cardiac devices [15]. An example of titanium implants is provided in Figure 7.

**Figure 7**: Two examples of titanium implants used in the medical field [16].

### 1.1.1 Phase Diagrams and Alloys Classification

Pure titanium is a quite ductile material, although its strength is fairly low, which is why very often other alloying elements are added. These can be divided into α phase stabilizers and β phase stabilizers, according to their effect on the β

transition temperature ($T_\beta$) (Figure 8). The former category raises $T_\beta$, enlarging the temperature range in which the α phase is stable, whilst the latter act in an opposite way. Of course, the elements that tend to stabilize a certain phase are more soluble in it. Moreover, some elements, such as Zr and Sn, have a more or less neutral effect, leaving $T_\beta$ substantially unchanged.

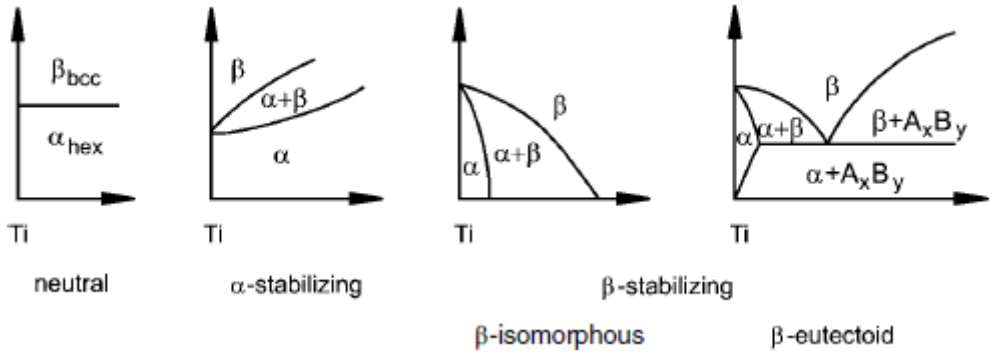


**Figure 8**: Schematic representation of the effect of the different types of alloying elements on $T_\beta$ [4].

The α stabilizing elements can be both substitutional (e.g. Al) or interstitial (e.g. C, N, O). Among this category, the most important and commonly used element is by far aluminium, which is fairly inexpensive, strengthens the material by solution hardening and improves the oxidation behaviour at high temperatures. Moreover, it reduces ductility by limiting the dislocation motion, even if less severely than interstitial α stabilizers. Figure 9 shows the variation of the tensile mechanical properties as a function of Al content. Up until 8%, the tensile strength drastically increases and the reduction in ductility appears acceptable. After this compositional threshold, the material is severely embrittled, due to the formation of the brittle intermetallic $Ti_3Al$ [5].

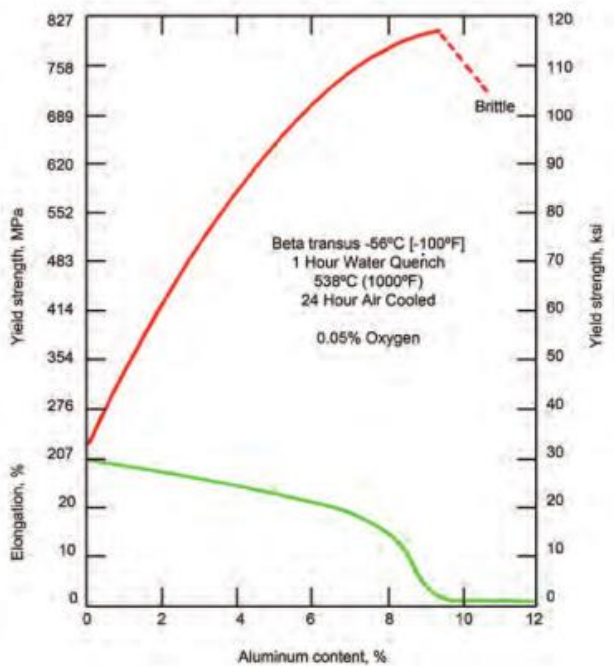


**Figure 9**: Tensile properties variations as a function of Aluminium content [7].

The β stabilizing elements can be furtherly split into: β-isomorphous (e.g. V, Mo) and β-eutectoid (e.g. Fe, Cr). The most soluble and important elements lie in the first group, while the latter category represents the elements that tend to form intermetallic compounds even if present in small quantities [4,6].

In order to understand the phases and classification of titanium alloys, since more phases are possible at room temperature, investigating the β→α transformation is a key aspect. Thermodinamically it is a shear type nucleation-driven process, which obeys the following crystallographic orientation relationship, described through Burgers vectors:

$$\{110\}_\beta \,//\, \{0001\}_\alpha$$
$$\langle 111\rangle_\beta \,//\, \langle 1120\rangle_\alpha$$

Where the most densely packed β phase planes {110} turn into the {0001} basal plane of the α phase. After the transformation, the distance between the basal planes increases, which causes a certain atomic distortion. This is the main reason why the c/a ratio is sensibly lower than 1.633, as stated before. The transformation is also related to a certain increase in volume. Unlike the bcc β, the hcp α phase is a close-packed structure. This difference results in a sensitive difference in terms of self-diffusivity ($D_{Ti}$) between these two phases. In fact, for example, at 1000 °C $D_{Ti-\beta}$ ($\approx 10^{-13}$ $m^2/s$) is two orders of magnitude greater than $D_{Ti-\alpha}$ ($\approx 10^{-15}$ $m^2/s$). This difference is very significant for creep behaviour, where α rich alloys act superiorly due to their far lower diffusivity. Since diffusion is the driving phenomenon for the β→α transformation, when the material is cooled from above the $T_\beta$ very rapidly, this transformation can be kinetically prevented, in favour of a martensitic transformation. Its product depends on the alloy composition and can be either α' martensite, which is hexagonal, or α" martensite, which is orthorhombic. A certain martensite start temperature ($M_S$) exists for each alloy that can form α'/α", below which the martensitic transformation begins. In general, $T_\beta > M_S$. Martensite can be decomposed through a heat treatment, causing the nucleation of α phase. Some studies available in literature suggest that α' and α" generally do not coexist in the same alloy [17].

Titanium alloys are classified according to their equilibrium composition near room temperature, which is defined by the type and amount of alloying elements.

The general classification divides this class of materials into 3 sub-categories: α alloys, α+β (or duplex) alloys and β alloys [6]. Although some authors suggest a further sub-division, adding the near α alloys, which can retain only small amounts of β phase at room temperature, and the metastable β alloys, which can achieve a 100% β phase (metastable) microstructure, through air cooling of thin section or water quenching of larger pieces [4,5]. All these groups can be represented in a three-dimensional phase diagram, function of the concentration of α and β stabilizers, as provided in Figure 10.

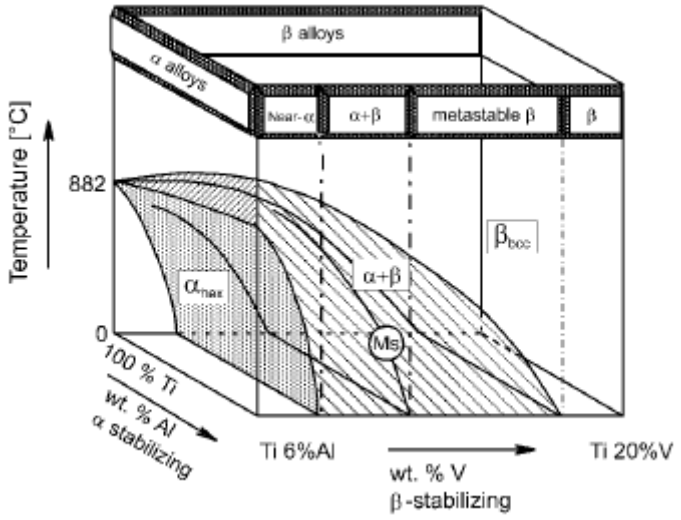


**Figure 10**: Titanium alloys classification on a 3D phase diagram [4].

α alloys contain neutral and α stabilizing elements only. If a low amount of β stabilizers is added, then the material becomes a near-α alloy. Both these categories allow the formation of α' hexagonal martensite. The duplex alloys, which are by far the more widely used, are characterized by 5% - 40% β phase near room temperature and can form both α' hexagonal and α'' orthorhombic martensite, according to their composition. α"-forming alloys, are characterized by a larger amount of β stabilizers, therefore are sometimes referred as near-β alloys [18]. β-stabilizing elements tend to lower the $M_S$. When these are in a sufficient concentration, $M_S$ can be lower than room temperature, which means that martensite cannot be formed through conventional processes. When this happens, the alloys are classified as metastable β, even if it can still show more than 50% α phase. In the end, β alloys show exclusively β phase at room temperature. These are very unconventional materials that are excluded by the classical titanium alloys [4,6].

The β phase stability index ($SI_\beta$) can be used as a useful parameter in order to investigate how each specific alloying element influences the phase diagram of a generic alloy, by describing substantially how prone a material is to show β phase retention at room temperature. It is calculated as the difference between the terms $[Mo]_{EQ}$ and $[Al]_{EQ}$ (wt.%) [6,19,20], where:

$$[Mo]_{EQ} \approx [Mo] + \frac{2}{3}[V] + \frac{1}{3}[Nb] + 3[Fe] + \frac{3}{2}[Cr] \quad (1)$$

$$[Al]_{EQ} \approx [Al] + \frac{1}{3}[Sn] + \frac{1}{6}[Zr] + 10([C] + [O] + 2[N]) \quad (2)$$

A $SI_\beta$ of -5 or lower characterizes near α titanium alloys, while in the range $-5 < SI_\beta < 10$ lie all the duplex alloys. In particular, the higher the index, the more likely the alloy shows α" martensite instead of α'. For a $SI_\beta > 10$ up until 30, the alloys are described as metastable β, hence $M_S <$ room temperature. In the end, a $SI_\beta$ value even greater corresponds to β alloys [21,22]. The evaluation of $SI_\beta$ for a

variety of titanium alloys, ranging from the near α to the stable β category, is provided in Figure 11.

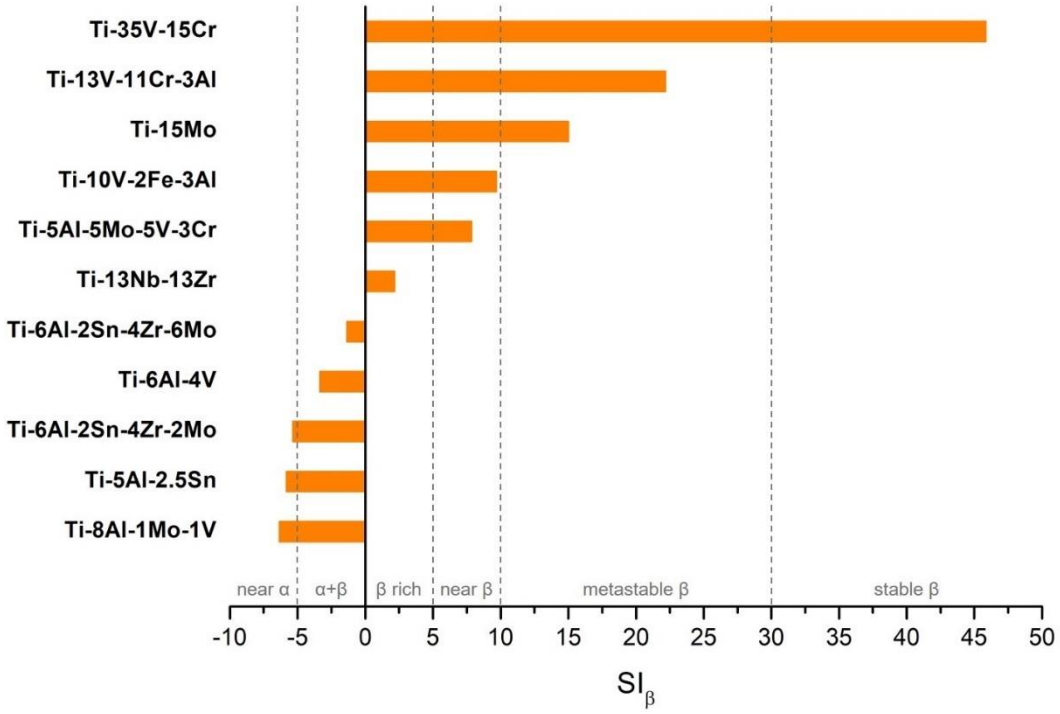


**Figure 11**: $SI_\beta$ calculated for some titanium alloys commercially available.

α/near α alloys are not very responsive to heat treatments, due to their impossibility to obtain β phase (Figure 10). Although these materials are characterized by a good creep resistance, toughness and weldability, in fact they are intended for high temperature performances. Instead, the duplex alloys have a compromise of properties typical of the α and β phases, such as good weldability, toughness and corrosion resistance. These materials are readily heat treatable and can be tailored, in terms of phase composition/amount and morphology according to the application intended. Through heat treatment, α+β alloys can achieve high strength. Instead, β alloys usually show good mechanical properties, although their creep resistance is fairly low, due to the higher diffusivity of the β phase [7]. Metastable β alloys show excellent formability, but these alloys are often characterized by a low yield strength. It is possible to strengthen these materials through some heat treatments, in which fine α phase particles are precipitated.

### 1.1.2 Hardening Mechanisms

In general, four strengthening phenomena exists for metals: solid solution, dislocation, boundary and precipitation hardening. Whilst the former and the latter are common for all the titanium alloys, and more dependent on the composition of the material (alloying elements), dislocation and boundary strengthening are more significant for duplex alloys, especially when heat treated above $T_\beta$ and rapidly cooled. This allows the formation of smaller grains, hence more concentrated grain boundaries, with relative increase of the concentration of dislocations in the

material. Solid solution hardening is more effective for the α phase, both for substitutional elements, such as Al, due to the large difference in atomic size, and for interstitials elements that fit into the hcp α lattice, such as oxygen. This last element is particularly effective in raising the hardness and tensile strength of titanium. Considering commercial purity titanium, its yield tensile strength (YTS) increases from 170 to 480 MPa when the concentration of oxygen is raised from 0.08% to 0.2%. Even if this alloying element is very promising in terms of strengthening, its concentration must be kept well under control, because its presence severely embrittles the material. Precipitation is quite uncommon in titanium alloys, although it is possible to obtain, among others, the intermetallic phase $Ti_3Al$ ($\alpha_2$), deploying the alloying elements partitioning in preferential phases during heat treatments, due to the preferential diffusivity of the elements, as mentioned previously. In fact, Al diffuses more likely in the α phase. Reaching the stoichiometric concentration to obtain $Ti_3Al$ is then possible and the intermetallic strengthens the material due to precipitation hardening [5,6].

### 1.1.3 Typical Heat Treatments

From now on in this work, only α+β alloys will be analysed, since all the investigation performed were conducted exclusively on materials that belong to this class.

Heat treatments are the most common method to achieve the desired combination of mechanical properties in duplex titanium alloys. The key material properties to understand, in order to design a proper heat treatment, are the specific alloy $T_\beta$ and $M_S$, illustrated in Figure 12 for the Ti-6Al-4V alloy. The former parameter, approximately 1000 °C for Ti-6Al-4V, represents the temperature threshold above which the whole microstructure recrystallizes [23]. The latter is the temperature from which, during cooling, the martensitic transformation β → α'/α" begins. Note that the product depends on the alloy composition. For Ti-6Al-4V $M_S$ is approximately 800 °C [24,25].

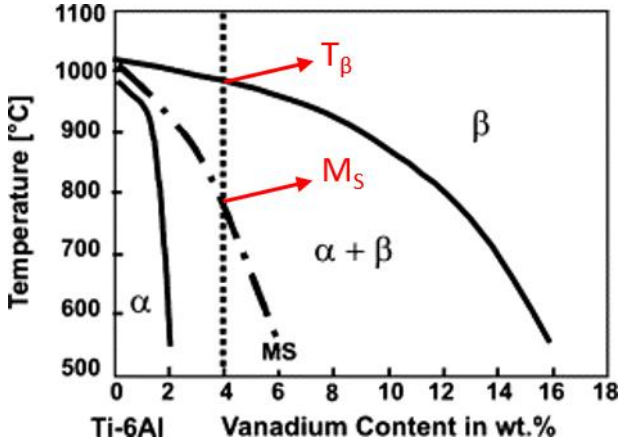


**Figure 12**: Schematic phase diagram, where the dashed line represents the Ti-6Al-4V alloy. The beta transus and martensite start temperatures are highlighted [26].

Usually, the heat treatments are conducted at temperatures slightly above or below the $T_\beta$, in order to induce a microstructural change in the material, but different approaches, for examples during ageing treatments, are quite common. Atmospheric protection is a markedly important aspect for every heat treatment of the titanium alloys, due to how prone these materials are to oxygen/nitrogen pick-up. In fact, often using a high vacuum furnace is necessary. Moreover, temperature control is also very important, especially when conducting a heat treatment very close, in terms of temperature, to $T_\beta$, because reaching this threshold means risking the complete recrystallization of the material.

**Stress relieving** is a possible heat treatment that aims at decreasing the internal residual stresses of the material, which improves the components shape stability, fundamental if it needs to be machined, and can slightly improve the material ductility. Considering that the internal residual stresses are the cause of the dislocation hardening mechanism discussed before, stress relieving is often related to a reduction in strength. The temperature for this heat treatments usually ranges from 500 to 700 °C for a duration that ranges from 15 minutes up until 8 hours. Both these parameters depend on the alloy composition and the component size. In general, higher temperatures are related to shorter durations and vice versa. Usually the specimen is then furnace or air cooled. Other cooling means, such as oil or water, would result in a higher cooling rate, inducing residual stresses in the material again, thus nullifying the overall effect of the heat treatment. Overageing, which is the result of an excessive temperature and/or duration choice, must be avoided, as it leads to a drastic decrease in strength. In general, this family of heat treatments is designed in order to induce as little changes in the microstructure as possible.

**Annealing** is a generic term used to describe a family of heat treatments that aim to increase toughness, ductility, dimensional/thermal stability and sometimes creep performances. Several sub-categories exist (e.g. mill annealing, duplex annealing, etc.), although their classification is challenging, as different producers tend to use personal nomenclatures. Annealing treatments can be conducted both below and above $T_\beta$, although in the latter case the temperature must be kept as low as possible, in order to prevent excessive grain growth.

**Solution annealing and ageing** is a standard sequence of heat treatments, usually performed to achieve high strength materials and optimum mechanical properties combinations. During the solution annealing, the temperature is raised in order to achieve a higher amount of equilibrium β phase, that can be maintained through quenching and then decomposed through ageing. For titanium alloys, the term “ageing” has a different meaning than in other metals, such as the aluminium alloys, in fact no significant precipitation occurs. Instead, in this case, the ageing process implies the decomposition of supersaturated retained β phase or martensite into α phase. The solution annealing temperature is usually set slightly above or below $T_\beta$. Heat treatments at $T > T_\beta$ imply a complete recrystallization of the material, hence the changes induced in the material cannot be recovered. Concerning the ageing, usually a temperature ranging from 400 to 750 °C is used

for a maximum duration as high as 8 hours for most conventional alloys. Of course, the combination of time and temperature is a key aspect and strictly depends on the specific property to emphasize. The type of cooling applied is usually fast, in order to retain the metastable characteristics achieved through the solution annealing phase. Lower cooling rates are usually avoided, as these can lead to significant diffusion, which is the driver of the $\beta \rightarrow \alpha+\beta$ decomposition, and variations in terms of ratio and compositions of the phases [23].

In order to understand how different cooling rates can induce significant changes in the microstructure, a general representation of the micrographs resulting from a heat treatment from $T > T_\beta$ is provided in Figure 13 for the Ti-6Al-4V alloy. When the cooling rate is very high, (Figure 13a), a completely martensitic microstructure (α'/α" depending on the alloy) is obtained. This is easily recognizable by its typical "needles" substructure. These laths are usually arranged in a ±45° fashion. For Ti-6Al-4V, the threshold cooling rate to obtain a completely martensitic microstructure lies around 410 °C/s [4,25]. If the cooling is lower (magnitude of 10 °C/s), a Widmanstätten pattern is obtained through nucleation and growth of the α phase at the expense of the β phase, where multiple variants (orientations) are available for the plates, resulting in the so called basket-weave morphology (Figure 13b) [27]. In the end, if a very low cooling rate is applied (magnitude of 1 - 10 °C/min) a typical lamellar pattern is still obtained. Although, in this case the morphology is usually formed by α plates arranged in large colonies, which share the same variant. Thus, the number of possible orientations is markedly more limited than in the previous case (Figure 13c).

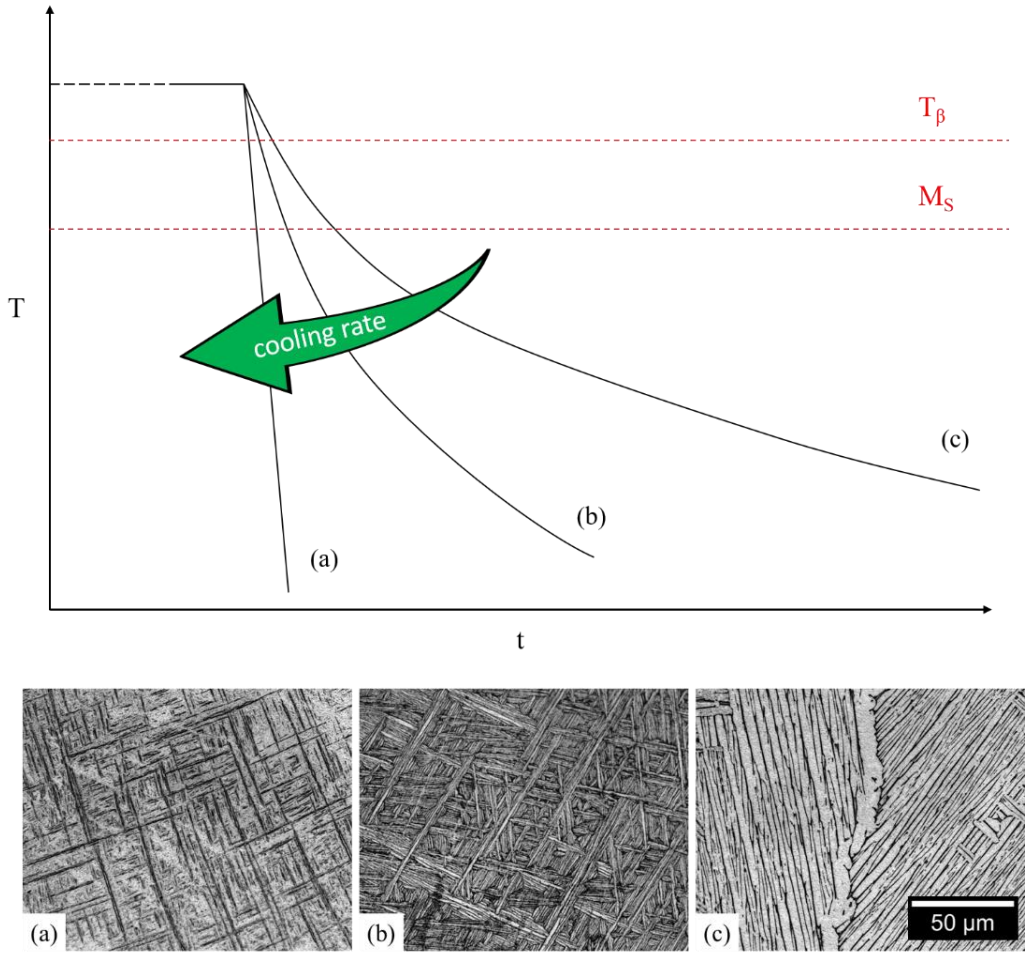


**Figure 13**: Schematic representation of the possible microstructure achievable through annealing of the Ti-6Al-4V alloy from $T > T_\beta$. A fast (a), intermediate (b) and slow (c) cooling rates were considered, which lead to microstructures characterized by martensitic needles, laths in a basket-weave morphology and laths grouped in colonies ($M_S$ was represented as a straight line even if it depends on the cooling rate).

## 1.2 Additive Manufacturing

Additive Manufacturing (AM) is a broad category of disruptive and innovative technologies that allow the production of semi-finished products in a layer-by-layer fashion from a digital input. Unlike most of the other conventional manufacturing technologies, AM techniques do not require subtractive operation per se, which is particularly appealing in terms of reduction of materials waste. These kind of systems result also promising in terms of higher flexibility of the overall process, reduction of the manufacturing time, possibility to produce highly complex parts and drastic decrease of product development cycle [28–30].

Whilst at the beginning AM was considered mostly viable for prototyping applications, it grew in popularity in recent years as industries are quickly adopting these kind of systems for actual components production. For example, in the aerospace field, AM was adopted in order to produce the F-15 Pylon Rib by

Boeing [31,32]. The world revenue for AM and associated services more than doubled from 2012 to 2016, growing from 2.25 billion to 6 billion $ [28].

Among all the classes of materials processable (e.g. polymers, composites), metals are quite promising and already successfully applied in several industrial sectors. One of the industrial fields more involved in AM development is certainly the aerospace industry. Major companies, such as Airbus, Boeing and NASA are heavily investing and contributing to the development of this industry. The drivers of this funding campaign are related to two key aspects: reduction of weight and manufacturing cost. The former, related to flying components, is strictly connected to reduce fuel consumption and greenhouse gases emissions. The former depends on the high cost of the high-performance materials typically used (e.g. titanium alloys, composites) and the high amount of wastes during their production, thus low material efficiency. The aim is to reduce the Buy-To-Fly (BTF) ratio, which represents the ratio between the overall mass of the raw material and the final component mass [33]. This value is markedly low for conventional manufacturing technologies, lying in the 12-25 range [28]. A reduction of the manufacturing costs in the aerospace industry can also be achieved through AM in terms of costs related to the production chain. In fact, in this industrial sector, small, complex and high-quality parts, produced in low numbers are usually needed. AM techniques results very cost efficient for small lots, also considering that production can start as soon as a digital design file is produced, thus making this technology particularly appealing. Another AM-oriented industrial sector is the automotive field, where the need for small lots of high complexity lightweight parts, due to fuel consumption reduction, is very similar to the aerospace case. Moreover, another significant advantage of AM lies in the possibility to produce on-demand in-house components only when needed, with a positive impact on inventory and shipping costs [30,34]. The healthcare industry is another important filed in which AM is growing in popularity, mainly due to the high customizability that this family of technologies can provide associated with relatively low production time and costs. This is a very important property, specifically to produce prosthetics, dental implants and other highly customizable components, which can be produced ad hoc according to the patient needs. This peculiarity would be otherwise unthinkable using more conventional manufacturing technologies [30,35]. Similar advantages make AM promising also in the medic field, especially for prosthetics production. Other fields in which AM was successfully applied are the tooling industry, architecture, jewellery, robotics, nanomanufacturing [30,36].

Currently several AM techniques were already developed, these can be grouped according to the feedstock material used and the heat source adopted to melt it, as represented in Figure 14.

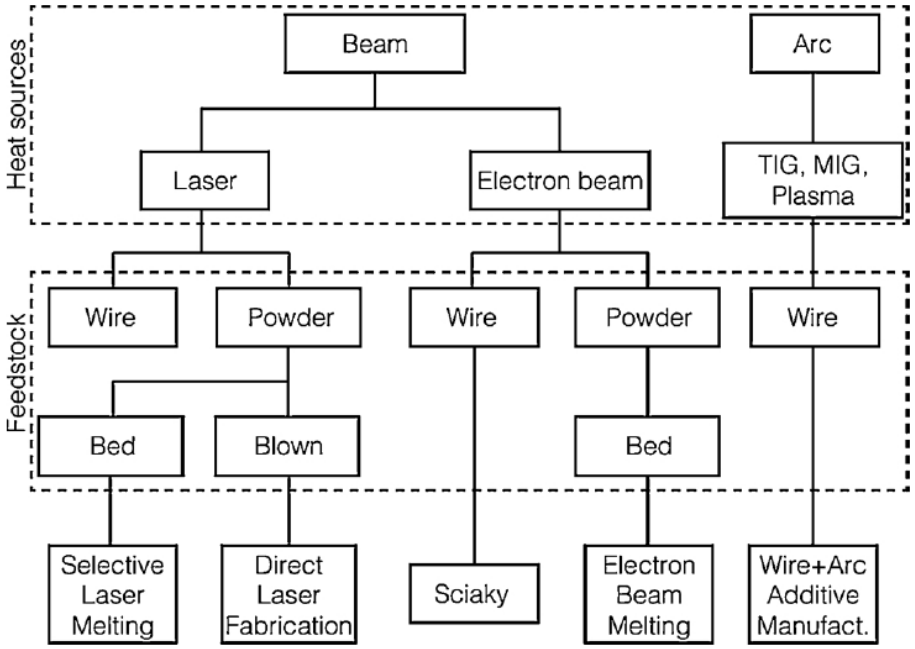


**Figure 14**: Metal AM technologies available, grouped according to the heating source and the feedstock material [28].

In this thesis, only technologies that are based on beams as a heating source are considered. These can be categorized into two main families: laser and electron beams. Both utilize the feedstock material in a prealloyed form, either in the form of a wire or powder. Laser technologies that utilize the latter type of feedstock material can be furtherly subdivided according to the way it is delivered onto the fusion area. A powder bed technology implies that the powder layer is selectively melted, according to the design desired, onto a "bed", usually a flat platform of the same composition. It is then subsequently lowered by a piston of a distance equal to the layer thickness, a new layer is deposited through a recoater/blade and the process keeps going on until the part in completed, as illustrated in Figure 15. Upon melting, the selected areas are fused together, but also welded to the substrate/previous layer. To achieve that, the heating source penetration depth must be higher than the layer thickness. This technology is defined as Selective Laser Melting (SLM) or Laser Powder Bed Fusion (LPBF) [28,37].

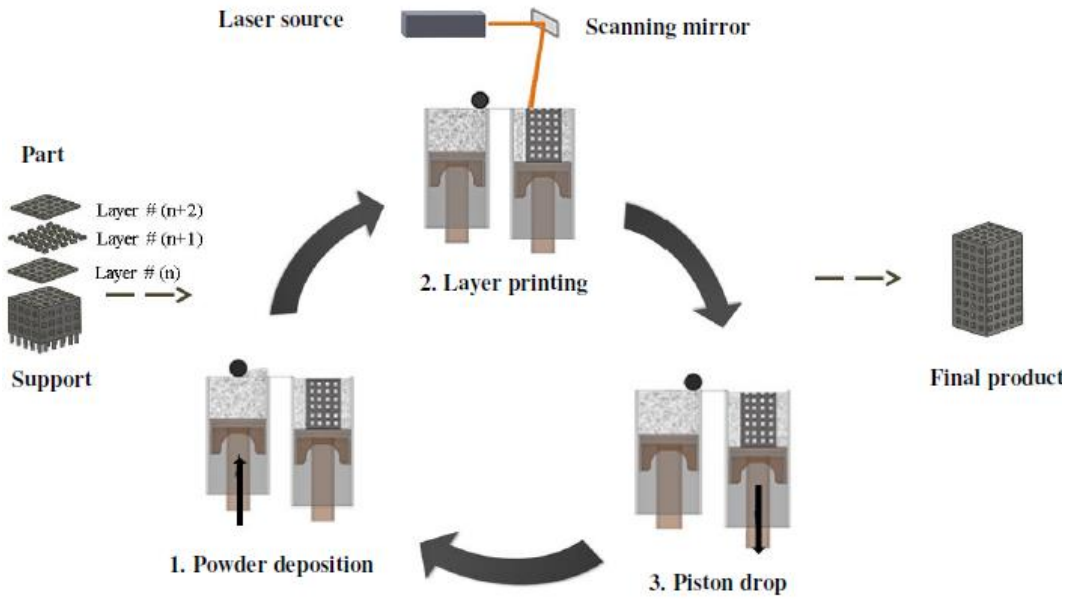


**Figure 15**: Schematic representation of a powder bed process [38].

Oppositely, a blown powder technology implies that the feedstock powder is directly delivered and melted onto the platform through nozzles and a carrier gas flow, as presented in Figure 16. The presence of the gas interferes with the possibility to use a vacuum chamber, necessary to operate an electron cannon, therefore this technology is suitable exclusively when opting for a laser source. It is labelled as Direct Laser Fabrication (DLF) or, most commonly, Directed Energy Depositipon (DED) .

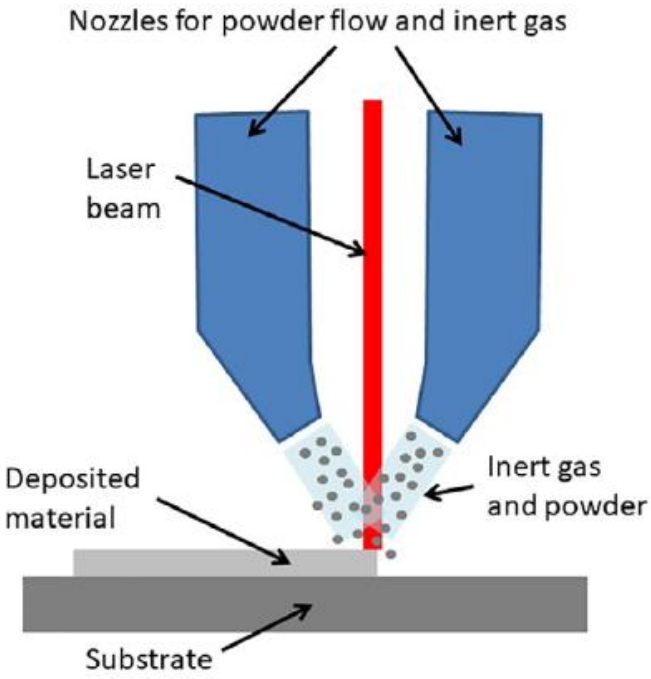


**Figure 16**: Schematic representation of a blown powder system [39].

A powder bed technology that deploys an electron beam, instead of a laser beam, is defined Electron Beam Melting (EBM).

### 1.2.1 Laser Powder Bed Fusion

In LPBF systems, the melting process happens inside a process chamber, which must be carefully controlled in terms, for example, of moisture content and oxygen concentration, which is kept under a threshold value by deploying an inert gas (e.g. N, Ar) flow. These arrangements aim to prevent excessive materials contamination, particularly critical when processing alloys characterized by a high affinity with oxygen (e.g. titanium alloys). Moreover, low concentrations of oxygen are mandatory for security reasons, as fine metallic powder particles might explode or cause a fire.

The final components obtained usually require some sort of post-processing treatment, which can be either mechanical or thermal. In the first case, for example, a common practice is to blast the surface in order to remove the particles not fully adhered to the component. Even after that, the typical surface of LPBF-components is quite rougher than machined components, which is an intrinsic outcome of using powder as a feedstock material. Thus, for applications where surface roughness is a limiting factor, a mandatory machining/polishing step is required. An example of the difference in terms of surface morphology between components produced via LPBF and casting is visible in the scanning electron microscope (SEM) images in Figure 17.

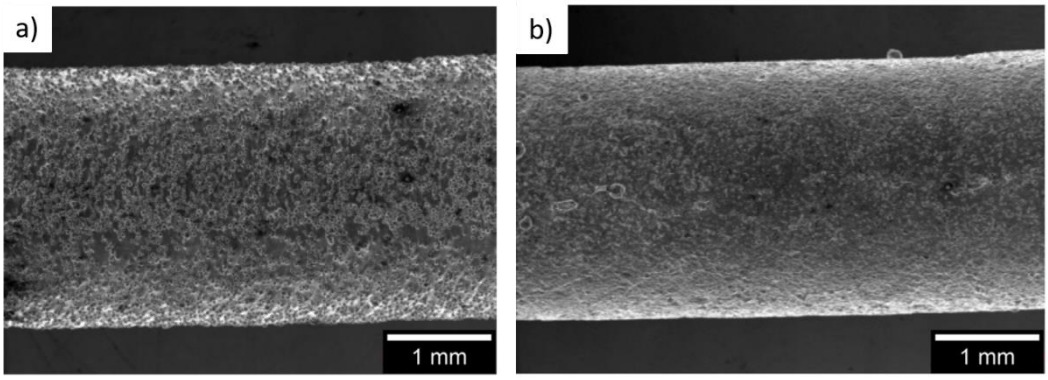


**Figure 17**: SEM images of the surface of Ti-6Al-4V bars produced via LPBF (a) and casting (b) [40].

Post-processing heat treatments are often necessary to relieve the high levels of stress accumulated in the material due to the localized thermal cycles, mentioned before, that cause stress build-up. This phenomenon is more critical for certain alloys that are more prone to accumulate stress (e.g. titanium alloys). Some other materials can effectively mitigate stress accumulation as a result of the platform heating (e.g. aluminium alloys).

Typical LPBF powders are characterized by a particle size distribution (PSD) ranging from 15 to 45 μm. The laser powers involved usually reach up to 500 W, although come machine can provide lasers that can achieve a power of 1 kW.

Compared with other AM technologies, LPBF systems provide smaller laser spots, which result in the possibility to build very thin layers, thus finer features. In fact, LPBF is the most suited AM technology in order to fabricate complex-shaped components characterized by fine and small details. Moreover, recycling of the processed powder is possible after a simple sieving operation. Furthermore, every material needs to be optimized for a certain machine, in terms of process parameters, such as laser power (P), scanning speed (v) and hatching distance (h.d.), which can be an expensive and mandatory step both in terms of money and time. Although, this also means that an ad hoc optimization according to the specific features, properties or geometries required can be performed on every component.

The main downsides of this technology lie in its process time, as a typical job is usually quite slow. In fact, small layer thicknesses and laser spots, hence meltpools, are adopted. These characteristics in addition to the high level of stresses induced in the material, due to the extreme thermal gradients reached, can cause cracking or extensive distortion of the components. The latter is partially solvable via proper design and platform temperature manipulation [37].

### 1.2.2 Electron Beam Melting

Even if LPBF and EBM are both powder-bed technologies, thus sharing a certain number of similarities, such as the presence of a powder bed and a sealed process chamber, there are significant differences between these two techniques. For example, unlike LPBF, the EBM technology, invented by the Swedish company Arcam, deploys an electron beam, which requires the process chamber to be in vacuum, with a small amount of helium acceptable. This is a necessity in order to operate the heating source, because in a gaseous environment (e.g. air, inert gas) the electron from the source would collide with the gas molecules and be deflected. Another important difference lies in the platform temperature, which is markedly higher in EBM, reaching up to 1100 °C when processing certain materials. Therefore, the typical thermal gradients of EBM are significantly less severe than in LPBF, resulting in a lack of stress building-up during the process. Hence, a post-processing heat treatment is often not necessary in order to stress relief the component, although heat treatments with the aim to increase certain properties are often applied. However, the combination of a vacuum environment and high temperatures can cause the depletion of some elements that evaporate during the process (e.g. Al in Ti-6Al-4V). This issue is only solvable by properly designing powders with an excess of the depleted element in composition, in order to counterbalance the variation in composition induced by the system itself.

An important step during the process, that completely lacks in LPBF, is the defocus phase. During this, the electron beam is defocused, in order to scan the whole powder bed, causing a slight sintering of the powder. This phenomenon causes the bed to be more stable and markedly more efficient in supporting the

parts built. This is advantageous in terms of design, as fewer external supports need to be designed and added to the original design, with consequent cost and time saving during post-processing operations. The semi-sintered powder is so stable that multiple parts can be stacked on top of each other, in order to utilize the chamber room more efficiently.

The typical power involved in this process is markedly high and can reach 6 kW. This means that powders characterized by larger particles can be used, in fact the typical PSD lies between 45 and 105 μm. Layer thickness is also generally higher than in LPBF reaching up to 0.2 mm. This means that EBM is a faster process than LPBF. Although the resulting surfaces are markedly rougher, as illustrated in Figure 18.

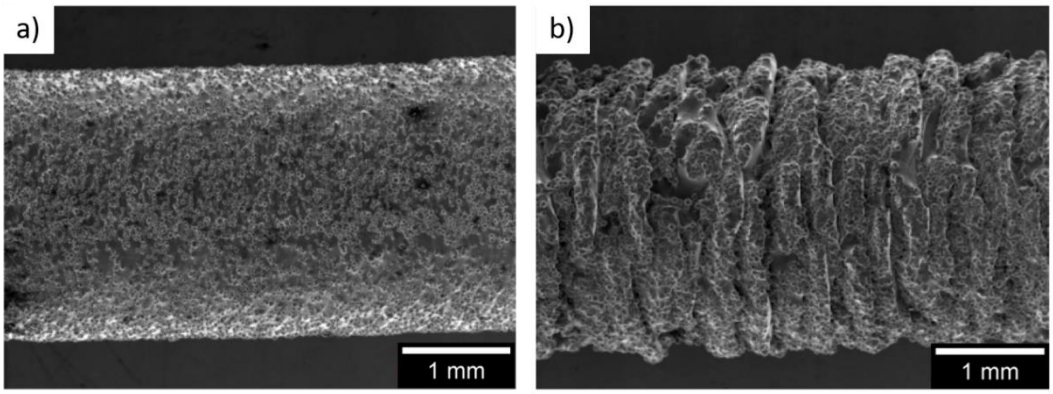


**Figure 18**: SEM images of the surface of Ti-6Al-4V bars produced via LPBF (a) and EBM (b) [40].

Surface roughness is noticeably higher mainly due to the presence of a conspicuous number of unmelted or partially melted particles (large in size) on the external surface of the components. This behaviour is associated with the higher thermal radiation typical of the EBM process and also with the larger meltpools created, as both these are detrimental in terms of surface quality [41]. As illustrated in Figure 19, the amount of poorly melted particles, that adheres to the external part of the grown object, can be very abundant, thus impacting enormously on the final surface morphology.

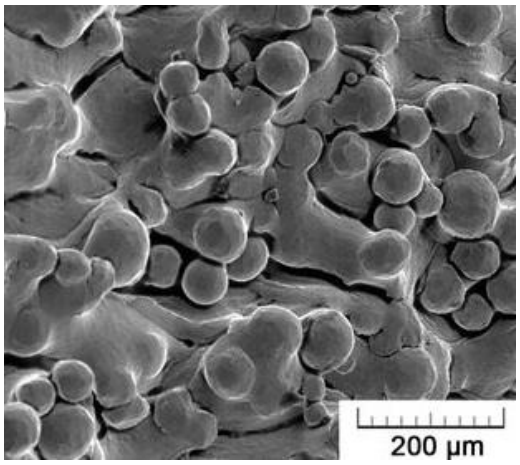


**Figure 19**: Representative higher magnification SEM image of the surface of a Ti-6Al-4V sample built via EBM [42].

At the end of the process, the components built are encapsulated in a cake of sintered powder. Unlike in LPBF systems, where the component is surrounded by unmelt powder, which can be easily removed, in EBM the cake is more difficult to remove and must be broken down by a specific machine, called powder recovery system (PRS). This system bombards the cake using a metal powder, in order to remove the unsintered particles from the component. The powder obtained from the PRS can then be sieved and reused [37].

Powder reuse is a very important feature of AM processes, as it drastically increases the level of material utilization. However, powders are affected by the processes they undergo, especially if used multiple times. Moreover, usually reused powder is added to virgin powder, making the tracking of the powder history very complex as it is used more and more. A general process can affect a powder by inducing a chemical change, which affects the final material composition, and/or a variation in physical properties (e.g. surface roughness, particles shape), which might result in issues during the process, such as clogging or process parameters inadequacy. Using the Ti-6Al-4V alloy as an example, several studies investigating this issue are available. For example, Zenou et al. [37] reported a study from Renishaw on LPBF, which highlights how the reused powder lost the finer fraction of particles, due to sintering and/or volatilization, thus increasing its D(50). The shape of the particles remained highly spherical even after processing, therefore the overall flowability increased. Concerning EBM, Tang et al. [43] found that, after being processed in the PRS, the powder became rougher and lost sphericity in its particles, moreover aluminium depletion was evident. In both casees oxygen pick-up was noticed.

The main advantages of the EBM systems lie in the possibility to control residual stresses, via low thermal gradients; faster processes, with respect to LPBF, which means that EBM is more suited for components bigger in size; in a reduced importance of the external supports, as the cake easily holds most of the components weight.

The limits of this technology are the choice of materials, as only conductive materials can be selected; the complex process necessary to recover the powder, which is quite unsatisfying in terms of powder reuse, due to the consistent morphological changes induced in the powder particles; possible element depletion.

### 1.2.3 Directed Energy Deposition

As mentioned before, DED technologies deploy a laser beam in order to deposit a powder on a baseplate, usually of the same composition, through nozzles mounted on a multiaxis arm. The feedstock material is then melted and the process keeps going on in a layer-by-layer fashion until the component is fully built. The most common DED machines are equipped with a 2/3-axis system, where the base is fixed and only the arms are raised at each layer, or a 4/5-axis

system, in which also the base can move, granting more movement freedom and the possibility to manufacture more geometrically complex components. An interesting feature of these system is the lack of a flat surface requirement in order to start the process. This characteristic is very promising for remanufacturing/repairing application. For example, Wilson et al. [44] proved the worthiness and attractiveness of these technologies for repairing applications in high-value industrial fields, such as the aerospace sector. The authors were able to repair a turbine blade by means of laser deposition.

Usually the process is conducted in a protective environment, such as an inert-filled chamber or a gas shroud. The optimization of the environment is particularly critical when handling reactive metals, which are very susceptible to contaminations.

Delivering the powder onto the layers through nozzles, DED systems are well-suited for high deposition rates. In fact, the typical deposition rate of laser DED machines lies around 3 kg/h, whilst for LPBF systems is typically an order of magnitude lower. Considering that and the higher freedom granted by the possibility to change the process chamber according to the user necessity, DED results the most suitable technology for producing larger, bulkier components.

A common phenomenon for DED processes is the residual stresses build-up, similarly to LPBF machines, due to the intense and localized thermal cycles, which induce very rapid expansions and contractions in the material. These phenomena might lead to undesired consequences, such as cracking and/or distortion of the component. Thus, a stress relieving heat treatment is usually mandatory.

The main advantages of DED systems are the possibility to build on non-flat surfaces, which makes this technology appealing for repairing or building on pre-existing parts; the high deposition rates granted; the possibility to mount on the multi-axis systems a CNC system, by deploying the high degree of freedom granted by the movement of the robotic arms and achieving a system than can perform additive and subtractive operations altogether.

The disadvantages of DED systems are mainly the quality of the components, which is worse than powder-bed fusion systems, both in terms of ability to build complex features and to create channels/voids; Spraying the powder on a layer is a quite inefficient way to deliver it, since most of it does not melt and results wasted, which means that the material efficiency of the process is quite low [37].

### 1.2.4 Materials for Metals Additive Manufacturing

Currently only a limited number of the alloys available in metallurgy are processed via AM techniques. Although a growth in the number of materials available to be processable is expected to grow in the near future. Consistent efforts are being made in studying, for example, intermetallic compounds and high entropy alloys specifically designed in order to be optimized for AM

applications [45]. Among the kind of alloys accessible at present, the main categories are:

- **Steels**. Probably the wider class, consisting of very different types of alloys, such as maraging, tool and stainless steels (precipitation hardenable and not). These materials are generally applied when strength and hardness need to be maximized. Some of the most commonly used steels are AISI 316, AISI 316L and PH 17-4.
- **Aluminium alloys**. Characterized by the relatively low cost of the feedstock material and high machinability, which are the reasons why initially these alloys were not thoroughly studied. Although this trend reverted recently as aluminium alloys are gaining increasingly attention. Aluminium alloys are characterized by some critical properties, which result in some difficulties when processed via AM. For example, most of them show low weldability, a key property for AM materials as in general a weldable material is also processable [37], high reflectivity for laser wavelengths used in AM systems and high liquid viscosity, which results in the impossibility to create large meltpools [29,32]. The latter property is a key aspect, which explains why most of the aluminium alloys are part of the Al-Si systems, as silicon increases fluidity in the molten state [46]. Moreover, Aluminium alloys are not processable via EBM, because the high temperature of the process in a vacuum environment results in extensive evaporation of the material. Aluminium alloys gained a lot of attention due to the studies made on scandium additions beyond the eutectic point, which resulted in AM materials very promising for the aerospace industry. These are characterized by both high strength and a ductile behaviour [47]. A typical AM aluminium alloy is AlSi10Mg.
- **Nickel superalloys**. Specifically designed for high temperature applications, due to their exceptional mechanical properties, and oxidation and creep resistance. Controlling the microstructure, in particular the precipitation of different secondary phases is of upmost importance for these materials. The most commonly used alloys are Inconel 625 and 718.
- **Titanium alloys**. As discussed before, this class of materials is ideal for AM, mainly due to the difficulties linked to processing/machining them using conventional technologies. The related long lead-time and high machining costs result in a high appeal of the AM technologies for reducing costs and wastes, especially when complex structures need to be produced [32]. These alloys are also the main focus of this thesis work; therefore their analysis will be conducted more thoroughly and deeply. The progress in research in this category are numerous and fast, leading to a number of alloys available increasingly growing. Alongside the conventional Ti-6Al-4V and cp-

Ti, several α+β and β alloys are currently processable via AM techniques (e.g. Ti5553 [48] Ti-6Al-7Nb [49], Ti-24Nb-4Zr-8Sn [50] and Ti-21Nb-17Zr17Zr [51]). Moreover, more unconventional compositions are gaining attention recently. For example, among the rare earths used as alloying elements, erbium resulted particularly promising, due to its high solid solubility in Ti. Bush et al. [52] studied the Ti-8Al-1Er alloy, which formed thermally stable $Er_2O_3$ upon precipitation (radius < 0.5 μm). Usually, oxide dispersion is beneficial in rapidly solidified alloys, as it can cause extensive strengthening.

In general, AM techniques involve rapidly cooled/heated layer by layer steps, which result in very complex temperature profiles throughout the whole process, which are also strictly time-dependant, as illustrated in an example in Figure 20. Each given layer is melted and heated multiple times, thus phenomena that induce several repeated transformations in the solid state and upon the solidus-liquidus transformation, depending on the material, occur.

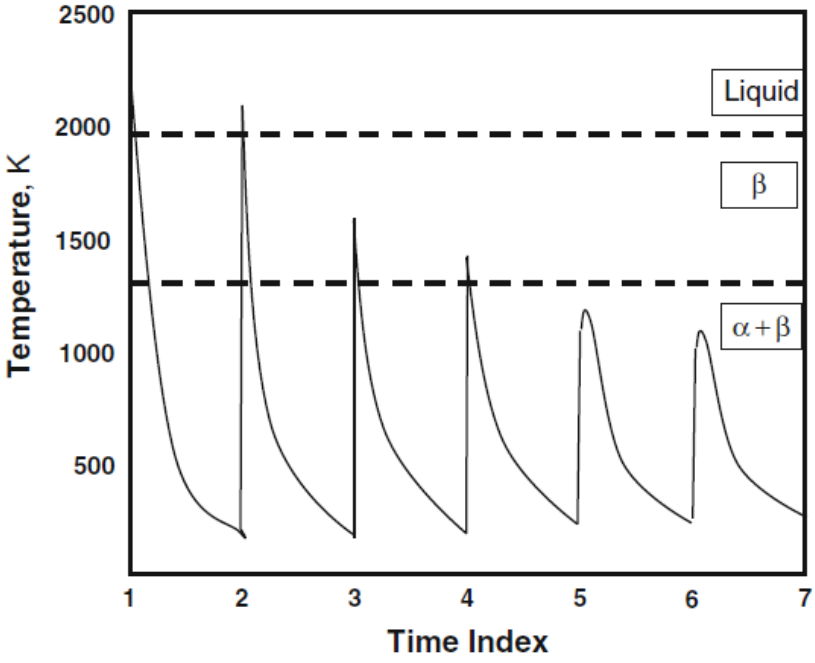


**Figure 20**: Thermal cycle of a given point of laser-deposited Ti-6Al-4V [29,53].

Moreover, during the cooling phase the heat flow is highly directional. This results in a mostly columnar microstructure, which leads, for example, to directional grain growth, thus columnar grains. Furthermore, the rapid solidification drastically reduces elements partitioning, which might result in metastable phases formation (e.g. martensite in steels), and that repeated thermal cycles can possibly induce phase transformations, leading to banding or properties dependant on a given layer. All these phenomena greatly influence the final microstructure of a material at a complexity level unfamiliar with most conventional manufacturing processes [29,54,55]. Even if this intricacy of

phenomena and properties might lead to materials characterized by even superior properties than their counterparts obtained through conventional manufacturing techniques, it is also the reason why most alloys are hardly processable via AM. In fact, most alloys do not result processable due to the melting/solidification dynamics typical of these technologies, which result in unacceptable features, such as extensive cracking [32]. Although new studies are trying to solve this issue, in order to make new alloys processable. For example, Martin et al. [56] were able to successfully 3D-print the high strength aluminium alloys 7075 and 6061, usually non processable via AM techniques, by inducing the nucleation of nanoparticles during the process, which granted control over the solidification behaviour of the material.

## 1.3 Additive Manufacturing of Ti-6Al-4V

As discussed before, AM is gaining popularity and importance throughout the years. The first techniques were already known more than 20 years ago, although these were only considered for the production of porous structures or prototypes [57]. The growth of these technologies in recent years has been very marked, especially for some types of alloys which are particularly promising for AM production, as these materials are already used in industrial sectors already characterized by the necessity of high-quality, customizable components or small lots production. In this category lie the titanium alloys, which recently gained a lot of popularity when associated to AM technologies, both in industry and academia. In Figure 21a is provided the annual number of papers published relative to the Ti-6Al-4V alloy produced via different AM technologies for the 2010-2019 decade. The data were gathered using Scopus as a data bank. A certain number of papers regarding simultaneously more than one technology might slightly change the resulting trend, as these were counted as separate works each time, providing a slight overestimation of the total number. Although, the overlaps were found to be quite negligible if compared to the total number of papers considered (3690), as illustrated in Table 1. Hence this little variation from the real number was considered acceptable.

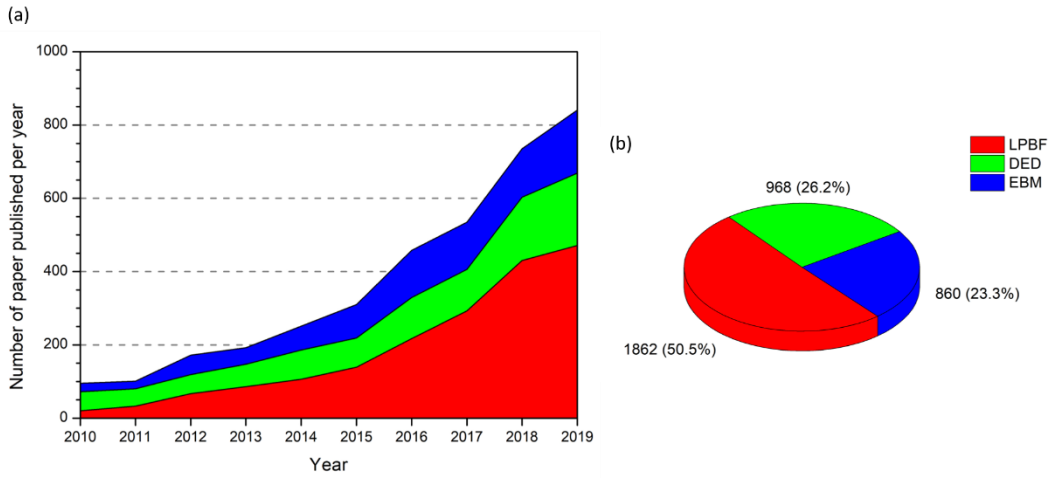


**Figure 21**: Number of paper published per year studying the Ti-6Al-4V alloy produced by means of LPBF, DED and EBM in the period 2010-2019 (a) and relative pie chart for the total amount of papers published throughout the last decade (b).

**Table 1**: Numbers of papers accounting for more than one technology throughout the whole decade (in couples).

| EBM - LPBF | EBM - DED | LPBF - DED |
|---|---|---|
| 143 | 28 | 51 |

A constant growth throughout the years is evident for all the technologies, particularly in the second half of the decade. In Figure 21b is presented the pie chart relative to the total number of publications, from which the marked interest for this alloy manufactured using the LPBF technology is evident, as the number of works available exceeds the numbers of the ones relative to EBM and DED combined. This manifest difference is probably correlated to the ability of this technology to produce higher quality components, which are particularly appreciated in the aerospace field, which is the industrial sector in which most of the titanium alloys are utilized, as mentioned before. Moreover, the EBM systems commercially available are currently considerably more expensive than LPBF systems. This translates in a harder diffusion of this technology in universities/research facilities.

## 1.3.1. Electron Beam Melting of the Ti-6Al-4V Alloy

The typical microstructure obtained in Ti-6Al-4V samples produced via EBM is usually complex, as it is composed of different phases and morphologies altogether. Commonly to most AM processes, the prior-β grains grow epitaxially and parallel to the building direction in a columnar morphology. These are usually very fine due to the combined effect of small meltpools and relatively high cooling rates [58,59]. The microstructure is composed by transformed α and β phases, arranged both in lamellar colonies and following a Widmanstätten pattern,

resulting from α' decomposition [60–63]. Additionally, a continuous layer of α phase commonly delineates grain boundaries ($\alpha_{GB}$). It forms due to the diffusive phenomena facilitated in the process chamber, whose temperature is quite high throughout the whole process (≈700°C). α phase nucleation is facilitated at grain boundaries and its growth is usually perpendicular to $\alpha_{GB}$ itself, thus generating lamellae. Their size, length and spatial distribution is a function of the meltpool temperature and the cooling rate. If the latter increases, the microstructure results finer, both in terms of grain size and α width [59]. A representative image of a typical Ti-6Al-4V microstructure obtained via EBM is provided in Figure 22.

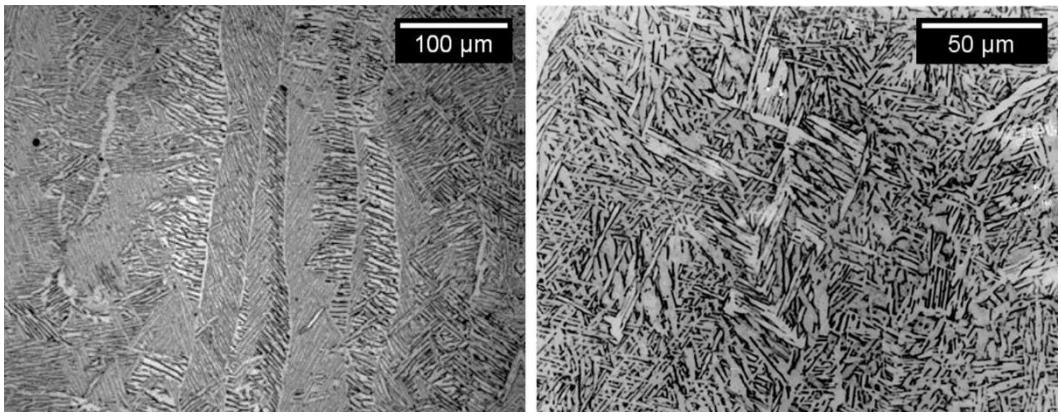


**Figure 22**: Representative optical micrographs of Ti-6Al-4V microstructures obtainable via EBM [61].

This type of microstructure is the result of multiple complex thermal cycles that the sample undergoes during fabrication. The solidification of the molten powder is rather quick. However, as the number of layers increases, a given point is also influenced by the numerous thermal cycles of the upper layers. As the process keeps going on, the overall cooling rate decreases and thermal accumulation becomes consistent. When a given point is melted for the first time, the cooling rate in high enough to accommodate α' martensite formation, which is although seldom present in the final microstructure, as the permanence in the process chamber acts as a prolonged annealing heat treatment, able to decompose it [62,64], as illustrated in Figure 23. Furthermore, the chamber temperature is relatively high, which results in unique microstructures granting a good combination of strength and ductility in the sample [65,66].

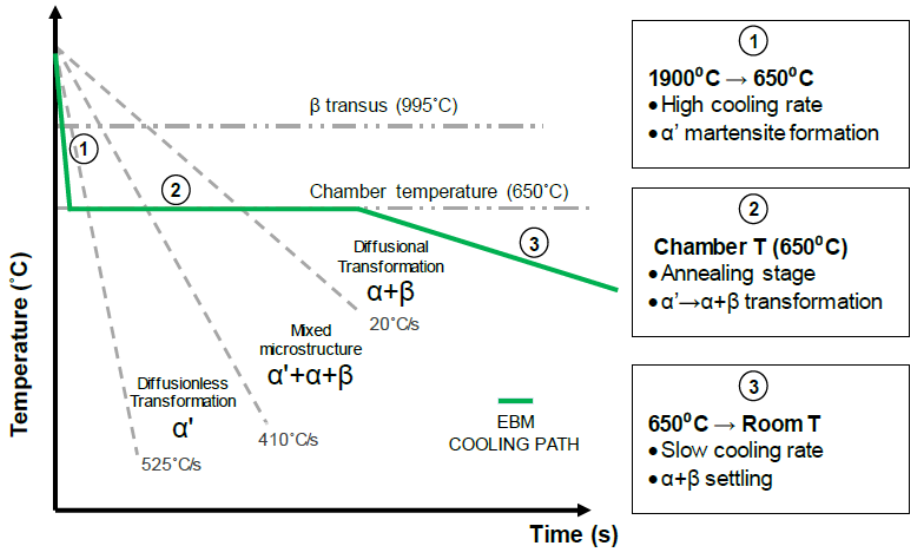


**Figure 23**: General representation of the overall thermal cycle that a Ti-6Al-4V part undergoes during EBM fabrication [64].

As mentioned before, the cooling rate varies during the process. As it is one of the most important factors that influence the final microstructure in titanium alloys, a certain degree of variation in the microstructure is present in the sample if different areas (e.g. top and bottom) are compared. For example, Tan et al. [60] highlighted significant differences in terms of phase spacing, grain width and mechanical properties between the top and the bottom parts of samples produced via EBM. For example, grain width increased accordingly to the sample height, in fact the cooling rate is reduced as multiple layers are added. Moreover, Zhao et al. [66] demonstrated how α-laths thickness is lower in components smaller in size, thus increasing the overall strength of the material. Oppositely, more ductile samples are associated with a bigger size. The geometry of the specimen is another factor influencing the microstructure. For example, Murr et al. [67] highlighted how the microstructures of mesh-type prototypes were instead composed mainly of α' martensite or a mixture of α and α'.

In general, a given set of parameters can provide an increase in grain size and a decrease in α width contemporarily. These two features variations act oppositely with respect of their influence on yield strength, as the former would decrease it, whilst the latter would act in an opposite way. Therefore, the micro-melting provided by the electron beam grants unique material properties in EBM Ti-6Al-4V, whose relationship between thermal history, process parameters, microstructural features and mechanical properties is still not completely understood [59]. Overall, the typical ultimate tensile strength (UTS) is close to that of wrought samples, but other tensile properties such as YTS and ductility (ε) are generally superior [59].

The orientation of the sample during the fabrication process is also markedly important. In fact, it has a strong influence on the mechanical properties of the component produced. Specimens built parallel to the development direction are usually characterized by a slightly higher YTS, mainly due to texture effects and

microstructural anisotropy [68]. The initial studies on the specimens of Ti-6Al-4V manufactured by means of EBM suggested contrasting results in terms of tensile properties with respect to the same material produced using conventional technologies [67,69]. Facchini et al. [70] were able to obtain samples characterized by a superior UTS than wrought or annealed ones, although ductility resulted lower. Oppositely, Koike et al. [40] highlighted how the tensile mechanical properties of EBM Ti-6Al-4V were inferior, both in terms of UTS and ε, than samples produced by means of casting. The opposite results in these two examples were probably caused by different process parameters adopted and possibly by variations, for example, in terms of powder composition or porosity [58]. Although, these works are now 10 years old and since then the knowledge on how the machines work sensibly increased. Moreover, the experience gained on the process allowed to achieve higher levels of optimization. In fact, EBM tensile properties are now widely accepted as comparable with other conventional manufacturing processes. In fact, EBM-ed Ti-6Al-4V can even meet the minimum requirements in order to be considered in the mill-annealed condition, according to ASTM-B348, which also correspond to the inferior threshold values for additive manufactured products in ASTM-F2924 [71], reported in Table 2.

**Table 2**: Minimum tensile mechanical properties for the mill-annealed condition.

| YTS [MPa] | UTS [MPa] | ε |
|---|---|---|
| 825 | 895 | 10% |

Even if there are reports highlighting that the requirement for ductility is not always granted, EBM is the only AM technology providing such a promising combination of mechanical properties already in the as-built state, without even stress relieving. In fact, the study on the possible heat treatments gathered much less attention than, for example, LPBF, in which thermal post-processing is mandatory [72]. However, some studies are available concerning the heat treatment of the Ti-6Al-4V alloy produced via EBM. Among those, the most interesting seem to be the ones performed at $T > T_\beta$, in order to achieve a completely acicular or Widmanstätten morphology, usually obtained via annealing in specimens produced using other AM techniques [59].

Data scattering is currently still an issue, as highlighted by the collection of data provided in Figure 24, where the dispersion of the number is evident, as the UTS ranges from approximately 900 to 1200 MPa and ε variates from 7% to 18%.

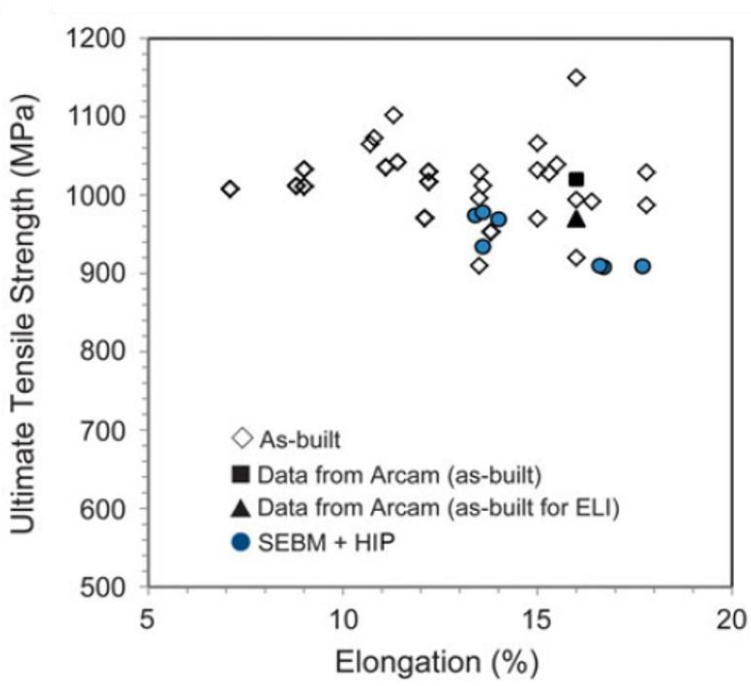


**Figure 24**: Collection of data on UTS and ε of EBM produced Ti-6Al-4V in different conditions [72].

The most probable causes of these phenomena are possible differences in terms of oxygen content/pick-up or the insurgence of some critical issues/defects, typical of the EBM process, during the manufacturing step. Of course, the latter depends on the choice of process parameters, which then have a direct influence on mechanical properties, by influencing for example the meltpool size, temperature and the cooling rate of the process, and an indirect influence by inducing the generation of process-related defects. Among these, the most common one is pores formation, which may be spherical (Figure 25a) or irregular (Figure 25b). The former type of pores is usually caused by residual gas entrapped into the feedstock material during the atomization process. The distribution of these defect throughout the sample is not uniform, as these tend to accumulate more consistently at the end of scanning lines [73]. Instead, the irregular shaped voids are often referred to as “lack of fusion”. In fact, these types of defects are strictly related to the process parameters and they often form when the energy delivered is insufficient to completely melt the layers underneath the powder. This kind of pores usually forms between layers and results perpendicular to the development direction [62].

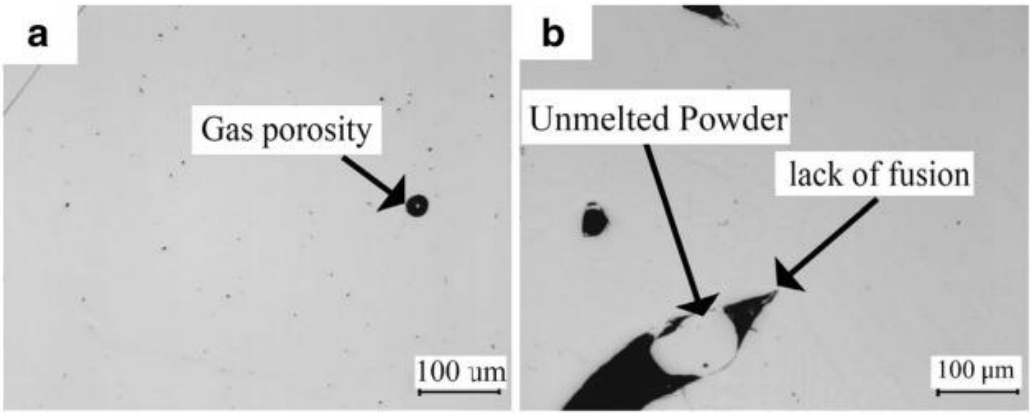


**Figure 25**: Example of a spherical gas pore (a) and a lack of fusion void (b) [74].

Even if the formation of lack of fusion voids can be avoided via proper process parameters choice, gas porosities can only be minimized, as these types of defect is intrinsic in the feedstock powder. In general, EBM samples achieve density values higher than 99.9% [65]. Gaytan et al. [75] investigated hot isostatic pressing (HIP) (0.1 GPa, 900 °C, 2 h) as a possible mean in order to solve the porosity issues of Ti-6Al-4V components produced by means of EBM. This technique resulted promising in eliminating most of the porosities, therefore showing a beneficial effect, for example, in extending the fatigue resistance of the material, as most initiations sites are usually near these defects [76]. However, the smaller pores (< 10 µm), which are also the most marginal in terms of impact on the tensile mechanical properties, were still present at the end of the HIP process. These voids are extremely hard to eliminate, mostly due to the low gas pressure and the high surface tension. In conclusion, HIP appears as a promising post-processing step in order to, most of all, improve the material fatigue resistance. Unfortunately, it also causes grain coarsening, therefore lowering YTS, nullifying one of the biggest advantages of the EBM technology. Adopting a lower temperature during HIP might partially limit this downside. Ideally, the optimal solution would consist in minimizing the porosity without using a HIP system. Although, the mechanism driving the formation of these defects is still not completely understood [60], the most likely causes might be the presence of pre-existing defects in the feedstock material, incorrect process parameters choice, balling, excessive element vaporization and inhomogeneous collapse of the keyhole [77]. The latter is a vapour capillarity forming due to the effect of a recoil pressure occurring due to the evaporation of the metal during the process, which pushes the liquid away from the melting area. In order to occur, the temperature of the meltpool must exceed the boiling point of the molten metal itself. This condition is more likely to happen in EBM systems, in which the vacuum environment aids evaporation. It is also more common in Ti-6Al-4V due to the aluminium depletion typical of this process [59]. Some defects form during the solidification of the capillarity, which corresponds to the central part of the meltpool. Furthermore, the electrons from the source are likely to be reflected by

the inner walls of the keyhole, thus being focalized at the bottom of it. This phenomenon causes a localized rise in temperature in the lower part, causing a deep penetration of the electrons into the material. In general, when the cooling rate is higher in the lower portion of the meltpool, pores, or similar defects, are generated [77]. An example of a typical keyhole-related porosity is provided in Figure 26.

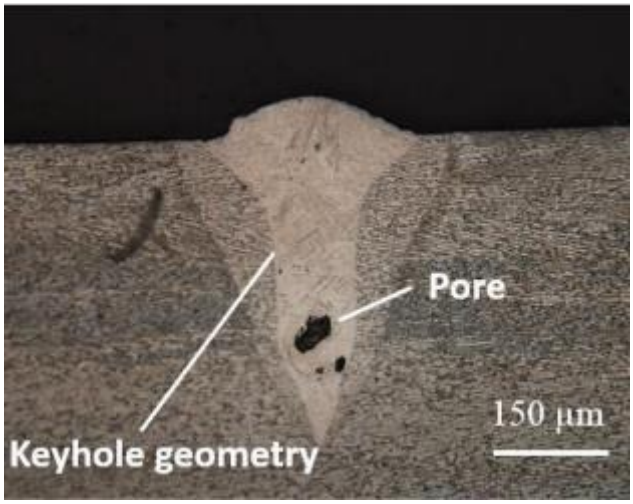


**Figure 26**: Example of a pore forming in the lowest part of the keyhole [78].

Delamination is another common process-related issue, consequence of the excessive selective heating of small areas, typical of the EBM technology, in conjunction with an unproper design, which cause the detachment/collapse of layers in the specimen (Figure 27). If the energy delivery is not properly designed and not uniform, the resulting residual stresses, caused during solidification, might exceed the bonding ability of the material [79].

**Figure 27**: example of delamination [80].

## 1.3.2. Laser Powder Bed Fusion of the Ti-6Al-4V Alloy

In general, the Ti-6Al-4V alloy produced via LPBF is characterized by a microstructure rather different than its EBM-manufactured counterpart. The columnar prior-β grains parallel to the development direction are a shared characteristic between these two powder bed technologies. However, in LPBF machines, the chamber temperature is rather low and the "annealing" phase, typical of the EBM technology is completely absent. Therefore, the resulting microstructure is mainly or completely formed by acicular α' martensite, as a very high cooling rate, lying in the $10^3$-$10^8$ °C/s range(>> 410 °C/s), is applied from temperature well above the $M_S$ [81], as a result of the very high temperature gradients typical of this technology. As discussed before, the cooling rate is one of the most impacting factors on the microstructure. Therefore, its control via proper process parameters manipulation is a powerful tool to tune the microstructure, hence the mechanical properties, for specific applications [35]. However, the influence of the process parameters on the microstructure of Ti-6Al-4V samples is still not understood completely. For example, Do et al. [82] obtained larger martensitic laths in correspondence of a lower cooling rate, derived from a high volumetric energy density (VED) value, suggesting that a slower cooling lead to the formation a coarser microstructure. Oppositely, Han et al. [83] found that an increase in VED resulted in a decrease in α' width and spacing, but grain width grew instead. Moreover, the process does not grant a lot of freedom in terms of process parameters variation, as these are strictly defined in order to maximize the density of the sample. Therefore, the final microstructure is still largely martensitic, if porosity minimization is considered [35]. An example of a representative microstructure is provided in Figure 28.

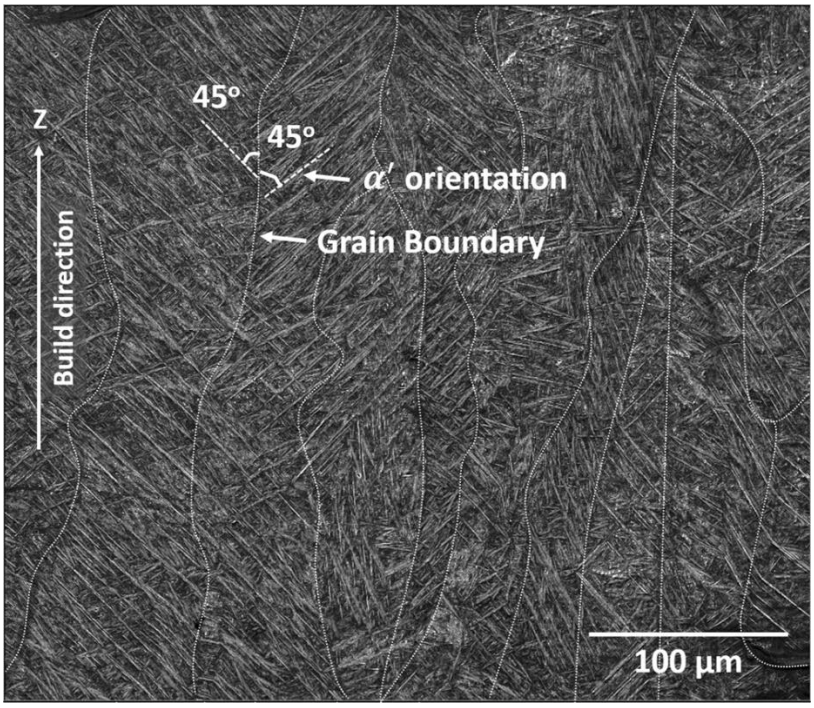


**Figure 28**: Representative microstructure of a Ti-6Al-4V sample built by means of LPBF [84].

Yang et al. [24] reported the presence of fine α' needles, ranging from primary (1-3 μm in width) to quartic (< 20 nm in width) martensite (Figure 29). Of course, the type and size of the martensitic features is directly dependant on the thermal history of the process, therefore depending on process parameters and scanning strategy. The formation of stable α phase is possible in small amounts in a α+α' mixture, if the process is properly planned in order to allow the production of a meltpool large enough to promote diffusion [85].

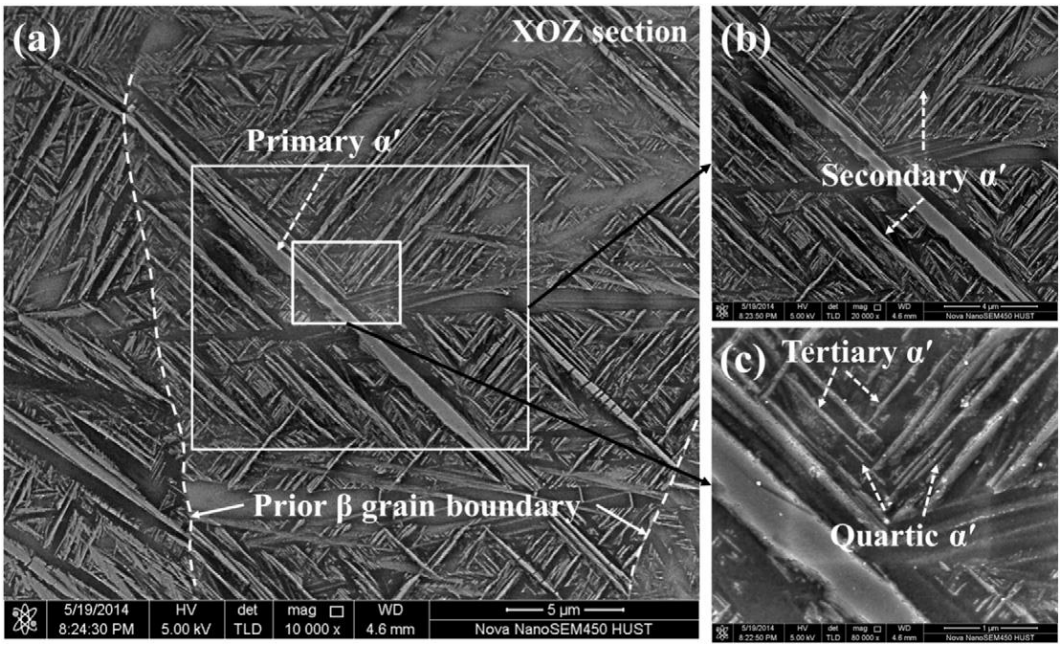


**Figure 29**: Hierarchical α' microstructure found in Ti-6Al-4V processed via LPBF [24].

In terms of the effect that the microstructure has on the mechanical properties, α' grains grown epitaxially are a more efficient barrier to dislocation motion than α grains in similar conditions. This outcome is interesting for some applications in which high strength and hardness are required. Although, ductility results severely reduced and well lower than 10%, which makes LPBF as-built components unacceptable, for example for biomedical applications, as described by the aforementioned ASTM-F2924 [71]. To achieve that, a more thermodynamically stable lamellar α+β microstructure is mandatory [35]. Martensite decomposition can be obtained via in-process or post-process steps. The former method aims at achieving the α' transformation in situ, via proper process parameters manipulation in order to induce a localized annealing heat treatment [86,87]. Another possible mean consists in powder bed pre-heating, a common way-to-go to reduce thermal cracking and residual stresses. If properly managed, a raise in platform temperature corresponds in a reduction of the cooling rate, which promotes diffusion, hence the α' → α + β decomposition [88]. However, all these methodologies require a certain freedom to manipulate process parameters, which are however only slightly adjustable, as mentioned before. Post-process microstructural changes are instead achievable via heat treatment and/or HIP [89,90]. These are usually the common way-to-go, which requires less time and

money to be optimized. However, a common consequence is usually grain growth, which has a negative impact, for example, on the yield strength. Moreover, the in situ decomposition, even if more expensive and less understood, can provide more precisely tailored microstructures [81].

In general, as the ability to model and deeply understand the LPBF systems and related phenomena increases and the process becomes more appealing, the focus of the research shifted from trying to obtain mechanical properties similar to the conventional technologies towards tailoring unique microstructures and optimized mechanical properties, deploying the added complexity and freedom granted by this technology [81]. Unlike in EBM technologies, which provide a good balance of strength and plasticity, SLM-manufactured Ti-6Al-4V is characterized by an outstanding yield strength (~ 1100 MPa) in the as-built state. Although, its ductility is rather low (5% - 7%) [89]. This outcome is the result of the presence of very fine α' martensite, which is particularly efficient at hindering dislocations motion. Not considering heat treatments, the same alloy produced via casting is comparably ductile (ε ~ 5%) but definitely less strong (YTS < 900 MPa) [91,92]. Being the mechanical properties already superior pre-heat treatment, naturally the study of post-processing gathered much more attention in the field of optimizing specific properties (e.g. ductility), without compromising the optimal mechanical properties obtained via LPBF, rather than achieving a close similarity to other conditions, typical of a different manufacturing route[93].

As mentioned before, a post-processing heat treatment is the most widely used approach in order to decompose α', as it is the main cause of the brittle behaviour of the samples. The main goal is usually to achieve a duplex microstructure with the proper morphology. This causes an increase in ductility, due to the intrinsic superior plasticity of α and β phases. In fact, α' slip length is confined within a single grain, resulting in dislocation pile-up. In a duplex lamellar microstructure instead, slip transfer is possible between different phases, resulting in an increase in dislocation movement, which results in improved ductility [94].

In general, a heat treatment is defined based on 3 important parameters: temperature (T), time (t) and cooling rate. Concerning the former, Wu et al. [95] conducted a study on the microstructural evolution of Ti-6Al-4V samples produced by means of LPBF via optical and SEM imaging. They obtained negligible variations when the heat treatment was performed at temperatures lower than 600 °C. However, when T was raised, especially in the 750 – 990 °C range, martensite disappeared in favour of an increasing volume fraction of α phase. Moreover, if a temperature higher than 1000 °C was used, value which lies above $T_\beta$, a similar result to the previous case was obtained, although the recrystallization, linked to the complete β transformation at high temperatures, allowed a change in the grain shape, from columnar to equiaxed. As the temperature is increased, the complete α' → α + β decomposition takes place, but at the same time the average grain size increases, leading to a reduction in YTS and UTS [89,96] (Figure 30). Therefore, the heat treatment must be carefully

planned in order not to nullify the excellent properties induced by the manufacturing route.

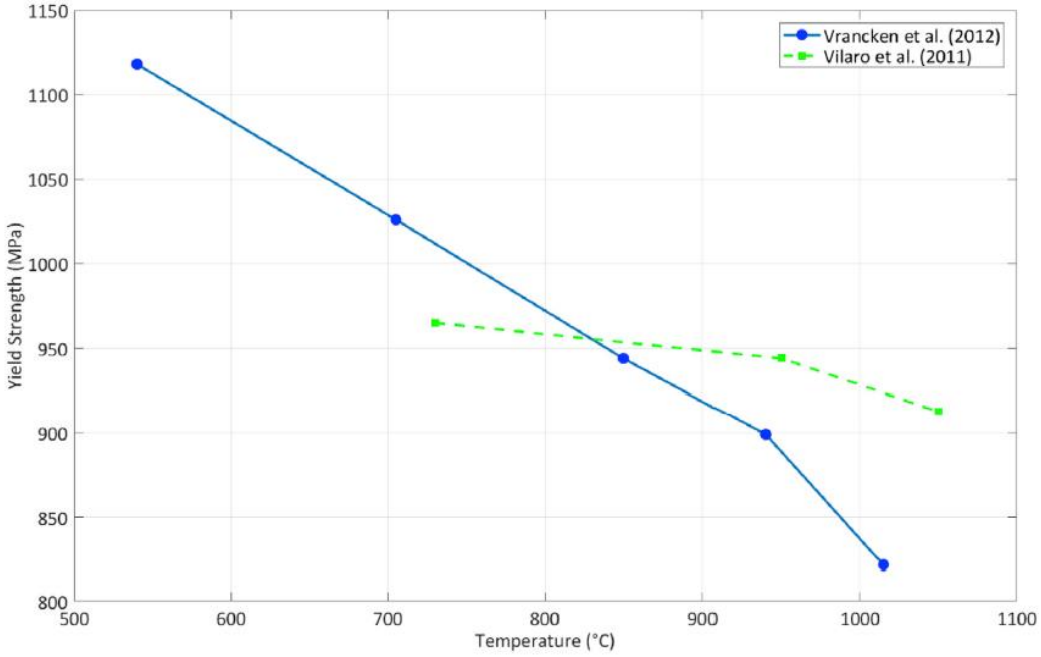


**Figure 30**: Two examples of the effect of different annealing temperatures on the yield strength of the Ti-6Al-4V alloy produced by means of LPBF [35,89,96].

Another important parameter in the planning of the post-processing heat treatment is the duration. Plaza et al. [97] evaluated how the residence time in the furnace during a heat treatment in the α+β field influenced the microstructure and mechanical properties of Ti-6Al-4V samples. In general, grain size is dependent on t, as grain growth is favoured during longer heat treatments, due to diffusive phenomena occurring. As previously discussed, a larger grain size provides more plasticity to the sample. This was also confirmed by Vrancken et al. [89], who also noticed that this effect is somehow more limited at high temperatures in the α+β field, as the equilibrium amount of α phase, which is more efficient at hindering grain growth, is limited, therefore grain enlargement takes place easily even for short periods. When the heat treatment is conducted at $T > T_\beta$, t must be controlled carefully, as in this case no α phase is present to limit grain enlargement, therefore extensive gran growth takes place almost uncontrollably, requiring prudent planning in order not to make YTS and UTS drop excessively [35]. Residence time is also important for its influence on microstructural coarsening. In Figure 31, two samples heat treated sub-transus for 2 (Figure 31a) and 20 (Figure 31b) hours respectively are compared. It is evident that the latter scenario provides a much rougher microstructure, characterized by larger α laths. Moreover, the formation of globular α began, as highlighted by the arrows. Of course, a rougher microstructure means a less strong sample.

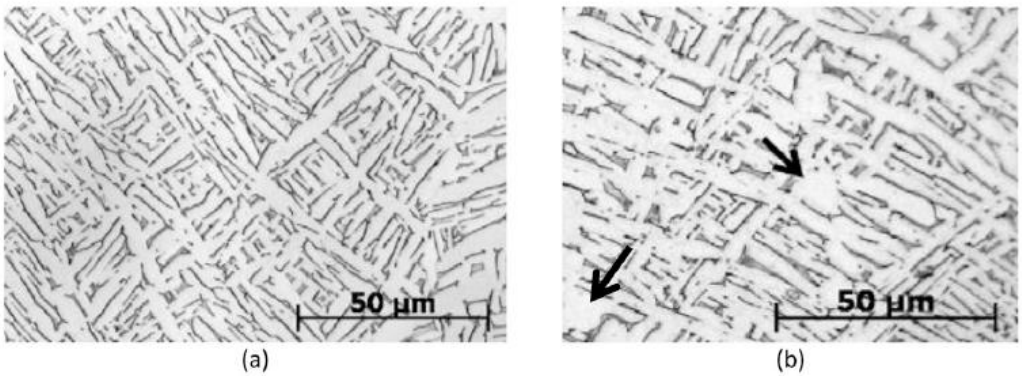


**Figure 31**: Microstructural comparison of two samples that underwent the same heat treatment in the α+β field for 2 (a) and 20 (b) hours respectively [89].

As mentioned before, the cooling rate is one of the most useful tools in order to control the outcome of a heat treatment for titanium alloys. Of course, at low temperatures its effect is marginal, as the high volume fraction of α phase slows down diffusive phenomena. Although, at higher temperatures in the α+β field, laths size is highly dependent on the cooling mean, as a higher α lamellar width corresponds to lower cooling rates. Vrancken et al. [89] evaluated the effect of different cooling rates (water, air and furnace cooling) on α' size, discovering that the effect is much more important at higher temperatures, where the variation is more consistent (Figure 32). Therefore, for temperatures close to $T_\beta$ or higher, the cooling rate results the most influencing parameter in order to determine α/ α' size and morphology [35].

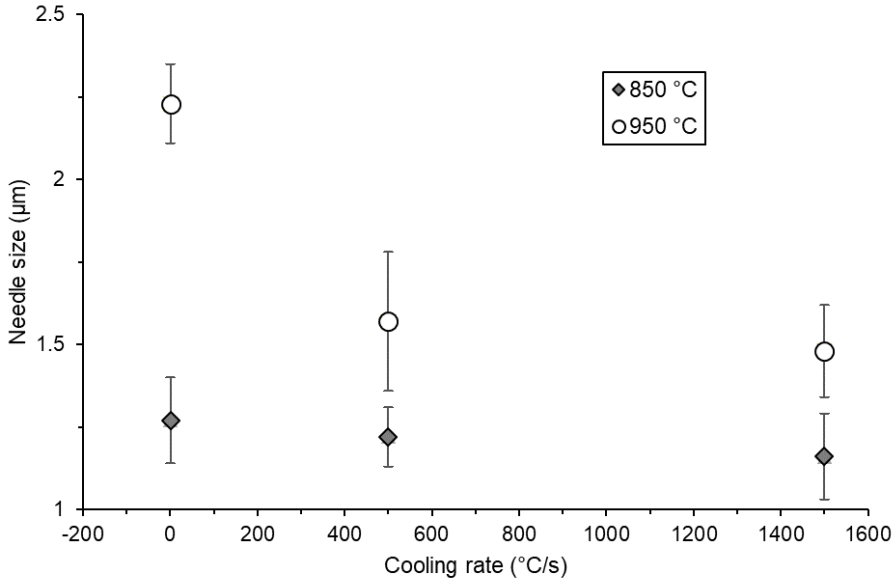


**Figure 32**: Needle size variation at different cooling rate after heat treatments at high temperatures in the α+β field [89].

If a very high cooling rate is applied from $T > T_\beta$, new martensite formation is possible in equiaxed grains [96].

The most common defects found in Ti-6Al-4V samples manufactured via LPBF are porosities, which are classified, similarly to EBM, as spherical and

irregular. The former type depends on gas entrapped in the feedstock powder due to the rapid solidification of the atomization process and on the process parameters used, that can minimize or emphasize this issue. Instead, the latter kind of porosity is usually caused by a lack of fusion, resulting from a poor choice of the process parameters that result in suboptimal metallurgical bonding between two neighbour layers. In general, irregular shaped pores are associated with a low energy input during the process [98]. These types of defects might be also induced by a non-uniform processing environment, in terms of gas flow, which results in an inefficient ability of the system to remove vaporized powder in certain area of the chamber. If this happens, in these localized zones the process parameters are less effective, due to the interference of the vaporized by-product, which can potentially cause lack of fusion defects. Moreover, if the debris are not removed, their presence might also induce a variation in layer thickness [99]. Overall, porosities should be avoided as much as possible due to their detrimental effect on fracture properties and most of all on fatigue performance as pores act as initiation sites for cracks propagation [35]. In general, a process window definition is possible, as described by Han et al. [83], in which density is evaluated as a function of the energy density (Figure 33).

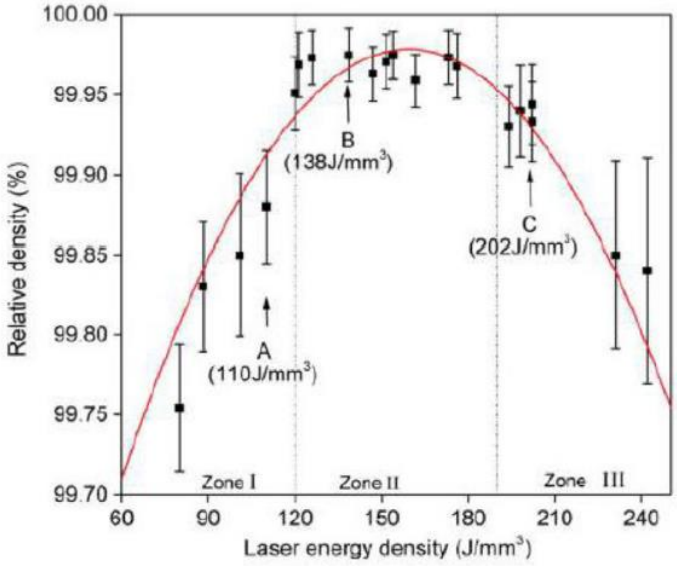


**Figure 33**: Process window determination of a group of Ti-6Al-4V samples by means of porosity minimization [83].

In general, three possible process zones can be found:

- Zone A, characterized by a low energy density and low density values due to the weak metallurgical bonding caused by the inability of the system to perform an optimal melting phase;
- Zone B, characterized by an intermediate energy density level, which is considered the optimized area, as it corresponds to the highest density values;

- Zone C, characterized by an excessive energy density, which results in an increase in porosity, mainly cause by a partial evaporation of the powder [83].

Another common defect is balling, which is caused by some residues of the molten material inability to wet the layer underneath due to consistent differences in terms of surface tension, result of a variation in thermal properties in the meltpool. The presence of these impurities hinders the correct deposition of the successive layer, that might cause a poor quality deposition or even cracking [100–102].

An additional critical issue of this process is the high amount of residual stresses induced in the samples, mainly due to the interactions of rapid expansion and contraction between neighbour layers. These phenomena mostly depend on the process parameters chosen and on the geometry of the sample. Of course, being absent the "annealing phase" typical of the EBM process, this issue is much more critical for LPBF systems. In order to partially mitigate that, the platform temperature is usually raised during the process with the aim of reducing the thermal gradients. Moreover, an optimized scanning strategy is helpful in avoiding excessive stresses build-up [81].

### 1.3.3. Directed Energy Deposition of the Ti-6Al-4V Alloy

The microstructure of Ti-6Al-4V components manufactured via DED is mostly determined by the peculiar thermal history typical of this process, which is defined, for example, by the high cooling/heating rates and thermal gradients [103]. Other important factors impacting on the final microstructure are the repeated re-heating cycles and, of course, possible post-processing heat treatments [104]. Another important influencing feature is the solidification rate of the meltpool, which has a primal role in determining the final microstructure and grain morphology. The latter is also influenced by the material properties and piece geometry. In order to obtain equiaxed grains, a high solidification rate value is needed, which corresponds to a low G to R ratio, where G is the thermal gradient at the solidus-liquidus interface and R is the cooling rate/thermal gradient ratio [105,106]. Moreover, G/R affects the shape of the solidification front, while G·R determines the dimension of the microstructural features obtained [107,108]. Equiaxed grains are usually considered the optimal outcome, although other morphologies are possible, such as columnar or equiaxed/columnar mix. The former type of grains is developed epitaxially along the building direction from the meltpool due to very high cooling rates, typical of this process, and results in a strong texturizing effect and anisotropy, similarly to LPBF and EBM. Working on single scans, Liu et al. [109] noted that the bottom part of the meltpool develops columnar grains due to the high thermal gradients present. Although, if the melting area is extended enough, the cooling rate decreases significantly along the meltpool height and the formation of equiaxed grains is allowed on the upper part.

Instead, the overlapping area between two neighbour single scans is characterized by the re-melting of these equiaxed grains which then reform again in a columnar morphology, due to the reduced depth of the meltpool in these regions, which are therefore characterized by consistent temperature gradients, thus cooling rates. Similarly, in a multi-layer system, melting does not occur exclusively on the last-deposited layer only, instead re-melting/heating of the areas underneath occurs. In these regions, the previously equiaxed grains act as nuclei for the epitaxial growth of the columnar grains in the lower part, effectively allowing their growth. Wang et al. [110] evaluated how the grain development mechanisms are influenced by the mass deposition rate (ṁ). This parameter is exclusive of DED machines, as in EBM and LPBF systems the feedstock powder does not need to be delivered onto the building platform during the melting step, due to the presence of the powder bed. According to their study, when the feeding rate is high enough, the formation of an almost completely (~80%) equiaxed grain morphology was possible. However, this parameter cannot be freely increased excessively. In fact, the penetration depth of the laser decreases as ṁ increases, which might prevent a fully dense component to be produced, due to the laser power not being high enough in order to melt all the particles. Therefore, a threshold ṁ value exists, below which, for a given set of process parameters, the resulting grain morphology is 100% columnar, as shown in Figure 34, in which is highlighted how the shift towards an equiaxed morphology is correlated to a reduction of the penetration ability of the laser.

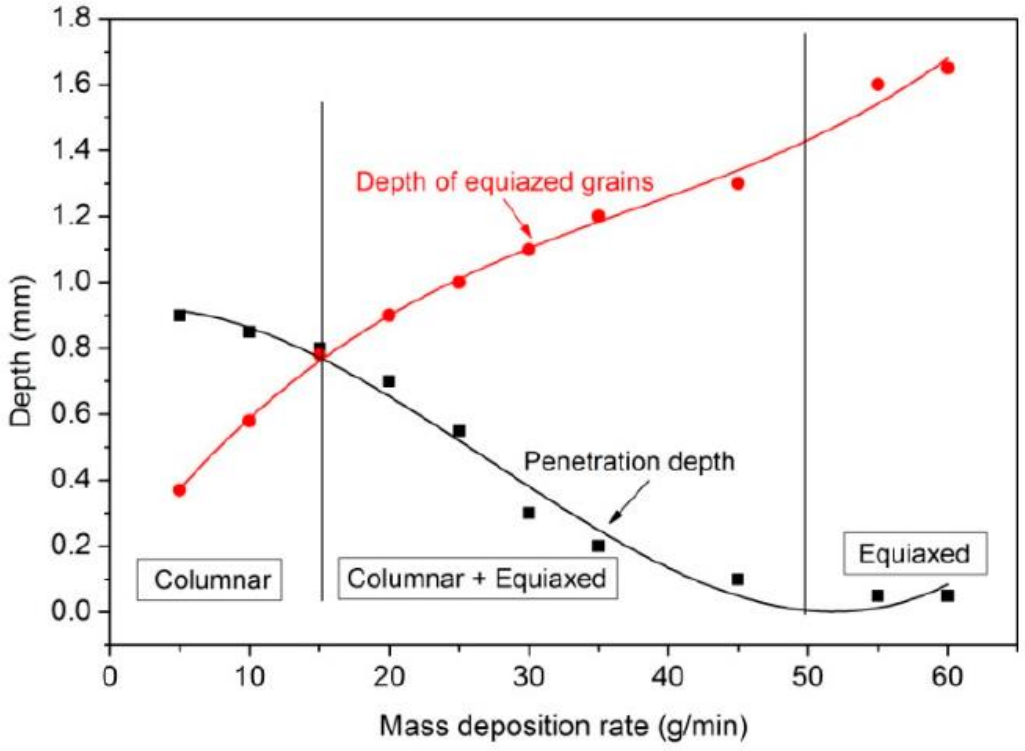


**Figure 34**: Depth on the equiaxed grains zone and melting depth as a function of the mass deposition rate for single scans [110].

In general, an equiaxed or mixed columnar/equiaxed grain morphology is related to a lower laser energy input [107]. A shift from a columnar microstructure towards a mixed one is correlated to an increase in the solidification rate [106], while a finer microstructure is the resulted of a process characterized by a high cooling rate [111]. Notwithstanding all the possible variations that might be induced by varying laser-related parameters or the feed rate, the typical microstructure obtainable in the Ti-6Al-4V alloy processed via DED is composed of columnar prior-β grains of a fine Widmanstätten morphology of α platelets/colonies in a β matrix and/or a mix of α/α' laths, depending on the process parameters chosen [104]. A representative microstructure, in which the columnar grain morphology and the α' laths are easily recognizable is provided in Figure 35.

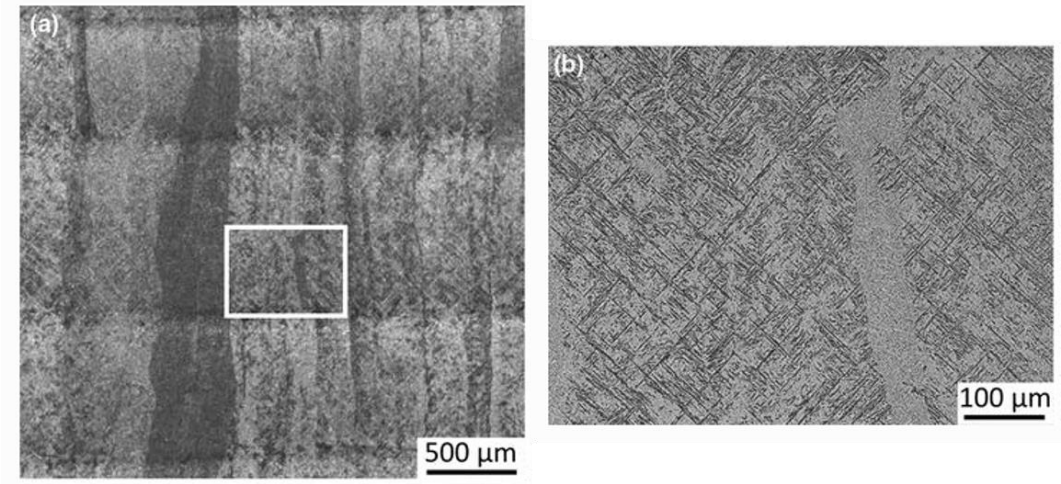


**Figure 35**: Representative micrograph of a mainly martensitic microstructure of a Ti-6Al-4V component built via DED (a) with the inset area zoomed (b) [112].

Another typical feature of DED-produced samples consists in local microstructural, hence hardness, variations inside the same sample, for example along the height, as reported by Baufeld et al. [113]. The authors attributed these dissimilarities to localized thermal effects induced by the thermal history during the fabrication process. These phenomena are of course reflected on the microstructure, possibly resulting in finer or coarser features. Specifically, they reported the top region of the sample (Figure 36a) to be mainly composed of fine lamellae, mostly grouped in colonies, while the lower part (Figure 36b) was characterised by a thicker lamellar structure. This phenomenon is correlated to a change in the heat dissipation mechanism, according to the reference height, or layer. In fact, in the lowest part heat flows rapidly through conduction, as the platform effectively acts as a heat sink. However, as the number of layer increases, this effect becomes somehow more limited, thus convection and radiation gain importance [107].

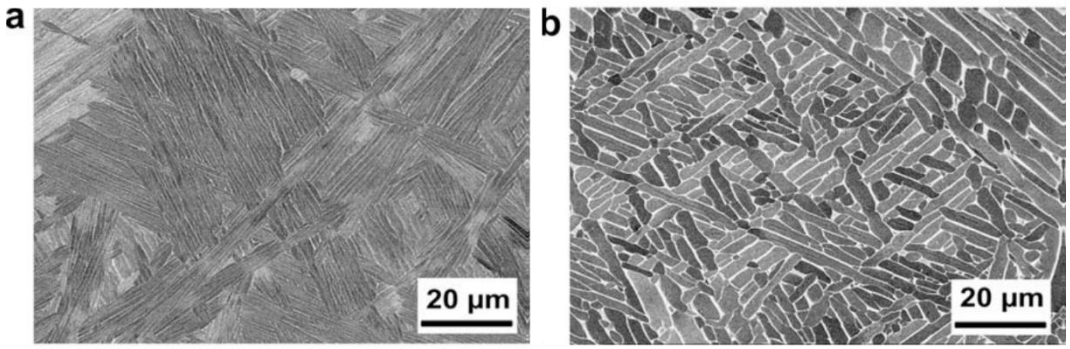


**Figure 36**: Optical micrographs of the top (a) and bottom (b) region of a DED-produced Ti-6Al-4V sample.

Microstructural inhomogeneity is a process-related issue of AM technologies, particularly relevant for DED systems. It is a direct consequence of the layer by layer approach used to build components, which relies on meltpools penetrating multiple layers, in order to provide the minimum metallurgical bonding required to build acceptable components. The overlap of multiple melting areas, as described before, leads to microstructural, hence mechanical, variations, mostly due to the differential cooling rates involved. For example, higher cooling rates allow α phase precipitation, during cooling, along prior-β grain boundaries. These precipitates act as nuclei for the formation of the duplex α+β Widmanstätten microstructure. Oppositely, low cooling rates induce the formation of a continuous α layer and the formation of coarser colonies within the grain itself [114]. Another typical issue is related to anisotropy, due to the preferential development of the columnar grains, parallel to the building direction, whose width is a function of the thermal history of the process. Moreover, texturing is also not negligible and mainly caused by the continuous remelting of the prior-β grains upon themselves [16].

Apart from porosities/voids, which can be minimized if the process is properly conducted, another typical defect of the samples produced via DED is the presence of consistent residual stresses, similarly to the LPBF technology. These are critical as they can drastically reduce the fatigue life and dimensional accuracy of the samples. Formed upon cooling, residual stresses are mostly dependant on the local material properties (e.g. thermal conductivity, Young's modulus), geometry of the component, scanning strategy, process parameters and the phase transformations [115]. Titanium alloys are particularly susceptible to residual stresses accumulation, being characterized by relatively high values of YTS at high temperatures. In fact, these types of material lack the ability to accommodate the volume variations thermally induced during deposition via plastic flow [116]. Residual stresses were found to be aligned along the scanning direction and more concentrated at the end of it. Furthermore, compressive stresses are commonly found at the centre of a scanning line, whilst tensile stresses tend to accumulate at the edge of it.

LPBF and DED technologies are markedly alike under multiple point of views: similar microstructures, related to comparable thermal histories, can be

achieved by both technologies, as well as typical defects/issues. However, in terms of process parameters, DED technologies are markedly dissimilar from powder-bed technologies in terms of the way the feedstock material is delivered onto the melting area, as described before. As a consequence of that, the process optimization/possibility to vary the machine parameters must be performed taking into account new variables related to the feeding system, such as the powder feed rate and the gas flow rate. The former is roughly proportional to the layer thickness [117]. Moreover, a higher feeding rate, at a fixed set of machine parameters, induces a coarser microstructure, as the amount of powder to be melted is increased, thus effectively reducing the energy density. This phenomenon is known as laser attenuation and it is more negligible when a high laser power is used. Instead, the gas flow rate influences the amount of powder injected into the system. These two values are roughly proportional, leading to an increase in layer thickness and powder density. Although, after a certain gas rate threshold value, a reduction in the amount of powder effectively deposited happens, due to mass reflection gaining importance, as the faster particles are delivered with a higher amount of kinetic energy.

The tensile properties of the Ti-6Al-4V alloy produced using a DED system are reported to be comparable, if not superior than cast or wrought ones, mainly due to the high cooling rates typical of this process (~5-10 · $10^3$ °C/s) [118,119] that allow the formation of a fine microstructure. Therefore, YTS and UTS are extremely high, even comparable with the LPBF properties. Reports of samples elastically deforming up until an applied stress of 1200 MPa are present in literature [120]. However, ductility is rather limited instead, with reports of it far lower than 5% [121]. A common way to increase ε is HIP, which also reduces porosity and anisotropy. This approach also provides the added value to improve the fatigue life of the components [16], and the formation of an α+β lamellar microstructure at the expense of α'. Although, HIP must be carefully planned as it might result in a YTS decrease too marked.

## 1.3.4. Effect of the Building Orientation

The orientation of a component during the manufacturing phase is a key parameter to consider, as it deeply influences, for instance, the final mechanical properties and surface quality of the material [122,123]. This phenomenon is important in all the AM technologies considered; thus, it is described in this separate section.

Barba et al. [124] compared the mechanical properties of several LPBF manufactured specimens, obtained from bars that were built along different directions. The authors found than the samples developed along the building direction were characterized by a lower strength, due to the columnar prior-β being aligned along the tensile test direction. This phenomenon causes a higher portion of the α-laths to be well oriented along the Z direction, causing a reduction in the yield strength.

Several studies [60,125,126] highlighted a similar relationship between the orientation and the mechanical properties in EBM produced specimens. For this particular technology, a reduction in ductility and strength was recorded for vertically-manufactured samples. Apart from the phenomena described earlier, for these systems the coarsening of the prior-β grains along Z is another important phenomenon which plays a key role in the reduction of the resistance.

In a work from Shamsaei et al. [105], the differences in terms of tensile properties in DED produced samples built along different directions, as highlighted in Figure 37, were assessed.

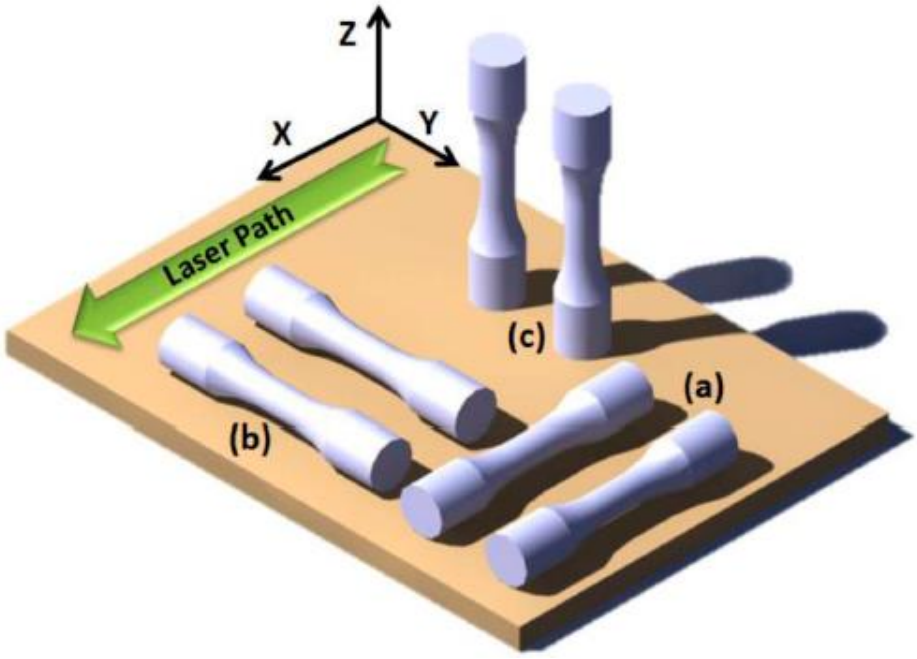


**Figure 37**: Schematic representation of bars produced horizontally (X-direction) (a), laterally (Y-direction) (b) and vertically (Z- direction) (c) [105].

The authors found that the samples built vertically were characterized by worse tensile properties, especially ductility, which resulted severely reduced. This effect was linked to the columnar grain morphology and to the limited possible grain growth perpendicular to the development direction [127]. Moreover, significant differences intercurring between the fracture surfaces, when comparing samples built along different directions, were reported by Qiu et al. [128], as visible in Figure 38.

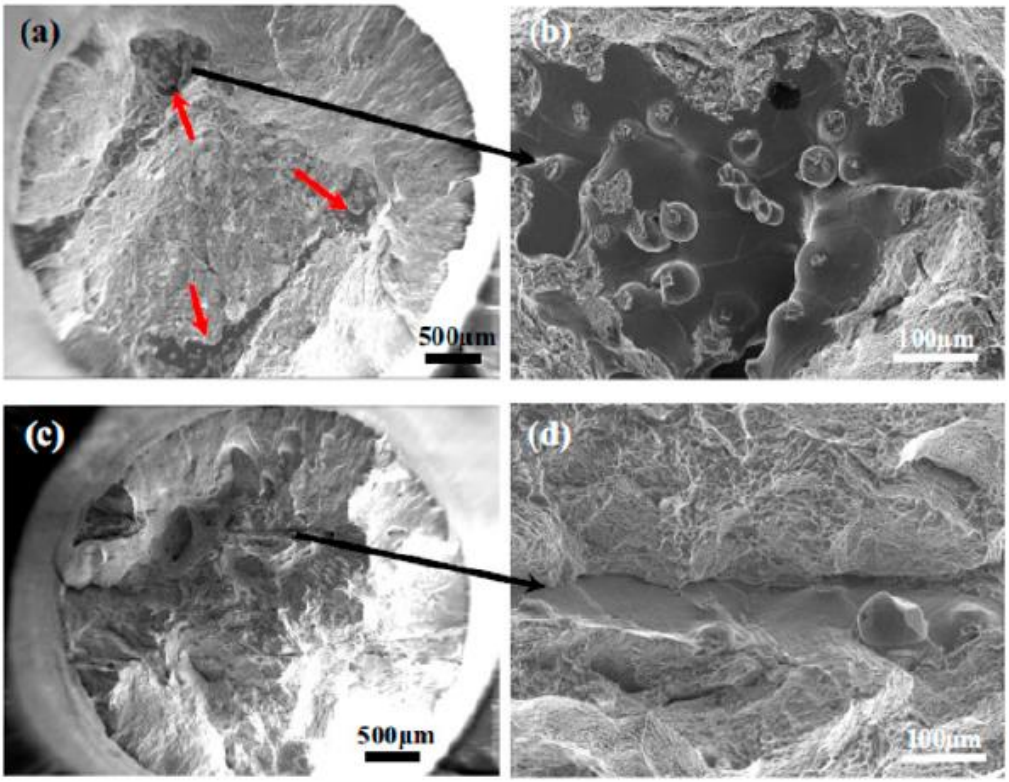


**Figure 38**: SEM images of the fracture surfaces of DED samples built vertically (a,b) and horizontally (c,d) [128].

The fracture surfaces of the vertically-built samples showed the presence of a certain number of large, open voids, characterized by the presence on unmelted or partially melted powder particles. Instead, the horizontally built samples were characterized exclusively by closed pores. This significant difference is due to the intrinsic anisotropy of the pores distribution typical of DED, related to the directional loading during the test. In fact, the irregular pores are induced in the material during the deposition, usually between layers and perpendicular to the development direction. During a tensile test, for a horizontally-built sample, the voids are parallel to the load, therefore they are closed during the test. In the opposite case, pores are torn apart instead [123,128].

### 1.3.5. Mechanical Properties Comparison

As explained in the previous sections, the Ti-6Al-4V alloy can present multiple types of microstructures in relation to the process parameters used, but most importantly on the AM technique adopted in order to process the material. Therefore, comparing the possible outcomes of the different major technologies available is very important in order to choose the most suitable technique for a given specific application. In Figure 39 are presented the YTS and ε data found in literature relative to the LPBF, EBM and DED technologies. In order to obtain the most accurate comparison possible, only the works in which the samples were built vertically and mechanically machined in order to obtain the tensile

specimens were considered. Of course, a great data variability is present and it is possibly mostly attributed to the effect of the process parameters choice on the mechanical properties, as well as possible differences in the feedstock material.

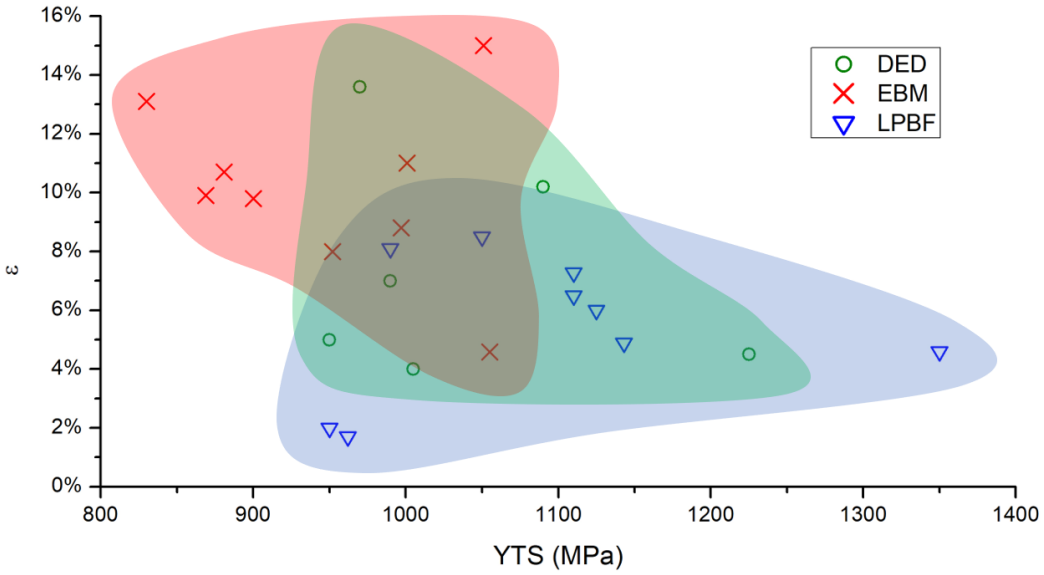


**Figure 39**: Tensile mechanical properties of the Ti-6Al-4V alloys produced using DED [128–131], EBM [68,70,130,132–136] and LPBF [89,90,96,132,137–141].

The LPBF technology appears to produce samples characterized by maximum YTS values unmatched by the other techniques, although ductility is fairly limited, not even reaching the 10% threshold given by the ASTM-F2924 [71]. This combination of mechanical properties is correlated mostly on the microstructure of the material. In fact, as discussed before, LPBF produces typically mostly α' martensitic microstructures with fine columnar prior-β grains, as a result of the localized extremely intense heating/cooling cycles, characterized by very high cooling rates. Therefore, as-built LPBF samples must undergo a post-processing heat treatment in order to be used in most conventional applications.

Oppositely, the EBM samples are mostly characterized by comparatively very high ductility, showing frequently $\varepsilon > 10\%$ already in the as-built state. Instead, YTS is markedly lower than LPBF's, rarely showing values significantly above 1000 MPa. Even if the typical cooling rates in the EBM process are very high, the process chamber is kept at high temperatures throughout the whole process, thus acting as an annealing heat treatment, characterized by a long duration, considering that a typical EBM job lasts several hours. This induces changes in the microstructure, most noticeably α' decomposition in favour of the formation of a lamellar α+β microstructure and in some cases $\alpha_{GB}$.

In the end, the DED technology is characterized by the greatest variability in terms of tensile mechanical properties. In fact, most of the data available in literature fit in an intermediate area between the properties of LPBF and EBM. This is probably mostly due to certain process-related factors that might greatly change the process outcome, such as the possibility to conduct the deposition in a

sealed environment or under a protective gas flow. Moreover, even if the process parameters typical of the laser AM technologies (e.g. scanning speed, laser power) are kept constant, in DED the user has more freedom to vary the final microstructure via proper feeding-related parameters variations (e.g. feeding gas flow rate, powder flow). In fact, both martensitic and lamellar microstructures are reported for this technology.

# Chapter 2

# Materials and Methods

## 2.1. Powders

Four different powders were used in this thesis: 3 different batches of Ti-6Al-4V Extra Low Interstitial (ELI) powder, each one of these was used in a different machine (DED, EBM and LPBF), and a single batch of Ti-6Al-2Sn-4Zr-6Mo powder, processed in a LPBF machine.

### *Ti-6Al-4V ELI Powder for DED*

A gas atomized Ti-6Al-4V ELI powder provided by LPW Technology Ltd, characterized by the chemical composition listed in Table 3, was used. Its particle size distribution (Figure 40a) was evaluated via SEM images analysis and provided a D(10), D(50) and D(90) of 49.08 μm, 79.92 μm and 119.92 μm, respectively. The observation of the powder particles via SEM (Figure 40b) and their cross-section (Figure 40c) highlighted an appropriate shape for being processed, since most particles appeared quite spherical and the satellites content was low, coupled with a high relative density.

**Table 3**: Nominal composition of the Ti-6Al-4V ELI powder processed via DED given by the supplier.

| Chemical element | Composition (wt.%) |
|---|---|
| Al | 6.3 |
| V | 4.0 |
| Fe | 0.16 |
| O | 0.09 |
| C | 0.01 |
| H | 0.001 |
| N | 0.001 |
| other | < 0.5 |
| Ti | bal. |

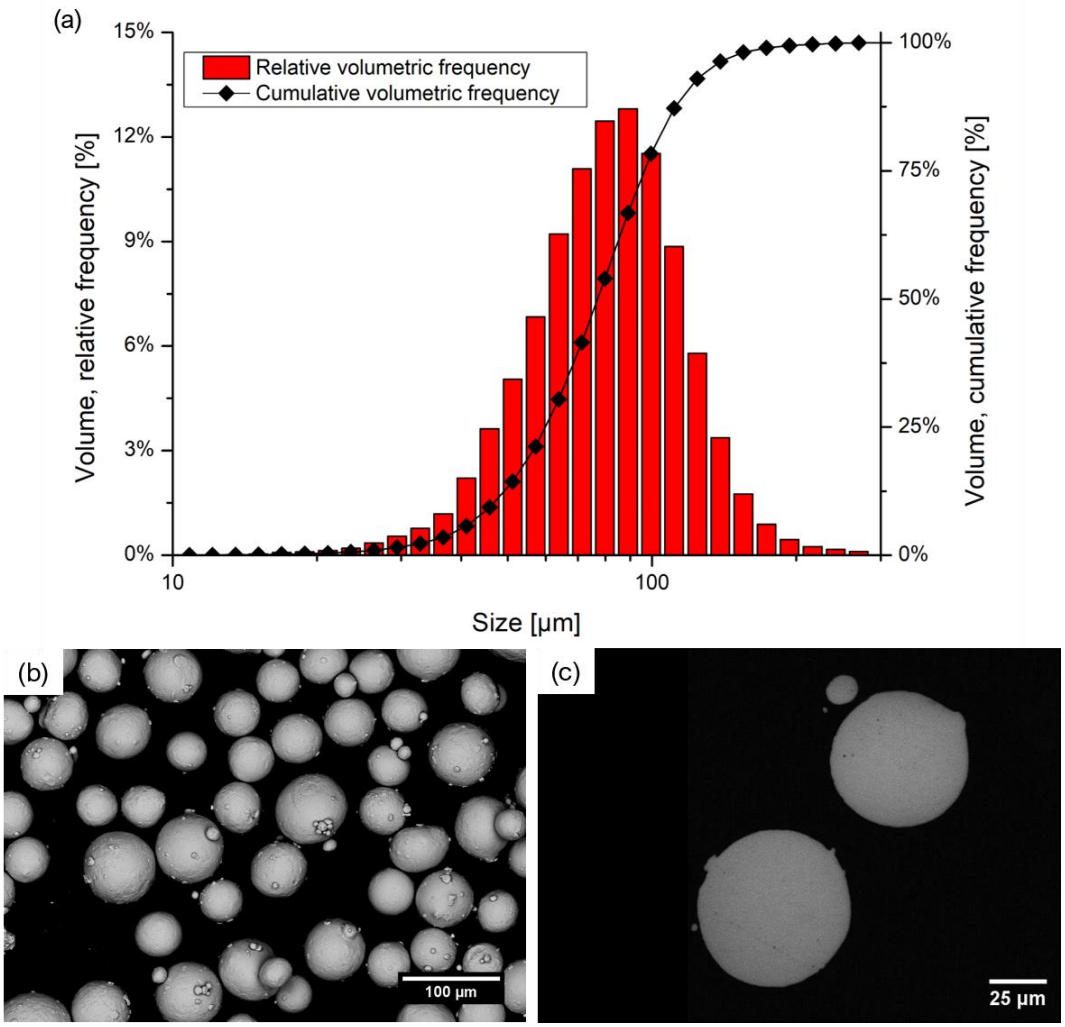


**Figure 40**: Particle size distribution of the Ti-6Al-4V ELI powder for DED (a), representative SEM image of the powder (b) and cross-section of some particles (c).

## *Ti-6Al-4V ELI Powder for EBM*

A gas atomized Ti-6Al-4V ELI powder provided by Arcam AB was used in this work. Its nominal chemical composition is available in Table 4. The powder particles appeared highly homogeneous and spherical by SEM observation (Figure 41a). Only a small number of elongated particles was visible and the overall satellite content appeared negligible. The particle size distribution, evaluated by image analysis and visible in Figure 41b, provided a D(10), D(50) and D(90) values of 44.63, 62.26 and 83.57 µm respectively.

**Table 4**: Nominal powder composition as provided by the supplier.

| Chemical element | Composition (wt.%) |
|---|---|
| Al | 6 |
| V | 4 |
| Fe | 0.1 |
| O | 0.10 |
| C | 0.03 |
| N | 0.01 |
| H | < 0.003 |
| Ti | bal. |

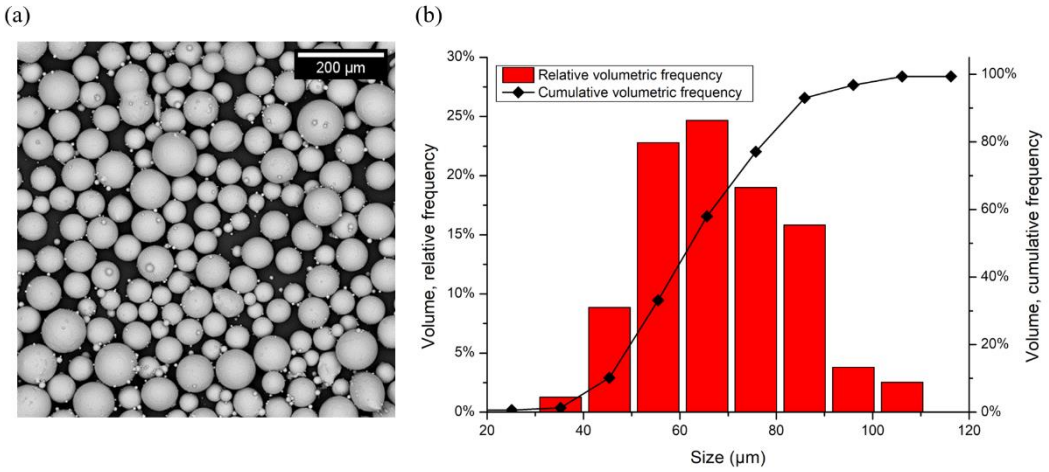


**Figure 41**: Representative SEM image of the particles (a) and the relative particle size distribution (b) of the Ti-6Al-4V ELI powder for EBM.

## *Ti-6Al-4V ELI Powder for LPBF*

A gas atomized Ti-6Al-4V ELI powder, supplied by TLS Technik GmbH, was used in this work. The chemical composition, measured by the supplier, is reported in Table 5. The particle size distribution was evaluated via SEM images analyses (Figure 42) and resulted in a D(10), D(50) and D(90) values of 22.26, 33.35 and 47.08 µm respectively. The powder was formed by highly spherical particles and no significant satellites presence was detected (Figure 42b).

**Table 5**: Chemical composition of the powder provided by the supplier.

| Chemical element | Composition (wt.%) |
|---|---|
| Al | 5.86 |
| V | 3.99 |
| Fe | 0.183 |
| O | 0.083 |
| C | 0.01 |
| N | 0.003 |
| H | 0.002 |
| Ti | bal. |

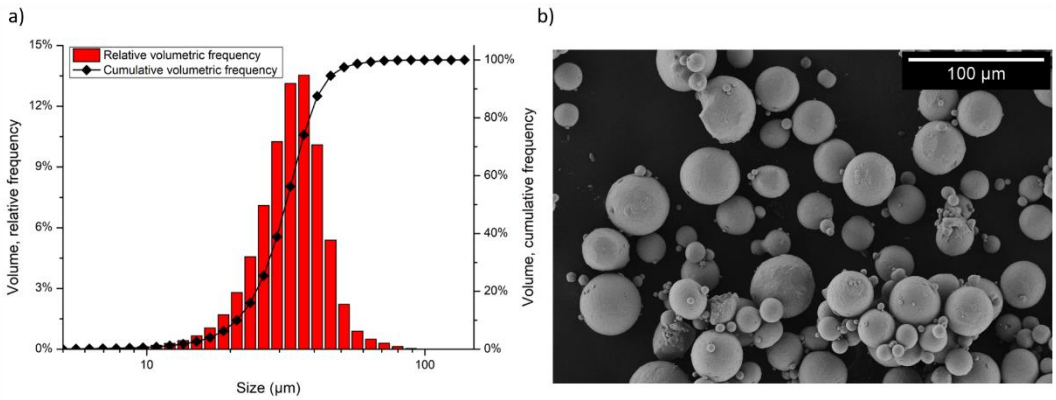


**Figure 42**: Particle size distribution (a) and representative SEM image (b) of the Ti-6Al-4V ELI powder for LPBF.

## *Ti-6Al-2Sn-4Zr-6Mo Powder for LPBF*

A Ti-6Al-2Sn-4Zr-6Mo powder, provided by TLS Technik GmbH, was used in this work. The nominal chemical composition was provided by the supplier (Table 6). Its particle size distribution was measured via SEM images analysis and appeared bimodal, providing a secondary peak in correspondence of approximately 5 µm (Figure 43a). Notwithstanding that, the powder did not provide significant flowability issues during processing. The relative D(10), D(50) and D(90) values were 24.1, 38.0 and 54.7 µm respectively. The observation of the powder particles allowed to investigate the shape, which resulted quasi spherical. A certain amount of satellites was also detected, as visible in Figure 43b.

**Table 6**: Nominal chemical composition of the powder.

| Chemical element | Composition range (wt.%) |
|---|---|
| Al | 5.5 – 6.5 |
| Mo | 5.5 – 6.5 |
| Zr | 3.5 – 4.5 |
| Sn | 1.75 – 2.25 |
| Fe | < 0.15 |
| O | < 0.15 |
| H | < 0.125 |
| N | < 0.04 |
| C | < 0.04 |
| other | < 0.4 |
| Ti | bal. |

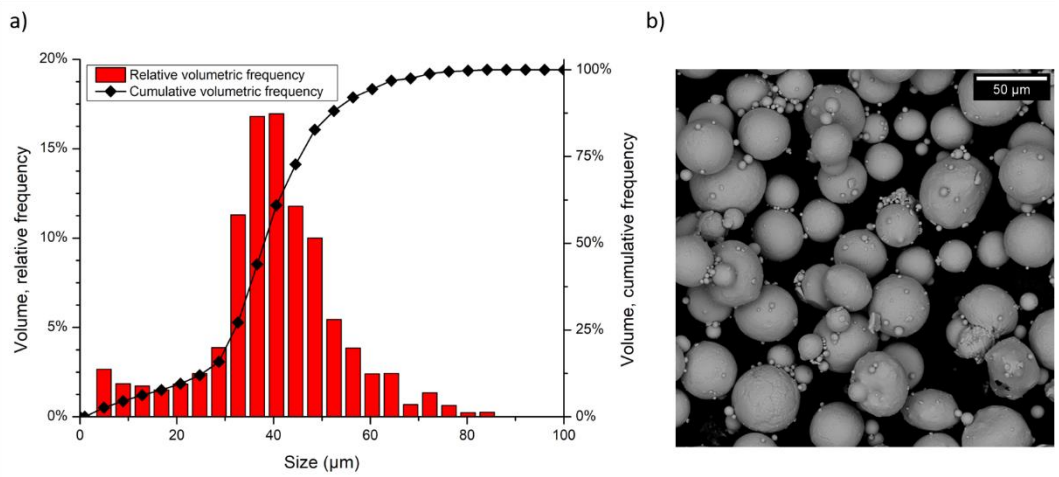


**Figure 43**: Particle size distribution (a) and representative SEM image (b) of the Ti-6Al-2Sn-4Zr-6Mo powder.

## *Comparison of the Powders*

All the powders presented in this work appeared quite homogeneous from a morphological point of view. The particles resulted highly spherical and the presence of satellites was negligible to fairly low. The most significant difference lied in the particle size distributions of the powders, which are graphically compared in Figure 44. As visible in the graph, the powders suitable for LPBF usage were characterized by the narrower curves shifted towards lower size values. Among these, the Ti-6Al-4V powder appeared finer than its Ti-6Al-2Sn-4Zr-6Mo counterpart. This is also confirmed by the D(50) values, equal to 33.35 and 38.0 µm for Ti-6Al-4V and Ti-6Al-2Sn-4Zr-6Mo powders, respectively. As discussed in the previous chapter, the powders to be used in EBM and DED systems are often characterized by larger particles. In this case, the powder processed in the EBM machine, with a D(50) of 62.26 µm, was significantly finer than that processed by DED, characterized by a D(50) of 79.92 µm.

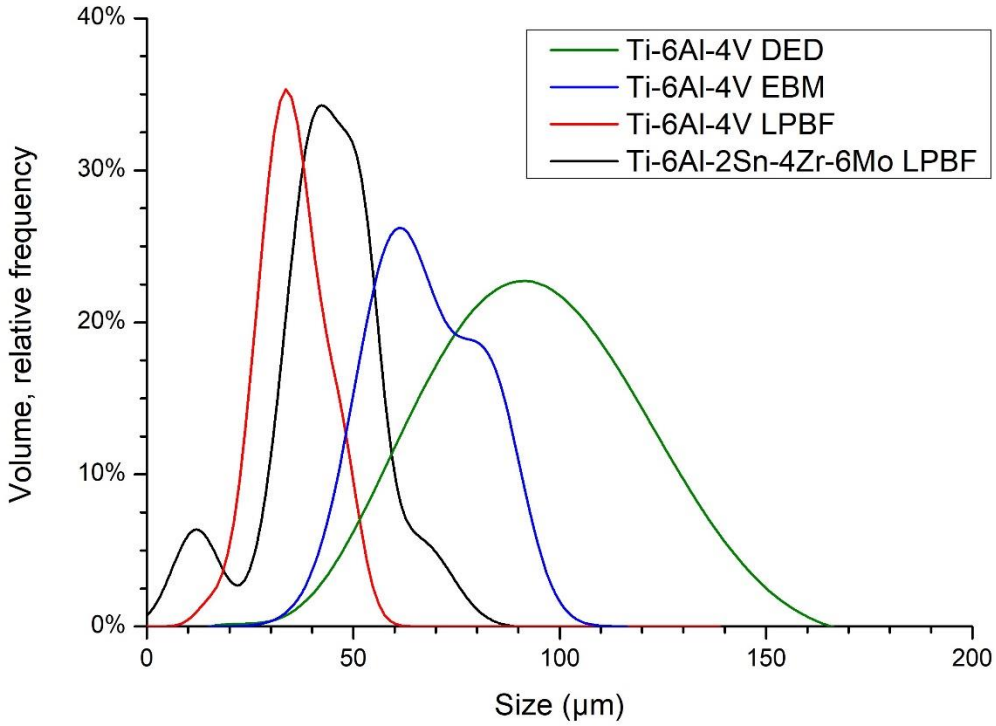


**Figure 44**: Particle size distribution curves of the powders used in this work. Possible significant differences between the LPBF curves provided in this graph and in the previous ones are due to the mandatory variation of the step size, performed in order to make all the curves present comparable.

## 2.2 AM Systems

In this thesis, different AM machines were used. The description of each specific set of parameters adopted is provided in the relative sections in the next chapter.

The DED produced samples were all built in a SUPSI (University of Applied Sciences and Arts of Southern Switzerland) laboratory (ARM lab – DTI). The Laserdyne®430 system used consisted of a customised three axis laser processing system that employed a Convergent Photonics CF1000 fibre laser, with a maximum laser power of 1000 W, a wavelength (λ) of 1070 nm and a laser spot diameter (D) of 1 mm. A multi-nozzle deposition head (Optomec Inc.) was also employed. Further details on the system are available elsewhere [142]. The gas used was argon (4.6 purity). Its flow rate was 4 l/min when used as a carrier. The same gas was also used at variable flow rates as a shielding gas in order to protect the melting area from oxidation and interstitial elements enrichment. Its delivery was performed by an external circular device equipped on the deposition head. This allowed to provide a homogeneous gas flow around the melt pool in an area of 89 mm in diameter.

The EBM produced samples were built using an Arcam A2X machine, whilst the LPBF Produced ones using an EOS M270 Xtended machine.

## 2.3 Furnaces

In the works presented in this thesis, multiple furnaces were used in order to thermally process the samples analysed. The equipment used depended on the requirements regarding the cooling rate that the specimens had to undergo.

When a low cooling rate was allowed, such as at the end of an ageing heat treatment, a Pro.Ba VF800/S high-vacuum furnace was used. This furnace provided the maximum control on the oxygen content during the heat treatment among all the systems used, since the internal gas pressure can be kept as low as $10^{-6}$ mbar.

For intermediate cooling rates (air cooling), a Tav minijet HP S/N 235 low pressure furnace, characterized by an operating pressure of $10^{-2}$ mbar, was used. In order to achieve a cooling rate of 10-20 °C/s, a nitrogen quench at a pressure of 6 bar was performed. To prevent the samples from nitrogen enrichment due to the interaction with the atmosphere inside the furnace, these were wrapped in a 0.5 mm AISI 304 stainless steel bag.

For even higher cooling rates via water quenching, a Nabertherm RHTC 80-170/15 tube furnace, using a protective argon flow of 1.5 l/min, was used. This resulted necessary as the samples had to be immediately removed at the end of the heat treatments and dropped in a steel bucket filled with water. The operation was performed as quickly as possible, in order to minimize the time that the hot samples spent in direct contact with the external atmosphere.

## 2.4 Characterization

For general metallographic observations, the samples were cut, mounted and mechanically polished using silicon carbide papers (#400 - #2400) for the grinding step and then colloidal silica (0.04 μm) for the finishing operations. The investigations of the microstructures were conducted after etching the samples using a Kroll solution (93% $H_2O$, 5% $HNO_3$, 2% HF). The on-top analysis of the single scans, aimed at evaluating the morphology of the samples, were performed using a Leica EZ4W stereomicroscope. The observation of the micrographs was conducted using a Leica DMI 5000M optical microscope and a Phenom-XL SEM.

The evaluation of the grain size was performed adopting the intercept method: a grid of vertical and horizontal lines, crossing the whole cross-section of the sample, was created. Therefore, the average grain size/width for every line corresponded to the $L/\#_{GB}$ ratio, where L is the length of the line and $\#_{GB}$ represented the number of grain boundaries that crossed the segment. The lines used were approximately 2 mm apart from each other, as schematically represented in Figure 45.

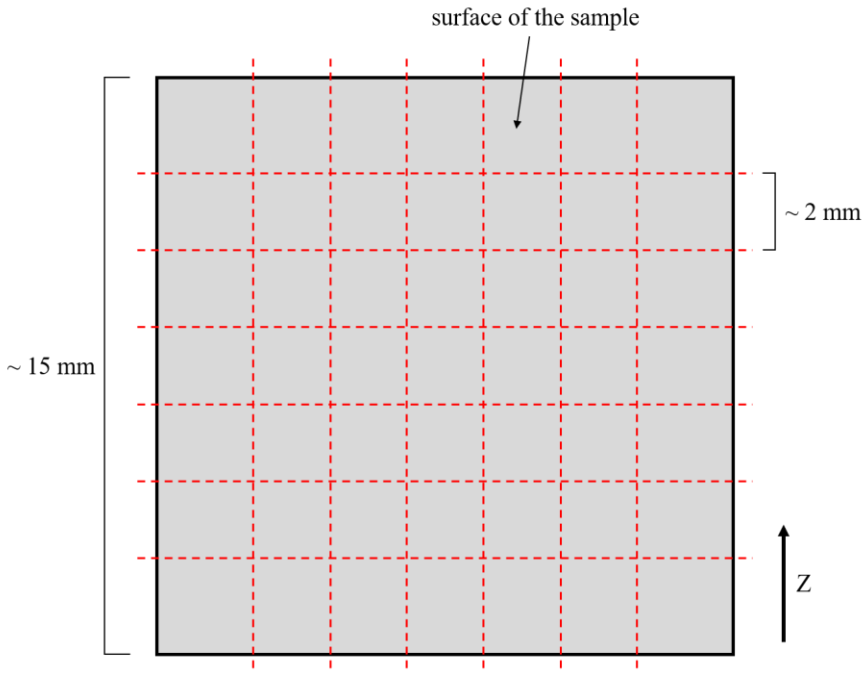


**Figure 45**: Schematic representation of the lines used as intercepts during the grain size evaluation.

The in-depth microstructural characterizations, such as the evaluation of the width of the α'/α" needles and α laths in a Widmanstätten pattern, were conducted using the software ImageJ to process the optical/SEM high-magnification (minimum 500x) micrographs, appositely pre-treated as described by Zhang et al. [143]. The measurements were obtained by manually selecting and measuring each feature. This resulted necessary as the different orientations of the needles/laths did not allow to use the intercept method, which would have been poorly representative. To provide statistical significance, the areas analysed were randomly taken throughout the whole cross-section. More than 20 micrographs per measurement were analysed, accounting at least 500 measurements per each value obtained. In order to perform this measurement on the single scans, a different methodology was used, in which the α' spacing was measured ($\sigma_t$), using the methodology described by Vander Voort [144] for evaluating the interlamellar spacing of paerlite in steels. 15 different optical micrographs per specimens were studied by superimposing a circular grid, whose diameter value was known ($d_c$), and counting the number of times an α' needle intersected the circle (n). The use of a circular grid allowed to obtain more accurate results, with respect of a straight line, when evaluating features oriented in multiple directions. The average spacing is then evaluated as:

$$\sigma_t = \frac{1}{2N_L} = \frac{\pi d_c}{2n} \tag{3}$$

Where $N_L$ is the number of intersections per unit length of test line.

This methodology was already successfully used to study titanium alloys by Galarraga et al. [134] in order to evaluate α-lath thickness ($\sigma_t$) in EBM produced Ti-6Al-4V samples. In this thesis, this procedure was used to determine the average spacing

between α' needles, instead of α laths. This is a good indicator as lower spacing corresponds to a higher martensitic density, hence a finer microstructure.

The width of the α laths in the samples that provided a more oriented microstructure, for instance colonies of lamellar α+β, was measured using the intercept method, described in ASTM-E112 [145]. Even if it is meant to be used for the determination of the average grain size, there are works available in literature in which it was adapted to measure other microstructural features [144]. The micrographs were pre-treated using the Otsu thresholding (Figure 46a), as described by Zhang et al. [143], and then a line was superimposed on a specific area, characterized by the presence of parallel lamellae. The software ImageJ allowed to remove the portions of the line that crossed a lamellar border (β phase), as highlighted in Figure 46b. The remaining segments were approximated as particles, in which the length corresponded to the maximum Feret's diameters, and analyzed using the software ImageJ, thus obtaining a distribution of data.

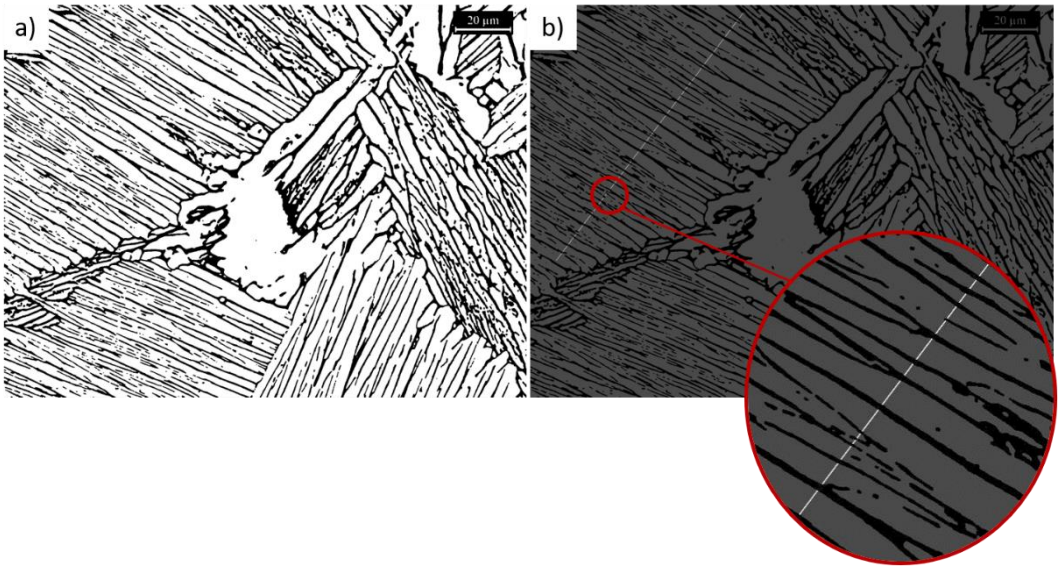


**Figure 46**: An example of a lamellar α+β micrograph treated using the Otsu filter (a) and relative segmentation of a line during the evaluation of the α width (b).

The identification of the phases constituting the samples and the calculation of the cell parameters were performed by analyzing the X-ray diffraction (XRD) data, gathered using a PANalytical X-Pert PRO diffractometer in a Bragg Brentano configuration. The instrument was set to work with a Cu $K_\alpha$ radiation, characterized by a wavelength of 1.5406 Å, at 40 kV and 40 mA. A 2θ range from 30° up to 90° and a step size of 0.013° were used. The cell parameters were obtained by combining the Bragg law and the plane spacing equation for the type of lattice investigated [146]. For a hexagonal system, the governing equation resulted:

$$\sin^2\theta = \frac{\lambda^2}{4}\left(\frac{4}{3}\cdot\frac{h^2+hk+k^2}{a^2}+\frac{l^2}{c^2}\right) \quad (4)$$

Where θ is the diffraction angle relative to the peak considered; h, k and l are its Miller indices; a and c are the hexagonal cell parameters.

Instead, for an orthorhombic system, the related equation was:

$$\sin^2\theta = \frac{\lambda^2}{4}\left(\frac{h}{a^2}^2 + \frac{k^2}{b^2} + \frac{l^2}{c^2}\right) \quad (5)$$

Where a, b and c are the cell parameters of the orthorhombic cell.

In order to avoid possible deviations due to texturing, each parameter was evaluated from multiple peaks, following an approach called “intensity averaging” [146].

The concentration of the interstitial elements was assessed by performing at least three measurements per condition, using a 736 series O/N LECO analyzer.

Vickers microhardness measurements were performed using a Leica VMHT microhardness tester, setting the instrument to apply a force of 300 g for a total of 15 s. The measurements were performed by virtually creating a grid on the cross-section, similar to the one illustrated in Figure 45, and indenting the samples every time a lines intersection occurred.

Tensile tests were performed in order to evaluate the mechanical properties of several specimens, using a Zwick Roell Z050 tensile tester, operating at a strain rate of 0.008 $s^{-1}$. All the samples analyzed were obtained via mechanical machining of bars and resulted compliant to ASTM E8 [147]. Specimens from different works had different geometries, sizes and were built with different orientations, as briefly described in Table 7.

**Table 7**: Geometries of the tensile specimens used in this work.

| Sample | Geometry | Gauge length (mm) | Diameter (mm) | Orientation |
|---|---|---|---|---|
| Ti-6Al-4V (DED) | flat dogbone | 25 | - | horizontal |
| Ti-6Al-4V (EBM) | cylindrical | 40 | 8 | vertical |
| Ti-6Al-2Sn-4Zr-6Mo (LPBF) | cylindrical | 16 | 4 | vertical |

# Chapter 3

# Results and Discussion

In this chapter, the data obtained from the various investigations conducted will be split into four main sub-chapters, defined as follows:

- **Analysis of the microstructure and the mechanical properties of the Ti-6Al-4V alloy produced by DED**. The samples analysed were built in SUPSI as part of a collaboration in the 4D HYBRID European project. The optimized process parameters had to be determined yet. Therefore, the initial analysis focused on the evaluation of the most suitable process window via single scan approach. After that, a further investigation on the effect of different environmental factors during deposition was conducted on 3D samples. In the end, the influence of different process parameters on the microstructure and mechanical properties was assessed.
- **Analysis of the microstructure and the mechanical properties of the Ti-6Al-4V alloy produced by EBM**. These samples were produced in Politecnico di Torino, using a system localized in the IAM (Integrated Additive Manufacturing) centre. The specimens were manufactured using the standard process parameters for this material suggested by Arcam. Thus, the analysis of the EBM produced samples focused on the significance and effect of different post-processing heat treatment and their effect on the microstructure and mechanical properties.
- **Analysis of the heat treatments on the Ti-6Al-4V alloy produced by DED and EBM**. The heat treatments performed as part of the previous investigation were also carried out on the DED samples. In this way, a comparative analysis between the heat treated samples manufactured using different AM technologies (DED, EBM) was possible.
- **Analysis of the microstructure and the mechanical properties of the Ti-6Al-2Sn-4Zr-6Mo alloy produced by LPBF**. The production and

analysis of the samples was part of the MANUELA European project. All the specimens were built in Politecnico di Torino, using a system localized in the IAM centre. The Ti-6Al-2Sn-4Zr-6Mo alloy is a duplex titanium alloy never processed before by LPBF. It is conventionally used for specific industrial application in which better mechanical properties (e.g. strength) are needed, with respect to the Ti-6Al-4V alloy. After assessing the most suitable process window, the related microstructure, mechanical properties and the significance and effect of a post-processing heat treatment were analysed. Moreover, since the industrial relevance of the Ti-6Al-2Sn-4Zr-6Mo alloy is intrinsically related to its ability to provide better mechanical properties than the Ti-6Al-4V alloy, a comparison between these two materials was conducted. Concerning the latter material, a mix of data self-obtained and available in literature was used.

## 3.1. Ti-6Al-4V Alloy Produced by DED

The determination of the most proper process window was a mandatory step for the DED system, since the Ti-6Al-4V alloy was processed using this machine for the first time. Consequently, the single scan approach was adopted in order to determine the most suitable parameters to process the Ti-6Al-4V alloy.

### 3.1.1 Determination of the Most Suitable Process Parameters to Process the Ti-6Al-4V Alloy via DED

The optimization of the process parameters in AM technologies is a mandatory step in order to manufacture components characterized by the desired properties, such as porosity, dimensional stability, microstructure and mechanical properties. This step is particularly critical for the DED technology, usually relying on prototypes or custom-made machines composed of parts from different producers [129,148,149]. Moreover, the optimization of the process parameters is very time consuming, as a large number of samples had to be produced and then characterized. Furthermore, it is far from a standardized methodology, as testified by several works available in literature, in which different methodologies were used [150–152]. For example, Kobryn et al. [150] studied the effect of several combinations of laser power and scanning speed on DED produced Ti-6Al-4V samples. The criteria used in order to evaluate the quality of the resulting samples were the average porosity, microstructure and the height of the samples. Instead, Mahamood et al. [152] used hardness as a parameter to choose the most suitable combination of process parameters. Most articles rely on the characterization of 3D samples, which is very expensive, both economically and in terms of time. A more cost-effective approach consists in investigating single scans (or beads), which results in a drastic reduction in the amount of feedstock material used and in the duration of the fabrication and characterization processes. However, this methodology cannot be used to evaluate the effect of some process parameters,

which are connected to the interaction of multiple meltpools, such as the layer height and hatching distance. Notwithstanding that, it is promising in order to study the effect of the laser power, scanning speed and some environmental factors, such as the mass flow rate of the shielding gas. The single scan approach was already used on several materials. For example, Peng et al. [153] investigated Nickel alloys single scans to study the relative meltpools and some cross-sectional geometrical features, such as the height and width of the bead itself. However, all the specimens obtained were cracked, probably due to an excessive oxygen enrichment of the alloy and/or residual stresses build-up. Therefore, the authors moved to bigger samples (single layers and cubes) to assess the most suitable process window. Similarly, Mazzucato et al. [142] utilized this approach in a work aimed at determining the effect of different scanning strategies on DED produced steel samples. In this work, the authors performed a stability investigation, by analysing the on-top view of several single scans and then categorizing them according to their morphology. The most promising specimens were also cross-sectioned in order to determine the one characterized by the lowest porosity and most proper substrate remelting. Aversa et al. [154] were able to correlate the stability and geometrical features of AlSi10Mg single scans to the process parameters used during the process. By doing so, they were able to assess the proper process window, proving that this type of analysis can be a powerful tool in order to characterize new powder compositions in future works.

Concerning the Ti-6Al-4V alloy, only a few works, in which the single scan approach was used, are available. For example, Gockel et al. [155] investigated how different machine-related parameters influenced the microstructure and meltpool size via simulation. Instead, Katinas et al. [156] investigated Ti-6Al-4V single beads in order to study the laser capture efficiency, without focusing on the material properties of the actual specimens.

The Ti-6Al-4V alloy is an optimal material to be processed by DED, mainly due to the high costs related to process it via conventional manufacturing technologies. However, its processing in general is fairly difficult, mainly due to its high susceptibility to oxygen pick-up [4,157]. The deposition of this material can be conducted either in a sealed environment (glovebox-like) or in an open environment [158,159]. The former grants a tighter control on the process and results in higher quality samples, but limits the maximum size of the component to the dimension of the chamber itself. The latter usually relies on a secondary protective gas flow to protect the melting area. In this case, the mass flow is another parameter to optimize , as it must be kept as low as possible, due to the high cost of the gas, usually argon [160]. However, the flow rate must be high enough to prevent extensive embrittlement in the material.

In this work, the single scan approach was used to find the proper process window (laser power, scanning speed) for DED produced Ti-6Al-4V samples through the analysis of several geometrical features (e.g. scan's height, width) and related parameters. The specimens were manufactured in an open environment, thus the effect of the shielding gas flow on the geometrical and microstructural

quality was also assessed. This step is fundamental in order to understand the applicability of an open deposition environment on DED manufactured titanium alloys, as this feature is very promising in terms of large components production. Moreover, the powder efficiency and resulting microstructure were also evaluated and incorporated in the final process map in order to further analyse the process.

50 different 20 mm long singles scans, corresponding to the combination of 5 laser power (P) values and 10 scanning speed (v) values were produced using a constant powder feed rate (F) of 0.017 g/s, as summarized in Table 8.

**Table 8:** Process parameters corresponding to the single scans analysed.

| P (W) | v (mm/min) |
|---|---|
| 100, 300, 500, 700, 900 | 150, 300, 450, 600, 750, 900, 1050, 1200, 1350, 1500 |

The machine was equipped with an external circular device, that provided a homogeneous flow of shielding gas around the deposition area. The samples were built in two different environmental conditions in order to evaluate the effect of the additional shielding gas:

- **ArS0**, without using the additional shielding gas system
- **ArS15**, using the additional shielding gas system at a flow rate of 15 l/min.

## *Geometrical Analysis*

The on-top analysis of the single scan tracks allowed to find the most critical samples from a morphological point of view. Whilst most tracks resulted highly homogeneous, the specimens built using a laser power of 100 W were markedly irregular due to incomplete melting of the feedstock material delivered onto the platform, as illustrated in Figure 47. This phenomenon resulted particularly evident when the samples built using a low scanning speed (e.g. ArS15, v = 300 mm/min in Figure 47) were considered. When a higher v value was applied, melting became even less efficient and merely any particle at all could be found adhered to the substrate (e.g. ArS15, v = 1200 mm/min in Figure 47).

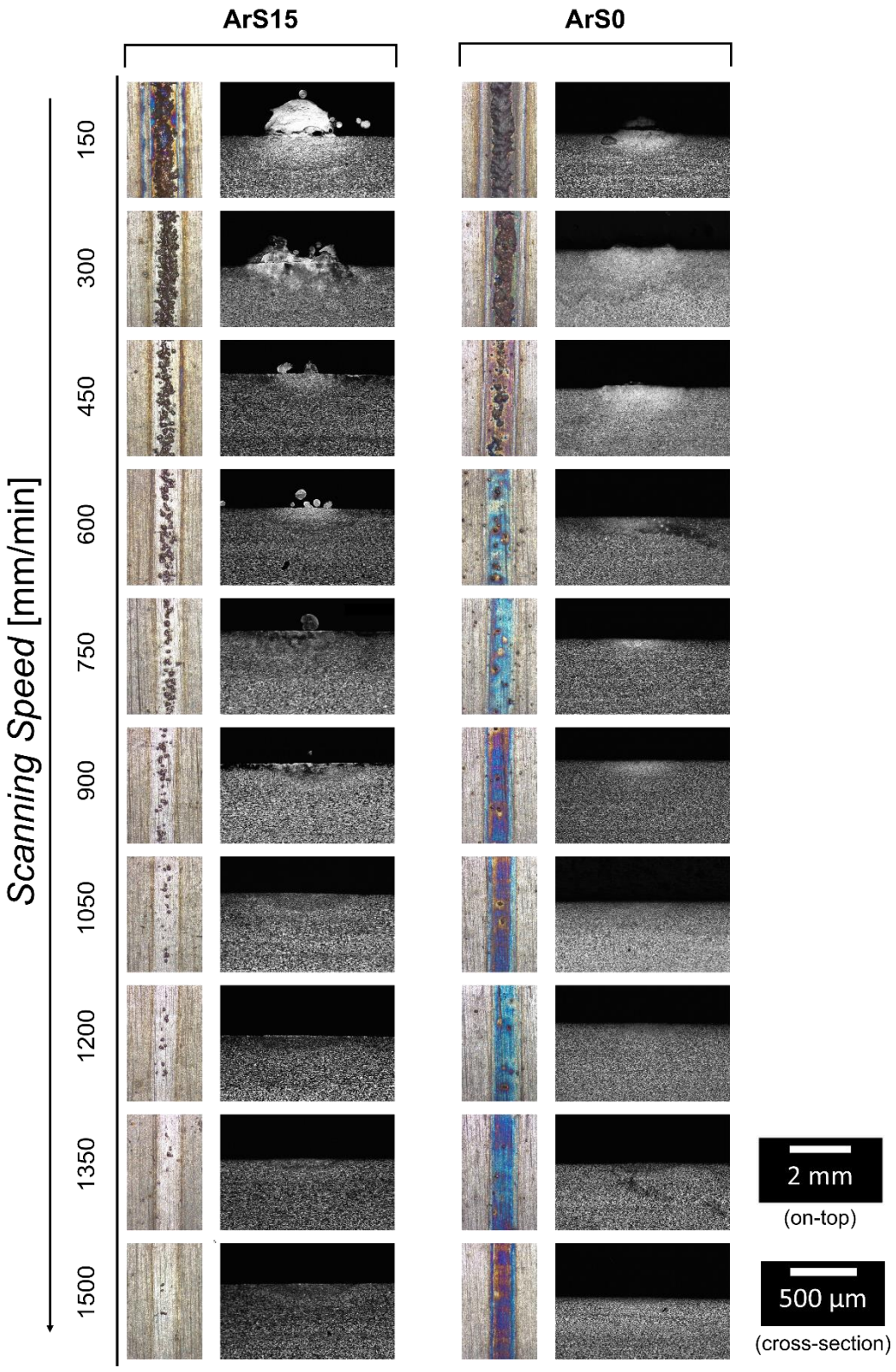


**Figure 47:** On-top and cross-section view of the DED Ti-6Al-4V scans built using P = 100 W, both ArS0 and ArS15 condition. The two different scalebars are related to the on-top and cross-sectional views.

By looking at the cross-sections, the poor adhesion between the platform and the scan was evident, even at low scanning speeds. In fact, the contact areas were characterized by delamination cracks (e.g. ArS15, v = 150 mm/min). Therefore, as

a consequence of the low deposition rates and defective adhesion between the specimens and the platform, the samples built using P = 100 W will not be considered in further analysis, as the use of such parameters would certainly generate very low-quality samples.

The on-top observation of the other samples highlighted the surface oxidation of the scan, which highly varied according to the process parameters (P, v, additional shielding gas) used, as illustrated in Figure 48.

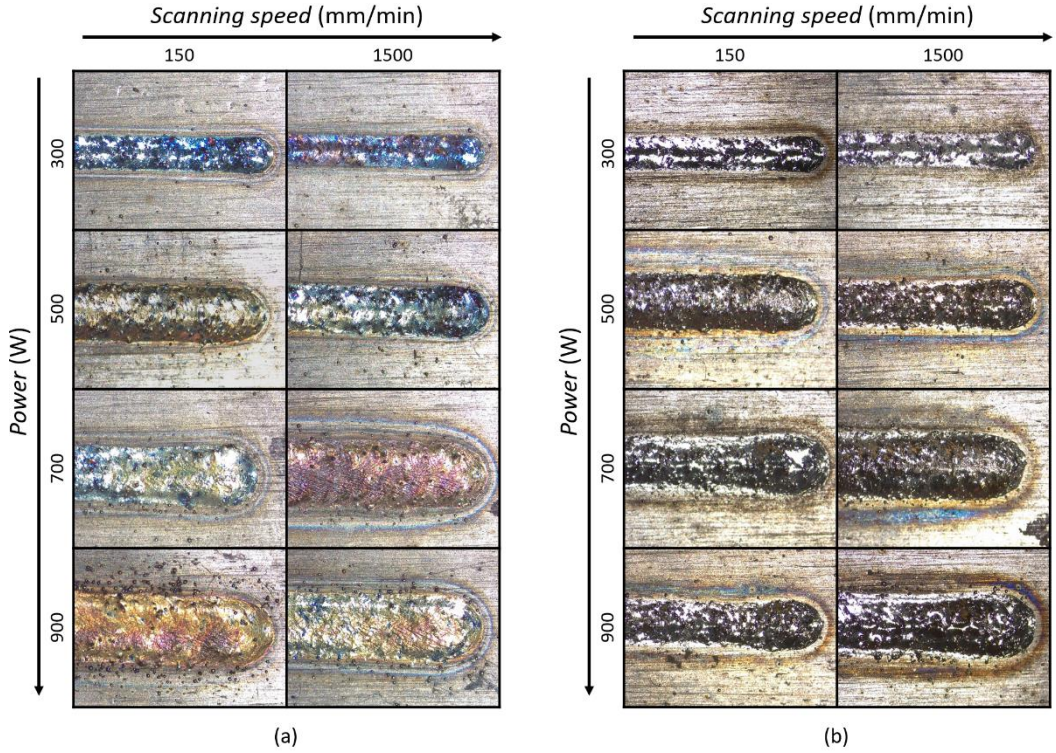


**Figure 48**: On-top view of the ArS0 (a) and ArS15 (b) DED Ti-6Al-4V samples built using P = 300, 500, 700, 900 W and v = 150, 1500 mm/min.

The ArS0 samples provided colorful external surfaces for all ranges of P and v considered (Figure 48a). This was correlated with oxidation. In fact, in α+β titanium alloys, the color of the surface can be linked to the temperature at which oxidation occurred [8,161]. The samples built without using the additional shielding gas system showed surfaces ranging from golden to blue-purple, which can be correlated to oxidation phenomena occurring in the 500-650 °C range. Usually different phases are involved, such as TiO, $TiO_2$ and $Ti_2O_3$. Such surfaces result unacceptable for fusion welding as correlated to excessive oxygen enrichment [161,162]. Even if this is just a qualitative analysis, the American Welding Association (AWS) has specifications for the application of fusion welding to aerospace components in which this simple observation is suggested in order to evaluate excessive oxidation in titanium welds [163]. Instead, the ArS15 specimens proved to be much more regular in terms of surface coloring (Figure 48b). In fact, all the samples resulted reflective, thus less oxidized. A similar comparison between the two shielding scenarios can be made by considering the substrate of the samples built using P = 100 W (Figure 47). This was clearly

visible, due to the poor number of particles adhered to the surface, which allowed to clearly see the "melting" area. When the additional shielding system was used, the substrate appeared reflective, while in the opposite scenario it showed severe oxidation. Therefore, a secondary gas flow proved to be markedly beneficial in terms of oxidation protection.

All the samples were then cross-sectioned and analyzed in order to evaluate several geometrical features, such as the scan's width (W), growth (G) and depth (D), which are schematized in Figure 49.

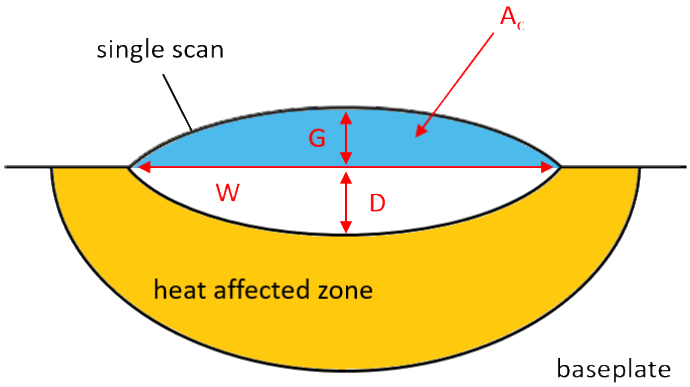


**Figure 49**: Schematic representation of the cross-section of a single scan and relative geometrical features.

In order to consider the influence of multiple parameters simultaneously, all the geometrical features were plotted as a function of the linear energy density (LED), which was calculated as:

$$LED = \frac{P}{v} \tag{6}$$

The corresponding trends are visible in Figure 50.

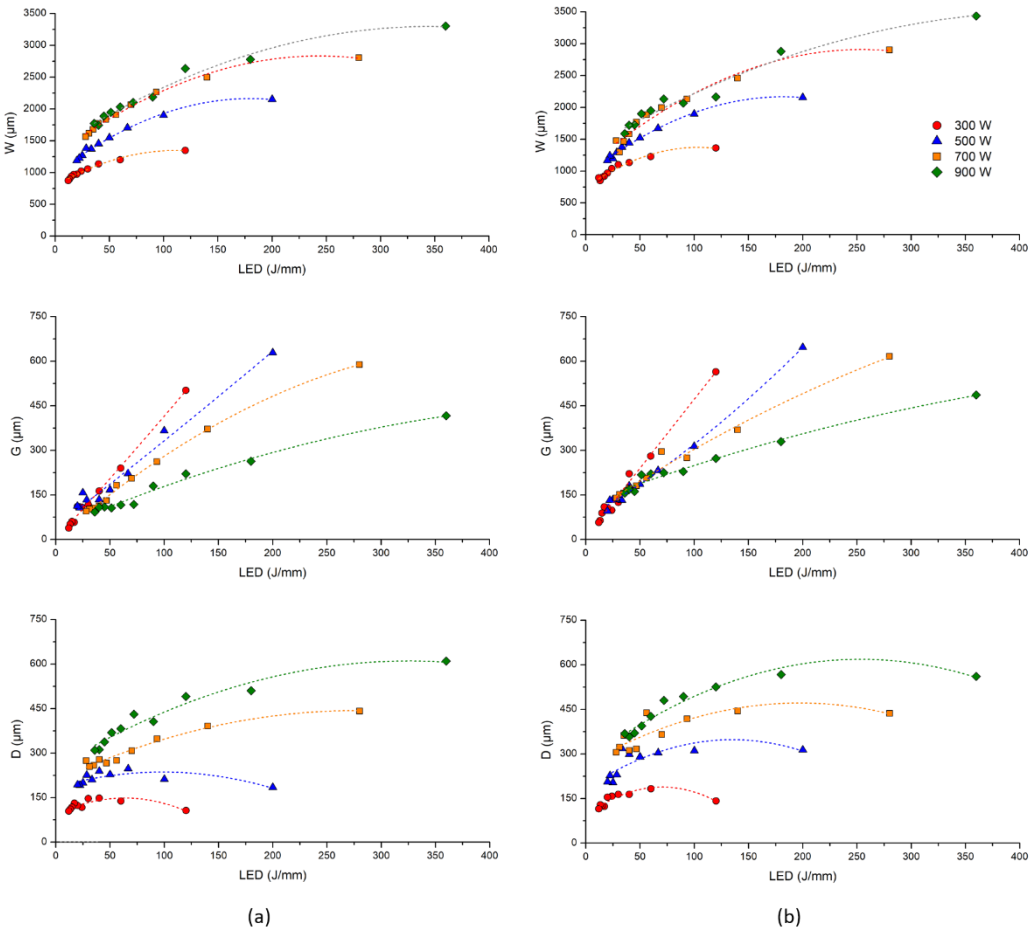


**Figure 50**: W, G and D evaluations for all the ArS0 (a) and ArS15 (b) DED Ti-6Al-4V specimens.

The analysis of W provided positive variations at increasing LED values, both for ArS0 (Figure 50a) and ArS15 (Figure 50b) samples. Moreover, for fixed laser power values, the samples built using a higher energy density, thus lower v, resulted larger. For low to intermediate LED values (< 200 J/mm), the trends for the high P samples (700 and 900 W) overlapped, suggesting a power threshold over which the width cannot grow anymore, by just varying the laser power used. Overall, the increasing W values correlated to higher LED used were probably due to the improved ability of the system to melt the feedstock powder, thus effectively depositing a higher amount of material. Considering G, this parameter was characterized by a different behavior with respect to W. In particular, steeper trends resulted linked to lower P values. However, a higher P allowed to reach higher LEDs, which still provided higher G values. Instead, D showed a similar behavior to W. However, a P threshold was not found, unlike in the former case. Furthermore, the slope of the curves at higher LED values decreased consistently. When comparing the two different shielding scenarios, negligible variations (< 10%) were detected on W. Oppositely, for G and D, the ArS15 samples were characterized by bigger features with the respect to the ArS0 ones, especially at higher LED values.

Most samples showed very negligible porosity values. As a consequence of that, the minimization of the porosity was not considered as a defining criterion in order to obtain the optimized process window. This proved that the process is quite stable in most of the conditions analyzed. The high densities reached are in good agreement with the values available in literature [128,129], which are also obtained with low powder feed rates (< 10 g/min).

Another important parameter that can be used in order to find the most suitable process window is the G to D ratio. Capello et al. [164] adopted it to discern the energy spent to effectively melt the deposited material from the one used to remelt the platform. Moreover, this parameter is an indicator of the quality of the metallurgical bonding between the scan and the baseplate. The authors also found a threshold value for G/D = 1, over which this bond is not strong enough, thus making the process parameters adopted to produce the samples characterized by such values to avoid. Basically, if G/D > 1, the growth of the deposited layer exceeds the ability of the system to fully remelt the previously deposited one. This can lead to the insurgence of undesired phenomena, such as debonding and pores/crack formation [153]. The evaluation of the G/D ratio provided the trends visible in Figure 51.

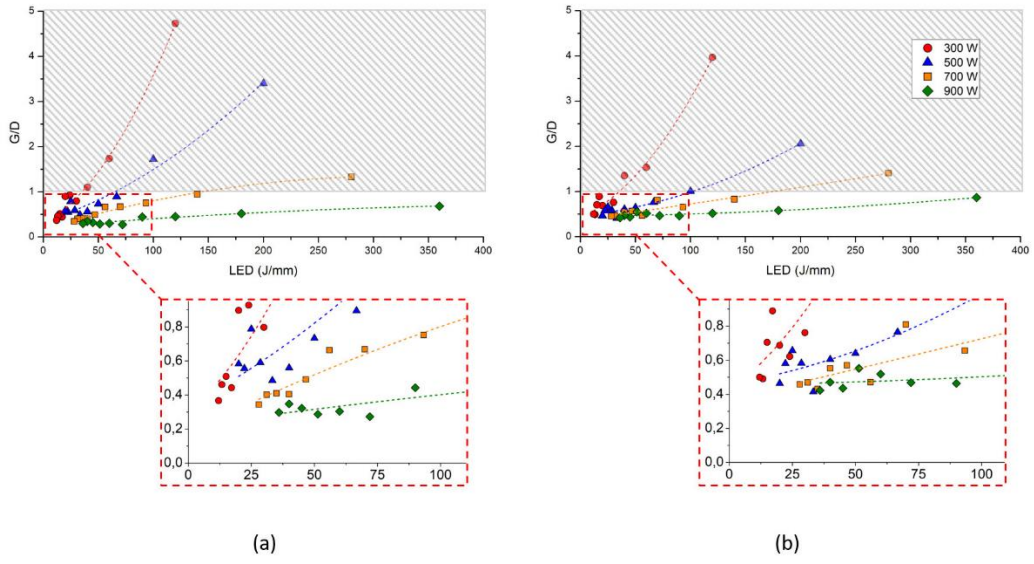


**Figure 51**: G/D plotted as a function of LED for the ArS0 (a) and ArS15 (b) conditions.

Most of the conditions analyzed provided G/D < 1. The exceptions were more frequent at lower P values. This means that, when a higher laser power is adopted, the user has more freedom to change the process parameters without compromising the quality of the 3D samples manufactured. The ArS0 samples showed higher G to D ratio values in correspondence of low powers (300, 500 W). This was a consequence of the stronger effect of the additional shielding gas flow on D, whilst G was mostly unchanged by the variations of this parameter at low P (Figure 50).

In order to further optimize the assessment of the process window, the powder efficiency ($P_e$) can be estimated. This parameter can be used to assess the amount

of the feedstock powder that is effectively delivered and then melted on the platform. Its evaluation is very important to make the process more efficient and reduce the production of waste material. De Oliveira et al. [165] estimated it using the following equation:

$$P_e = 100 \cdot \frac{A_C \cdot v \cdot \rho_p}{F} \ (\%) \tag{7}$$

In which $A_c$ represents the upper area of the cross-section, as highlighted in blue in Figure 49, $\rho_p$ is the density of the powder (4.43 g/cm$^3$).

The resulting trends, provided in Figure 52, highlighted a marked increase in the deposition efficiency for high P values. Overall, an increase in LED leaded to more consistent increases for lower P values instead.

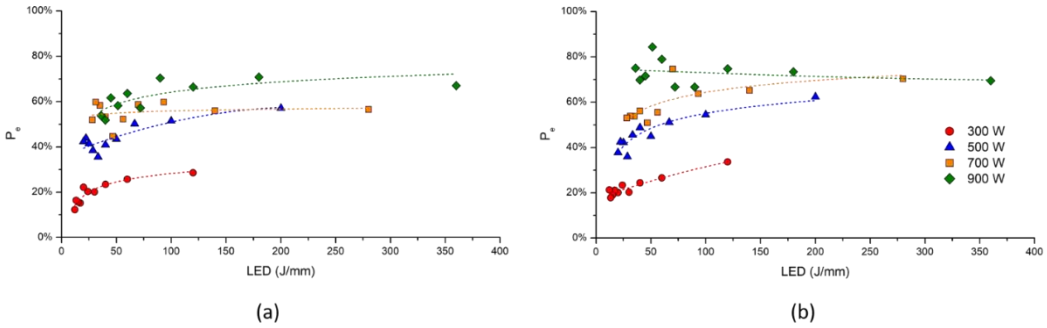


**Figure 52**: Pe plotted as a function of LED for ArS0 (a) and ArS15 (b) shielding conditions.

When comparing the ArS0 and ArS15 results, the former (Figure 52a) provided $P_e$ values lower than 60%. The only exceptions were the low LED specimens built using the highest power (900 W). The maximum efficiency detected in this condition corresponded to 70.9% for the scan built using a LED of 180 J/mm (900 W, 300 mm/min). When the ArS15 case is considered (Figure 52b), comparably with the former case, most $P_e$ values resulted lower than 60%. However, the exceptions were more numerous (samples built using P = 700, 900 W) and characterized by even higher efficiencies. The maximum value detected was 84.3% for the specimen built using a LED of 51.4 J/mm (900 W, 1050 mm/min). Therefore, the adoption of an additional shielding gas system seemed to provide a beneficial effect on the system, in terms of deposition efficiency. In order to further analyse the impact that the shielding conditions have, the $\Delta P_e$ parameter was also evaluated and plotted in Figure 53. It was calculated as the difference in powder efficiency between the two shielding scenarios:

$$\Delta P_e = P_e^{ArS15} - P_e^{ArS0} \tag{8}$$

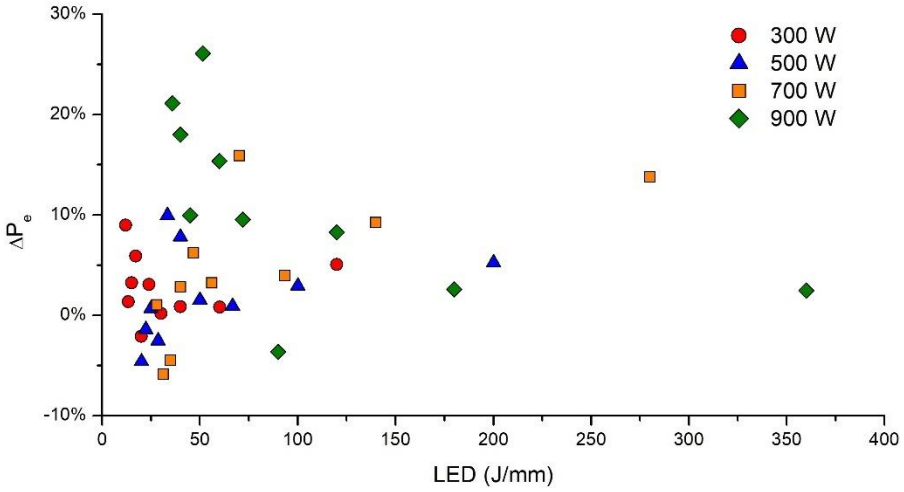


**Figure 53**: Comparison of the shielding efficiency via $\Delta P_e$ evaluation.

According to the data gathered, the beneficial effect of the additional shielding gas was marginal for lower P values. In fact, considering the low power samples (300, 500 W), all the relative points lied in the range between -5% and 10%. For P = 700 W, the rise in $\Delta P_e$ resulted more consistent, specifically for the samples built using a high LED, which provided increases ≥ 10%. When the highest laser power was considered (900 W), the increase in efficiency, connected to the shielding scenario, was markedly evident, in particular for low-LED samples (< 75 J/mm), which provided a variation ranging from approximately 10% to more than 25%. These specimens were also the ones that were characterized by the highest efficiency values (Figure 52). This confirms the beneficial effect of the supplementary protective flow, particularly if high P and low LED, thus high v, are used.

$P_e$ depends on several parameters ($A_c$, v, $\rho_p$, F), however only the specimens built using the same process parameters were compared, during the $\Delta P_e$ evaluation, and the density was considered constant. Therefore, $\Delta P_e$ was exclusively dependent on the geometrical features of the scans in this evaluation. When analysing the deposition efficiency of DED produced Ti-6Al-4V, Mazzucato et al. [160] encountered a similar $P_e$ behaviour. They found that the additional shielding gas system allowed to better concentrate the flux of feedstock powder, allowing the delivery of an increased amount of material in the melting area. A similar phenomenon was encountered in this analysis, as testified by the on-top images of the single scans built using a P of 100 W and a v of 750 mm/min, as illustrated in Figure 54.

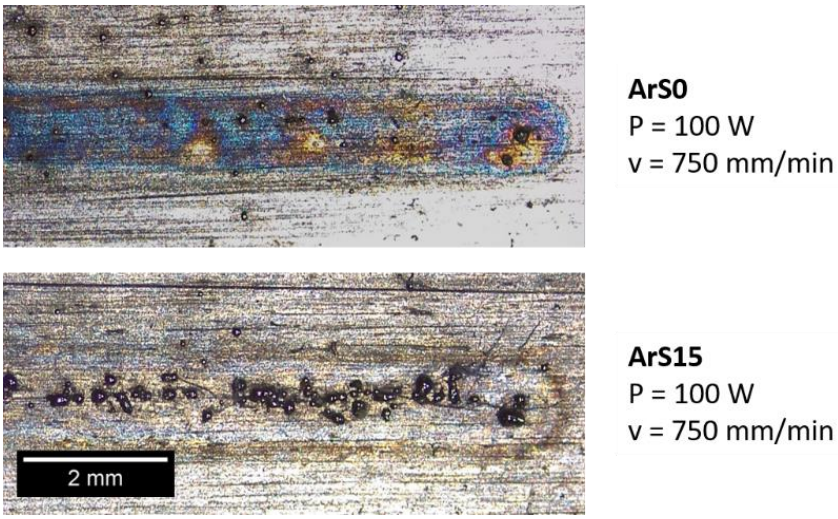


**Figure 54**: On-top views of two scans, characterized by the same machine parameters, but different shielding conditions.

The specimens characterized by P = 100 W were already rejected in this evaluation, due to the very poor powder delivery rates, connected with the lack of effective melting phenomena. However, the absence of an actual single scan allowed to investigate how the powder behaved during the process, as only sparse particles poorly adhered to the surface were available in most samples. Considering the samples built using the same process parameters, a greater concentration of particles in the central area of the single scan was evident in the ArS15 scenario. Then, the beneficial effect of the supplementary shielding gas apparatus was probably due to an increase in the total gas flow for the system, resulting from the additional shielding gas and carrier gas flow. This augmented flow rate reduced the chances of the particles to flow outside of the melting area, thus reducing $P_e$.

## *Microstructure*

All the samples analyzed showed prior-β grains in a columnar morphology, characterized by a mainly martensitic microstructure, in which the α' needles were clearly recognizable. In order to be able to numerically quantify the microstructures, the α' spacing was chosen as the most representative parameter.

In order to compare the effect that different laser power values had on the microstructure, all the samples built using P = 300 W and 500 W were analyzed, as illustrated by the trends available in Figure 55.

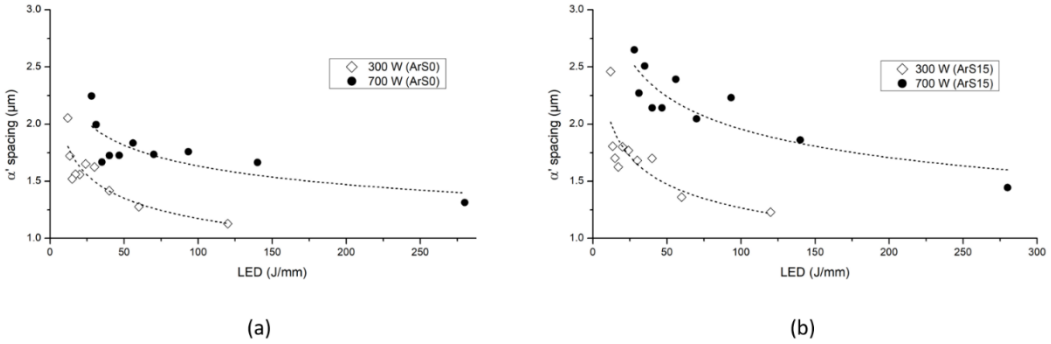


**Figure 55**: α' spacing evaluated for all the DED Ti-6Al-4V samples built using a laser power of 300 W and 700 W, in both the ArS0 (a) and ArS15 (b) conditions.

Martensite formation and size are strictly dependent on many factors, in particular the cooling rate that the sample undergoes [24,25]. The evaluation of the martensitic spacing, which is correlated to its size, is fundamental in order to assess how the process parameters influence several properties of the material, including the mechanical ones. All the conditions considered provided a clear downward sloping trend for increasing LED values, thus an inverse correlation was found between these two parameters. In fact, the samples characterized by the finer martensitic microstructure (lower α' spacing) corresponded to the highest energy densities. In fact, as confirmed by a study by Yan et al. [166], the samples built using higher LED values undergo a lower cooling rate, which results in a finer martensitic microstructure [157].

When comparing the ArS0 (Figure 55a) and ArS15 (Figure 55b) conditions, a similarity in the relative trends is evident, even if the samples of the former group provided finer microstructures overall. This might have been correlated to a more consistent enrichment in interstitial elements (e.g. O, N) that the ArS0 samples underwent during fabrication, which can be reasonably assumed to be superior with respect to the case where the additional shielding system was used. This enrichment in the concentration of interstitials elements in the alloy must be avoided at all costs. In fact, even in low concentrations, these elements can cause severe embrittlement, a moderate increase in the $M_S$ and a sudden rise in $T_\beta$ [167]. These variations cause an enlargement of the temperature range between $T_\beta$ and $M_S$, thus favouring the $\beta \rightarrow \alpha+\beta$ transformation upon cooling from the molten state. This assumption is in good agreement with the experimental data and with a previous work [157], in which the DED produced Ti-6Al-4V specimens characterized by a higher concentration of interstitials provided a finer microstructure, characterized by traces of α and β phases alongside α'.

To further investigate the assumptions made, a further microstructural comparison between the ArS0 and ArS15 condition was conducted. The samples built using the same parameters (P, v) were compared to better understand the effect of the additional shielding system on the microstructural quality of the single scans, as representatively illustrated in Figure 56.

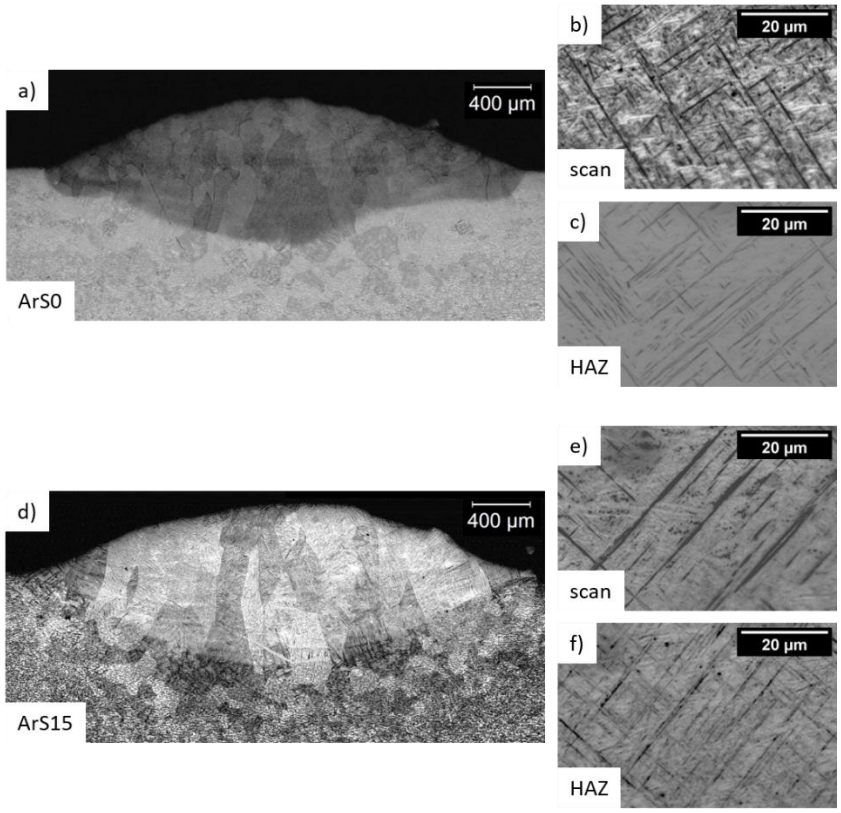


**Figure 56**: Representative cross-sectional micrograph of an ArS0 sample (a) and relative higher-magnification microstructures of the scan (b) and heat affected zone (c); representative cross-sectional micrograph of an ArS15 sample (d) and relative higher-magnification microstructures of the scan (e) and heat affected zone (f). The samples shown share the same building parameters (P = 700 W, v = 300 mm/min).

Whilst all the ArS15 samples provided a completely martensitic microstructure (representative micrograph in Figure 56d), most of the ArS0 specimens showed (representative micrograph in Figure 56a) the mixed α'/α+β microstructure mentioned before, in which the martensitic needles lie in a α+β matrix. This difference was even more evident when comparing the microstructure of the scan and its heat affected zone (HAZ). The samples built in the ArS0 condition, provided a microstructure (Figure 56b) markedly different from their HAZ (Figure 56c), which appeared completely martensitic instead. Similarly to the bulk area and relative HAZ of the ArS15 specimens (Figure 56e,f), both the scan area and the HAZ recrystallized due to the energy input provided by the laser, that caused the temperature to rise above $T_\beta$. However, in the former case the temperature exceeded the melting temperature ($T_m$) of the alloy, whilst in the latter case $T_\beta < T < T_m$, only resulting in the recrystallization of the material. In general, oxygen pick-up and oxidation are phenomena markedly more efficient in the molten state, in which oxygen mobility is greatly increased, allowing it to efficiently disperse [168]. The mixed microstructure was only found in the bulk area of the ArS0 sample, whose HAZ resulted instead martensitic. As oxygen dispersion is less efficient in the solid state, a direct correlation between the lack of an additional shielding flow and a microstructural variation was found. In another work from the authors [157], the Ti-6Al-4V

samples, whose interstitial elements enrichment resulted consistent enough to induce a microstructural change, resulted very brittle and correlated to some in-process unacceptable issues, such as the insurgence of cracks and/or layer debonding. Therefore, as a result of these considerations, the additional shielding gas must be used at all times in order to avoid the formation of such defects. Consequently, when evaluating the process window, the ArS0 condition was not considered.

## *Process Window Evaluation*

In order to obtain the most promising parameters to process the Ti-6Al-4V alloy, the following criteria were considered:

- The ArS0 condition was not considered as a result of the investigation of the microstructures, as it was connected to excessive oxygen pick-up. Therefore, the process window had to be applied exclusively to the ArS15 condition.
- The samples built deploying a laser power of 100 W were rejected, due to the low deposition rate and defective interface between the scan itself and the platform.
- The combinations of parameters that provided specimens characterized by $G/D > 1$ were unacceptable, as these would result in low quality 3D components.

The remaining possible combinations are illustrated in Figure 57. These were numerous, proving the stability of the process for this alloy, which implies a certain degree of freedom in the choice of parameters.

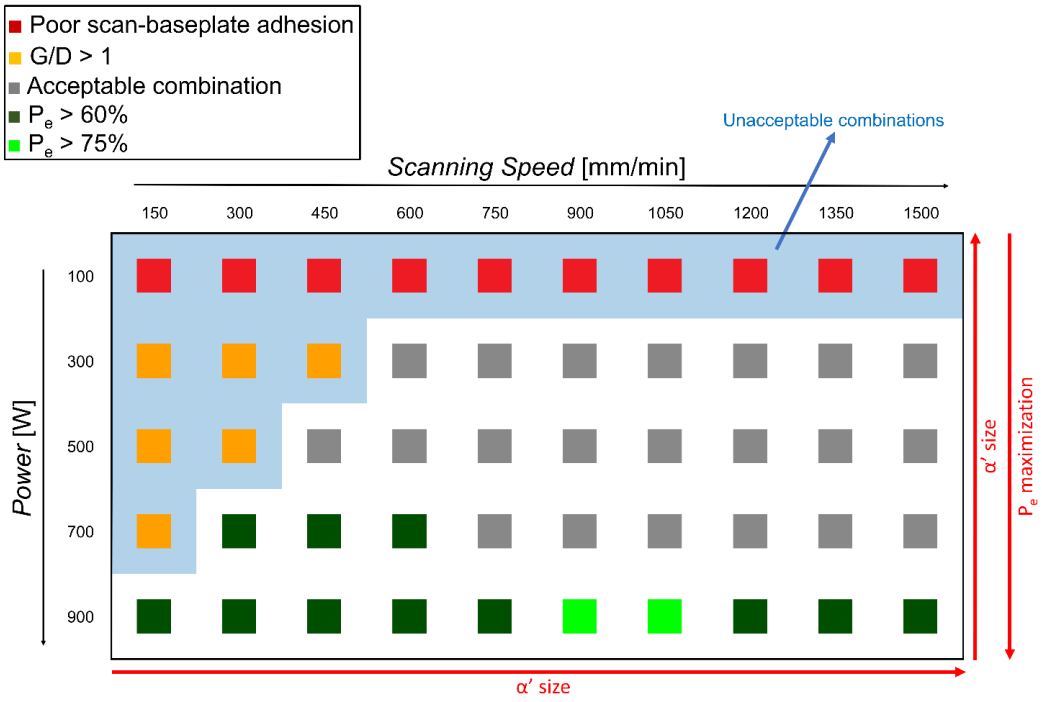


**Figure 57**: Color-coded process window obtained as a result of all the analysis performed in this work; the environmental condition considered is ArS15.

Choosing to operate the laser at high powers provided more promising efficiency values. However, a lower P resulted in a rougher microstructure (α' spacing), which might be beneficial in terms of processability, as a tight martensitic spacing provides a microstructure in which the dislocation motion is severely hindered. This results in the embrittlement of the material, which might cause debonding or cracking [24].

## *Conclusions*

The aim of this work was to investigate how several process parameters (P, v, shielding) affected the quality of DED produced Ti-6Al-4V. The final goal consisted in finding the proper parameters combinations in order to process the material. Moreover, the influence of these parameters on the microstructure was also identified. The most significant results obtained were:

- The laser power must be higher than 100 W, value too low to effectively melt the delivered feedstock powder.
- Using a supplementary argon flow to protect the melting area allows to avoid undesired phenomena, such as interstitials pick-up and severe oxidation of the samples, which result in a severe embrittlement of the material.
- G/D proved to be a useful parameter in order to discern the acceptable process parameters. In particular, its adoption allowed to exclude some parameters combinations, characterized by low P and v values.
- The efficiency of the process resulted higher when high P values were used. Moreover, the additional shielding flow allowed to better

concentrate the feedstock material, resulting in a further increase in $P_e$. Among all the combinations considered, the one that provided the highest efficiency had P = 900 W and v = 900-1050 mm/min.

- A correlation between the process parameters adopted and the microstructure was found. Finer microstructures (lower α' spacing) corresponded to higher LED values. This information allows to customize the process according to the desired properties to achieve, as in fact α' influences, for example, the mechanical properties (e.g. hardness, strength) of the material.
- An overall best combination was not found, proving that the DED process is quite stable and flexible for the Ti-6Al-4V alloy. A proper choice of process parameters allows the user to customize the process according to his necessities (e.g. microstructural customization, efficiency maximization).

### 3.1.2 Investigation of the Effect of the Process Environment on the Quality of Ti-6Al-4V Samples Built via DED

Most works on the optimization of the deposition process of the Ti-6Al-4V alloy available in literature focus on the determination of the machine process parameters, such as the laser power and scanning speed [150–152]. However, a correlation between the properties of the final component (e.g. microstructure, mechanical properties) and the process environment is still lacking.

One key aspect is the process atmosphere, which is fundamental to optimize, as some gaseous elements, such as nitrogen and oxygen, are critical for titanium alloys containing mainly α phase, such as Ti-6Al-4V. As mentioned in the introduction, these α-stabilizing elements fit well in the octahedral vacancy of the hcp α lattice (≈ 0.60 Å). Moreover, even if present in small concentrations, these elements cause a drastic reduction of the ductility [4]. Furthermore, this aspect is even more critical for AM produced components, usually characterized by the extensive presence of the embrittling α' martensite. Yan et al. [169] estimated a 0.22% threshold value for the concentration of oxygen allowed in a Ti-6Al-4V component produced by means of AM, over which the embrittlement of the material results unacceptable. Thus, the interstitial elements pick-up must be carefully controlled during DED processes in order to avoid undesired consequences in terms of ductility reduction. Carrying the process in a sealed environment filled with inert gas (e.g. glovebox) is surely the safest option to conduct the deposition, as this choice provides a strict control over the process atmosphere, resulting in negligible increases of oxygen concentration in the final specimens [128]. However, this limits the maximum size of the component, which must be smaller than the chamber itself in order to fit, and makes repairing operations of larger components, one of the most promising aspects of the DED technology, more complex. Therefore, a certain number of authors investigated the possibility to conduct the deposition in an open environment, aided by a

shielding gas flow in order to avoid excessive interstitials enrichment in the alloy [159,170]. However, a direct comparison between these two process environments is lacking.

Another important aspect to consider is the platform temperature. Raising this is a key strategy in order to reduce excessive stress build-up in the samples [115]. This phenomenon is particularly critical for titanium alloys, which are usually characterized by high strength even at high temperatures [104]. In fact, excessive residual stresses might result in cracks or shrinkage (distortion) of the samples [171].

To sum up, most works available in literature evaluated the influence of different machine-related process parameters by varying them in a fixed environment. Instead, in this work an opposite approach will be followed and the process environment (atmosphere, temperature) will be varied as the machine parameters will be fixed, as described in Table 9.

**Table 9:** Process parameters used to build the Ti-6Al-4V samples.

| Power (W) | Scanning Speed (mm/min) | Powder Feed Rate (g/s) | Hatching distance (mm) | Z-Step (µm) | Scanning Strategy |
|---|---|---|---|---|---|
| 300 | 700 | 0.017 | 0.58 | 100 | 0°/90° |

Several 15x15x15 mm cubic samples and 10x10x100 horizontal bars were built in order to assess possible differences given by the size of the specimen. Three total conditions were considered:

- **SE-CB** (Sealed Environment, Cold Base), for the samples built using a glovebox-like chamber and a non-heated platform;
- **SE-HB** (Sealed Environment, Hot Base), for the samples built using a glovebox-like chamber and a heated platform (220 °C);
- **ArS** (Argon Shielding), for the samples built in an open environment using an additional shielding gas system in order to protect the samples from contaminations.

## *Microstructure*

The optical micrographs of the cross-section of the samples analysed are provided in Figure 58. All the samples shared the presence of columnar prior-β grains, developed perpendicularly to the baseplate via epitaxial growth [148,172]. This is a typical outcome for samples produced via several AM techniques, as the ability of the system to dissipate heat is highly directional towards the platform direction. Moreover, banding, another typical DED feature, was noted in all the samples (Figure 58a,c,e). The microstructure of the samples built in a sealed chamber (SE-CB, SE-HB) (Figure 58b,d) resulted quite homogeneous and characterized by the presence of α' martensite. Massive martensite formation is usually the results of manufacturing processes/heat treatments in which the sample undergoes a very fast cooling. Therefore, α' formation is kinetically favoured over more

thermodynamically stable phases, such as α and β. Oppositely, the ArS samples showed, other than martensitic needles, a lamellar microstructure, arranged in a ± 30°/60° fashion (Figure 58f). This is a duplex microstructure of α+β in a basket-weave morphology. Its formation might be caused by α' decomposition.

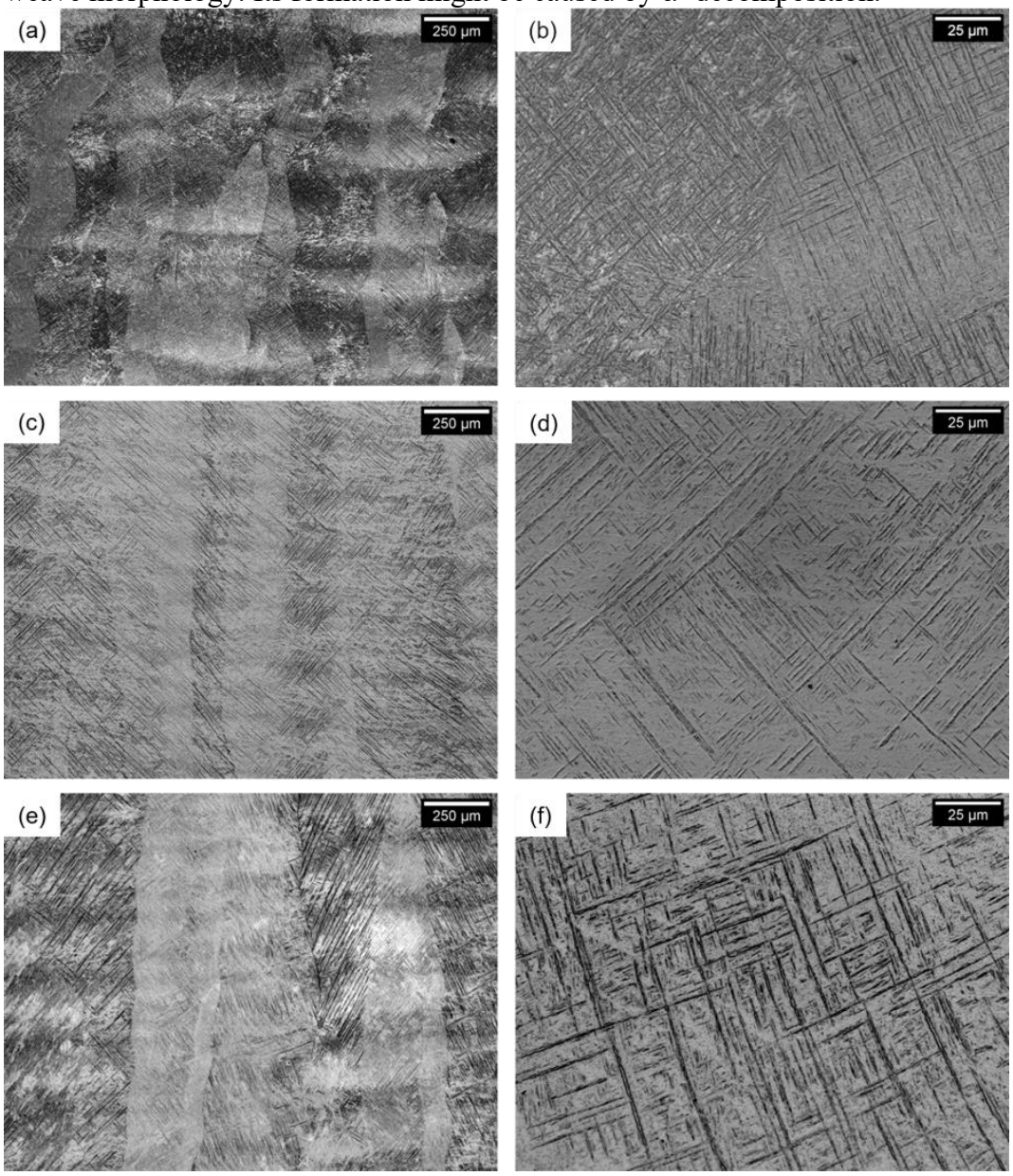


**Figure 58**: Optical micrographs of the ArS (a,b), SE-CB (c,d) and SE-HB (e,f) DED Ti-6Al-4V samples.

In order to confirm the assumptions made during the analysis of the micrographs, the XRD patterns of all the three groups of samples were investigated. These were all characterized by the peaks relative to the α/α' phases [24], as visible in Figure 59. A complete distinction between the pattern of α and α' is very complex, due to those two phases sharing a common hcp lattice [173,174].

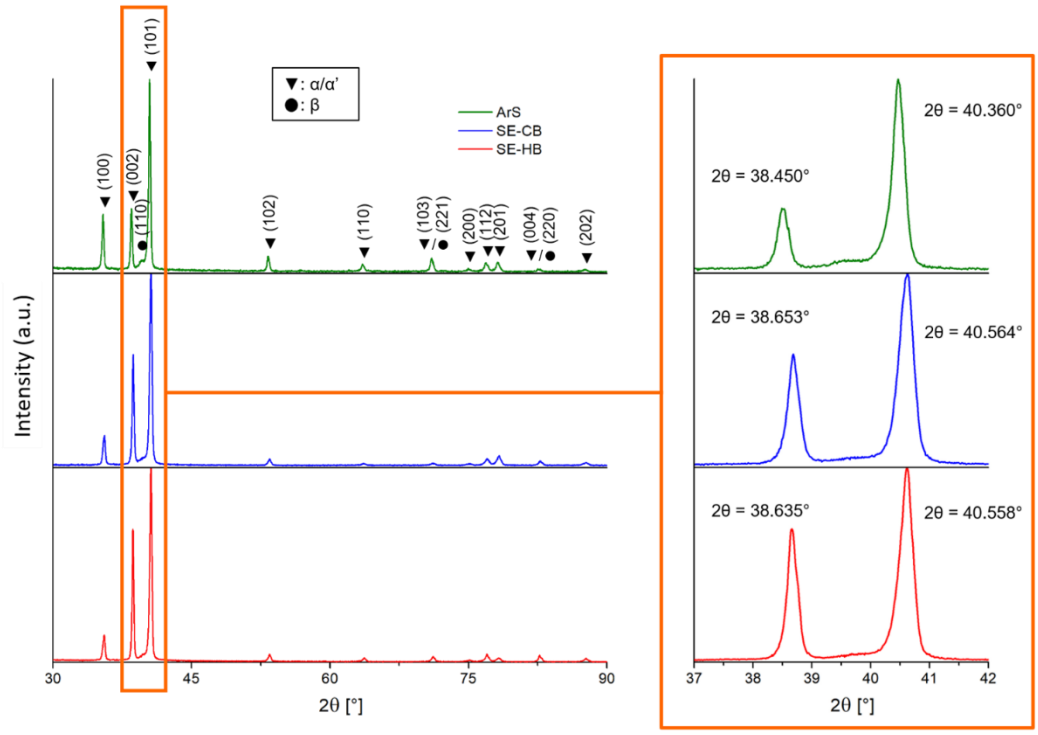


**Figure 59**: XRD patterns of all the conditions considered.

The samples built in a sealed environment provided a shift of the peaks towards higher angles, with respect to the ArS specimens. This might be possibly caused by a different level of internal stress/dislocation concentration. Moreover, the samples built using the additional shielding gas system provided the (110) peak relative to the β phase (bcc) [175]. Thus, confirming that in this group of specimens there is a non-negligible amount of this phase, alongside α', as supposed by the micrographs observation. Considering the possible differences in the manufacturing of the samples, a possible explanation might be the O/N pick-up in the ArS specimens, which would result in a change in composition and phase diagram.

To further investigate the microstructures, the determination of the cell parameters of α/α' was conducted. Then the c/a ratio and cell volume were used as parameters to compare the three families of samples, as visible in Figure 60.

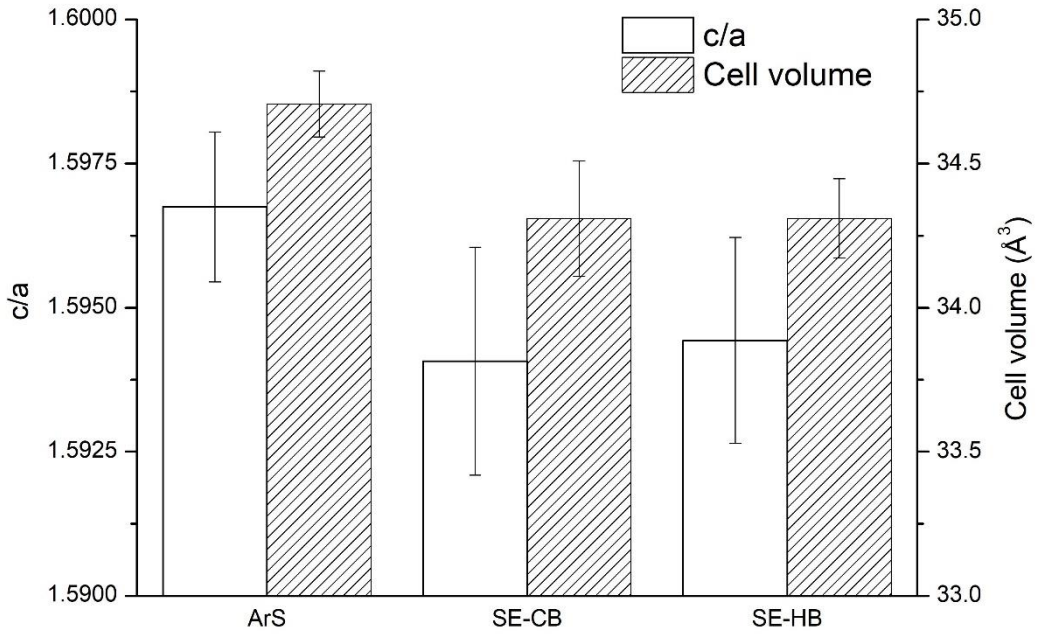


**Figure 60**: c/a ratio and cell volume for all the conditions considered.

Once again, the samples built in a sealed and controlled environment provided similar results. Instead, ArS resulted characterized by a higher c/a ratio and larger cell. This is coherent with the assumption of an increase in the interstitial elements concentration, particularly oxygen, in the ArS samples [176,177]. However, in order to confirm that, the concentration of the interstitials elements must be quantified. To evaluate the effect of multiple elements (O, N) simultaneously, the equivalent oxygen concentration ($[O]_{EQ}$) can be used. This parameter is used to express the impact of different interstitial elements and it is defined by Ogden et al. [9] as:

$$[O]_{EQ} = [O] + 2[N] + \frac{2}{3}[C] \quad (9)$$

The outcome of the evaluation, resumed in Figure 61, provides the lowest O and N concentration, hence $[O]_{EQ}$, in the powder. This means that during the deposition a slight increase in interstitials concentration occurs in all the environments considered.

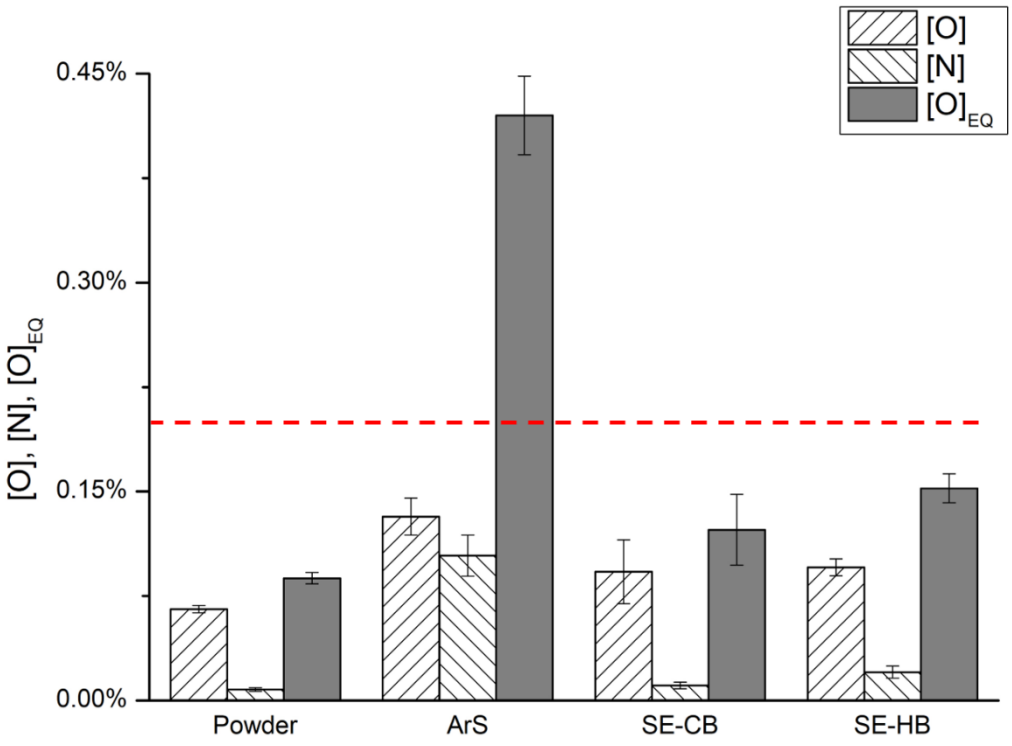


**Figure 61**: Oxygen, nitrogen and relative equivalent oxygen concentrations evaluated for all the conditions considered. The 0.22% threshold is highlighted in red.

The samples that provided the greatest $[O]_{EQ}$ were the ArS ones, with a value of 0.42%, which greatly exceeds the 0.22% threshold over which the embrittlement of the materials results unacceptable, as mentioned before. Instead, the samples built in a sealed environment provided $[O]_{EQ}$ values well below the limit. SE-HB was slightly more enriched in interstitials elements (0.152%) than its cold-based counterpart, possibly due to an increase in oxygen and nitrogen diffusivity, due to the slightly higher temperature of the system, because of the heated platform. To sum up, the evaluation of the concentration of the interstitial elements confirmed and explained two main assumptions made on the ArS specimens:

- The abundant presence of oxygen and nitrogen in the ArS samples can effectively explain the difference in microstructure observed for these samples. In fact, these α stabilizers have a fairly low effect on $M_S$, leaving this temperature substantially unaffected, when relatively low concentrations are considered. However, they imply a significant increase in $T_\beta$, even if present in very low amounts. Substantially, the temperature range between $M_S$ and $T_\beta$ is increased, thus favouring the $\beta \rightarrow \alpha+\beta$ transformation [167]. In fact, these two temperatures represent the edges of the interval in which the formation of an α+β transformation is the only possible phenomenon occurring.

- The larger cell of the ArS samples is the result of oxygen and nitrogen fitting in the octahedral vacancy in the hcp cell, which results in the distortion of the lattice.

After assessing the types of microstructures involved and the relative causes of the differences observed, a more in-depth analysis and numerical quantification of the micrographs allowed to furtherly investigate the solidification behaviour of the specimens in all conditions.

One of the microstructural features that is mostly influenced by the complex thermal history of the process is certainly the grain size. However, in this case and in general in AM, grains show a columnar morphology, which leads to a strictly anisotropic microstructure. These grains can reach up to the height of the sample and are roughly perpendicular to the baseplate, hence parallel to the development direction [89,178]. Therefore, in AM the typical property used to evaluate grains is the grain width, which is then perpendicular to Z. Grains characterization is extremely important in titanium alloys, as it has a direct impact on mechanical properties. However, the complex heating/cooling cycles typical of DED are not homogeneous throughout the whole samples. In fact, the ability of the system to dissipate heat depends on how close a given point is to the platform. In particular, the typical cooling rates of layers characterized by low Z values are higher, as the baseplate effectively acts as a heatsink [105,179]. A correlation between the position of a given point and its relative grain width is then possible. To investigate this phenomenon, the intercept method was used to evaluate grain width at different heights (Z values) in the samples, as illustrated in Figure 62.

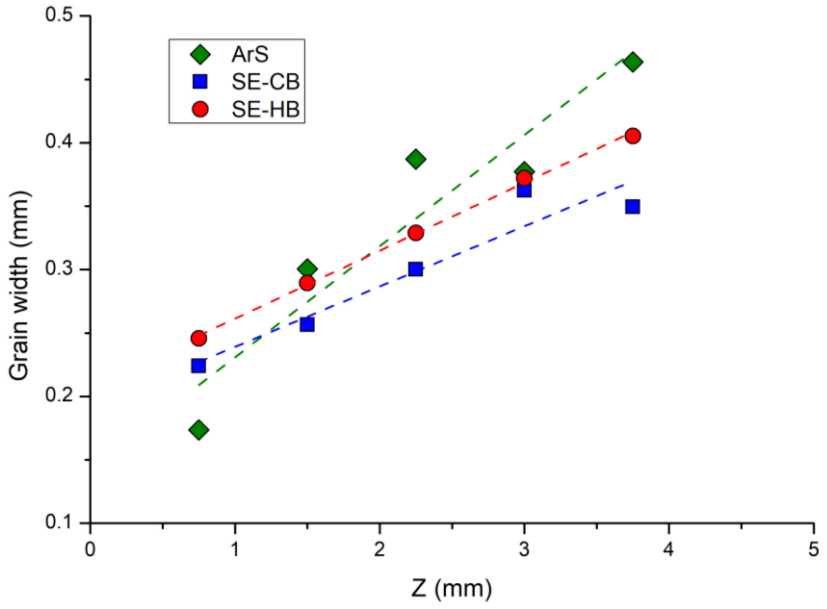


**Figure 62**: Width of the prior-β grains at relative heights and relative linear interpolations for all the conditions considered.

For all the conditions considered, there was a clear upward sloping trend, which was consistent with the considerations made on the cooling rate variations along the samples. The ArS samples provided a steeper slope, which was probably

related to the change in the solidification behaviour given by the different compositions, as demonstrated by the interstitial elements' evaluation. Considering the samples built in a sealed environment, the SE-HB samples were characterized by larger grains. In fact, the heated platform kept the system at a higher temperature during deposition, thus lowering the thermal gradient and relative cooling rate.

Another microstructural feature that can be quantified, in order to further investigate the samples, is the size of the α' needles. This is directly influenced by the process environment and has a strict correlation with mechanical properties [24,180]. α' width was chosen as the representative parameter to investigate. Its evaluation provided the data distributions shown in Figure 63.

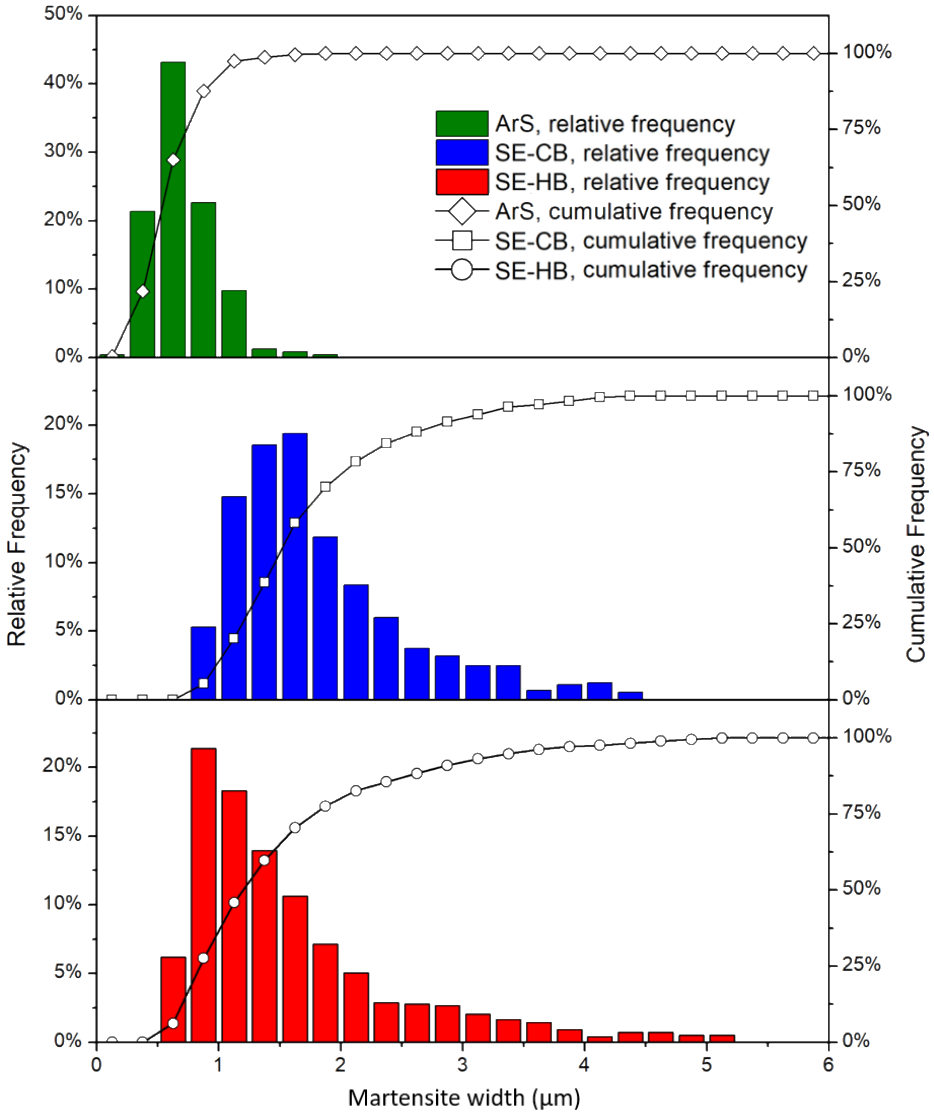


**Figure 63**: α' width relative and cumulative distributions for all the conditions considered.

The ArS samples provided a very fine martensitic sub-structure, with an average α' width value of 0.69 µm, markedly finer than 1.83 and 1.60 µm of the SE-CB and SE-HB samples, respectively. However, the different microstructures

involved must be considered, as the ArS specimens also provided a lamellar α+β microstructure. This significant difference, related to the process environment, had certainly an impact on this measurement. Concerning the samples built in a sealed chamber, their different martensitic width values were mostly due to the different cooling rates involved in the process, as in the grain width evaluation. During cooling (solidification), conduction is the most important heat dissipation phenomenon occurring determining the final cooling rate [25,105]. It is mostly dependant on the difference in temperature between the meltpool and the platform. Therefore, different thermal gradients lead to different cooling rates which then cause a difference in α' size. SE-HB underwent a lower cooling rate, as confirmed by the grain width evaluation. However, their microstructure was finer, when compared to SE-CB. α' growth is an athermal transformation and SE-HB samples were characterized by larger grains, which lead to a slightly lower $M_S$ and $\Delta g_{el}$ [181,182]. The last term is a thermodynamic parameter roughly correlated with the dislocation density of the material [183]. Wollants et al. [184] used it in order to describe the change in Gibbs free energy (ΔG) in a transformation which forms martensite as a product, by approximating it as an elliptic inclusion in the β phase:

$$\Delta G = 2\pi r^2 \gamma - \frac{4}{3}\pi r^2 c(\Delta g_{ch} - \Delta g_{el}) \quad (10)$$

Where c is half the thickness of the inclusion, r is the radius, $\Delta g_{ch}$ is the chemical driving force per volume unit. The ΔG value is in fact a balance between this last term and the elastic strain energy [181]. Moreover, a correlation between a lower $\Delta g_{el}$ value and the growth of the martensitic needles was proved [182].

From a phenomenological point of view, a lower cooling rate induces less stress-related defects in the material, such as the insurgence of dislocations, which favour the nucleation of growth of α' [24,185]. Therefore, samples characterized by a higher cooling rate, such as SE-CB, were characterized by a rougher microstructure, as confirmed by the experimental data. It must be considered that this thermodynamic behaviour is exclusively typical of martensite in titanium. In fact, more stable microstructures, such as lamellar α+β, which formation and growth are diffusion-driven, act oppositely [186].

## *Hardness*

In order to evaluate the mechanical properties of the small samples studied, hardness measurements were performed at different heights, similarly to the grain width evaluation. By doing so, a correlation between this last property and the hardness was possible. The outcome of this evaluation is provided in Figure 64.

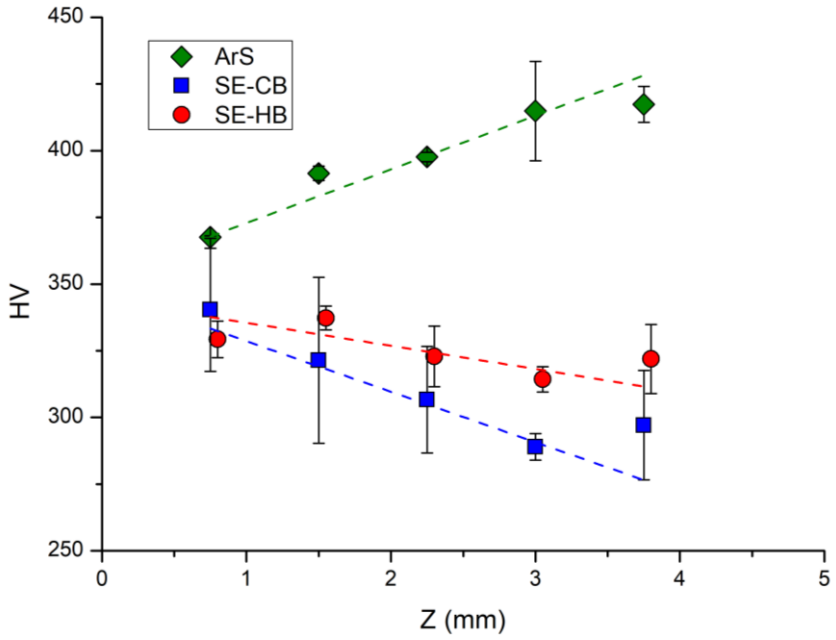


**Figure 64**: Vickers hardness at different heights (Z) in the samples for all the conditions considered.

The ArS samples provided an average hardness of 398 ± 20 HV, which was markedly higher than 311 ± 27 and 325 ± 11 HV values, obtained for the SE-CB and SE-HB samples, respectively. The increase in hardness of the former samples is probably due to the finer martensite (Figure 63) and the different microstructures involved (Figure 58). Instead, the slight difference in hardness between the samples built in a sealed environment was probably correlated to the microstructural refinement. In fact, the SE-HB samples were characterized by a slightly finer microstructure.

A clear correlation between the grain width and the hardness was observed in all the conditions considered. Unlike the samples built in a sealed environment, the ArS samples appeared harder as the distance from the platform increased. This markedly opposite behaviour was probably due to the different microstructure and interstitials content involved. Instead, the other group of samples provided a strict correlation between cooling rate, grain width and hardness. All the specimens provided a highly anisotropic behaviour.

However, these intrinsic variations in local microstructural and mechanical properties were localized in small samples in direct contact with the platform. The resulting anisotropy might become negligible for specimens bigger in size. Moreover, a certain portion of the DED produced components is usually removed via machining, due to the low quality surface, typical of this process. In this case, this phenomenon becomes even more negligible. Although, intrinsic anisotropy must be carefully considered for repairing applications, as usually the rebuilt areas are rather small. Further studies are needed on this subject, in order to identify how the variations in cooling rate impact the quality of bigger specimens.

In order to investigate more deeply how some properties, specifically hardness, change along Z, being able to distinguish between the effect of the microstructural refinement and the effect of the grain width variation, is

important. Both these phenomena are strictly related to the cooling rate and they influence directly the mechanical properties of the material, including hardness.

The Hall-Petch equation [187,188] correlates the grain size and strength, but also hardness, in polycrystalline metals [189,190]:

$$\sigma_y = \sigma_0 + \frac{k}{\sqrt{d}} \tag{11}$$

Where $\sigma_y$ is the material strength, $\sigma_0$ and y are material constants and d is the grain diameter. The evaluation of the last parameter is quite difficult in AM produced materials, characterized by columnar grains, however other works are available in literature in which this investigation was performed [60]. In this case, the grain width was used in order to account the grain size in this equation. The Hall-Petch curves are comparable only if the same type of microstructure is involved, otherwise a discrepancy occurs and the results are not directly relatable, due to the influence of multiple effect on the strengthening mechanisms of the material. In this case, instead of comparing different samples, characterized by different grain sizes, different areas of the same specimens were analysed. These portions were obtained by virtually slicing the samples at different distances from the baseplate, in a similar way to the grain width and hardness evaluations. Therefore, a local measurement (grain width) was correlated with a local mechanical property (hardness). Of course, this comparative analysis works under the assumption that the Hall-Petch equation can be applied to local measurements. The outcome of this investigation is provided in Figure 65.

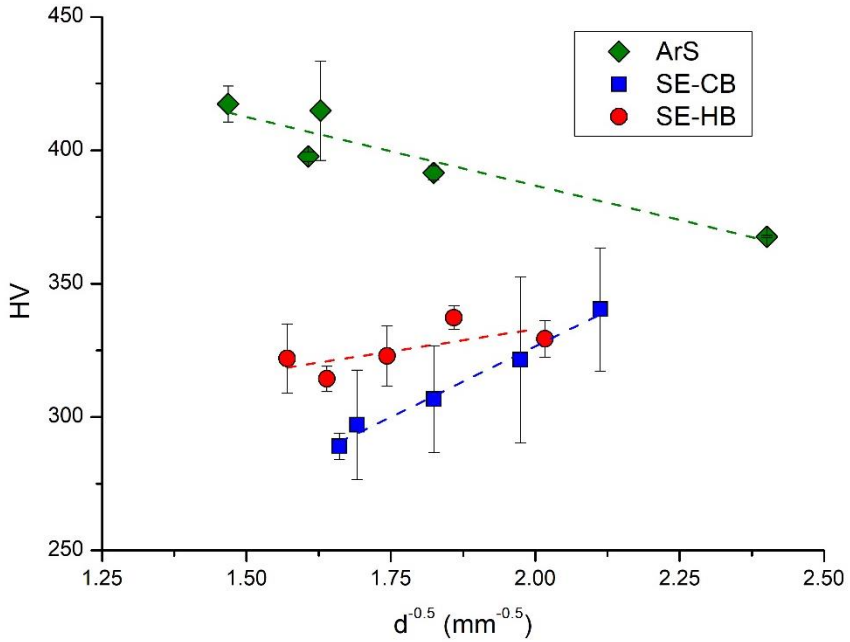


**Figure 65**: Localized Hall-Petch plots for all the conditions considered.

The ArS samples were characterized by an opposite behaviour, with respect to the others, which is a direct consequence of the direct correlation between

hardness and grain width highlighted in Figure 64. Concerning the samples produced in a sealed environment, $k_{CB} \neq k_{HB}$, which suggests that the variation in the baseplate temperature (the only difference between SE-CB and SE-HB) had a certain influence on the Hall-Petch plots, independently from the grain width. This was probably correlated with the slight differences in microstructure (α' size) between these two types of specimens. In fact, Tan et al. [60] stated both grain boundaries strengthening and microstructural refinement must be taken into account when considering variations in strength, or hardness, in Ti-6Al-4V. From a local point of view, Z influences the grain width directly and might influence the microstructure both directly and indirectly. The former phenomenon is correlated with the cooling rate variations along the sample during solidification. The latter depends on the fact that Z, thus cooling rate, impacts on the grain width, thus grain boundaries concentration. Since martensite generation is heavily favoured in presence of grain boundaries [4], a sort of graded microstructure along Z, in terms of martensitic size, is possible. Therefore, inter-grain local average α' width variations along the height of the samples appear possible. Although, further analyses are needed in order to confirm the presence of this phenomenon.

### *Effect on Larger Pieces*

The horizontal bars, manufactured using only an additional shielding gas system as a mean of protection from oxidation and interstitials pick-up, illustrated in Figure 26, presented visible cracks and partial oxidation throughout the whole surface of the sample (Figure 66a,b,c). The analysis of the cross-section highlighted how these critical features extended also inside the bar itself (Figure 66d). Moreover, layer debonding resulted evident.

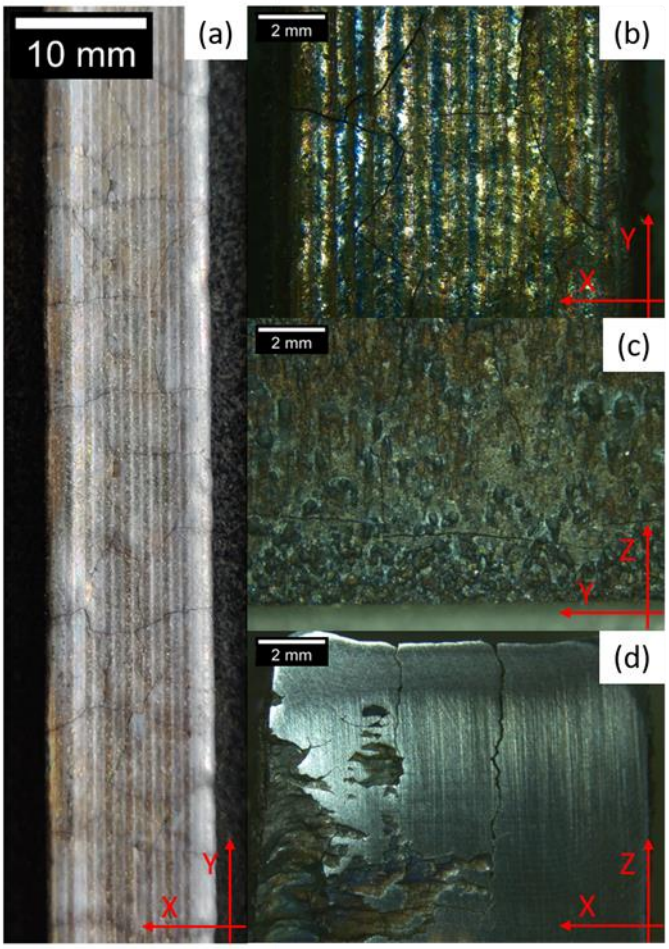


**Figure 66**: ArS DED Ti-6Al-4V horizontal bars: top (a,b), side (c) view and cross-section (d).

The same type of visual analysis was also performed on the samples built in a sealed environment (Figure 67), which instead did not provide any critical feature.

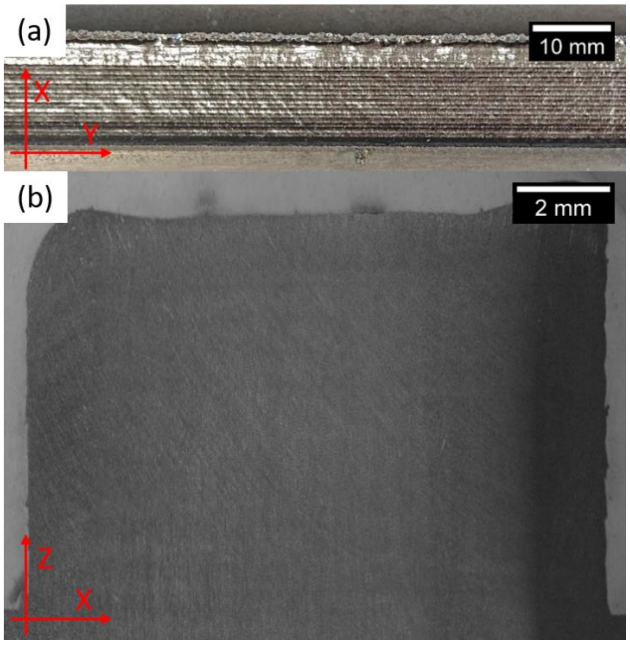


**Figure 67**: Representative image of the top view (a) and cross-section (b) of a DED Ti-6Al-4V horizontal bar built in a sealed environment.

The most important difference between these two sub-groups of samples lied in the process atmosphere. As discussed before, the ArS samples underwent extensive interstitial elements pick-up, which resulted in the $[O]_{EQ}$ value for these specimens to rise well above the embrittlement threshold. This resulted in extensive cracking phenomena during the deposition, even if the Ti-6Al-4V alloy has a low tendency to act so [191]. Therefore, the use of a glovebox-like process environment is critical for the production of samples with large dimensions. Concerning smaller components or repairing applications (usually limited in size), the lack of such equipment appeared acceptable, as an outcome of this analysis. However, the process environment deeply affects the material and mechanical properties of Ti-6Al-4V. This behaviour must be taken into consideration when designing the process.

### *Conclusions*

The aim of this investigation was to evaluate how the baseplate temperature and the use of a sealed environment, compared with a shielding gas flow as only mean to protect the samples from oxidation and interstitial elements pick-up, affected the final quality of DED produced Ti-6Al-4V samples. The most significant results can be summarized as follows:

- The process atmosphere has a great impact on the final properties of the material, in particular microstructure, grain width and hardness are deeply influenced. This effect is so important that an incorrect design of the process atmosphere might even prevent the possibility to produce large samples.
- In order to produced crack-free large components, oxygen and nitrogen contents must be carefully controlled. In fact, the use of a sealed process chamber to protect the samples from these elements' diffusion is mandatory, in this case.
- Using an additional shielding gas flow is possible for producing smaller components or for repairing small portions of larger pieces, that can hardly fit in a sealed chamber. However, this procedure must be carefully studied, as acting so deeply changes the microstructure and mechanical properties of the material. For example, ductility might become a limiting factor, due to the extensive brittleness induced by excessive interstitials enrichment.

## 3.1.3 Study of the Heat Treatments for DED produced Ti-6Al-4V samples

The typical tensile properties related to the as-built condition of DED produced Ti-6Al-4V samples are usually unsatisfying for most applications, due to the severely limited ductility. As mentioned before, this is mostly related to the

massive presence of α', induced during the fabrication process as a result of very fast heating and cooling steps [29,53]. Therefore, in order to decompose this problematic phase, a post processing annealing treatment is mandatory. This type of heat treatments for Ti alloys can be mainly divided into sub-β transus and super-β transus, according to the temperature at which the component is held with respect to $T_\beta$. Several works are available in which a sub-β transus annealing was chosen [170,192–194]. Moreover, some authors also investigated the effect of a post-annealing ageing process [195]. Klimova-Korsmik et al. [158] performed water quenching on the annealed samples, which were then aged and air cooled. However, this path did not induce a significant improvement in ductility for the samples subject of this investigation. Little to no reports of super-β annealing heat treatments conducted on laser deposited Ti-6Al-4V samples are available [170]. The main advantage of such procedure lies in the complete recrystallization of the microstructure, which removes the columnar grain morphology, in favour of an equiaxed one, which provides more homogeneous mechanical properties throughout the sample.

Moreover, an analysis of the effect and significance of an ageing heat treatments on a super-β annealed sample is also missing, according to the author's knowledge.

Therefore, in this work the impact and significance of a super-β annealing heat treatment, followed by either furnace cooling, air cooling or water quenching, and subsequent ageing treatment on the microstructure and mechanical properties of DED produced Ti-6Al-4V ELI samples was assessed. The specimens studied in this investigation were built on two separate baseplates, one of which was not preheated, whilst the other was kept at 220 °C throughout the whole deposition process. For clarity purpose, the samples built on the first substrate were defined **CB** (Cold Base) and the other **HB** (Hot Base). For both condition 5 15x15x15 mm cubes and 3 95x15x15 mm horizontal bars were built, see for instance Figure 68.

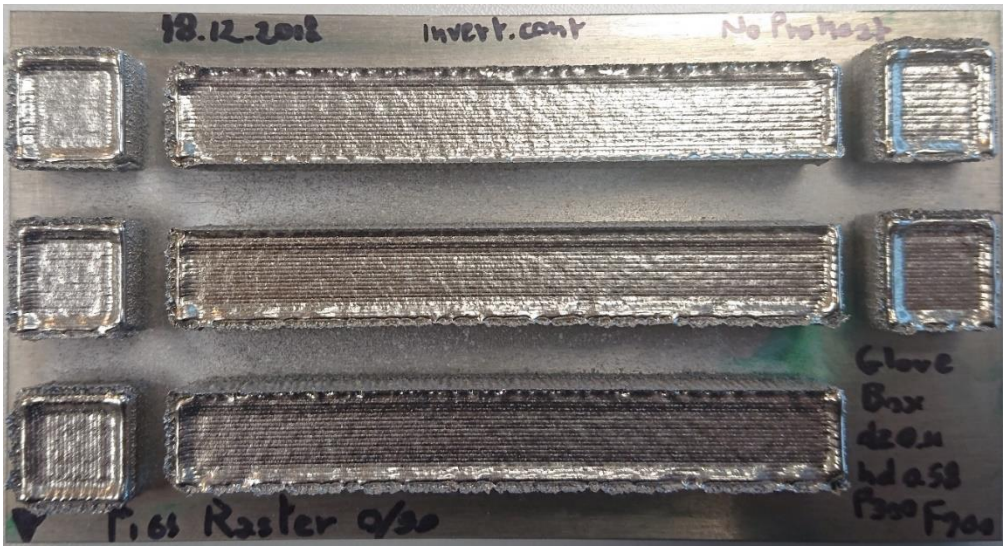


**Figure 68:** On-top view of a platform and relative samples part of this investigation.

The manufacturing process was conducted in a sealed environment filled with argon in order to protect the samples from oxidation and excessive interstitial elements enrichment. The process parameters adopted are reported in Table 10.

**Table 10**: Process parameters adopted to build the specimens for the analysis of the heat treatments.

| Power (W) | Scanning Speed (mm/min) | Powder Feed Rate (g/s) | hatching distance (mm) | Z-Step (µm) | Scanning Strategy |
|---|---|---|---|---|---|
| 300 | 700 | 0.017 | 0.58 | 100 | 0°/90° |

3 cubic sample per condition (CB, HB) were then subjected each to a different heat treatment, as illustrated in Table 11.

**Table 11**: List of the heat treatments investigated in this work with relative specifications.

| | Annealing | Ageing |
|---|---|---|
| **FC+A** | 1050 °C for 1h followed by furnace cooling | 540 °C for 4 h followed by furnace cooling |
| **AC+A** | 1050 °C for 1h followed by air cooling | 540 °C for 4 h followed by furnace cooling |
| **WQ+A** | 1050 °C for 1h followed by water quenching | 540 °C for 4 h followed by furnace cooling |

All the horizontal bars were cut along the length, thus obtaining 6 half-bars per platform. Half of these specimens were heat treated, following the FC+A specifications. By doing so, a total of 12 bars were obtained in the following conditions: CB-AB (as-built), HB-AB, CB-FC+A, HB-FC+A. The bars were subsequently mechanically machined in order to become dogbone tensile specimens, compliant with ASTM-E8 [147], as clarified in Figure 69.

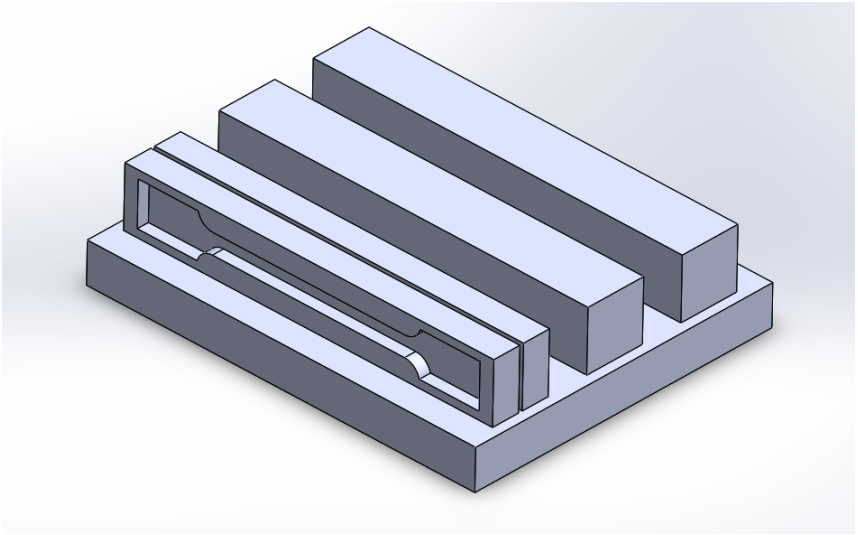

**Figure 69**: Schematic representation of the machining operation used in order to obtain the tensile specimens.

## *Microstructure*

The micrographs relative to all the conditions analysed in this work did not provide visible differences in terms of microstructural observation between CB and HB samples. However, the different heat treatments provided significantly dissimilar microstructures (Figure 70), mostly due to the differences in cooling rate, which is certainly one of the most influencing factors for the final microstructure of a Ti-6Al-4V recrystallized component.

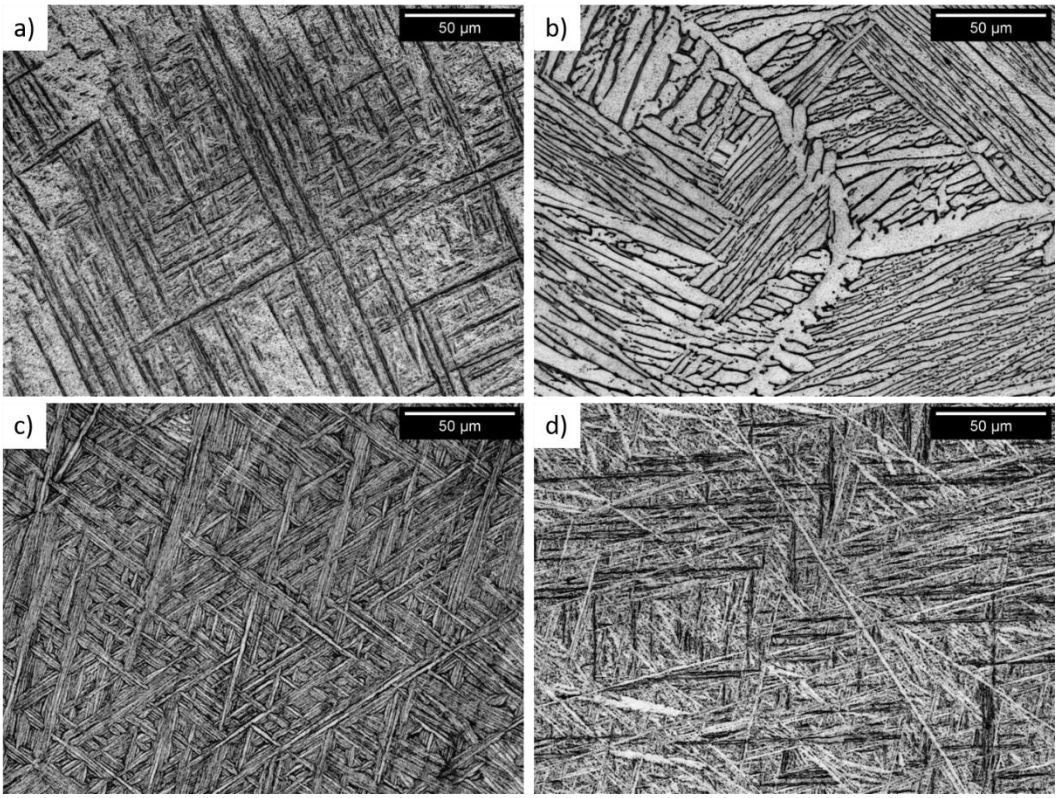


**Figure 70**: Representative optical micrographs of the AB (a), FC+A (b), AC+A (c) and WQ+A (d) samples.

The AB specimens, already described in **Chapter 3.1.2.**, provided a largely α' martensitic microstructure, characterized by columnar prior-β grains, resulting from very fast heating/cooling cycles, typical of the DED process. Oppositely, all the heat treated specimens provided equiaxed grains, due to the recrystallization process that occurred in the material when it was held at $T > T_\beta$. The FC+A samples underwent the slowest cooling rate, approximately 2 °C/min, which resulted in a completely lamellar α+β microstructures in which α colonies were easily recognizable. Moreover, $\alpha_{GB}$ was present throughout the whole surface analysed. Similarly, the AC+A condition was characterized by α lamellae surrounded by a thin layer of β phase. Although, no colonies were detected. In fact, a Widmanstätten morphology was recognized, by the typical ± 30°/60° angles between neighbour lamellae, typical of intermediate cooling rates (≈ 10 °C/min). Oppositely, the WQ+A specimens provided a mainly martensitic microstructure, similar to the AB case. However, a relevant number of α laths were detected homogeneously dispersed throughout the whole sample. The formation of such features via water quenching is possible, as the typical related

cooling rate is lower than 410 °C/s [196,197]. However, the insurgence of a greater amount of α phase and its growth are probably due to the decomposition of the martensite during the ageing step of the heat treatment. In fact, the long duration and relatively high temperature of this step facilitate the diffusive phenomena.

An in-depth microstructural investigation was also conducted in order to better relate all the conditions. Since the comparison between different microstructures is challenging, two separate parameters were studied: the width of the α laths and the width of the α' martensitic needles. The former was used to compare the heat treated samples (FC+A, AC+A, WQ+A), whilst the latter was used to investigate the AB and WQ+A samples.

The outcome of the evaluation of the α width of the heat treated samples is provided in Figure 71 and Table 12.

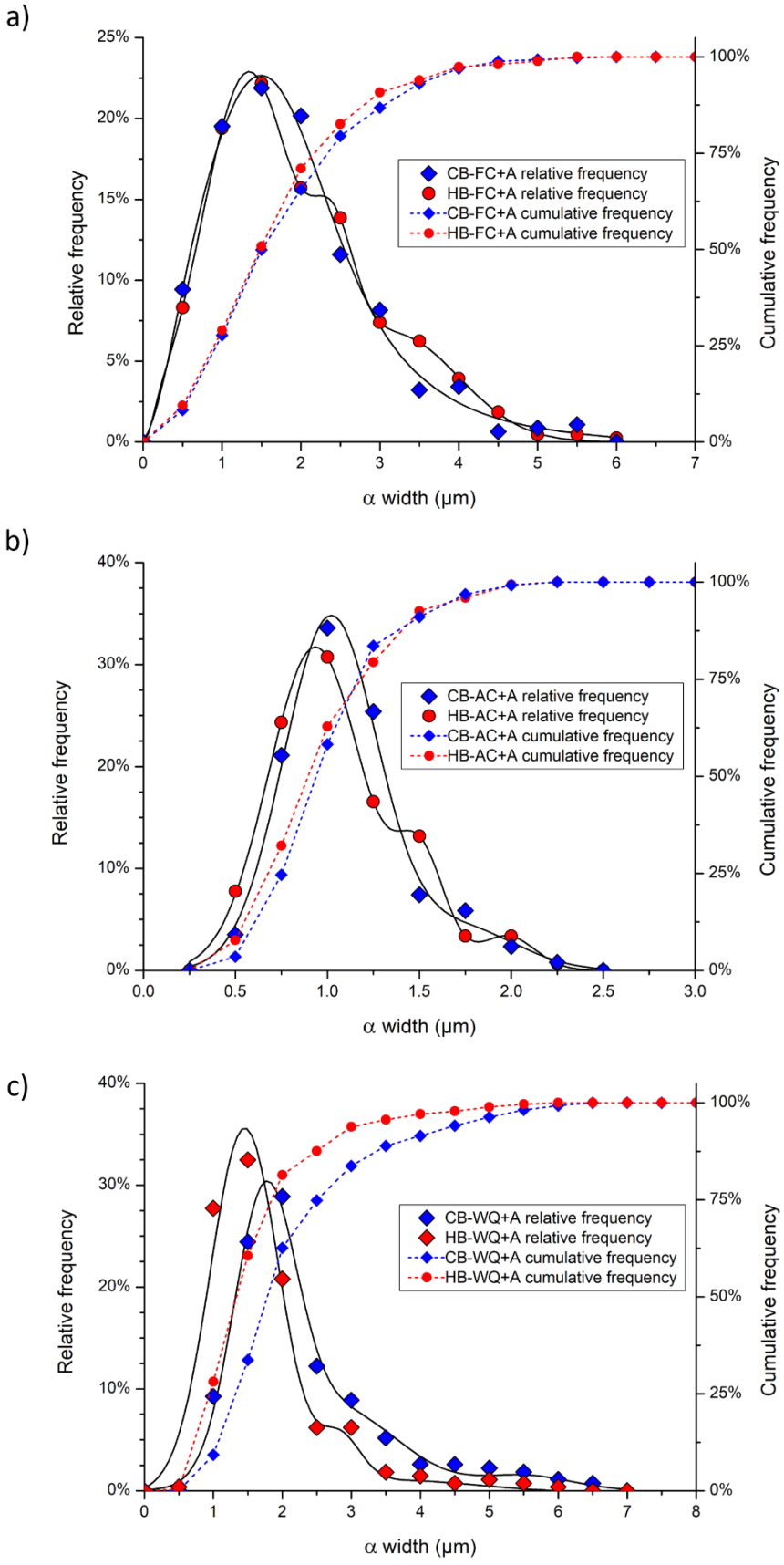


**Figure 71**: Frequency curves related to the width of the α laths in the FC+A (a), AC+A (b) and WQ+A (c) conditions.

**Table 12**: Average α width values.

| Condition | α width (µm) |
|---|---|
| **CB-FC** | 1.73 |
| **HB-FC** | 1.65 |
| **CB-AC+A** | 0.98 |
| **HB-AC+A** | 0.96 |
| **CB-WQ+A** | 2.14 |
| **HB-WQ+A** | 1.55 |

No significant differences induced by the pre-heating of the platform during manufacturing were found in the FC+A and AC+A samples. The comparison between the different heat treatment conditions (Figure 72) highlighted how the AC+A samples provided a markedly finer α phase, which is a typical outcome for Widmanstätten morphologies compared to lamellar colonies. In fact, the formers are obtained in correspondence of higher cooling rates, thus providing less time for diffusive phenomena (e.g. α growth) to occur. The α laths obtained in the WQ+A samples were also significantly larger. However, a direct comparison between this condition and the others is not possible. In fact, in the former case α is sparsely present in the microstructure, which is mostly formed by α'. Instead, in the FC+A and AC+A scenarios, the α lamellae, and relative thin β layers, formed the whole microstructure.

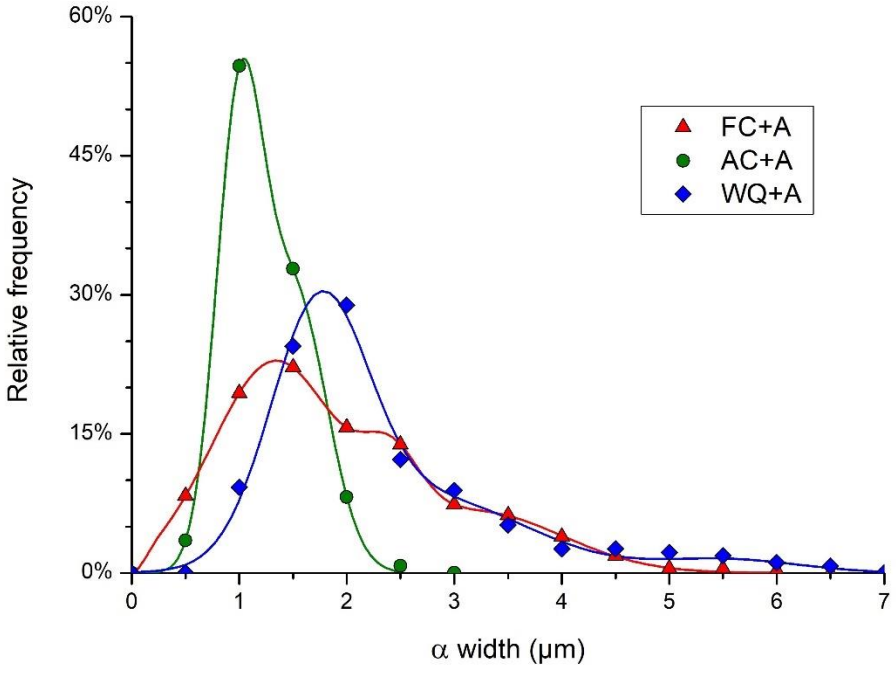


**Figure 72**: Representative comparison of the α width distribution curves of the heat treated specimens (CB curves shown).

The comparison of the α' width (Figure 73 and Table 13) for the AB and WQ+A conditions highlighted the effect of the process parameters and

environments on the microstructure of the as-built sample. In fact, the CB-AB specimen was characterized by a rougher α' microstructure than its HB counterpart. This was due to the former undergoing a higher cooling rate, which resulted in larger needles, as explained in **Chapter 3.1.2.** The WQ+A samples also provided a certain difference in terms of martensitic size, which might have been caused by a certain difference in terms of grain size and/or composition.

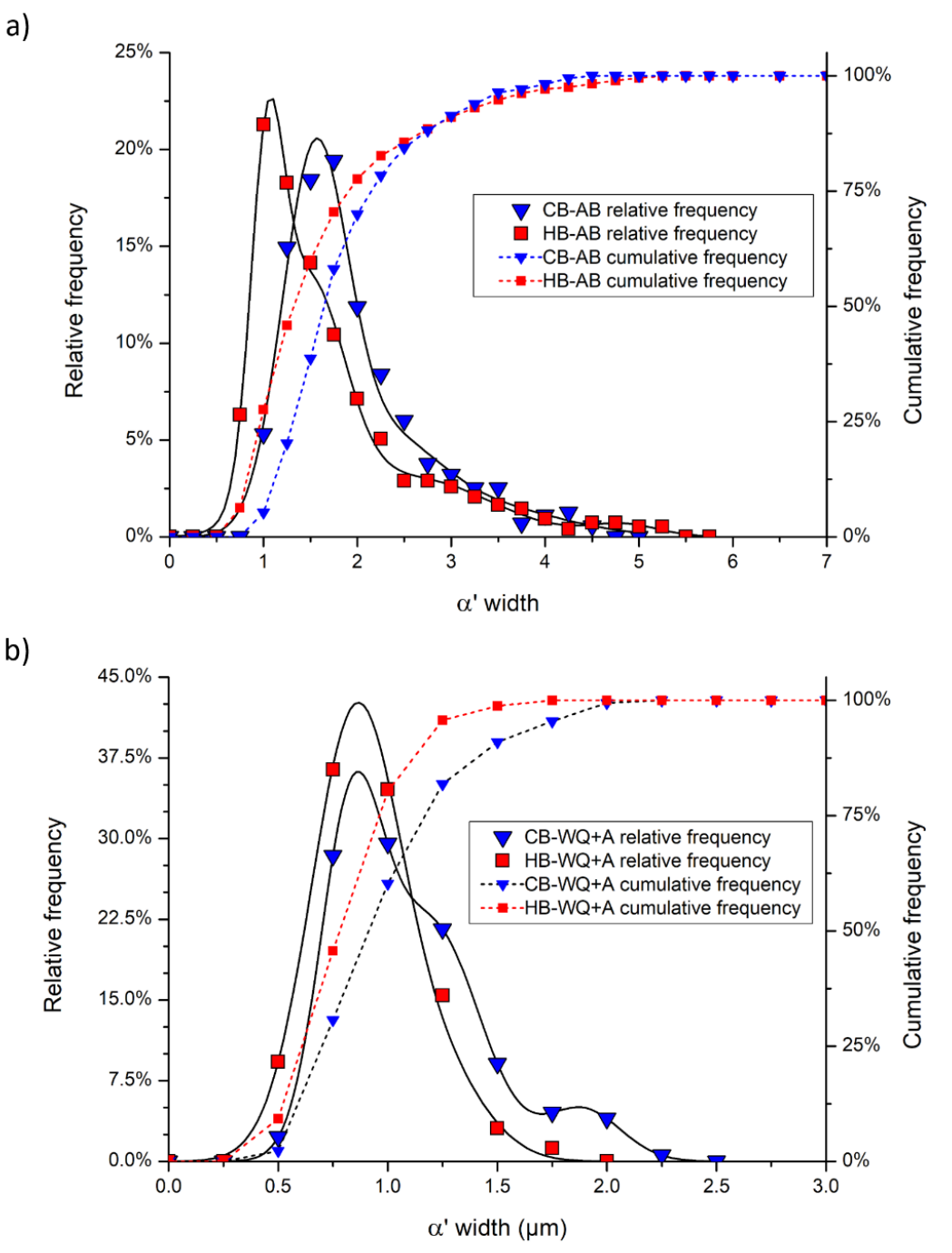


**Figure 73**: Frequency curves related to the width of the α' needles in the AB (a) and WQ+A (b) conditions.

**Table 13:** Average α' width values.

| Condition | α width (µm) |
|---|---|
| **CB-AB** | 1.83 |
| **HB-AB** | 1.60 |
| **CB-WQ+A** | 0.98 |
| **HB-WQ+A** | 0.80 |

By comparing the α' width for the AB and WQ+A conditions (Figure 74), the latter appeared markedly finer. Since the microstructural feature in analysis is highly dependent on the cooling rate, this result was in good agreement with the data available in literature, which confirmed that the cooling rate is significantly lower during the quenching step (≈ $10^2$ °C/s) than in the DED process (≈ $10^3$-$10^4$ °C/s) [118,119,196,197].

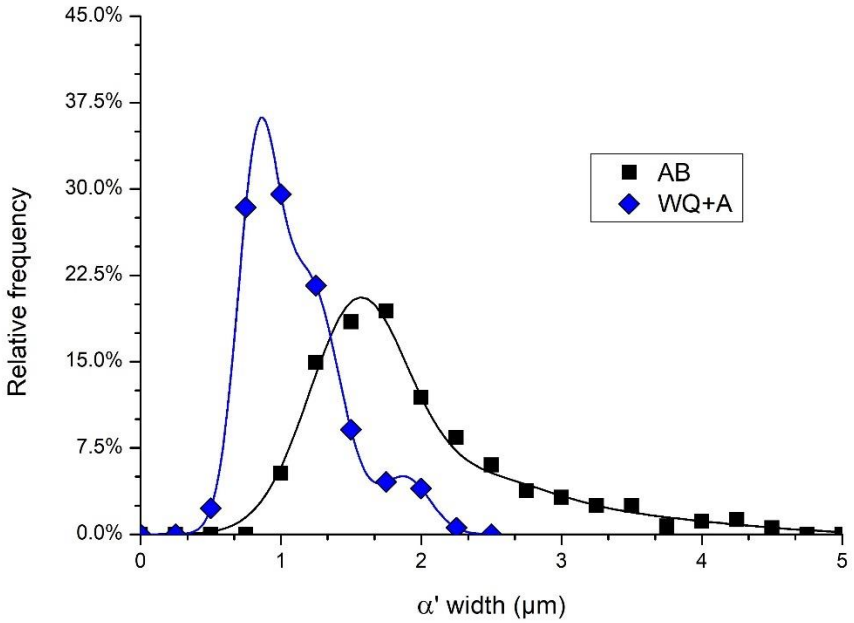


**Figure 74**: Representative comparison of the α' width distribution curves of the AB and WQ+A specimens (CB curves shown).

As mentioned before, all the heat treated samples provided equiaxed grains. For sake of comparison with the AB condition, the grain width, instead of size, was used. This approximation appeared appropriate as the aspect ratio (AR) of the equiaxed grains resulted consistently higher than 0.90. The comparison of the grain width, provided in Figure 75a, highlights an overall increase in the parameters after the heat treatment. No relevant differences were noted between the CB and HB conditions.

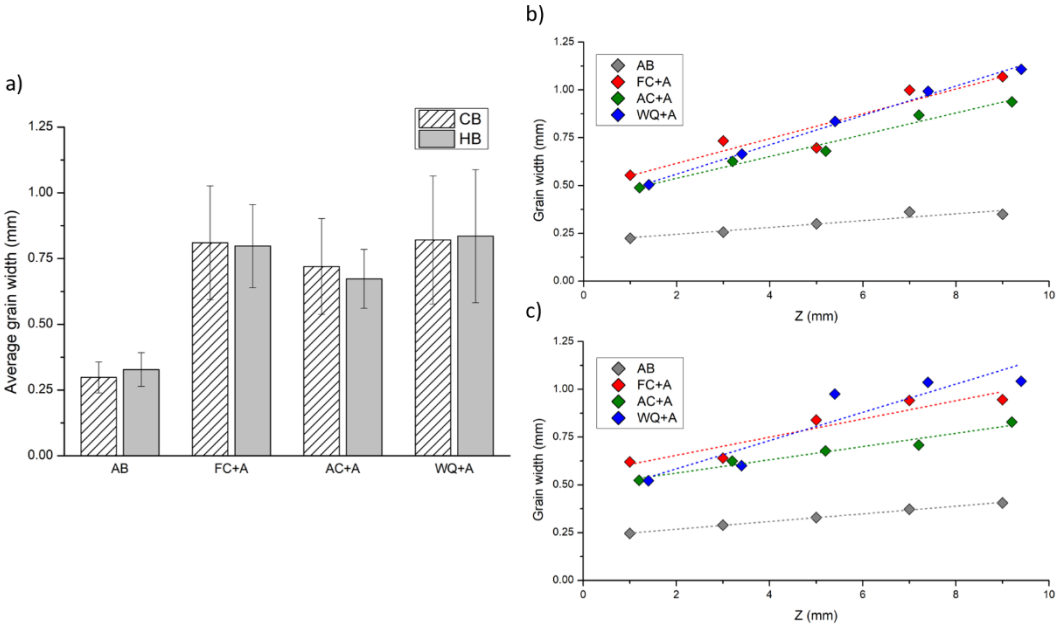


**Figure 75**: Comparison of the grain width for all the conditions considered (a) and relative trends along the height of the samples for the CB (b) and HB (c) conditions.

In a procedure specular to the one showed in **Chapter 3.1.2**, the evolution of the grain width along Z for all the samples in the CB (Figure 75b) and HB (Figure 75c) conditions was investigated, in order to understand whether the recrystallization of the grains was influenced by the intrinsic anisotropy of the DED produced samples or not. In fact, as already stated, this manufacturing process induces a grain size variation along the sample's height as a result of a difference in the cooling rate during deposition. In both pre-heating conditions, a clear upward sloping trend was observed. For instance, the CB-FC+A sample provided a grain width variation from 0.55 mm in proximity of the base to 1.07 mm at 9 mm height roughly. This means that, even if a complete recrystallization of the material occurs via super-β transus heat treatments, a certain "grain memory" effect took place, preventing the microstructure to be effectively and completely homogenised. This phenomenon was probably due to the grain boundaries being preferential nucleation sites for new grains in the β field [198]. In fact, during a super-β annealing, the new grains develop preferentially at pre-existing boundaries and then grow at the expense of the residual α phase [199]. This behaviour is greatly favoured by the presence of the β phase, sensitively less effective at preventing diffusion-related phenomena than the α phase.

In order to confirm the assumptions made on the microstructures during the analyses of the micrographs and to investigate the phases involved more deeply, the XRD patterns of all the samples were obtained and studied, as visible in Figure 76.

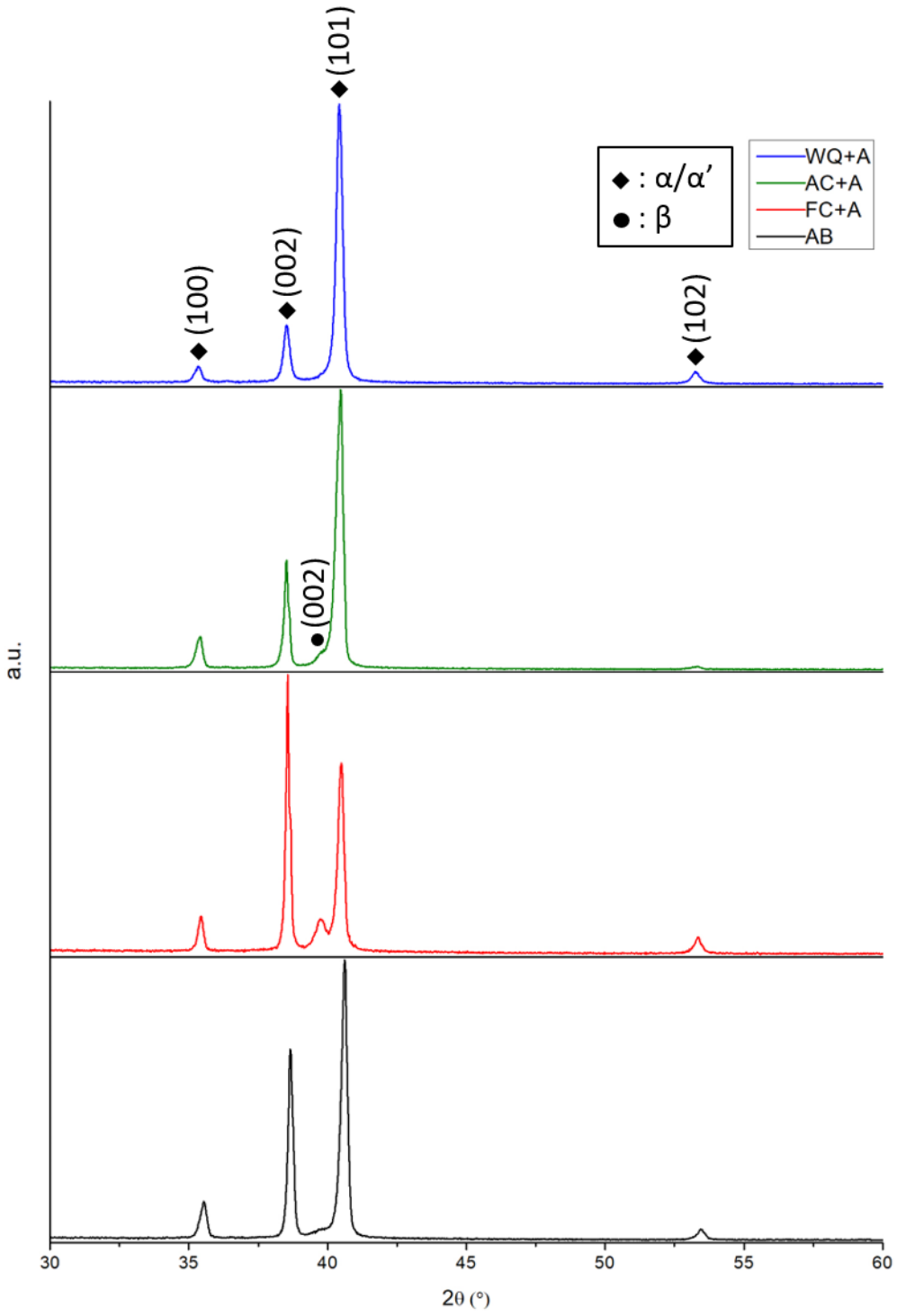


**Figure 76**: XRD patterns of all the conditions considered in this work.

All the samples provided the peaks relative to the α/α' phase. Although, the distinction between these two phases is challenging by only means of XRD patterns observation, as both are characterized by the same hexagonal structure. The (002) peak relative to the β phase was found in the AC+A and FC+A samples. The presence of a non-negligible amount of this phase is in good agreement with the heat treatments conducted, as these two conditions provided the overall slowest cooling rates which facilitated the diffusive phenomena, thus

the α' → α+β decomposition. Moreover, the β presence confirms that the AC+A and FC+A conditions were characterized by the thermodynamically stable α, since no transformations during cooling allow the formation of β without α.

The cell parameters for the α phase were also assessed from the patterns recorded in the XRD analyses. The α cell volume was chosen as the most suitable parameter in order to compare all the specimens. The results are reported in Figure 77 and Table 14. All the specimens characterized by the presence of α phase provided markedly similar cell volume values, ranging from 34.79 to 34.83 $Å^3$. Instead, the AB samples were characterized by a smaller cell, in good agreement with the data found elsewhere for martensitic Ti-6Al-4V microstructures [200]. This information confirmed that the as-built samples were completely martensitic. Moreover, the WQ+A samples provided a cell volume markedly similar to the samples characterized by a more stable microstructure from a thermodynamic point of view (AC+A, FC+A). Therefore, the water quenched samples provided a microstructure which was overall significantly close to the equilibrium state than the AB state. This is also confirmed by the presence of a significant amount of α phase, obtained via α' decomposition.

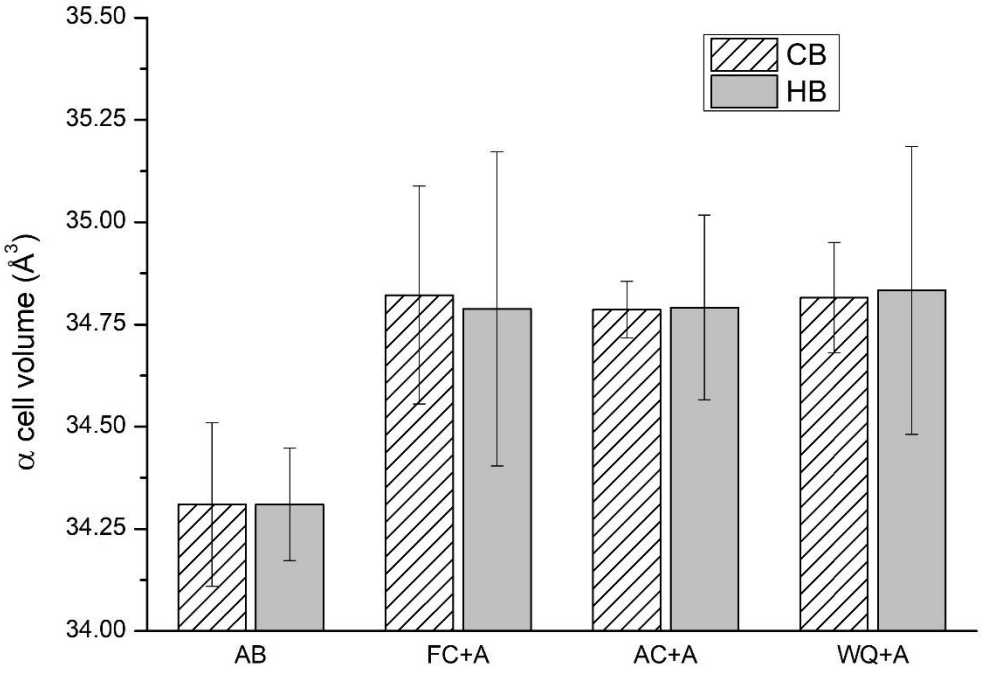


**Figure 77**: α cell volume for all the conditions considered.

**Table 14**: α cell volume evaluated from the XRD patterns.

| Sample | Cell volume ($Å^3$) |
|---|---|
| **CB-AB** | 34.31 ± 0.20 |
| **HB-AB** | 34.31 ± 0.14 |
| **CB-FC+A** | 34.82 ± 0.53 |
| **HB-FC+A** | 34.79 ± 0.77 |
| **CB-AC+A** | 34.79 ± 0.07 |

| | |
|---|---|
| **HB-AC+A** | 34.79 ± 0.23 |
| **CB-WQ+A** | 34.82 ± 0.13 |
| **HB-WQ+A** | 34.83 ± 0.35 |

To further assess if any type of contamination occurred during the process or the post-processing heat treatments, an analysis of the quantity of interstitial elements in all the samples was conducted. In general, this type of test is important to assess the causes of possible variations in the behaviour of the samples. The outcome of the evaluation is provided in Figure 78.

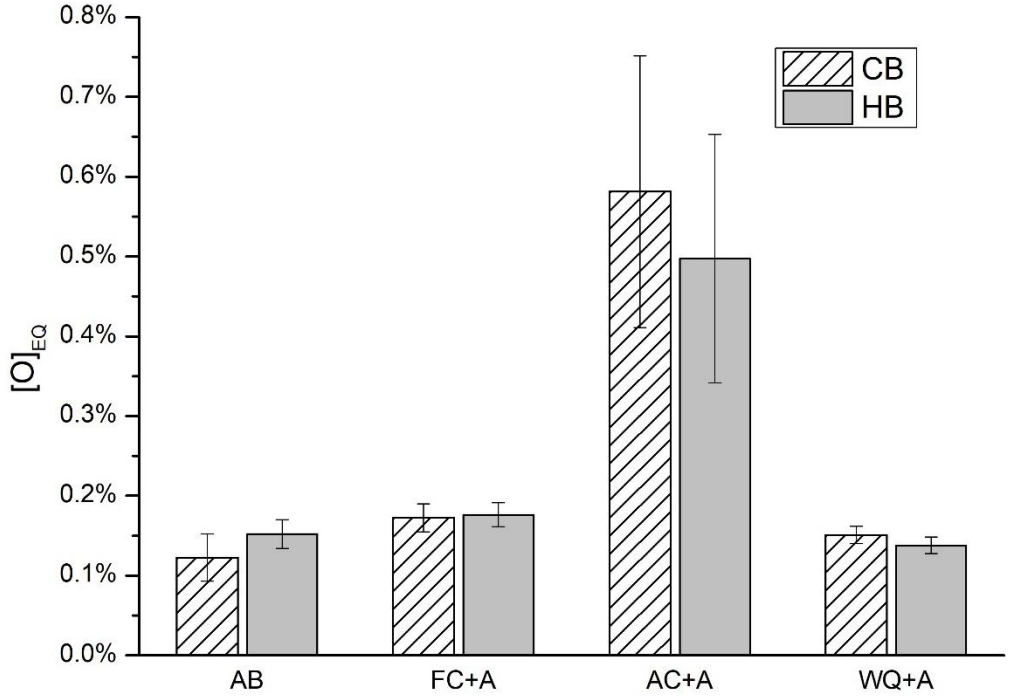


**Figure 78**: $[O]_{EQ}$ evaluation for all the conditions considered in this work.

The AB samples resulted poorly enriched by interstitial elements (O, N) in both CB (0.123% ± 0.030%) and HB (0.152% ± 0.018%) conditions. In this case, the differences induced by the process environment appeared marginal. A similar behaviour was encountered in the FC+A and WQ+A scenarios. In fact, these provided an interstitials content comparable with the as-built ones, namely 0.131% ± 0.001% and 0.135% ± 0.026% for CB-FC+A and CB-WQ+A, respectively, and 0.176% ± 0.015% and 0.138% ± 0.011% for HB-FC+A and HB-WQ+A. Concerning the AC+A samples, in both building conditions the materials provided a high content of interstitials (0.581% ± 0.170% and 0.497% ± 0.156% for CB and HB, respectively). In this scenario, the insurgence of some sort of issue during the heat treatment appeared more likely, as the solution in order to air cool the sample was custom-made and the sensitivity of the Ti-6Al-4V alloy to oxygen and nitrogen enrichment is very high.

## *Mechanical Properties*

The Vickers microhardness was measured on all the samples part of this study by measuring the average values at different heights along the cross-section of the samples. However, unlike in the AB condition, no clear trend was found for the heat treated samples, suggesting that a super-β transus annealing followed by ageing can be an effective mean to eliminate the intrinsic hardness anisotropy induced by the DED fabrication process. Since a clear trend for the grain size was found in the microstructural evaluation, a direct correlation between grain size and hardness was lacking, unlike in the study provided in **Chapter 3.1.2**. The average values for each condition are reported in Figure 79.

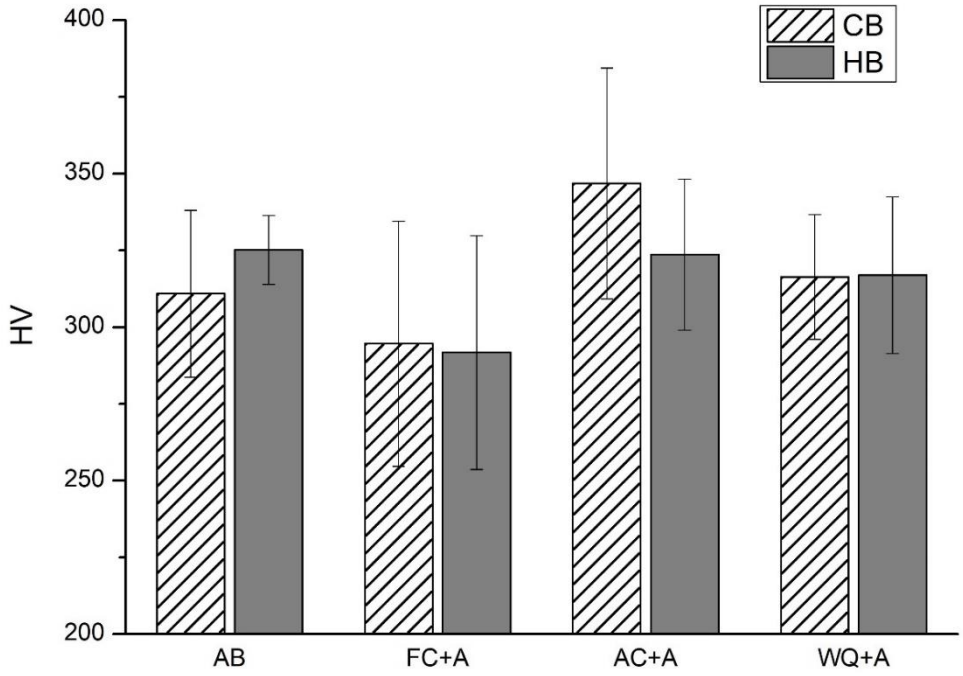


**Figure 79**: Average Vickers microhardness values for all the conditions considered.

The AB samples were characterized by an average hardness of 311 ± 27 and 325 ± 11 HV for the CB and HB conditions, respectively. After the FC+A heat treatment, these values dropped to 295 ± 40 and 291 ± 38 HV. No significant differences were found to be relatable to the building conditions and/or interstitials content in this case. The decrease in hardness was linked to the disappearance of the α', which is a moderate hardener. The highest value overall was measured on the CB-AC+A specimen, characterized by a microhardness of 347 ± 38 HV. Instead, its HB counterpart provided a value of 323 ± 25 HV, which was comparable to the AB condition. The CB-WQ+A and HB-WQ+A samples provided significantly similar values: 316 ± 20 and 317 ± 25 HV, respectively. Overall, the most promising results were given by the AC+A samples, probably due to their markedly fine microstructure (Figure 71). Whilst, the FC+A samples resulted the worse in terms of hardness.

The AB and FC+A specimens obtained via machining of the horizontal bars were tensile tested, thus providing the results in Figure 80 and Table 15.

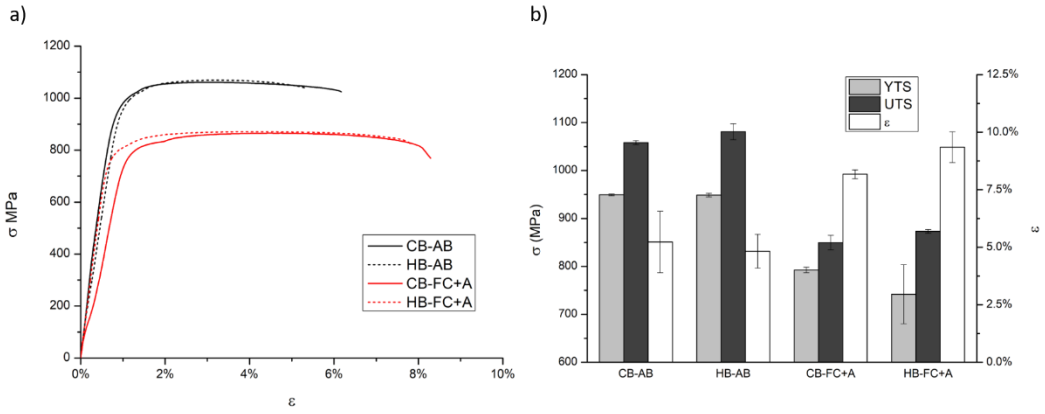


**Figure 80**: Representative curves of the trends obtained during the tensile tests (a) of the DED Ti-6Al-4V as-built and FC+A samples with relative average YTS, UTS and ε values obtained (b).

**Table 15**: Outcome of the tensile tests on the AB and FC+A samples.

| | YTS (MPa) | UTS (MPa) | ε (%) |
|---|---|---|---|
| **CB-AB** | 949 ± 2 | 1058 ± 4 | 5.2 ± 1.3 |
| **HB-AB** | 949 ± 4 | 1081 ± 17 | 4.8 ± 0.7 |
| **CB-FC** | 793 ± 9 | 849 ± 15 | 8.2 ± 0.2 |
| **HB-FC** | 742 ± 61 | 873 ± 3 | 9.3 ± 0.7 |

The AB samples provided high strength values, associated with a limited ductility. This was related to the fine grained microstructure of α' needles. No significant differences were found in terms of tensile properties between the CB and HB conditions. Similarly, the CB-FC+A and HB-FC+A specimens were characterized by comparable mechanical properties. The latter provided a slightly higher ε. In general, the post processing heat treatments allowed a significant increase in ductility. However, it was not sufficient in order to make the samples comply with the limits imposed by ATSM-F2924 (ε ≥ 10%). Moreover, the reduction in YTS and UTS resulted so consistent that even the threshold values of the normative for the yield strength were not met (YTS ≥ 825 MPa, UTS ≥ 895 MPa). Overall, a drastic decrease in strength was caused, without granting a reasonable enough augment in plasticity.

## *Conclusions*

In this work, different super-β transus heat treatments were conducted on DED produced Ti-6Al-4V samples. Different cooling paths (furnace cooling, air cooling and water quenching) followed by post-annealing ageing step were considered. Moreover, two different building conditions (pre-heated platform and non-pre-heated platform) were also studied. The specimens were analysed by comparing microstructures and hardness values. Furthermore, the as-built and furnace cooled samples were also investigated via tensile testing. To sum up, the most important results obtained can be reported as follows:

- All the heat treatments part of this study allowed to obtain markedly different microstructures. The as-built specimens provided completely martensitic microstructures with columnar prior-β grains. The heat treated and furnace cooled samples were characterized by colonies of α+β lamellae. The heat treated and air cooled specimens provided a α+β lamellar Widmanstätten microstructure. The heat treated and water quenched samples were characterized by a mainly martensitic microstructure, in which sparse α laths resulted clearly visible.
- The heat treated and air cooled samples provided the finest α laths, characterized by an average width of 0.96-0.98 μm.
- The heat treated and water cooled samples provided the finest α' needles, characterized by an average width of 0.80-0.98 μm.
- A super-β transus annealing was performed, which allowed the complete recrystallization of the microstructure, thus changing the grain morphology from columnar to equiaxed. However, the intrinsic anisotropy of the grain width (size) of the as-built samples, induced by the manufacturing process, remained even after heat treatment. In fact, the grain boundaries, more concentrated in the bottom region of the sample, acted as preferential nucleation spots for new grains at $T > T_\beta$. Therefore, a sort of "grain memory" effect was found.
- The heat treated and air cooled samples proved to be the most performing in terms of hardness, whilst the heat treated and furnace cooled specimens were the worst.
- In terms of tensile properties, the heat treatment with furnace cooling did not appear as a viable post-processing path. In fact, the increase in ductility was modest and associated with a severe drop in yield and ultimate tensile strengths.
- Overall, for the heat-treated conditions, no significant differences induced by the pre-heating of the platform during deposition were found. This suggested that a super-β transus annealing might be a viable way in order to "erase" possible differences induced in the samples by such procedure.

## 3.2. Ti-6Al-4V Alloy Produced by EBM

The process parameters determination step was not necessary for the EBM system, as these were already defined by Arcam.

The EBM process allows to manufacture a 3D component via micro-melting of small areas of partially sintered powder. This results in unique microstructures in the Ti-6Al-4V alloy, that provide excellent combinations of mechanical properties, even in the as-built state. This is mostly related to two main process-related factors:

- the high thermal gradients generally involved, which result in a fast cooling from the molten state, providing fine columnar grains [201];
- the high temperature of the process chamber (≈ 700 °C) in conjunction with the long duration of the process. Both these factors favour diffusive phenomena, promoting the decomposition of the embrittling α' phase into a more optimal lamellar α+β microstructure [62].

Since the as-built state already provides interesting combinations of strength and ductility, the study of the post-processing heat treatments on the EBM produced Ti-6Al-4V samples did not gather much attention initially, if compared to other AM techniques, such as LPBF [202,203]. Since EBM produced samples do not usually provide high levels of residual stresses, the stress relieving heat treatments are usually not considered [62,202]. Instead, annealing heat treatments appear more interesting. These can be conducted either above or below $T_\beta$. In the former case, a complete recrystallization of the microstructure occurs and the grains turn from columnar to equiaxed, reducing the anisotropy. In the latter scenario, the fine grains obtained during the EBM process can be retained, which is beneficial for achieving a high strength component. After annealing, an ageing step is possible, which is usually conducted at lower temperatures and longer durations, with respect to the prior heat treatment. Its goal is to promote diffusive phenomena in order to favour the decomposition of α' and/or supersaturated retained β phase [23].

Several works available in literature investigated the effect of different combinations of time, temperature and cooling means on the properties of EBM produced Ti-6Al-4V samples. However, little to no work is available on the significance of a super β-transus annealing ($T > T_\beta$) followed by different cooling paths and then by an ageing heat treatment.

Raghavan et al. [203] investigated several combinations of heat treatments on EBM produced Ti-6Al-4V grade 5. The authors considered durations ranging from 1 to 3 hours and temperatures from 930 (sub-β) to 1050 °C (super-β). They also evaluated the significance of a post-annealing ageing phase, which was performed exclusively on the samples annealed at a temperature of 1050 °C and then air cooled. The aim of this last combination of heat treatments was to decompose the martensite obtained during the annealing step, without coarsening excessively the material. However, the resulting mechanical properties appeared barely comparable, if not inferior, to the ones of the as-built samples, obtained from the authors. De Formanoir et al. [68] studied a sub-β (950 °C) and a super-β (1040 °C) annealings, performed on samples that underwent hot isostatic pressing (HIP), confirming marked microstructural variations after the recrystallization heat treatment. However, no investigation related to an ageing step after the first heat treatments was conducted. Galarraga et al. [134] conducted a thorough investigation on the effect of several heat treatments on EBM produced Ti-6Al-4V samples, using as a feedstock material a mix of 50% used and 50% virgin powders. Water quenching, furnace and air cooling were the cooling means

considered by the authors. While the former led to extensively martensitic microstructures, which implied good strength values, but rather limited ductility; furnace and air cooled samples were characterized by bimodal α+β microstructures. The effect of a post-annealing ageing heat treatment was also considered. However, it was only applied to samples that previously underwent sub-β heat treatments. The authors concluded that this last combination of post-processing steps resulted the most optimal method in order specifically tailor the resulting mechanical properties, according to the application needed, via proper manipulation of temperature, duration and cooling rate.A relevant number of other works focused on annealing heat treatments conducted at $T < T_{\beta}$, considering different cooling paths [70,136,204,205]. However, none of these assessed the significance and consequences of a subsequent ageing step. Thus, in this work, the effect of a super-β annealing heat treatment, followed by either furnace cooling or water quenching, on the microstructure and mechanical properties of EBM produced Ti-6Al-4V ELI was assessed and compared to the as-built and annealed-only conditions. The samples used were 15x15x15 mm cubes and vertical cylindrical bars of 140 mm length and 15 mm diameter. All the samples were EBM produced using an Arcam A2X machine, using the standard parameters for this material given by the machine supplier. The samples underwent separate heat treatments, achieving a total of 5 different conditions, as summarized in Table 16.

**Table 16**: List of all the heat treatments investigated and relative specifications.

| | **Annealing** | **Ageing** |
|---|---|---|
| **as-built** | - | - |
| **FC** | 1050 °C for 1h followed by furnace cooling | - |
| **FC+A** | 1050 °C for 1h followed by furnace cooling | 540 °C for 4 h followed by furnace cooling |
| **WQ** | 1050 °C for 1h followed by water quenching | - |
| **WQ+A** | 1050 °C for 1h followed by water quenching | 540 °C for 4 h followed by furnace cooling |

## *Microstructure*

The micrographs of the as-built condition, visible in Figure 81, provided a complex microstructure, typical outcome for EBM produced Ti-6Al-4V samples.

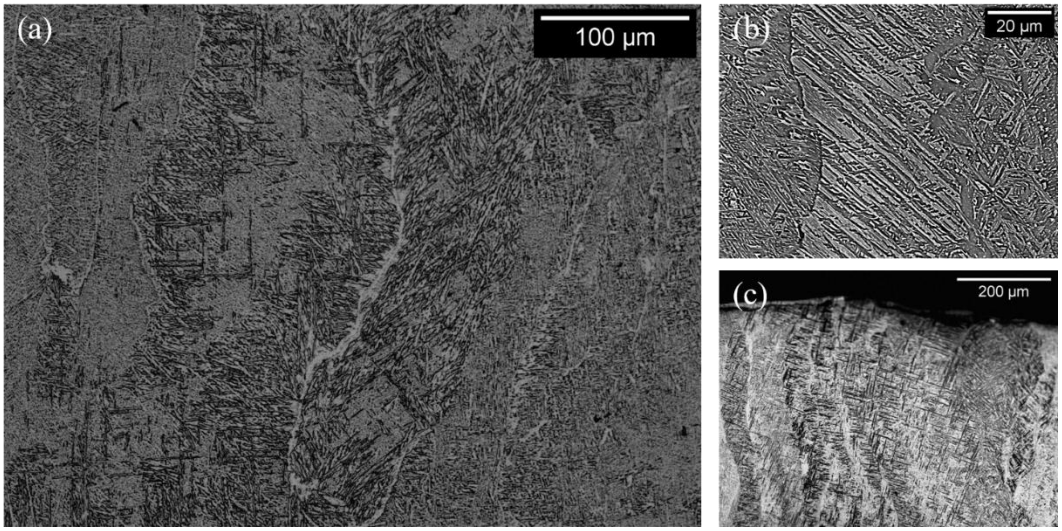


**Figure 81**: Micrographs obtained by optical (a) and SEM (b) imaging of as-built EBM Ti-6AL-4V samples. Martensite found in the upper part of the specimen (c).

Prior-β grains were detected, alongside α phase continuous layers located at grain boundaries, commonly marked as $\alpha_{GB}$ (Figure 81a). The presence of this last microstructural feature in EBM produced Ti-6Al-4V samples was also highlighted in other works [68,206]. Overall, the micrographs provided a lamellar α+β microstructure, as visible in Figure 81b. The α laths were found to be arranged both in a Widmanstätten pattern and grouped in colonies. As mentioned before, these morphologies are mainly due to the permanence of the samples in the high temperature process chamber, resulting in a prolonged annealing heat treatment. In the upper part of the specimens, which corresponds to the last layers obtained during the fabrication process, a mainly α' martensitic microstructure was found (Figure 81c). Considering that the martensite formation is associated with high cooling rates/thermal gradients, its presence on top of the samples is probably correlated to the annealing heat treatment mentioned before, which can provide the decomposition of the martensite: α'→ α+β. In fact, the area of the samples in which such features were found corresponded to the portion that underwent the "intrinsic heat treatment" for a shorter duration, resulting in a lack of time in order to fully decompose α'. Martensite presence in EBM produced Ti-6Al-4V was also found by other authors [207,208].

The observation of the microstructures of the heat treated samples provided results considerably different, as visible in Figure 82.

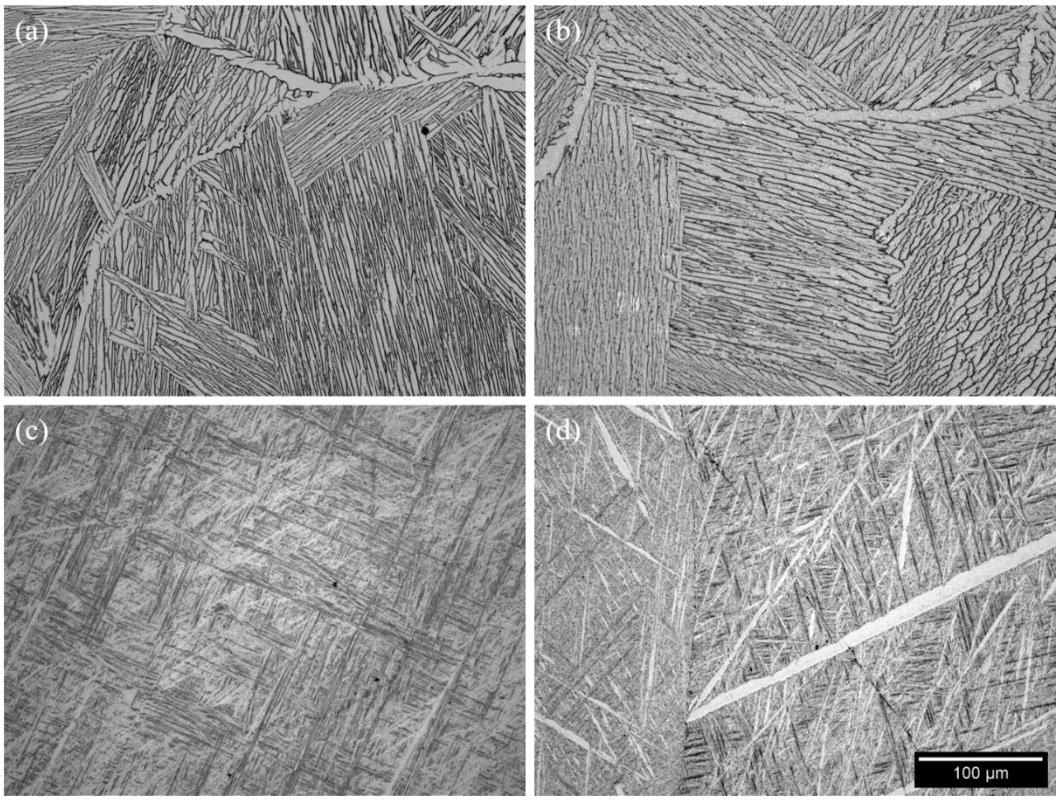


**Figure 82**: Microstructures found via optical observations of the FC (a), FC+A (b), WQ (c) and WQ+A (d) samples.

All the heat treated specimens provided prior-β grains characterized by an equiaxed morphology, confirming the recrystallization happened due to the temperature exceeding $T_\beta$. The FC and FC+A samples (Figure 82a,b) were constituted exclusively by α+β lamellae (α laths surrounded by β layers), arranged in colonies, thus sharing the same crystallographic variant. This resulted from the very slow cooling rate applied, which allowed only a limited number of possible orientations [27]. No significant differences between these two groups of specimens were found by means of optical observation. Instead, the WQ samples (Figure 82c) provided markedly different micrographs, mainly formed by α' needles, arranged in the typical ±45° morphology. In addition to that, a small amount of α laths was detected. Similarly, the WQ+A samples (Figure 82d) showed a similar martensitic microstructure. However, the α phase appeared in laths characterized by a larger size. Since the only significant difference between WQ+A and WQ was the post-annealing ageing, α growth at the expense of α' seemed reasonable. In fact, the decomposition of the martensite is one of the typical goals of such heat treatment.

In order to be able to numerically quantify and better understand the different microstructures involved, the width of the α laths was estimated for all the heat treated conditions, as provided in Figure 83. In fact, this microstructural feature is shared by all the samples part of this investigation. The as-built specimens were not considered in this assessment, as the relative microstructure is rather complex

and characterized by several morphologies and phases simultaneously, thus resulting inhomogeneous.

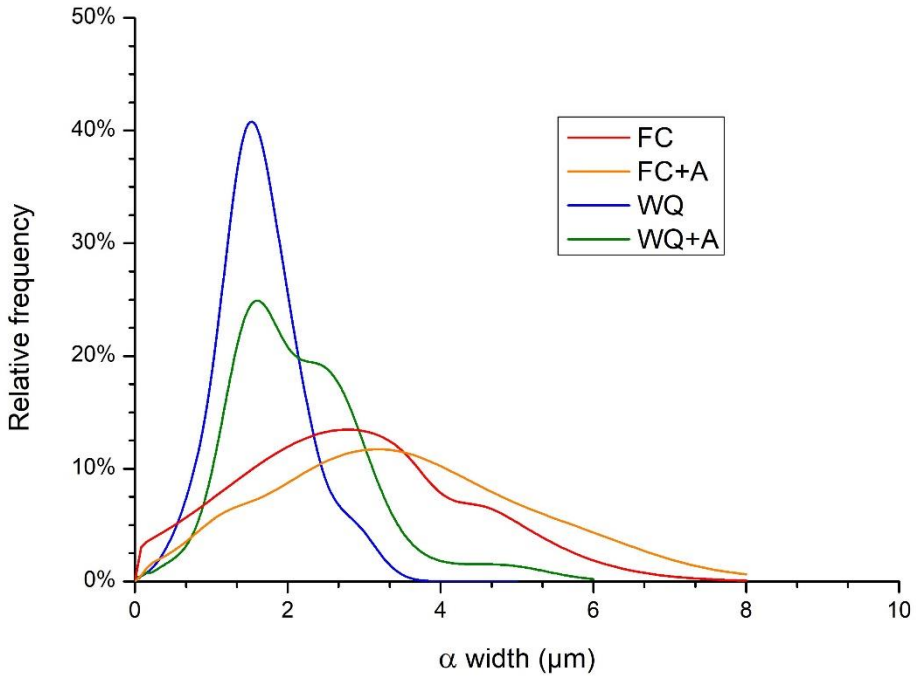


**Figure 83**: α width distribution, relative to the heat treated samples.

The furnace cooled samples were characterized by the largest laths, providing as average value of 2.72 and 3.29 μm, for the FC and FC+A conditions, respectively. Instead, the WQ and WQ+A specimens had an average value of 1.46 and 1.98 μm, respectively. The marked differences between the samples obtained via different cooling means were the result of significantly different thermal histories, which also resulted in two main categories of microstructures, hereby compared: lamellar α+β (FC, FC+A) and acicular α' with sparse α laths (WQ, WQ+A). Therefore, the main result of this comparison lies in the evaluation of the growth rate of the α phase, which is diffusion-dependant and resulted more consistent in the samples that were left to cool in the furnace after annealing. In fact, these specimens remained for a longer period of time at high temperatures, favouring α growth. Similarly, the ageing heat treatment provided α growth too. This phenomenon resulted particularly evident in the water quenched samples, even by optical observation of the micrographs, in which the condition WQ+A provided a visibly coarser microstructure than WQ (Figure 84).

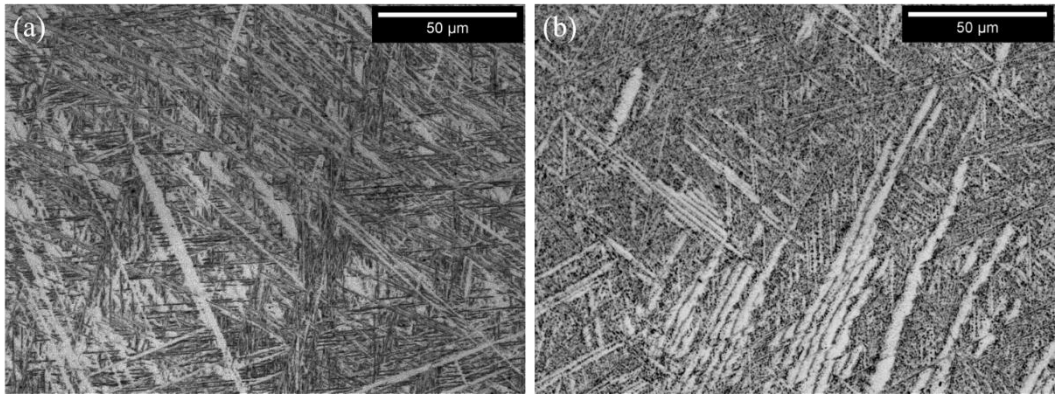


**Figure 84**: Highlight of the α laths in the WQ (a) and WQ+A (b) conditions.

Another important microstructural parameter to consider is the grain size, which provides a direct influence on the mechanical properties of the material, for instance via grain boundaries strengthening [89,209]. This parameter was measured for all the heat treated specimens. Instead, the as-built condition was excluded due to the difficulty to optically resolve the fine columnar grains, as testified by Galarraga et al. [210]. Moreover, a direct comparison between equiaxed grains and columnar grains is difficult, due to the significantly different morphologies involved. The results of the evaluation of the grain size are provided in Figure 85.

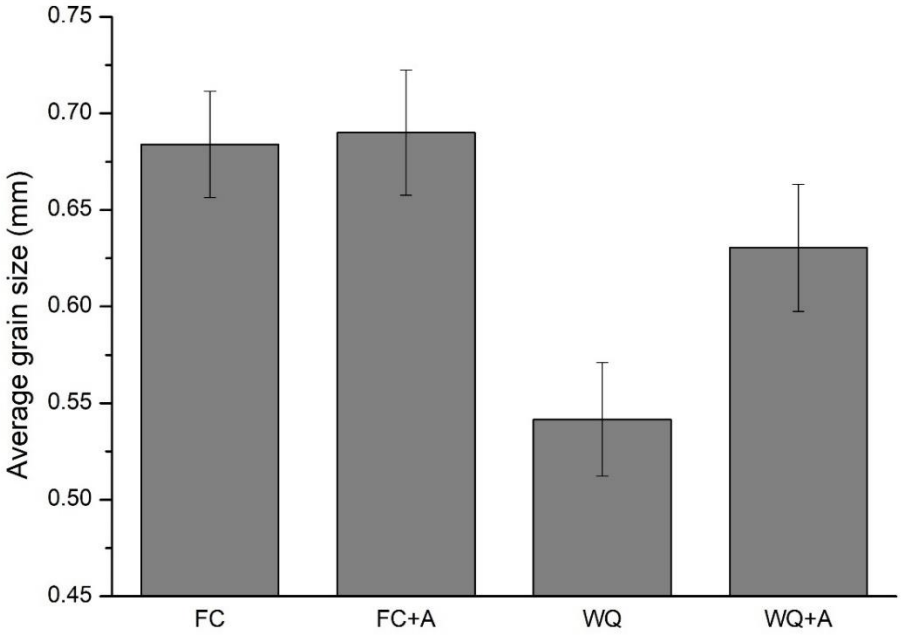


**Figure 85**: Average grain size of the heat treated samples

The samples that underwent a slow furnace cooling after annealing (FC, FC+A) were characterized by the largest grains. This was related to the prolonged permanence at high temperatures due to the low cooling rate applied. In fact, grain enlargement is a diffusion-driven phenomenon [4,198]. Furthermore, the heat treatments were conducted at 1050 °C, which allowed the complete recrystallization of the material into β phase. In this phase, the self-diffusivity

coefficient for titanium ($D_{Ti-\beta} \approx 10^{-13}$ $m^2/s$) is much greater than in the α phase ($D_{Ti-\alpha} \approx 10^{-15}$ $m^2/s$) [35]. Hence, the duration of the super-β transus heat treatments must be carefully controlled, due to the lack of α phase, much more efficient in preventing grain enlargement. Otherwise, the resulting microstructure might be characterized by very coarse grains, resulting in a poor strengthening effect. Comparing the FC and FC+A samples, the difference in terms of grain size appeared negligible. This was probably correlated with the presence of $\alpha_{GB}$ (Figure 82a,b), which is significantly efficient at hindering grain growth [68]. The WQ specimens provided instead finer grains, as a result of the very high cooling rate used after annealing, which prevented diffusive phenomena from happening. However, during ageing (WQ+A), grain enlargement occurred, as no barrier for diffusion ($\alpha_{GB}$) is present, such in the FC+A samples.

In order to confirm the hypotheses made on the phases present in the EBM produced Ti-6Al-4V samples and to investigate them more deeply, XRD analyses were conducted. The results are provided in Figure 86.

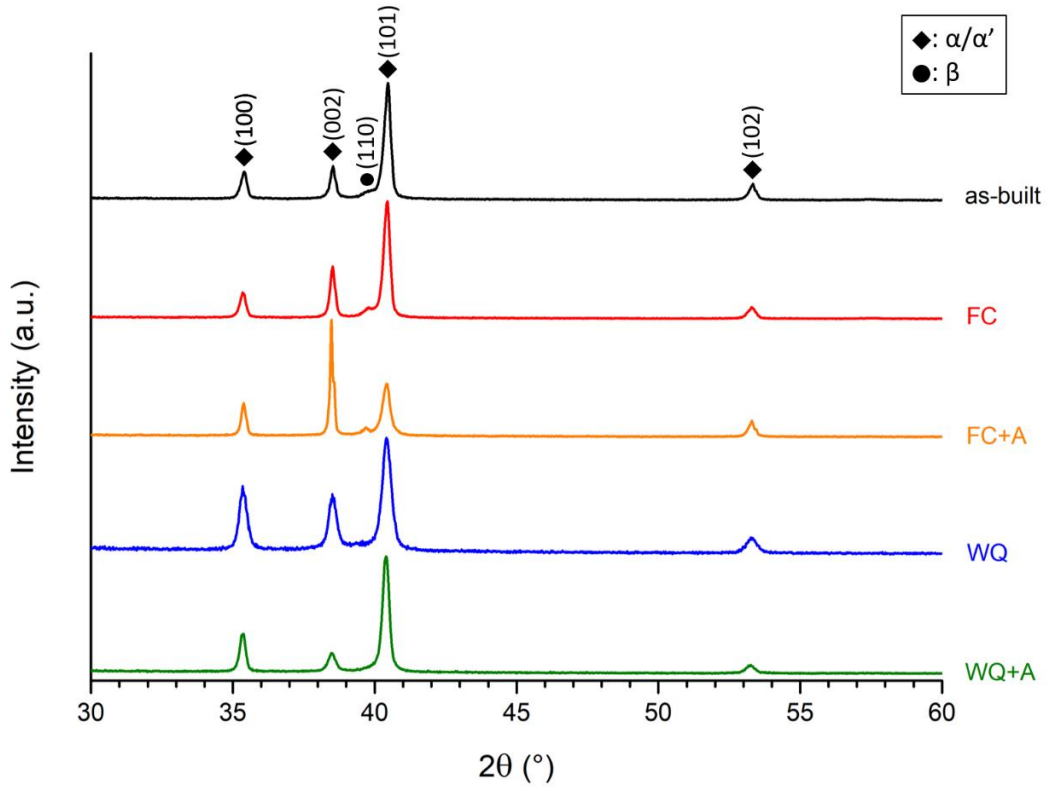


**Figure 86**: Patterns obtained from the XRD analyses on all the conditions considered in this study.

The peaks relative to the α/α' phases were clearly visible in all the samples. Instead, the (110) peak relative to the β phase was present only in the as-built, FC and FC+A specimens. Since for the composition of the Ti-6Al-4V alloy the presence of β implies the presence of α as well, near room temperature. The samples that provided the β peak were likely to be characterized by α phase, instead of martensite. Oppositely, since the martensitic transformation β → α'does not allow α generation, the samples that did not provide the β peak (WQ, WQ+A)

resulted more likely to show α' instead of α. Both these assumptions were in good agreement with the observation of the micrographs. In fact, the as-built, FC and FC+A samples provided a lamellar duplex α+β microstructure, whilst WQ and WQ+A were characterized by a mainly martensitic microstructure, recognizable by the typical needles in a ±45° orientation. The investigation of the α phase of the FC+A samples provided a (002) peak higher than the (101) peak. This phenomenon was supposed to be related to texturing.

To further assess the phases found and relate them to the processing route the samples underwent, the determination of the cell parameters of the hexagonal lattice of the α/α' phase from the XRD data was conducted (Figure 87). The c/a ratio was chosen in order to compare all the samples.

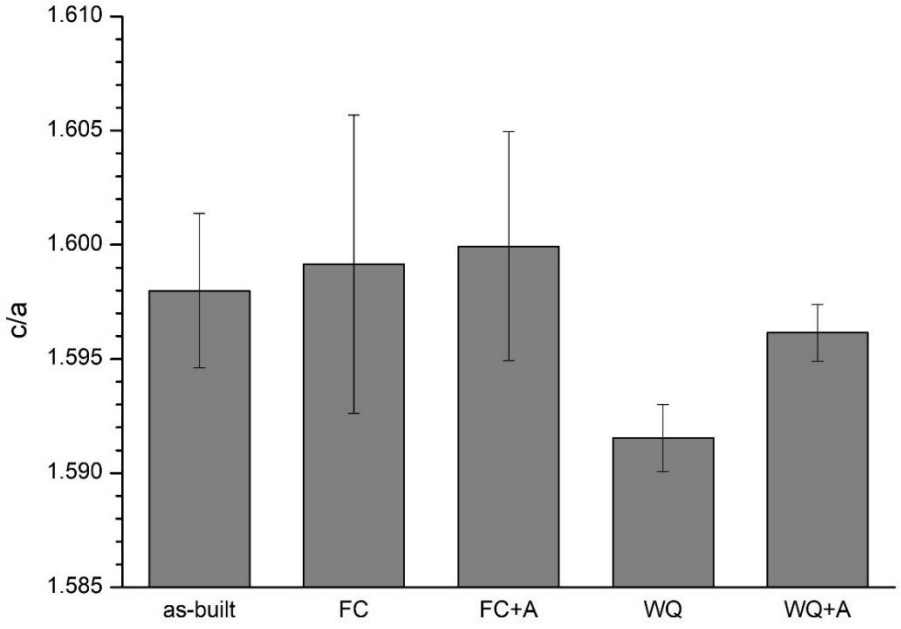


**Figure 87**: c/a ratio evaluation from the XRD data.

The as-built and furnace cooled samples were characterized by similar c/a values, ranging from 1.598 to 1.600, consistently with other data available in literature for similar microstructures [211,212]. Oppositely, the specimens that underwent water cooling, resulted characterized by lower c/a ratio values. In particular the WQ samples had an average value of 1.592 ± 0.02. This variation might have been correlated to the supersaturation of β stabilizers in the α' lattice [213,214]. This assumption is in good agreement with the data available in some works, in which a lower c/a ratio corresponded to martensitic Ti-6Al-4V samples [157,167]. The WQ+A samples underwent partial α' decomposition, in favour of α phase. This can effectively explain why the resulting c/a ratio was higher than that of WQ, but still lower than the other samples, due to the significant amount of martensite still present.

## *Mechanical Properties*

Vickers microhardness was evaluated for all the conditions. The results obtained are summarized in Figure 88. The as-built material provided an average value of 349 ± 23 HV. This value is set below some results obtained in other works available in literature [134,204]. This is possibly caused by different process parameters used during fabrication, which had a great impact on the final material properties. The FC and FC+A samples highlighted a significant decrease in microhardness to 307 ± 35 and 307 ± 23 HV, respectively. These specimens were characterized by a lamellar α+β microstructure in which colonies sharing the same orientation were clearly visible. This microstructural feature, associated with a very slow cooling rate, is often associated with a low hardness [215]. Comparing these two conditions, the difference in terms of HV appeared completely negligible, even if their typical lamellar α widths were significantly different (Figure 83). Oppositely, the grain size evaluation provided very similar results for these two conditions (Figure 85), as a consequence of the presence of $\alpha_{GB}$. Therefore, the analysis of the data suggested that the effect of the microstructural size on the microhardness of the FC and FC+A samples was marginal with respect to that of the grain size. The significance of this last effect seemed to be confirmed by the WQ and WQ+A samples. The former resulted the hardest in this work (380 ± 15 HV), possibly due to its martensitic microstructure, known for slightly increasing hardness [4,20]. Instead, the WQ+A specimens highlighted a significant drop of HV to an average value of 327 ± 19 HV, which was also markedly lower than the as-built condition. This sudden decrease might have been caused by the combined effect of the grain enlargement (Figure 85) and the coarsening of the microstructure (Figures 83,84). However, the latter was not only correlated to the size, as in fact α laths grew at the expense of α', effectively changing the relative α/α' phase composition. Therefore, the post-annealing ageing heat treatment seemed to have a negligible effect in terms of hardness of the slowly cooled samples (FC, FC+A), whilst it caused a significant drop in performances of the quenched samples (WQ, WQ+A).

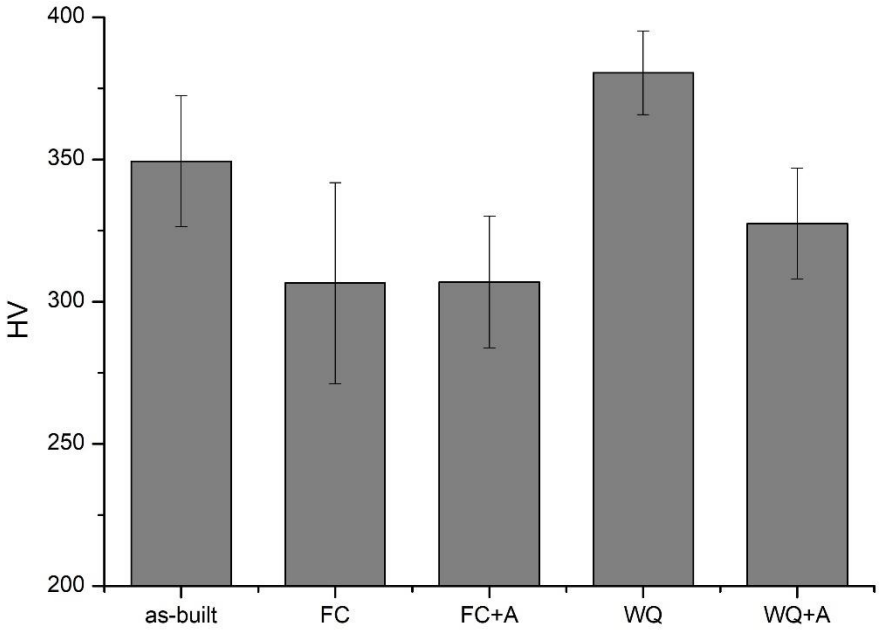


**Figure 88**: Microhardness measurement of all the conditions considered in this work.

The tensile properties of the mechanically machined specimens, obtained from vertical bars, in all the conditions considered were also assessed, providing the results visible in Figure 89 and Table 17.

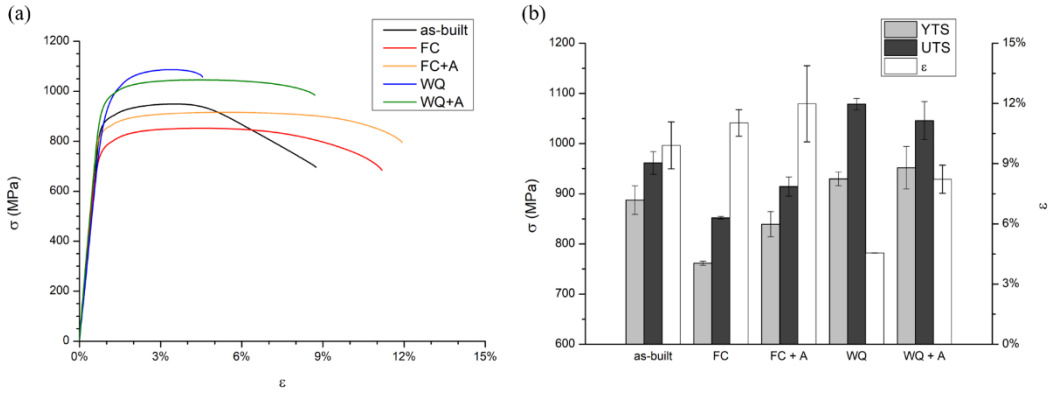


**Figure 89**: Representative tensile curves for each conditions (a) and relative average YTS, UTS and ε.

**Table 17**: Data obtained from the tensile tests.

| | YTS (MPa) | UTS (MPa) | ε (%) |
|---|---|---|---|
| **as-built** | 887 ± 28 | 962 ± 23 | 9.9 ± 1.2 |
| **FC** | 762 ± 4 | 852 ± 2 | 11.0 ± 0.7 |
| **FC+A** | 839 ± 25 | 914 ± 19 | 12.0 ± 1.9 |
| **WQ** | 930 ± 13 | 1079 ± 12 | 4.5 ± 0.1 |
| **WQ+A** | 952 ± 42 | 1046 ± 38 | 8.2 ± 0.7 |

The as-built specimens provided YTS and UTS values well above the threshold imposed by the ASTM-F2924 [71], which describes the mechanical properties requirements for the EBM produces Ti-6Al-4V components. The elongation was very close to the minimum required (10%). The FC and FC+A provided the highest ductility in this investigation. This resulted coherent with the literature, as lamellar α+β microstructures characterized by the presence of colonies are often associated with a good plasticity [4,6]. Usually this effect is linked with a decrease in strength, as confirmed by the experimental data. For example, the average YTS of the FC samples resulted significantly lower than in the as-built condition. However, after ageing, the YTS increased, reaching 839 ± 25 MPa, which was definitely closer to the initial value, than the non-aged counterpart. Furthermore, a higher ε was reached. Hence, for furnace cooled samples, the post-annealing ageing treatment appeared beneficial both in terms of strength and ductility. In particular, the combination of mechanical properties reached by the FC+A samples appeared appropriate and also compliant to the ASTM-F2924 [71]. Considering the quenched specimens, The YTS and UTS values obtained were the highest of all the conditions examined. The relative strengthening effect could be caused by the presence of α' martensite and finer grains, with respect to the other heat treated samples. However, the α' increase in strength resulted in a significant decrease in ductility (e.g. 4.5% ± 0.1% for WQ), as this was an embrittling phase. However, the WQ+A specimens showed a drastic increase in ductility (8.2% ± 0.7%), without a loss of strength. This augmentation was probably due to the synergic effect of grain enlargement and microstructural coarsening/α growth at the expense of α'. In particular, the WQ+A samples provided the highest YTS value of this investigation (952 ± 42 MPa). Therefore, the post-annealing ageing appeared as a mandatory step for water quenched samples, as it resulted in a drastic increase in ductility, associated with the retained outstanding strength.

## *Conclusions*

In this work, different super-β transus heat treatments on EBM produced Ti-6Al-4V samples were investigated. Different cooling paths (furnace cooling, water quenching) were considered in addition to the effect and significance of a post-annealing ageing step. The specimens were analysed from a mechanical properties and microstructural point of view. To sum up, the most important results obtained can be reported as follows:

- A super-β transus annealing results in a shift in grain morphology from columnar to equiaxed. Moreover, the resulting microstructure is dependent on the cooling rate applied. In particular, a fast cooling leads to the formation of α' martensite, while a slow cooling allows the formation of colonies of α lamellae surrounded by a β layer.
- The ageing step caused a significant enlargement of the α laths in all conditions. In particular, in the WQ+A samples, this happened at the expense of α'. Moreover, this heat treatment caused an enlargement of

the grains in this last condition, whilst this phenomenon was prevented from occurring in the FC+A samples due to the presence of $\alpha_{GB}$, which acted as a growth barrier.

- Apart from the WQ samples, the specimens representing all the other heat treated conditions resulted less performing than the as-built specimens in terms of hardness.
- The furnace cooled samples were associated to improved ε values and a significant decrease in YTS and UTS with respect to the as-built samples. However, the ageing heat treatment allowed a partial recovery of the strength, without compromising the plasticity. The FC+A samples were the only ones to provide a combination of mechanical properties meeting the requirements of ASTM-F2924.
- Water quenching the annealed samples resulted in a significant strengthening effect. However, the ductility decreased substantially. The addition on an annealing step provided an almost complete recovery of the initial ductility, without losing the excellent YTS and UTS reached.
- In terms of tensile properties, a post-annealing ageing step appears to improve the quality of the samples, independently from the cooling path applied.

## 3.3. Comparison of the DED and EBM Produced Samples.

Several heat treatments were conducted on samples produced either via EBM or DED. A comparison is possible between the FC+A and WQ+A conditions, presented in the work on the heat treatments on DED and EBM samples, since the same operative conditions were selected. In this section, using the same nomenclature adopted before, the samples were defined as explained in Table 18.

**Table 18**: Nomenclature used and specification for the heat treatments considered in this chapter.

| | **Annealing** | **Ageing** |
|---|---|---|
| **FC+A** | 1050 °C for 1h followed by furnace cooling | 540 °C for 4 h followed by furnace cooling |
| **WQ+A** | 1050 °C for 1h followed by water quenching | 540 °C for 4 h followed by furnace cooling |

In this section only the DED produced samples built without pre-heating the platform during the process were examined. Considering that no significant differences induced by the platform temperature during deposition were found, this condition was preferred for a simpler system and a more economic process.

## *Microstructure*

The sample produced via DED and EBM presented significant differences in the as-built conditions. These were mostly resulting from the markedly different microstructures generated by the different manufacturing technologies adopted. In particular, the DED produced samples provided a completely martensitic microstructure, resulting from the intense cooling rates typically involved in this process (Figure 90a). Instead, the EBM produced samples were characterized by a more complex microstructure of α+β lamellae arranged both in a Widmanstätten pattern and in colonies (Figure 90b), resulting from the high cooling rates of the EBM process, in conjunction with the prolonged annealing heat treatment, caused by the high temperature at which the process chamber is kept during the manufacturing step. Both samples provided prior-β grains in a columnar morphology, due to the strongly directional cooling capacity of the systems involved, which headed towards the baseplate.

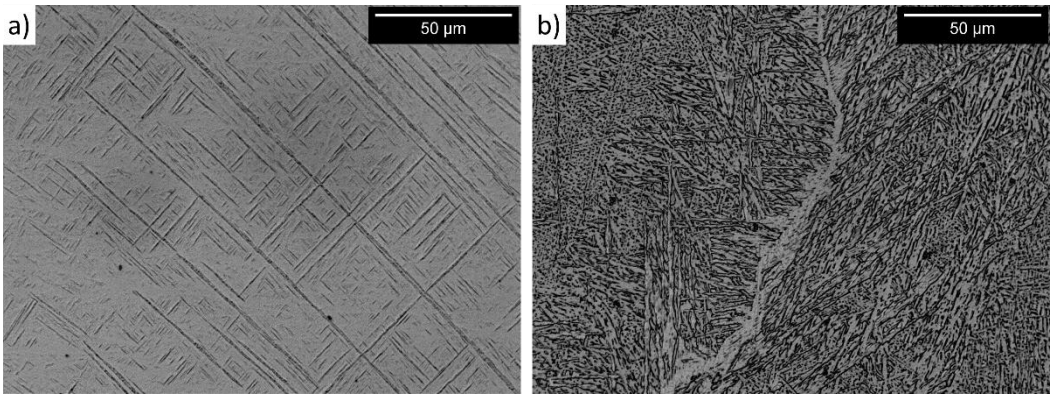


**Figure 90**: Optical micrograph of the DED produced (a) and EBM produced (b) samples in the as-built state.

The DED and EBM heat treated samples provided similar microstructures if the same cooling path was considered after annealing. The DED-FC+A (Figure 91a) and EBM-FC+A (Figure 91b) specimens were characterized by a completely lamellar microstructure of α lamellae enveloped in a thin β layer. Instead, the DED-WQ (Figure 91c) and EBM-WQ+A (Figure 91d) samples were characterized by a mainly α' martensitic microstructure, recognizable by the presence of fine needles, in which sparse α laths were clearly visible.

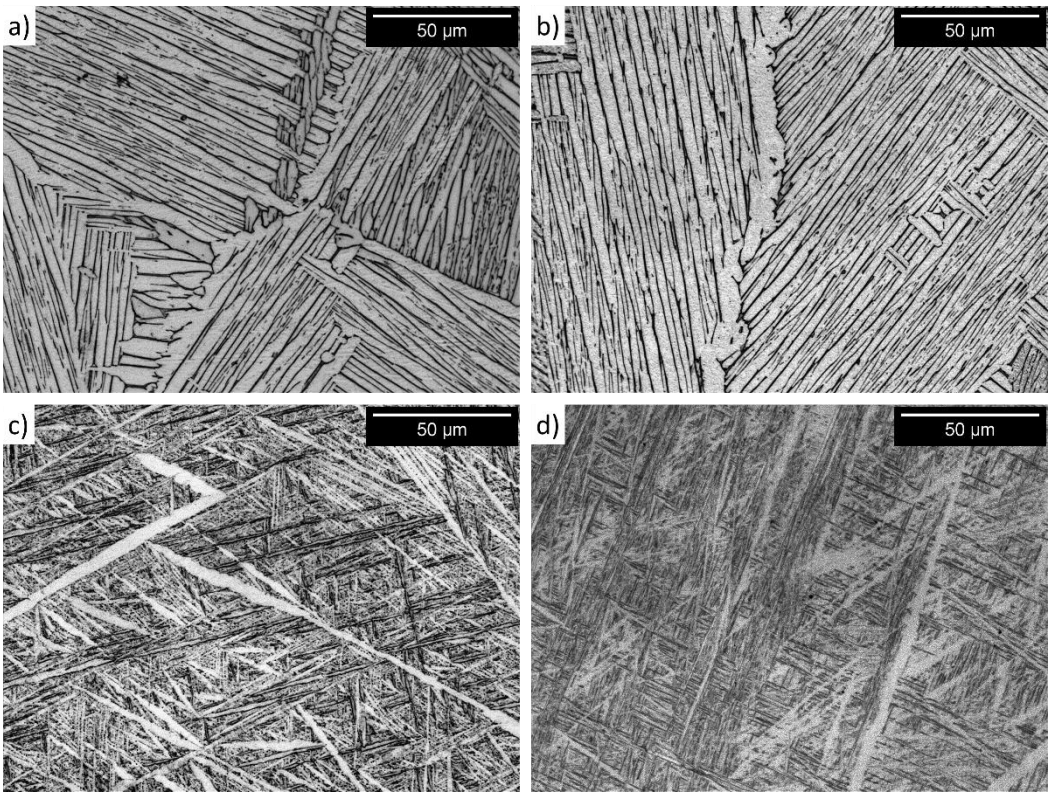


**Figure 91**: Optical micrographs of the DED-FC+A (a), EBM-FC+A (b), DED-WQ+A (c) and EBM-WQ+A (d) samples.

All the heat treated samples provided an equiaxed grain morphology, as a result of the recrystallization super-β transus heat treatment. The comparison of the relative average grain size is illustrated in Figure 92.

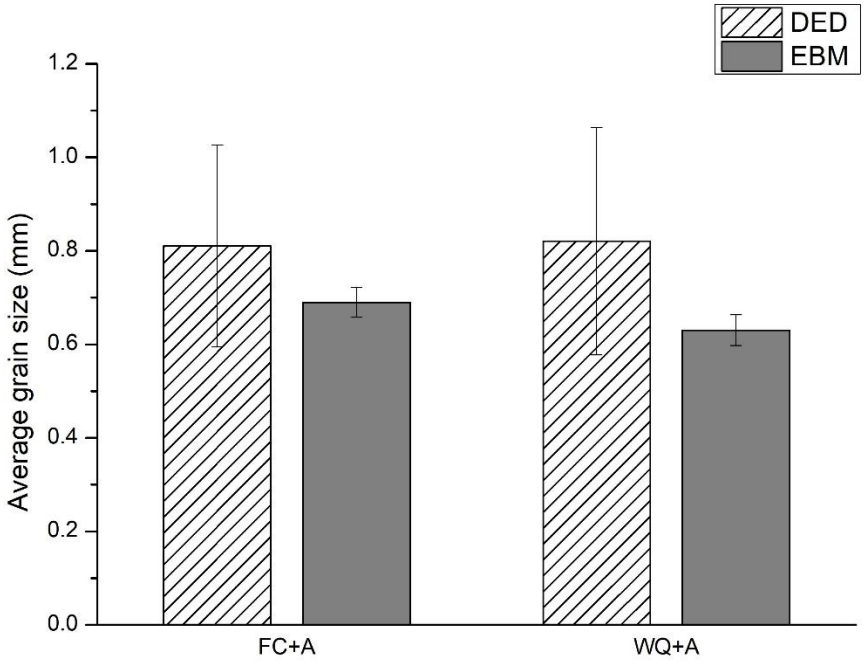


**Figure 92**: Comparison of the grain size of the DED and EBM produced heat treated samples.

The specimens built using the same technology presented similar grain size values, even if a different heat treatment was conducted. This result appeared reasonable, as most of the grain growth occurred at high temperature, during the annealing phase. During this phase, no α phase was present to slow down diffusive phenomena, thus grain growth was greatly favoured. Overall, the DED produced specimens were characterized by slightly bigger grains. This might be the result of a lower concentration of grain boundaries for this type of samples in the as-built condition, which resulted in fewer spots in which the nucleation of new grains was encouraged at high temperatures. In fact, the DED prior-β grains provided width values approximately ranging from 200 to 500 µm in the as-built state. Tan et al. [60] evaluated a grain width of 40-55 µm for EBM produced samples, in the as-built condition. This marked difference is the result of the different cooling rates applied during the process. In fact, the typical value of cooling rate for the DED technology lies between $10^1$ and $10^3$ °C/s, instead it ranges from $10^3$ up to $10^5$ °C/s for the EBM technology [111,118,216]. As a consequence of that, the grain boundaries were markedly more concentrated in the latter condition, resulting in slightly finer grains after the heat treatment.

A deeper analysis of several micrographs allowed to determine the average value and investigate the distribution of the α width for all the conditions considered in this comparison, as illustrated in Figure 93 and Table 19.

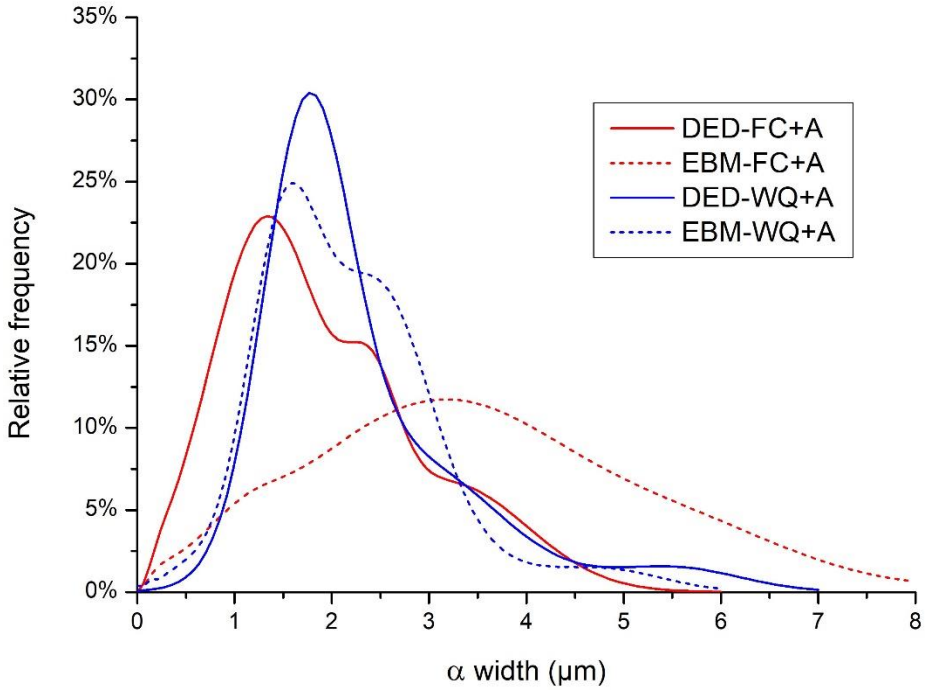


**Figure 93**: α width distribution of the FC+A and WQ+A Ti-6Al-4V samples produced by means of EBM and DED.

**Table 19**: Average α width values for all the conditions considered in this comparison.

| Condition | α width (µm) |
|---|---|
| **DED-FC+A** | 1.73 |
| **EBM-FC+A** | 3.29 |
| **DED-WQ+A** | 2.14 |
| **EBM-WQ+A** | 1.98 |

The EBM-FC+A samples provided a significantly wider distribution curve, shifter toward higher α laths widths. Therefore, the resulting average value provided by these samples was abundantly exceeding the DED-FC+A condition. A possible cause for this behaviour was not yet found. In fact, both samples should present the same high temperature microstructure (100% β) when kept at 1050 °C. Moreover, the subsequent cooling paths was the same for DED and EBM produced specimens. Since the heat treatment was performed using the same equipment in the same conditions, relevant differences during cooling appeared unlikely. However, this last option cannot be fully excluded. The only significant difference found between DED-FC+A and EBM-FC+A was the grain size. This might have had a certain influence on the formation of the lamellar α+β microstructure, since α laths formation is greatly favoured in correspondence of the grain boundaries. However, this sole explanation seems somehow unlikely in order to describe such a significant difference in terms of α widths. The WQ+A samples provided more comparable results. This information seemed to be in good agreement with the difference between DED and EBM produced samples in terms of grain size, as the nucleation and growth of α phase during the WQ+A heat treatment did not provide evidence of being favoured along the grain boundaries. Oppositely, the majority of the α laths were found inside the prior-β grains.

Similarly to the α laths, the α’ needles were analysed in the DED-WQ+A and EBM-WQ+A conditions. The relative width distributions and average values are presented in Figure 94 and Table 20.

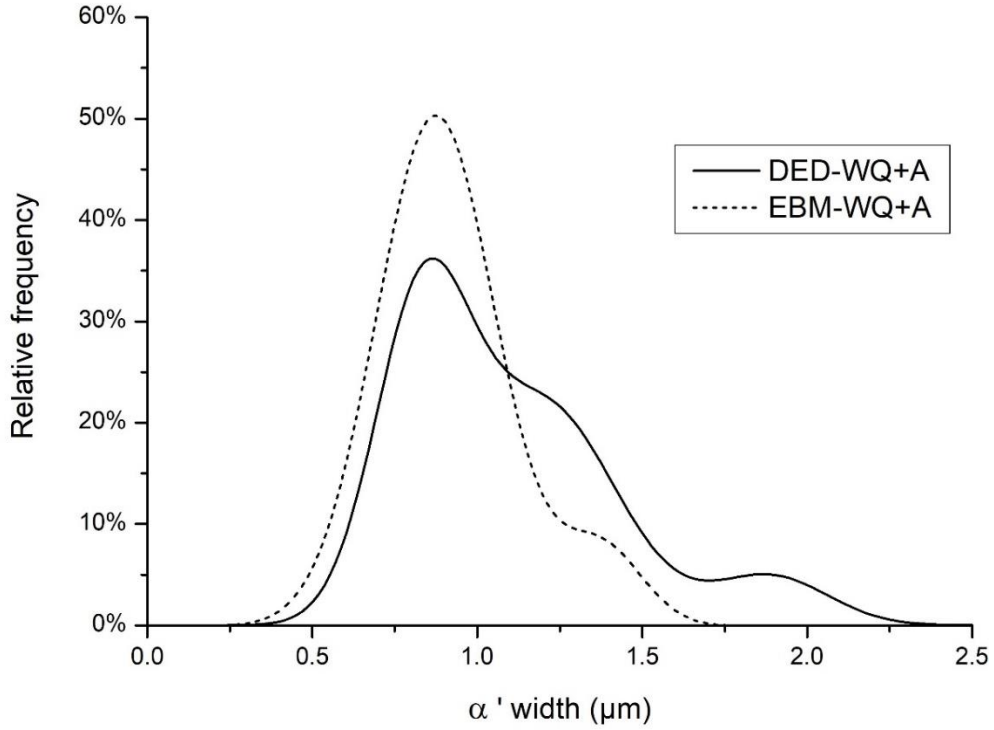


**Figure 94**: α' width distribution of the WQ+A samples produced by means of EBM and DED.

**Table 20**: Average α width values for all the conditions considered in this comparison.

| Condition | α' width (μm) |
|---|---|
| **DED-WQ+A** | 0.98 |
| **EBM-WQ+A** | 0.78 |

The EBM-WQ+A sample was characterized by an overall finer martensitic microstructure, mainly due to a less consistent presence of larger needles (> 1.25 μm), found mainly in the DED produced sample. This difference was probably induced by a different interstitials content, however further analyses are needed in order to confirm this.

In terms of mechanical properties, the comparison of the average Vickers microhardness for the as-built and heat treated conditions is provided in Figure 95. The as-printed EBM specimens were characterized by a higher mean hardness value than the DED ones. This was probably the result of the finer microstructure induced by the extremely high cooling rates related to the electron beam use in EBM systems. The abundant presence of α' in the DED samples was insufficient to fill the grain width gap, in terms of hardness. In fact, the hardening effect of the martensite is moderate [4,6], whilst the difference in terms of grain size appeared significant [60]. Considering the heat treated specimens, in general the FC+A samples were characterized by a markedly lower hardness than their WQ+A counterparts. Moreover, if the same type of heat treatment is considered, the EBM produced samples appeared more performing, both in the FC+A and WQ+A conditions. This is probably related to the reduced grain size, as in the as-built

state, which had a major impact on the outcome of this evaluation, as already highlighted in **Chapter 3.1.4**.

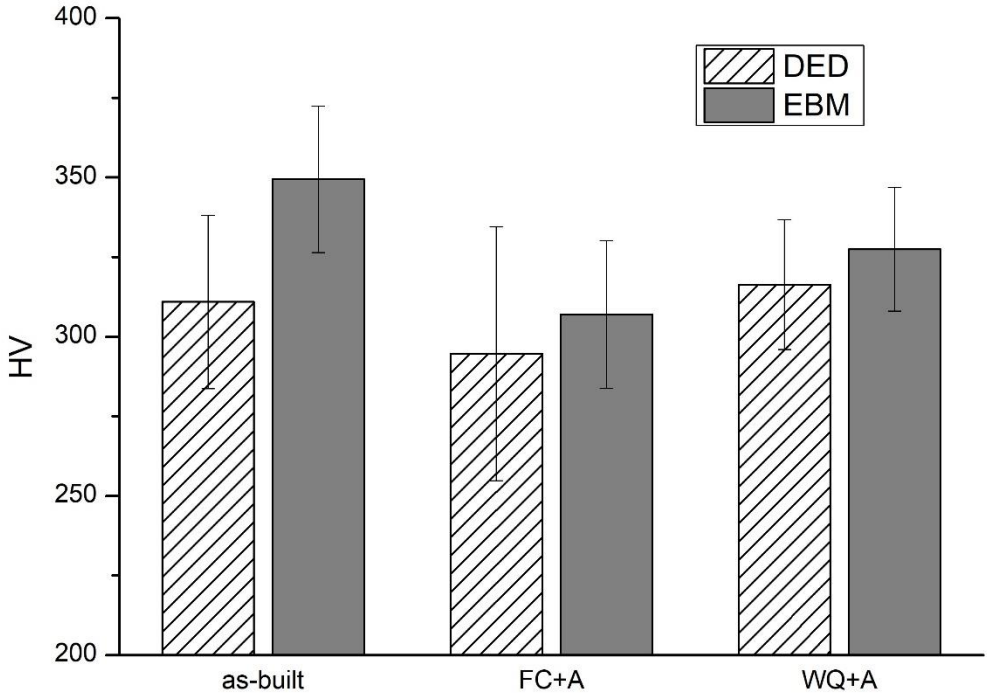


**Figure 95**: Comparison of the average hardness values of the FC+A and WQ+A samples fabricated via DED and EBM. The as-built data were added in order to consider the HV values pre-heat treatment. The DED as-built data are relative to the samples built without pre-heating the platform.

The only DED and EBM produced tensile samples that shared a common heat treatment were the ones that underwent the FC+A heat treatment. These samples and the as-printed ones were compared in Figure 96. The as-built DED specimens appeared significantly more fragile, although their strength was markedly higher than the EBM ones. After the recrystallization heat treatment was performed, providing comparable microstructures, the EBM samples resulted significantly more performing in terms of YTS (+6%), UTS (+8%) and ε (+46%). The slightly higher resistance was probably a result of the finer grains observed in the EBM samples, whilst the markedly higher ductility was likely correlated with the coarser microstructure. The DED and EBM tensile specimens were characterized by different building orientations, horizontal and vertical, respectively. This difference might have played an important role in the determination of the mechanical properties in the as-built state. As discussed in **Chapter 1**, this phenomenon is mostly linked to the presence of highly anisotropic columnar prior-β grains and related microstructural features. However, the influence of the orientation and the consequent anisotropic microstructures on the mechanical behaviour of the heat treated samples was considered negligible due to the complete recrystallization of the microstructure that occurred, allowing a shift from a columnar to an equiaxed grain morphology.

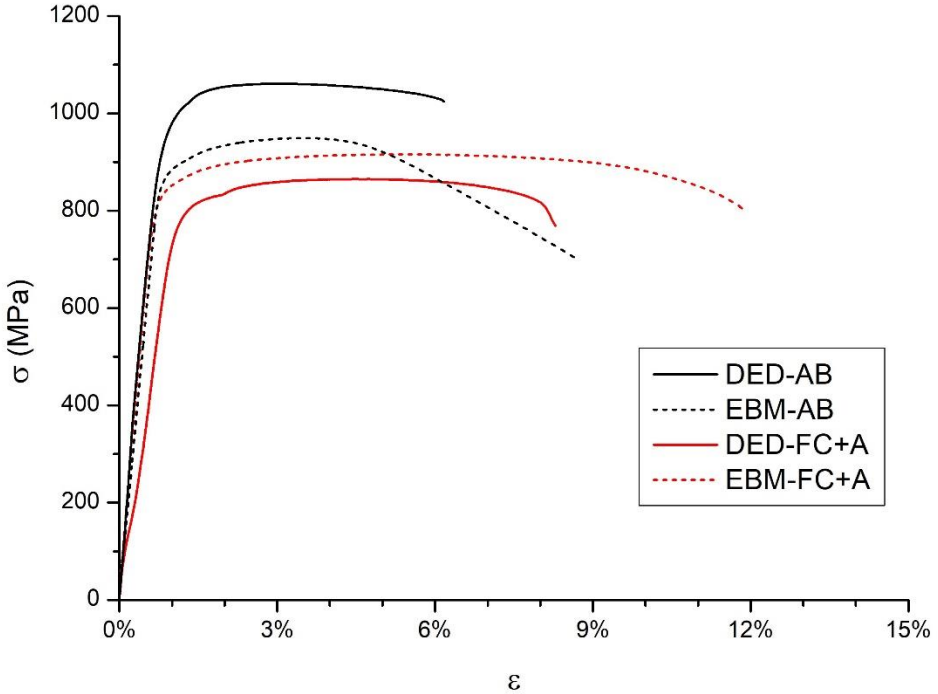


**Figure 96**: Representative tensile curves for the DED-FC+A and DED-WQ+A samples. The as-built data were added in order to consider the tensile properties pre-heat treatment. The DED as-built data are relative to the samples built without pre-heating the platform.

## *Conclusions*

In this section, a comparison between the DED and EBM produced heat treated samples was conducted in terms of microstructure and mechanical properties. The most significant findings can be summarized as follows:

- Performing the same type of heat treatments provided overall the same type of microstructures in the samples, independently from the manufacturing technique adopted.
- A deeper investigation of the micrographs highlighted how the heat treated EBM produced samples were characterized by finer grains than their DED counterparts. This was possible due to the finer grains that the EBM samples had in the as-built state. Therefore, a "grain memory" effect, similar to the one noted in **Chapter 3.1.3** was found.
- The EBM produced samples provided much larger α laths than the DED ones in the heat treated condition. The reason for this phenomenon is still to be understood.
- The EBM-WQ+A and DED-WQ+A samples provided closer values both in terms of α and α' width. The EBM produced samples had a slightly larger α phase, although their α' needles resulted quite finer.
- In all conditions, the EBM produced samples were harder.
- The DED-FC+A produced specimens resulted less performing in terms of YTS, UTS and ε with respect to the EBM-FC+A samples, as a result of the tensile tests performed. Thus, for the Ti-6Al-4V alloy, the EBM technology can manufacture samples overall more

performing in terms of mechanical properties, even after a recrystallization heat treatment.

## 3.4. Ti-6Al-2Sn-4Zr-6Mo Alloy Produced by LPBF

In this chapter, the applicability of the LPBF technology in order to process the Ti-6Al-2Sn-4Zr-6Mo alloy was investigated. No records were found in literature regarding this material manufactured using this technology. The only source found, in which this material was processed using AM , was a work from Blackwell et al. [217], in which the authors used a DED technique. Therefore, this work can be considered as innovative, since its aim is to provide a novel titanium alloy to be processed by an innovative manufacturing technique, such as LPBF. Subsequently, the properties obtained were compared with the ones of the Ti-6Al-4V alloy produced by means of LPBF.

### 3.4.1. A study on the Microstructure and the Mechanical Properties of the Ti-6Al-2Sn-4Zr-6Mo Alloy Produced via Laser Powder Bed Fusion

The Ti-6Al-2Sn-4Zr-6Mo alloy is a high-strength α+β titanium alloy. This material finds most of its usage for specific applications, mostly in the aerospace and race cars industry. It is commonly used in compressors disks and blades in aero gas turbine engines and in some sections of race car engines, which are meant to operate at relatively high temperatures [19,218]. It is generally preferred over the Ti-6Al-4V alloy for applications in which higher strength values are needed, such as some compressor parts in aero-engines [6,219]. Overall, this material provides good mechanical properties at high temperatures, for being a duplex titanium alloy.

The Ti-6Al-2Sn-4Zr-6Mo has a higher beta stability index ($SI_{\beta,Ti6246}$ = -1.33) than Ti-6Al-4V ($SI_{\beta,Ti64}$ = -3.33). Therefore, it is more prone to retain a higher amount of β phase near room temperature, hence it is often labelled as a near β alloy [18,220]. With respect to Ti-6Al-4V, the Ti-6Al-2Sn-4Zr-6Mo alloy provides a lower Young's modulus, but improved ductility [6,7].

Previous studies on this alloy [17] highlighted how the increased β-stabilizers content, which results in the increased beta stability index, causes the martensite formed upon fast cooling from $M_{S,Ti6246}$ = 880 °C to be α" (orthorhombic). In terms of microstructure, this is the most significant difference between this alloy and the Ti-6Al-4V alloy, which forms α' (hexagonal) from $M_{S,Ti64}$ = 800-830 °C [6,17,221–225]. These two phases provide a markedly different effect on the mechanical properties:

- α' formation results in a slight strengthening effect, coupled with a severe reduction in ductility, due to a marked reduction of the dislocations mobility [4,24,226].

- α" softens the material and provides an increase in ductility [227].

From a morphological point of view, both α’ and α” develop in an acicular shape, often referred to as needle [221].

The Ti-6Al-2Sn-4Zr-6Mo alloy is mainly used in industrial fields (e.g. automotive, aerospace) that heavily rely on high quality, customizable and complex components, usually produced in small lots. All these features are promising in terms of AM applicability. Moreover, being a Ti alloy, this material is intrinsically well suited to be produced via AM, as seen in **Chapter 1**. For these reasons, investigating the possibility to apply this family of technologies to this specific material appears very favourable.

In this study the LPBF technology was investigated. Even if most of the works concerning titanium alloys manufactured using this technology focused on Ti-6Al-4V [228–230], some papers can be found on commercial purity titanium (cp-Ti) [231], Ti-6Al-7Nb [49], Ti-24Nb-4Zr-8Sn [50] and Ti-21Nb-17Zr [51]. However, no works are available on the Ti-6Al-2Sn-4Zr-6Mo alloy, according to the author’s knowledge. Nevertheless, in a work from Gebisa et al. [232], the authors declared the importance of manufacturing components in this material using powder-bed AM technologies, especially for compressors production in the aerospace field.

Considering this gap and the aforementioned reasons, in this work the processability of the Ti-6Al-2Sn-4Zr alloy via LPBF was assessed. At first, the most suitable process parameters had to be found, using porosity minimization as a criterion. Afterwards, the analysis of two different sets of parameters was conducted simultaneously in order to determine the effect of the microstructure and mechanical properties. The effectiveness of a post-processing heat treatment was also studied.

A first series of 36 15x15x15 mm samples were built in order to determine the most promising process window in order to process the material. The first combination of parameters considered was characterized by a P of 170 W, a v of 1250 mm/s and a h.d. of 0.1 mm. This are the standard parameters used to process the Ti-6Al-4V alloy [114]. The other combinations were obtained by slightly changing every parameter, providing a total of 18 different combinations, as illustrated in Table 21. This methodology was followed under the assumption that the Ti-6Al-2Sn-4Zr-6Mo and Ti-6Al-4V alloys might be characterized by similar optimized process parameters, since both the materials are α+β titanium alloys. The other parameters, such as the platform temperature ($T_P$) and the layer thickness (t) were kept constant instead.

**Table 21**: Process parameters values considered for the investigation.

| P (W) | v (mm/s) | h.d. (mm) | $T_P$ (°C) | t (μm) | Scanning strategy |
|---|---|---|---|---|---|
| 150, 170, 190 | 1100, 1250, 1400 | 0.1, 0.13 | 100 | 30 | Standard 67° EOS strategy |

The volumetric energy density (VED) was chosen as the most valid variable in order to keep track of multiple parameters simultaneously. It was calculated as:

$$VED = \frac{P}{v \cdot t \cdot h.d.} \tag{12}$$

In a second job, other 15x15x15 mm cubes and 100 mm long horizontal cylindrical samples (12.5 mm diameter) were built. The process parameters adopted were the two most promising ones highlighted by the analysis on the cubes built in the previous jobs. Furthermore, a portion of the specimens was heat treated at 750 °C for 2 hours, in order to evaluate the effect of a post-processing heat treatment on the microstructure and mechanical properties.

## *Determination of the Process Parameters*

The mean porosity value for each sample, corresponding to a different combination of process parameters, was evaluated by means of image analysis. The outcome of this investigation was plotted as a function of VED, as illustrated in Figure 97. The resulting downward sloping trend showed the minimum porosity values in correspondence of increasing energy densities. In particular, the specimens characterized by the highest density values (>> 99%) were found at VED ≥ 40 J/mm$^3$.

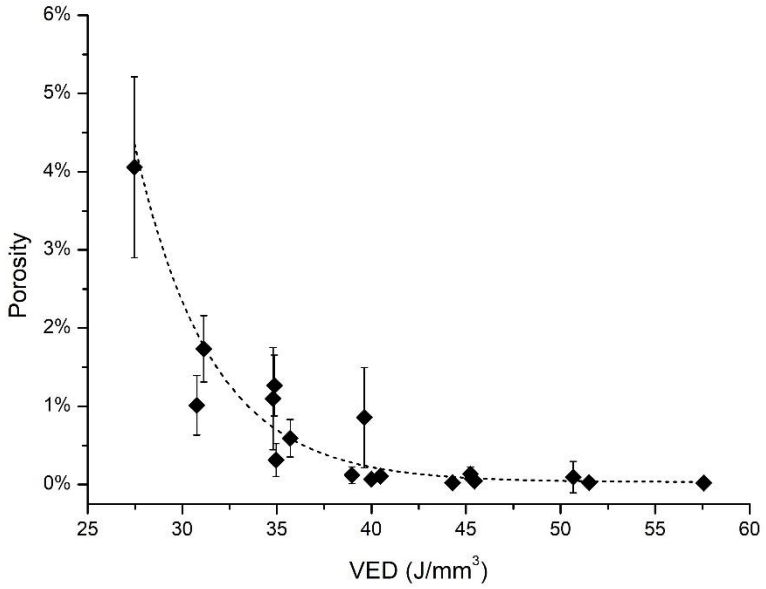


**Figure 97**: Mean porosity values corresponding to all the sets of process parameters considered.

Since the minimization of the porosity was chosen as the most important criterion to meet in the definition of the most suitable process window, only two sets of parameters were considered for further investigation. These are summarized in Table 22.

**Table 22**: Process parameters of the sets considered for manufacturing the final samples and relative porosity values.

| Set | Porosity (%) | P (W) | v (mm/s) | h.d. (mm) | VED (J/mm$^{3)}$ |
|---|---|---|---|---|---|
| A | 0.01 | 190 | 1100 | 0.1 | 57.58 |
| B | 0.05 | 150 | 1250 | 0.1 | 40.00 |

Set A was characterized by the combination of process parameters that provided the lowest overall porosity in correspondence of the highest VED used in this investigation. Oppositely, set B resulted less dense in comparison with set A and characterized by a lower VED and slightly higher build-up rate. Notwithstanding this, it still provided a density higher than 99.9%, which is a promising outcome for LPBF produced specimens [233,234]. The main reason behind the choice to further analyse set B was to compare samples produced adopting a different VED value in order to understand the influence of the energy density on the final quality of the components built.

Apart from the rough mean porosity values, other indicators can be used to further analyse sets A and B, such as the mean pore size and shape. The average pore area (S) was estimated via software analysis. Then, the equivalent diameter (D), which represents the diameter of a hypothetical perfectly circular pore characterized by the same area, was calculated as $D = 2\sqrt{S/\pi}$.

Sets A and B were characterized by a D of 1.20 µm and 2.36 µm, respectively. Therefore, a higher VED appeared to induce the formation of finer pores in the material. According to ISO 9276 [235], the aspect ratio (Ψ) can be used in order to estimate the pore shape in a material. This parameter can be

$$\Psi = \frac{x_{Fmin}}{x_{Fmax}} \tag{13}$$

calculated as:

Where $x_{Fmin}$ and $x_{Fmax}$ are the minimum and maximum Feret diameters. In general, $0 < \Psi \leq 1$, where 1 indicates a perfectly circular body. In this case, a higher aspect ratio means that the shape considered is closer to sphericity. The aspect ratio was evaluated for sets A and B and plotted as a distribution, as illustrated in Figure 98.

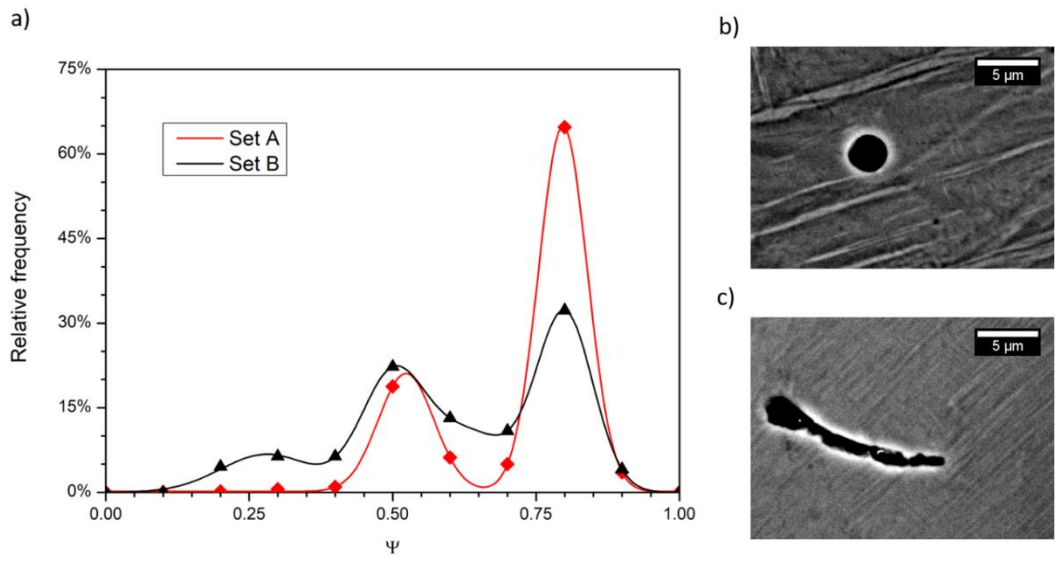


**Figure 98**: Relative distribution of the pores aspect ratio for sets A and B (a). Representative SEM micrographs of a spherical (a) and elongated (c) pore.

Set A was characterized by a bimodal distribution, characterized by a main peak at high Ψ values (≈ 0.8), corresponding to a quasi-spherical shape (Figure 98b), and a secondary peak at intermediate Ψ values (≈ 0.5). The former resulted predominant and accounted almost 70% of the relative frequency. Instead, the distribution relative to set B was broader and more evenly distributed throughout the whole Ψ range. Specifically, a certain amount of pores was characterized by rather low aspect ratios (< 0.35), thus providing an elongated shape, as illustrated in Figure 98c. Since set B accounted a non-negligible presence of highly elongated pores, absent in set A, the latter was expected to provide more promising results in terms of mechanical properties (e.g. ductility, fatigue resistance).

## *Microstructure*

The micrographs of the as-built samples (Figure 99) highlighted the presence of prior-β grains, developed via epitaxial growth perpendicularly to the baseplate (Figure 99a). This typical microstructural feature for the Ti-6Al-4V was then also noted in the Ti-6Al-2Sn-4Zr-6Mo alloy. The meltpool borders were also clearly visible in the cross-section (Figure 99a). The microstructure was characterized by the presence of elongated needles. These were arranged in a ±45° fashion, a typical outcome for titanium alloys built using a 0°/90° scanning strategy [24,41,221]. The presence of martensite in LPBF produced samples is consistent with the extremely high cooling rates evaluated for this technology, which can reach up to $10^5$-$10^7$ °C/s [84,236].

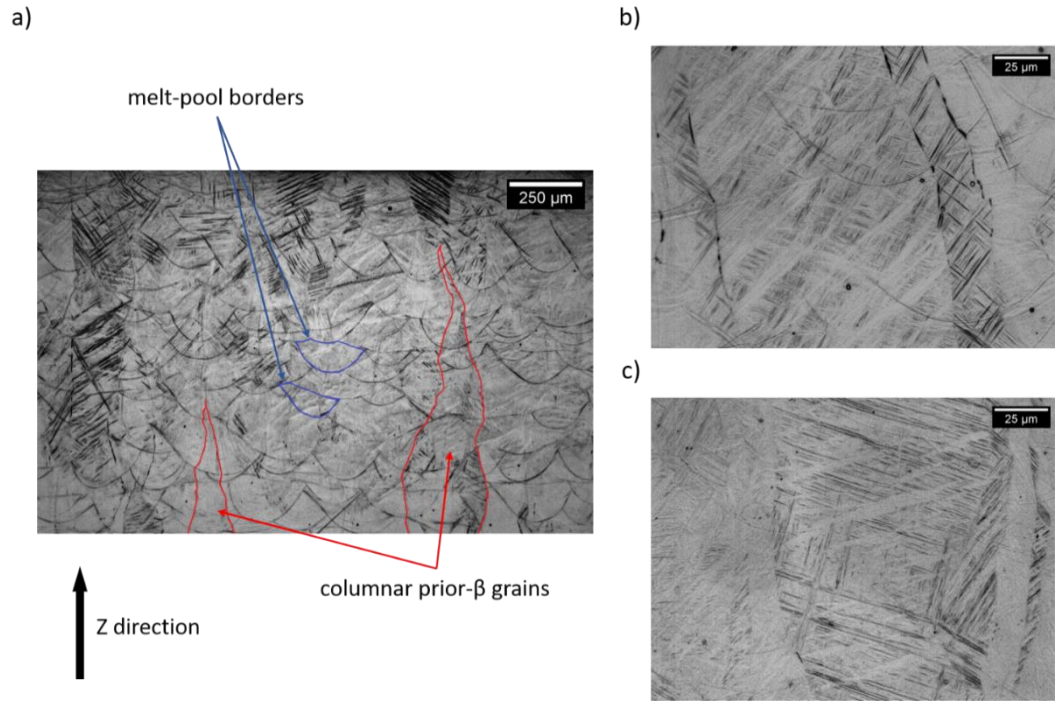


**Figure 99**: Representative optical micrograph of the microstructure of the Ti-6Al-2Sn-4Zr-6Mo alloy produced by means of LPBF (a); higher magnification micrographs of sets A (b) and B (c).

No significant difference was found between the micrographs relative to set A (Figure 99b) and set B (Figure 99c). In order to conduct a more in-depth investigation, the distribution of the martensitic width was evaluated and compared for both conditions. This indicator was commonly used in several works concerning titanium alloys in order to properly evaluate and numerically quantify the martensitic microstructures [24,157,180]. Moreover, it is strictly correlated with the thermal history of the process, with relevant consequences on the mechanical properties of the final component [4,24]. Therefore, the α" width was measured and studied as a statistical distribution for sets A and B, as illustrated in Figure 100.

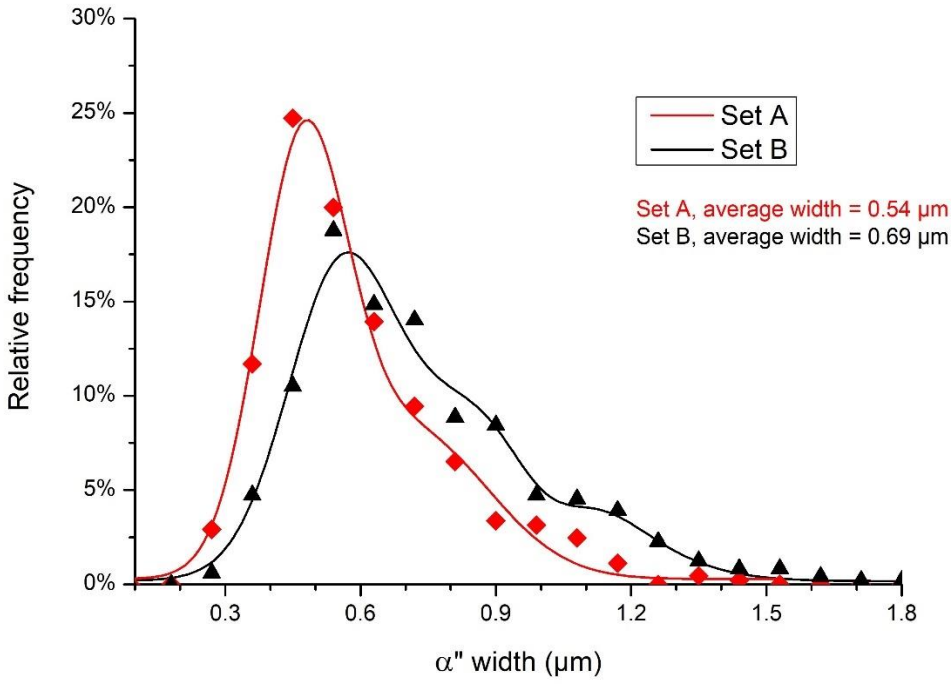


**Figure 100**: α" width relative distribution curves for sets A and B.

Set A was characterized by a narrower distribution curve, peaking at 0.47 μm and providing an average α" width of 0.54 μm. Instead, set B provided a broader curve that was overall shifted towards higher width values and peaked at 0.58 μm. The relative average value was 0.69 μm. Therefore, the sample built using the process parameters combination corresponding to the higher VED value (set A) provided an overall finer microstructure.

In general, the martensitic size in titanium alloys is strictly dependent on the thermal history of the process, in particular on the cooling rate. Previous studies on α' in the Ti-6Al-4V alloy [24,157] highlighted how a faster cooling was associated with larger martensitic needles. Thampy et al. [237] demonstrated that a higher laser power used during the process lead to a lower cooling rate in LPBF produced Ti-6Al-4V. A similar result was obtained by Li et al. [238]. These authors found that a lower energy density decreased the solidification time, thus increasing the cooling rate. Therefore, since set A was characterized by a high P and VED and its martensite resulted finer than in set B, the outcome of the martensite width evaluation appeared in good agreement with the data available in literature.

A post-processing sub-β annealing at 750 °C for 2 hours was conducted on the samples from both sets in order to reduce the internal stresses accumulated during fabrication and decompose α", which has a negative impact on hardness, as mentioned before [227]. The micrographs relative to the heat treated samples, provided in Figure 101, were characterized by the presence of a lamellar microstructure, resulting from the α"→ α+β decomposition. Moreover, $\alpha_{GB}$ was detected in correspondence of the grain boundaries. Its presence must be carefully controlled, as this microstructural feature can reduce ductility in duplex titanium

alloys [239]. Furthermore, some traces of globular α phase were found. These might indicate the beginning of a transition from a lamellar to a globular morphology.

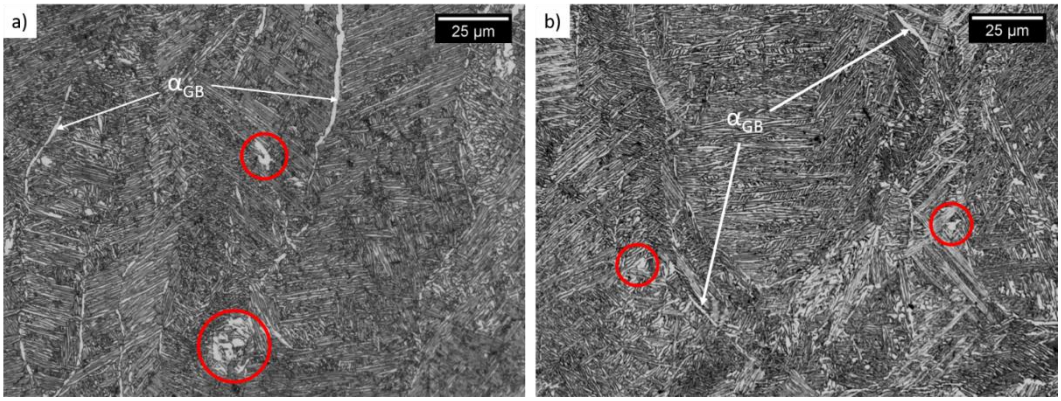


**Figure 101**: Optical micrographs of sets A (a) and B (b) after the post-processing heat treatment. The globular α phase is highlighted by the red circles.

Analogously to the methodology applied for the evaluation of the α" width, the lamellar α width was evaluated for the heat treated samples. The aim of this analysis was to investigate if the microstructural differences, induced by the choice of the process parameters adopted for the fabrication, remained after the sub-β annealing. The outcome of this evaluation is provided in Figure 102 and highlighted how the micrographs of the two sets resulted markedly more similar, providing similar α distribution curves and a mean width value of 0.65 and 0.62 µm, for sets A and B respectively. Thus, the outcome of this evaluation suggested that a sub-β annealing proved to be a useful tool in order to almost totally erase the differences, induced by different process parameters adopted during fabrication.

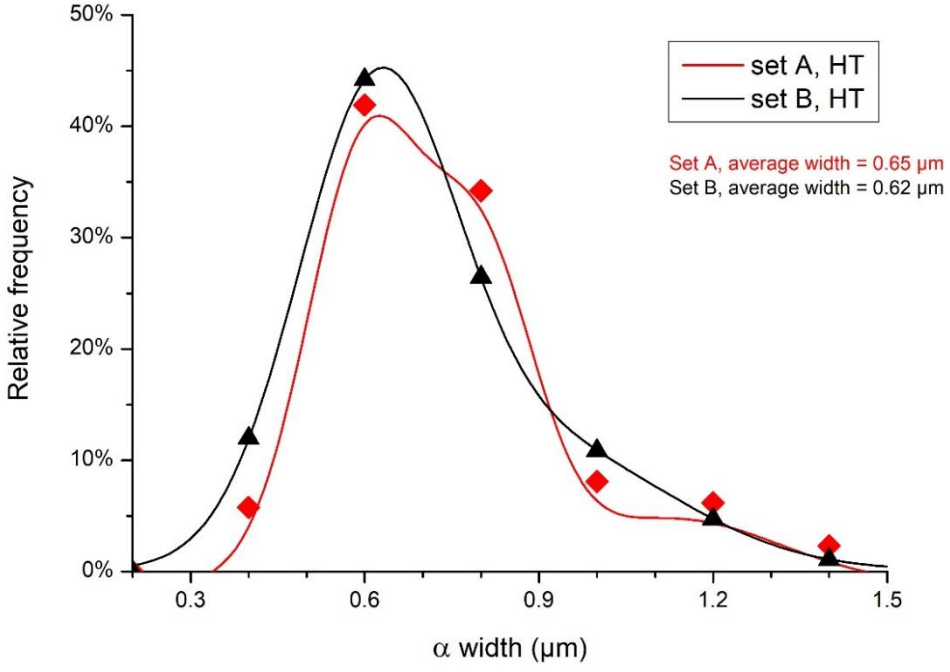


**Figure 102**: α width relative distribution curves for sets A and B.

The as-built samples provided a largely out-of-equilibrium martensitic microstructure, whilst the heat treated samples were characterized by more thermodynamically stable α+β lamellae. Thus, a non-negligible amount β phase was present and its quantification was possible, using a methodology already utilized by Atallah et al. [220] on the Ti-6Al-2Sn-4Zr-6Mo alloy. Several SEM micrographs were analysed (Figure 103) and the β phase content was measured by properly adjusting the threshold using the software imageJ. The measured amount of β was 27.6% ± 4.5% and 25.8% ± 3.2% for the sets A and B, respectively. Hence, the microstructures were characterized by similar α widths and amount of β phase.

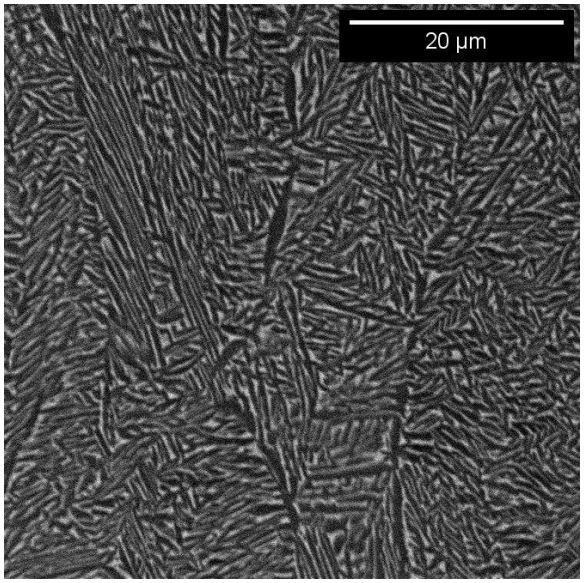


**Figure 103**: Representative SEM micrograph of a Ti-6Al-2Sn-4Zr-6Mo sample that underwent the sub-β annealing.

To further assess the microstructure and confirm the assumptions made on the micrographs, all the conditions were analysed via XRD measurements. The resulting pattern are available in Figure 104.

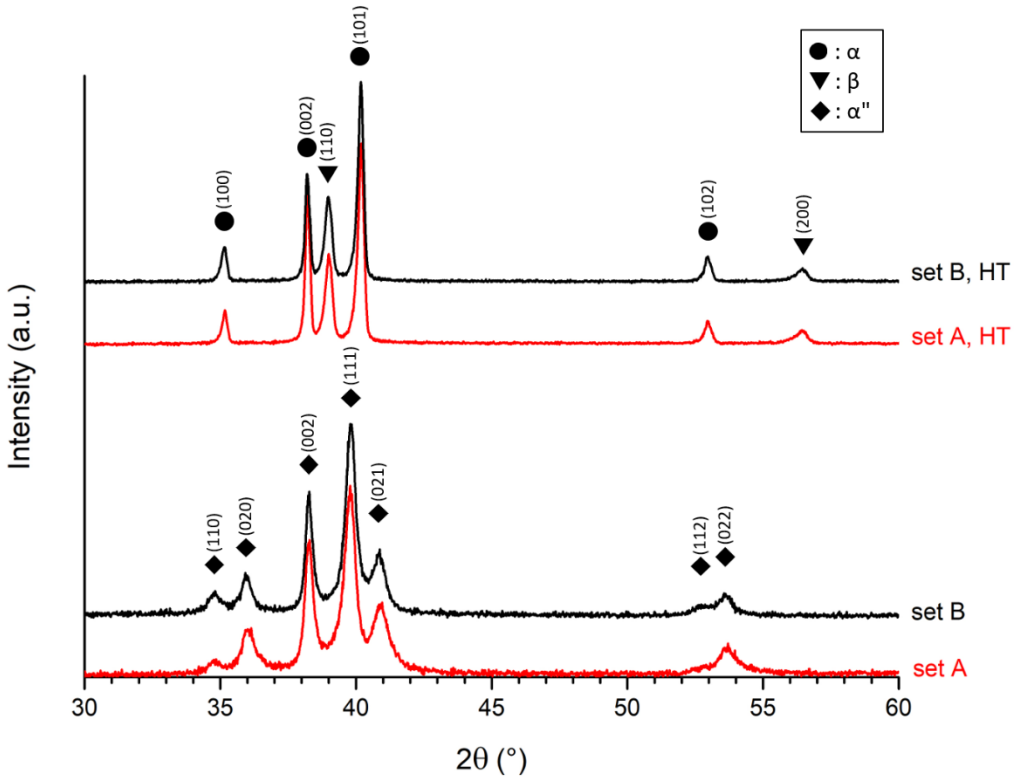


**Figure 104**: XRD patterns relative to sets A and B, both in the as-built and heat treated (HT) states.

Confirming the analysis of the microstructures, the as-built samples (set A, set B) provided only the peaks relative to the α" phase. This result was consistent with other works on the same material, in which a similar pattern was achieved in samples fast cooled from high temperatures via water quenching [222,240]. These peaks completely disappeared in the heat treated (HT) samples, which instead were characterized by the presence of α and β phases.

The cell parameters relative to α" and α were also assessed and then used to evaluate the cell volume for each of these phases. The former was representative of the samples in the as-built state, whilst the latter for the HT samples. This evaluation was not performed for the β phase, since a low number of peaks relative to it was visible and the analyses might have been poorly representative. The values obtained are reported in Table 23, in which are presented also the cell volumes for the orthorhombic (abc) and hexagonal cells ($\sqrt{3}a^2c/2$).

**Table 23**: Cell parameters and volume obtained via XRD spectra analysis.

| Set | Phase | Lattice | Cell parameters (Å) | Cell Volume (Å$^3$) |
|---|---|---|---|---|
| A | α" | orthorhombic | a = 3.029 ± 0.018<br>b = 4.985 ± 0.007<br>c = 4.694 ± 0.027 | 70.787 ± 0.931 |
| B | α" | orthorhombic | a = 3.005 ± 0.013<br>b = 4.971 ± 0.013<br>c = 4.692 ± 0.049 | 69. 947 ± 1.226 |
| A, HT | α | hexagonal | a = 2.937 ± 0.045<br>c = 4.733 ± 0.036 | 35.345 ± 1.563 |
| B, HT | α | hexagonal | a = 2.936 ± 0.044<br>c = 4.733 ± 0.036 | 35.360 ± 1.550 |

In the as-built condition, both sets A and B provided markedly similar cell parameters, thus the difference in terms of α" size was probably not related to significant changes, for example in the content of interstitial elements. Moreover, the cell parameters obtained were consistent with the data available in literature for water quenched Ti-6Al-2Sn-4Zr-6Mo [19,223]. Another parameter that can be evaluated for the samples in the as-built condition is the degree of orthorhombicity ($b/a\sqrt{3}$), that can be used to further study the α" (orthorhombic) → α (hexagonal) transition [223]. The values found were 0.950 and 0.955 for sets A and B, respectively. Since their degrees of orthorhombicity were markedly similar, these two groups of samples did not show significant differences in terms of tendency to decompose in a more thermodynamically stable phase (α), even if the thermal history of the fabrication processes were different, as testified by the dissimilar α" width values. The HT samples provided markedly similar cell parameters and volume values, thus confirming the homogeneity of the properties achieved after the adopted heat treatment.

## *Mechanical Properties*

Several Vickers microhardness tests were performed on the as-built and heat treated samples, providing the mean hardness values reported in Figure 105.

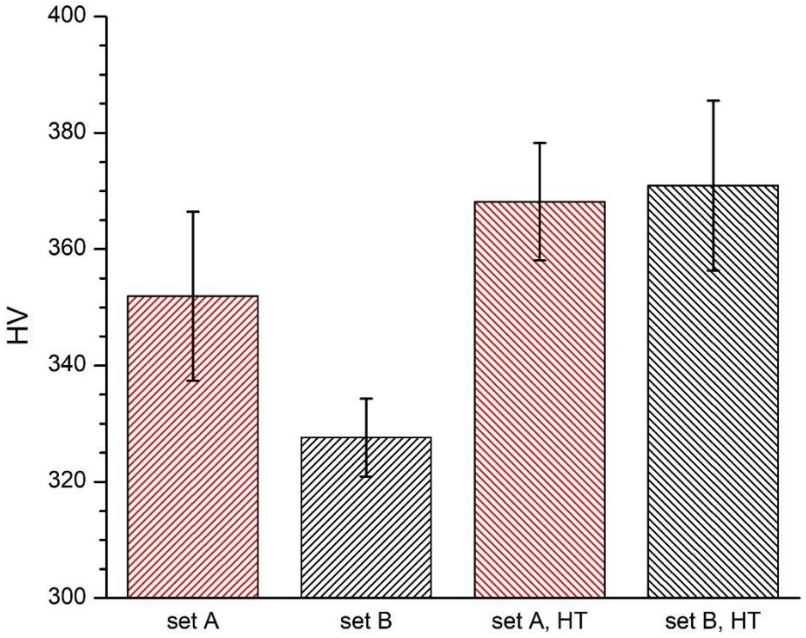


**Figure 105**: Average Vickers microhardness for sets A and B in the as-built and HT states.

In the as-built state, sets A and B provided mean average values of 352 ± 15 HV and 328 ± 7 HV respectively. The difference between these two values was probably caused by the different microstructures involved, in terms of α" size. In fact, set A was characterized by a finer microstructure and provided a significantly higher hardness in comparison with set B. Instead, the heat treated samples were characterized by markedly more similar hardness values (set A = 368 ± 10 HV and set B = 371 ± 14 HV). The overall increase was due to the absence of the softening martensite. The similarity of the values obtained for sets A and B further proved that the heat treatment was an effective tool in order to align the material properties affected by the different process parameters used. Since the main microstructural difference between the as-built samples and the heat treated ones was the presence of the martensite in the former specimens, its detrimental effect on hardness was confirmed. Therefore, due to the intrinsic softness of that phase, it was reasonable to state that its presence in LPBF produced Ti-6Al-2Sn-4Zr-6Mo is unacceptable for applications in which a high hardness is required. Moreover, the effectiveness of a sub-β annealing in improving hardness and in erasing the differences induced by the process parameters was proved. For these reasons, opting for a lower VED during fabrication, usually associated with a higher build-up rate, appeared as a more cost-effective alternative for this material, being porosity kept under control.

A series of tensile tests was conducted on the samples from sets A and B, both in the as-built and HT state. These were obtained from horizontal bars that were machined. The representative curves and relative mean values are provided in Figure 106 and Table 24.

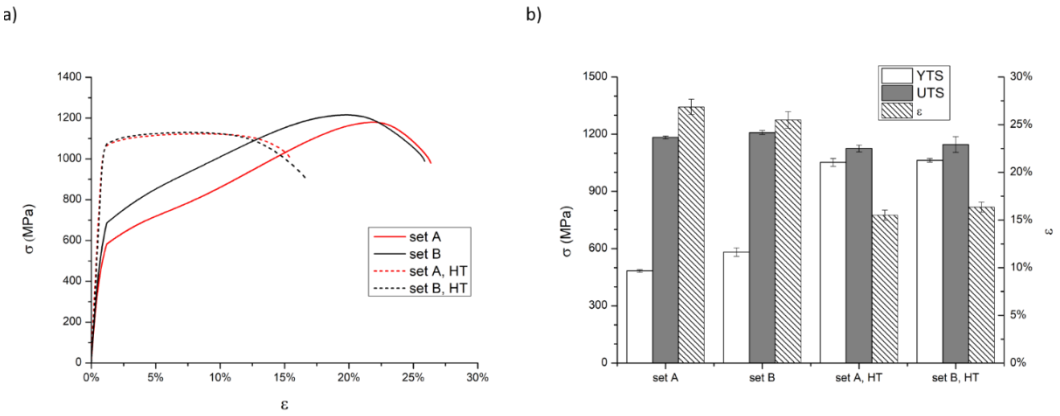


**Figure 106**: Representative tensile curves (a) and average YTS, UTS and ε for all the conditions considered in this work.

**Table 24**: Mean tensile properties obtained from the tensile tests and values relative to the wrought condition found in literature. The best mechanical properties found concerning this last condition were considered. To achieve those, a post processing duplex annealing was performed: 870 °C for 1 h, followed by air cooling; then 540 °C for 8 h, followed by air cooling [20].

| | YTS (MPa) | UTS (MPa) | ε (%) |
|---|---|---|---|
| **set A** | 483 ± 6 | 1183 ± 7 | 26.9 ± 0.8 |
| **set B** | 582 ± 23 | 1209 ± 11 | 25.5 ± 0.9 |
| **set A, HT** | 1052 ± 20 | 1125 ± 18 | 15.5 ± 0.5 |
| **set B, HT** | 1064 ± 10 | 1146 ± 41 | 16.4 ± 0.5 |
| **wrought** [20] | 1035 | 1100 | 10 |

By looking at Figure 106a, consistent work hardening can be noticed in the as-built samples. This is a quite common feature in titanium alloys, which are quite prone to be strengthened due to an increase in dislocation density [241]. However, this was not found in the HT samples, suggesting that work hardening occurred in such a relevant manner due to the presence of α".

The as-built samples were characterized by a fairly low strength, which was although coupled with a high ductility. Set B provided a YTS significantly higher than set A.

After annealing, YTS increased significantly, up to 1052 ± 20 MPa and 1063 ± 10 MPa for set A and set B respectively. Similarly, to the hardness measurements, the sub-β annealing allowed the mechanical properties of both sets to rise to similar values, thus making the differences induced by the process parameters adopted during fabrication negligible. Also, the UTS values slightly increased. However, the ductility after heat treatments appeared significantly lower, as expect due to the disappearance of the softening α" martensite. In Table 24 were also reported the tensile properties relative to the corresponding wrought material [20], which provided YTS and UTS values similar to the ones obtained in this work. However, the HT samples studied in this investigation were characterized by a ductility significantly higher (> +50%). The overall mechanical

properties for the LPBF produced alloy resulted well comparable with the data relative to the conventionally processed Ti-6Al-2Sn-4Zr-6Mo available in literature [242,243], suggesting LPBF as a viable alternative to conventional processing for this material. However, in order to achieve an optimal combination of strength and ductility a post processing heat treatment appeared mandatory.

## *Conclusions*

In this work the possibility to process the Ti-6Al-2Sn-4Zr-6Mo alloy using a LPBF system was investigated. The aim was to investigate if this type of technology can be applied, since this specific alloy is already widely used in industrial fields that already proved to benefit from AM technologies. The most significant results obtained can be summarized as follows:

- Porosity can be used as a defining criterion in order to determine the most promising process window. For this alloy, multiple combinations of P, v and h.d. were found to provide satisfactory relative density values. The lowest porosity was achieved by applying high VED values.
- VED also influences the pores shape and size. The data suggested that a more consistent energy density resulted in finer pores characterized by an aspect ratio closer to that of a sphere.
- Typical microstructural features of LPBF produced titanium alloys (e.g. Ti-6Al-4V) were obtained also for Ti-6Al-2Sn-4Zr-6Mo, such as columnar prior-β grains and a martensitic microstructure. However, the type of martensite obtained resulted orthorhombic (α'') instead of hexagonal, as in most duplex titanium alloys (e.g. Ti-6Al-4V).
- The size of the martensitic needles was influences by the process parameters adopted. In particular, a higher VED provided finer α" needles in the as-built conditions.
- A sub-β annealing at 750 °C for 2 hours, followed by slow furnace cooling, provides a complete martensitic decomposition, achieving a lamellar α+β microstructure. The size of the lamellae resulted independent from the initial α" size.
- In the as-built state, hardness was dependent on the size distribution of martensite, thus on the process parameters. This effect is erased by the heat treatment, which resulted in an overall increase in hardness, due to the disappearance of the soft α" martensite.
- The as-built samples were characterized by low yield strength values, but extremely high ductility. Instead, the heat treated specimens proved a significant increase in strength at the cost of a reduction in plasticity.
- The heat treated LPBF produced specimens showed comparable strength and significantly higher ductility values with respect to the

wrought material. Therefore, this technology appears very promising in order to achieve an optimal combination of strength and ductility.

### 3.4.2. Investigation of the Microstructure and the Mechanical Properties of the Ti-6Al-4V alloy Produced by LPBF

The Ti-6Al-4V alloy is a widely established material in the AM industry, especially concerning the LPBF technology. Therefore, a comparison with the novel Ti-6Al-2Sn-4Zr-6Mo alloy appeared mandatory, since both these materials share being α+β titanium alloys. Moreover, since Ti-6Al-2Sn-4Zr-6Mo is mostly used for applications in which a higher strength is needed, the comparative investigation of the mechanical properties is of industrial interest [6,219].

The Ti-6Al-4V standard process parameters (P = 170 W, v = 1250 mm/s and h.d. = 0.1 mm), already mentioned in the previous section, were adopted to build the samples analysed in this investigation. 15x15x15 cubic samples were produced and subsequently characterized in order to investigate the microstructure and hardness of the LPBF produced Ti-6Al-4V, both in the as-built and heat treated conditions. In order to make the comparison accurate, the heat treatment was conducted at 800 °C for 2 h, followed by a low furnace cooling. These parameters were chosen in order to mimic the heat treatment that the Ti-6Al-2Sn-4Zr-6Mo specimens underwent. In this case, a higher temperature (800 °C) than that fixed in the previous study (750 °C) was adopted in order to compensate the difference in terms of $T_\beta$ between the two alloys (≃ 940 °C for Ti-6Al-2Sn-4Zr-6Mo and ≃ 995 °C for Ti-6Al-4V) [223,244].

#### *Microstructure*

The LPBF Ti-6Al-4V samples provided a mainly martensitic microstructure, recognizable by the typical needles arranged in a ±45° fashion as visible in Figure 107. As for the Ti-6Al-2Sn-4Zr-6Mo specimens, these features resulted from the very fast cooling rates intrinsically related to the manufacturing technology used. Moreover, the typical columnar grains parallel to the development direction were also found.

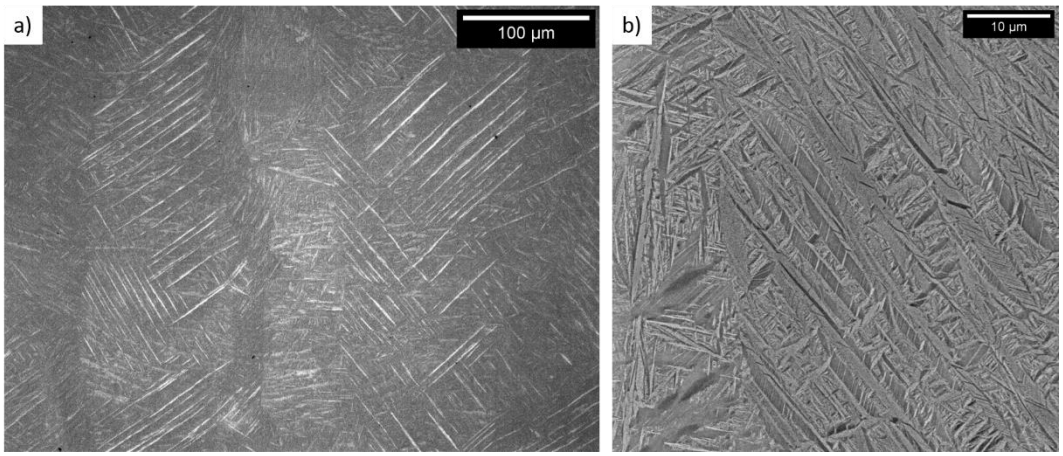


**Figure 107**: Optical (a) and SEM (b) micrographs of the Ti-6Al-4V samples produced by LPBF.

The α' width was chosen as the most suitable feature in order to investigate the size of the martensitic needles, consistently with the other evaluations provided in this thesis. The LPBF produced Ti-6Al-4V specimens were characterized by a significantly fine martensitic microstructure, as highlighted in Figure 108, providing an average value of 0.64 µm.

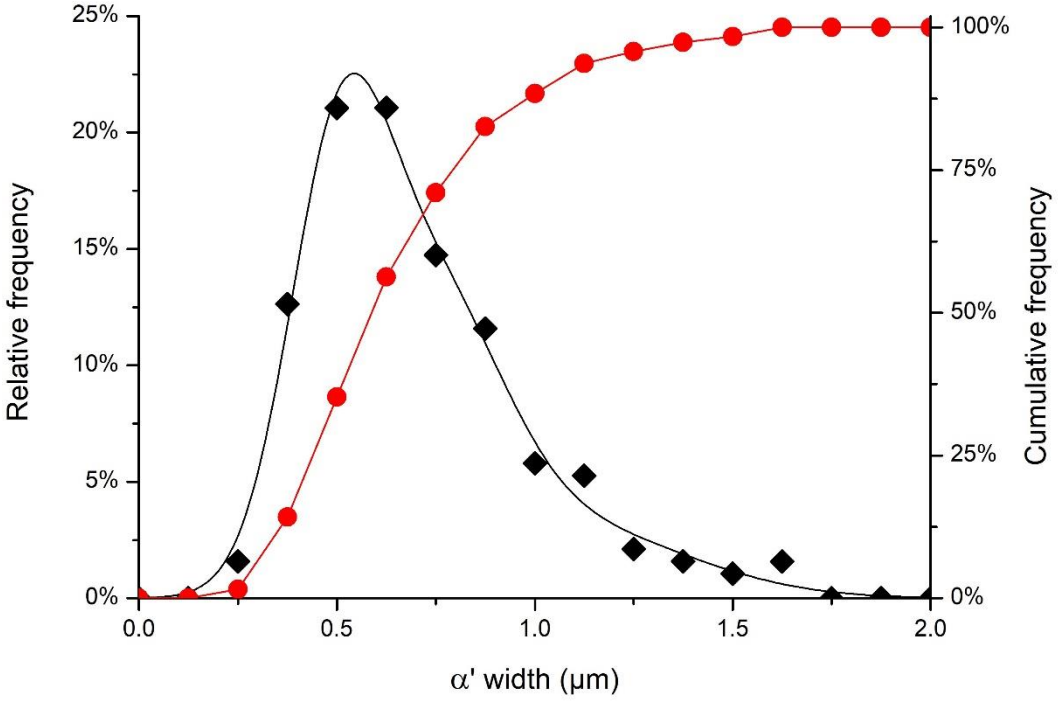


**Figure 108**: α' width evaluated on the LPBF produced Ti-6Al-4V samples.

After the post-processing heat treatment, the microstructure changed drastically, since no significant martensite presence was detected. In fact, α lamellae surrounded by thin β layers were found throughout the whole sample (Figure 109). The way in which the α laths were arranged highlighted the presence of several crystallographic variants. Moreover, large α lamellae arranged in a morphology resembling the as-built martensitic microstructure were found (Figure 109a). These might either be formed directly upon the decomposition of

α' or might be the first laths to form at the transition from a low-order α+β microstructure to a high-order α+β microstructure characterized by colonies. Both options appeared plausible as the α laths were strictly parallel. The analysis of the β fraction present in the heat treated samples, evaluated by image analysis of the SEM micrographs, provided an average value of 5.02% ± 1.31%. This results was in good agreement with the results obtained from Cao et al. [245] working on the same LPBF produced alloy and performing a similar heat treatment.

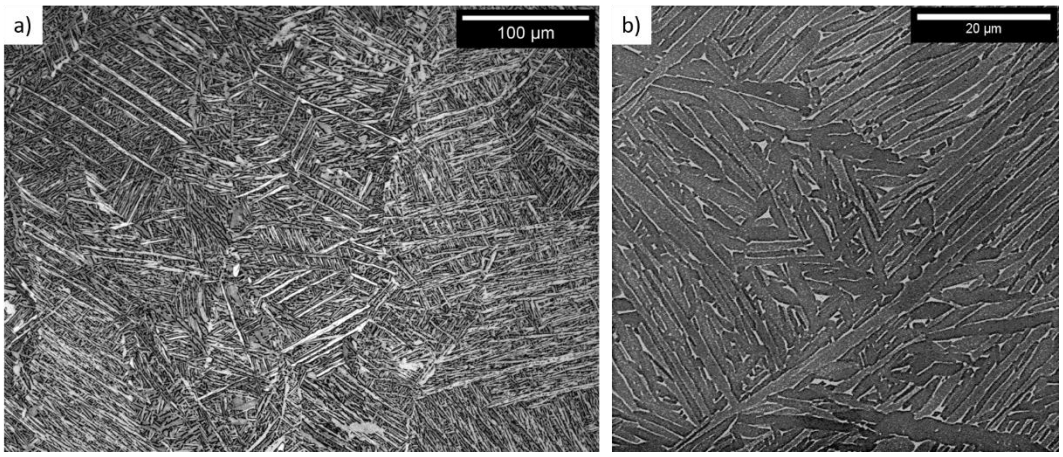


**Figure 109:** Optical (a) and SEM (b) micrographs of the heat treated Ti-6Al-4V samples produced by LPBF.

The evaluation of the width of the α laths was performed on the heat treated samples in order to numerically quantify the microstructure. The outcome of this analysis, reported in Figure 110, provided a α width average value of 1.39 µm.

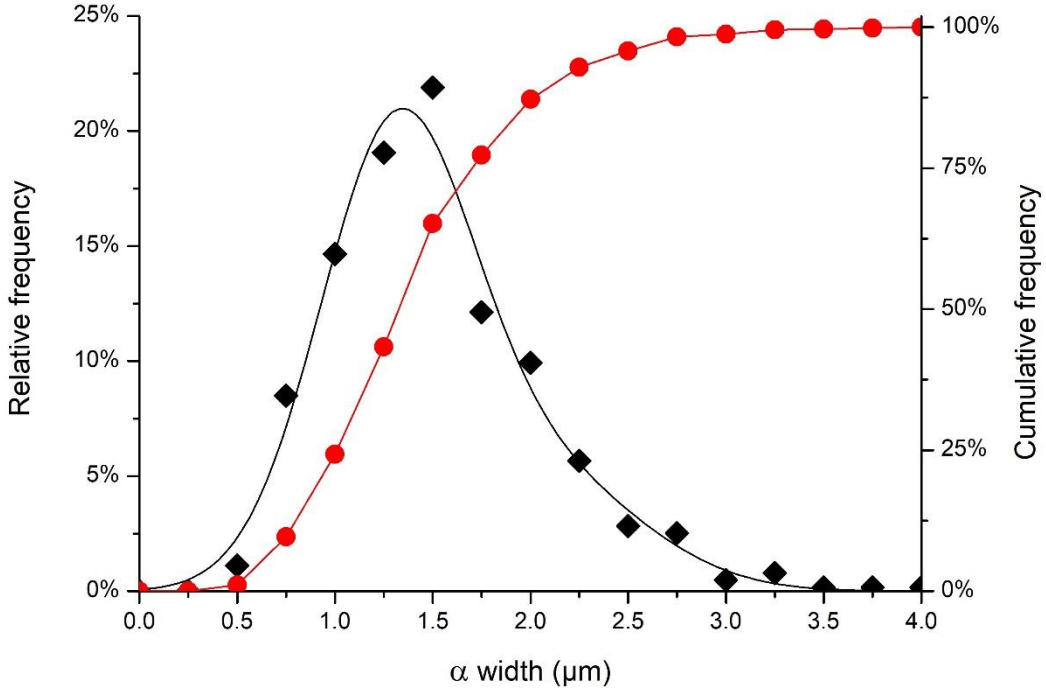


**Figure 110:** α width evaluated on the LPBF produced Ti-6Al-4V samples that underwent a heat treatment.

In order to confirm the assumptions made during the observation of the micrographs and to further characterize the phases analyzed, XRD analyses were

conducted on both the as-built and heat treated samples. The resulting trends (Figure 111) confirmed the presence of an overall martensitic phase composition for the former and the presence of α and β phases for the latter. Moreover, the cell parameters and relative c/a ratio and cell volumes were also estimated, as illustrated in Table 25. The heat treated samples provided a higher c/a ratio, closer to the theoretical value for an ideal hexagonal cell (1.633 Å). This outcome confirmed that the heat treated samples were characterized on average by a cell closer to the thermodynamic equilibrium than the as-built specimens. In fact, the latter were characterized by a more distorted cell, a typical result for martensite in titanium alloys [246].

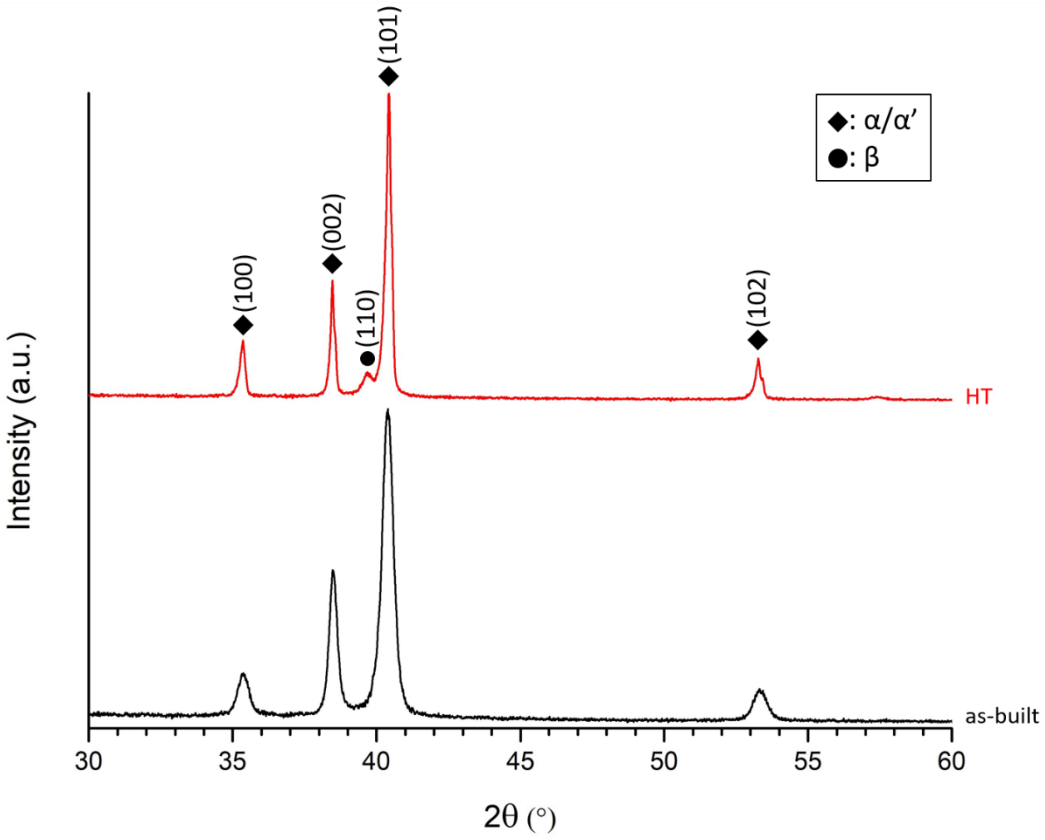


**Figure 111:** XRD patterns relative to the as-built and heat treated (HT) states for the LPBF produced Ti-6Al-4V samples.

**Table 25:** Cell parameters and volume obtained via XRD spectra analysis.

| Condition | Cell parameters (Å) | c/a ratio | Cell Volume (Å$^3$) |
|---|---|---|---|
| **As-built** | a = 2.933 ± 0.017<br>c = 4.677 ± 0.014 | 1.595 ± 0.005 | 34.843 ± 0.597 |
| **Heat treated** | a = 2.929 ± 0.014<br>c = 4.685 ± 0.011 | 1.599 ± 0.004 | 34.815 ± 0.468 |

### *Mechanical Properties*

25 Vickers hardness measurements using a microindenter were performed on samples in the as-built and heat treated conditions. These evaluations provided the average hardness values illustrated in Figure 112.

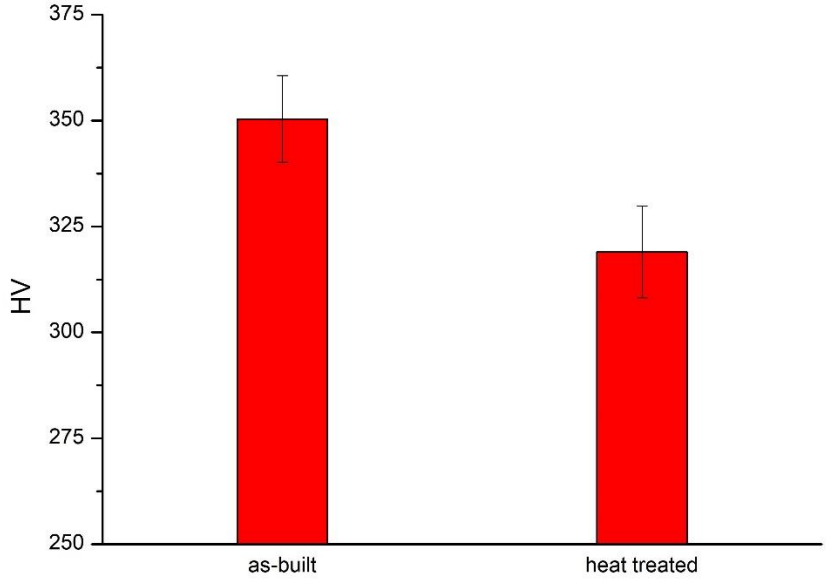


**Figure 112:** Average Vickers microhardness for the as-built and heat treated samples.

The as-built samples provided an average value of 350 ± 10 HV, which resulted significantly higher than 319 ± 11 HV of the heat treated specimens. This difference was probably mainly correlated to the different microstructures involved. In fact, α' martensite has a slight hardening/strengthening effect in titanium alloys, mainly due to its ability to limit the dislocations' motion [91,92].

## 3.4.3. Comparison of the Microstructure and the Mechanical Properties of the Ti-6Al-2Sn-4Zr-6Mo and Ti-6Al-4V alloys Produced by LPBF

The Ti-6Al-4V and Ti-6Al-2Sn-4Zr-6Mo alloys find usage in common industrial fields, such as automotive and aerospace, which share a great potential for AM applications, as highlighted before. Moreover, the Ti-6Al-4V alloy is defined as the "workhorse" titanium-based material in multiple industrial sectors due to its predominance [7,179]. In contrast, the Ti-6Al-2Sn-4Zr-6Mo alloy is seldom adopted, with respect to Ti-6Al-4V, as this material is often chosen for niche applications, in which higher strength values are needed (e.g. race car engines' parts), for example. Therefore, the appeal of this alloy often comes from a superior resistance. Since the LPBF technology was chosen and optimized in order to process this material for the first time, a comparison with the Ti-6Al-4V alloy appeared natural. In fact, AM technologies can achieve microstructures unobtainable via other techniques, which result in greatly differing combinations

of mechanical properties. For instance, AM processed Ti-6Al-4V was proved to be characterized by overall better tensile properties with respect to the same alloy manufactured via conventional manufacturing technologies [59,93]. Therefore, a comparison between the LPBF processed Ti-6Al-2Sn-4Zr-6Mo and Ti-6Al-4V alloys was conducted in order to assess if the former material still provided higher tensile strength values than the latter. The assessment was conducted on the samples built using the same LPBF machine (EOS M270 Xtended machine), both in the as-built and heat treated conditions. The latter comparison appeared acceptable even if the temperature chosen for the heat treatment differed by 50 °C, which is roughly the difference between the $T_\beta$ of the two alloys.

## *Microstructure*

Both the Ti-6Al-4V and Ti-6Al-2Sn-4Zr-6Mo alloys provided an extensively martensitic microstructures in the as-built state, characterized by columnar prior-β grains of α'/α" needles (Figure 113a,c). The observation of the micrographs highlighted the presence of different phases and microstructural features' arrangements after the post-processing heat treatments. In fact, both the alloys were characterized by a α and β phases (Figure 113b,d). The α laths were arranged in a complex fashion in both the materials and the resulting microstructures were neither strictly Widmanstätten nor characterized by big colonies or parallel lamellae. These microstructural features were found in both the types of samples, even if they were observed only locally in certain points throughout the whole cross-sections. Therefore, the overall microstructures were considered as an intermediate step between the basket-weave/colonies transition. The β phase fraction appeared markedly lower in the post processed Ti-6Al-4V alloy, which was characterized by a mean value of 5.02% ± 1.31%, with respect to 27.6% ± 4.5% and 25.8% ± 3.2% of heat treated sets A and B, used to produce the Ti-6Al-2Sn-4Zr-6Mo alloy, respectively. This marked difference was mainly due to the higher $SI_\beta$ of the latter material. In fact, the Ti-6Al-2Sn-4Zr-6Mo alloy can retain a significantly higher amount of β phase at room temperature in thermodynamic stability conditions.

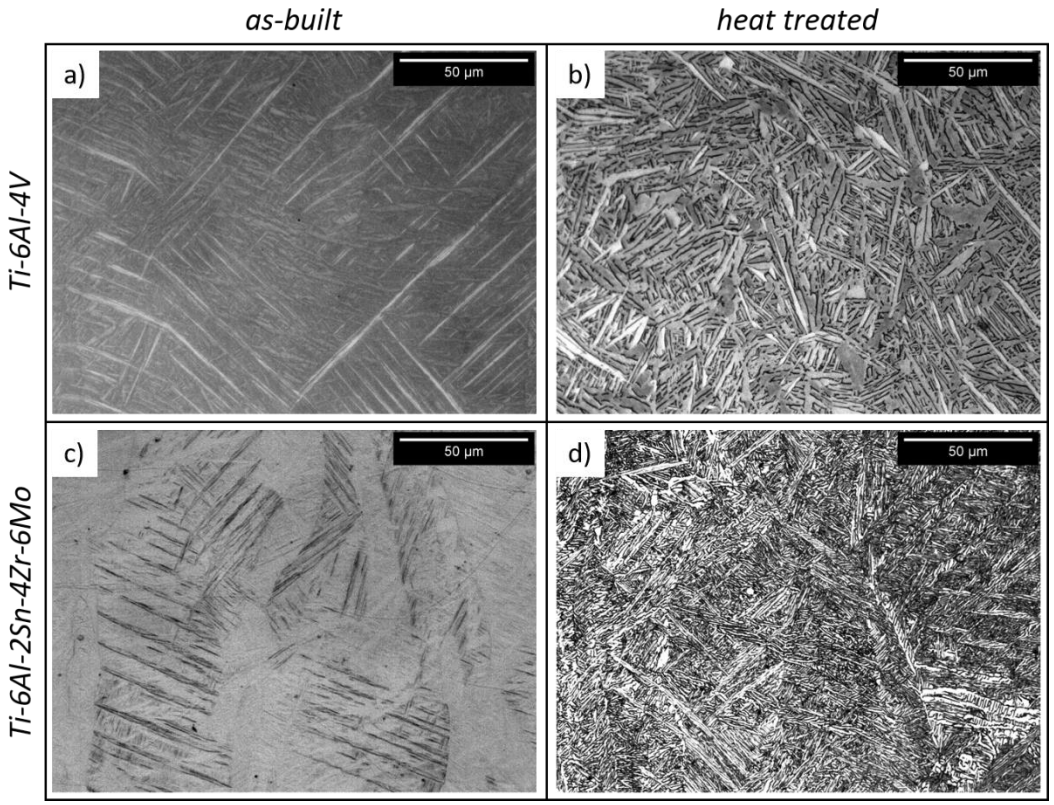


**Figure 113**: Optical micrographs of the Ti-6Al-4V and Ti-6Al-2Sn-4Zr-6Mo alloys in the as-built (a, c) and heat treated (b, d) states respectively.

In terms of microstructural sizes (α/α'/α") quantifications, the data distributions of the width of the needles/laths are provided in Figure 114, along with the mean values in Table 26. In the as-built state, the Ti-6Al-2Sn-4Zr-6Mo alloy provided a finer martensitic microstructure. However, a direct comparison between the two martensitic microphases is not possible, since two different types of martensite were present (α' and α"). These are characterized by different nucleation and growth behaviors, cells and martensite start temperatures. Considering the heat treated state, a largely more significant difference between the two materials was observed. The Ti-6Al-4V alloy was characterized by a significantly coarser microstructure, in terms of width of the α laths. This can be also appreciated from the micrographs in Figure 113. This phenomenon might be related to the different diffusion coefficient in titanium of vanadium and molybdenum, the two most important β-stabilizers of the two alloys considered. In fact, Mo was reported to have a slightly lower diffusivity than V [247]. Semiatin et al. [248] already used the information on the diffusive behavior of different elements in order to investigate and predict the microstructural changes in titanium alloys during an heat treatment. Furthermore, the α' → α+β decomposition is a diffusion-driven transformation during which the β-stabilizers are gradually depleted from the martensite interface [249]. Thus, considering all these phenomena and the higher temperature at which the annealing of the Ti-6Al-4V alloy was held, the decomposition of the martensite and the subsequent α growth appeared comparatively favored in Ti-6Al-4V. Hence, the resulting

microstructure resulted coarser. Nevertheless, this explanation is a hypothesis that must be experimentally confirmed. Moreover, the different types of martensite involved must be taken into account, as this information certainly influences the outcome somehow. Unfortunately, being α' and α" characterized by a hexagonal and orthorhombic lattice respectively, a comparative XRD analysis in order to investigate which type of martensite was more prone to decompose appeared impossible. This resulted from the related lattice parameters (c/a ratio and degree of orthorhombicity) not being directly comparable.

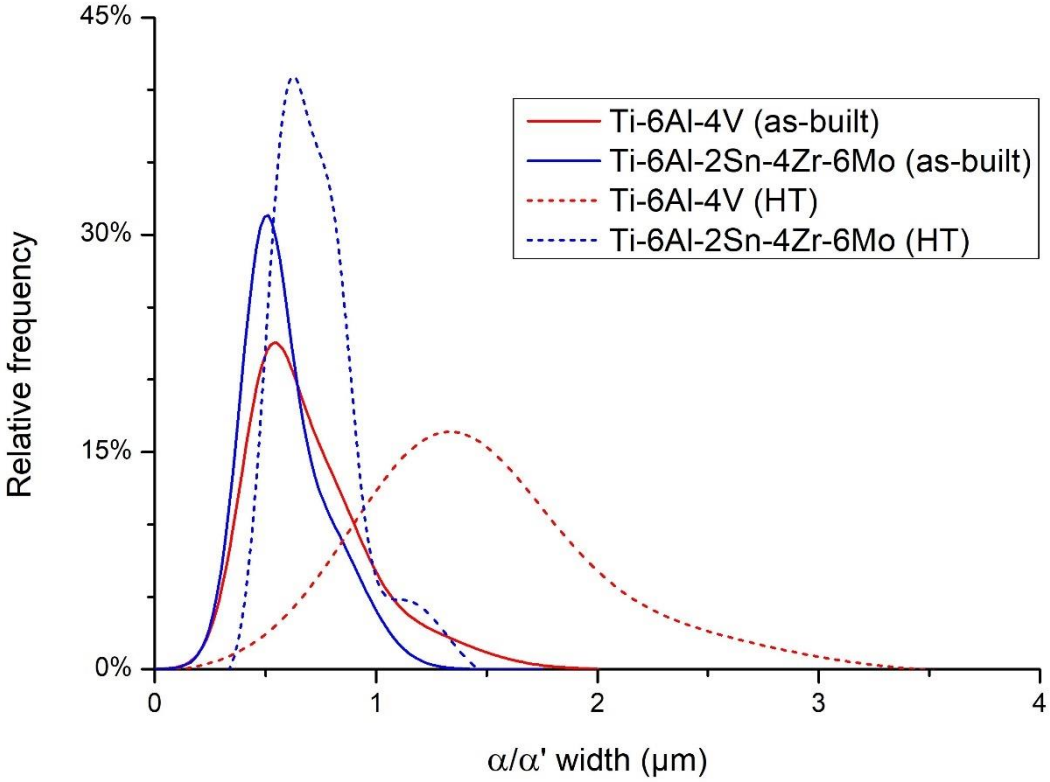


**Figure 114**: α/α'/α" widths distribution curves of the LPBF processed Ti-6Al-4V and Ti-6Al-2Sn-4Zr-6Mo alloys, both as-built and heat treated (HT). Only the process parameters set A is provided for Ti-6Al-2Sn-4Zr-6Mo, since the differences between set A and B appeared marginal in comparison.

**Table 26**: Mean α/α'/α" widths values. Only the process parameters set A is provided for Ti-6Al-2Sn-4Zr-6Mo, since the differences between set A and B appeared marginal in comparison.

| Material | Condition | Mean α/α'/α" Width (μm) |
|---|---|---|
| **Ti-6Al-4V** | As-built | 0.64 |
| | HT | 1.39 |
| **Ti-6Al-2Sn-4Zr-6Mo** | As-built | 0.54 |
| | HT | 0.65 |

## *Mechanical Properties*

The mean average microhardness of the Ti-6Al-4V and Ti-6Al-2Sn-4Zr-6Mo alloys were compared both in the as-built and heat treated state, using the data

obtained in the previous sections of this chapter. Moreover, in order to provide an increased reliability to the comparison, data from several sources available in literature, related to the Ti-6Al-4V alloy, were also considered in this assessment [95,229,250–254]. This was possible as the Ti-6Al-4V alloy is a well-established material in the LPBF industry and several works on the subject are available. The outcome of this evaluations is illustrated in Figure 115.

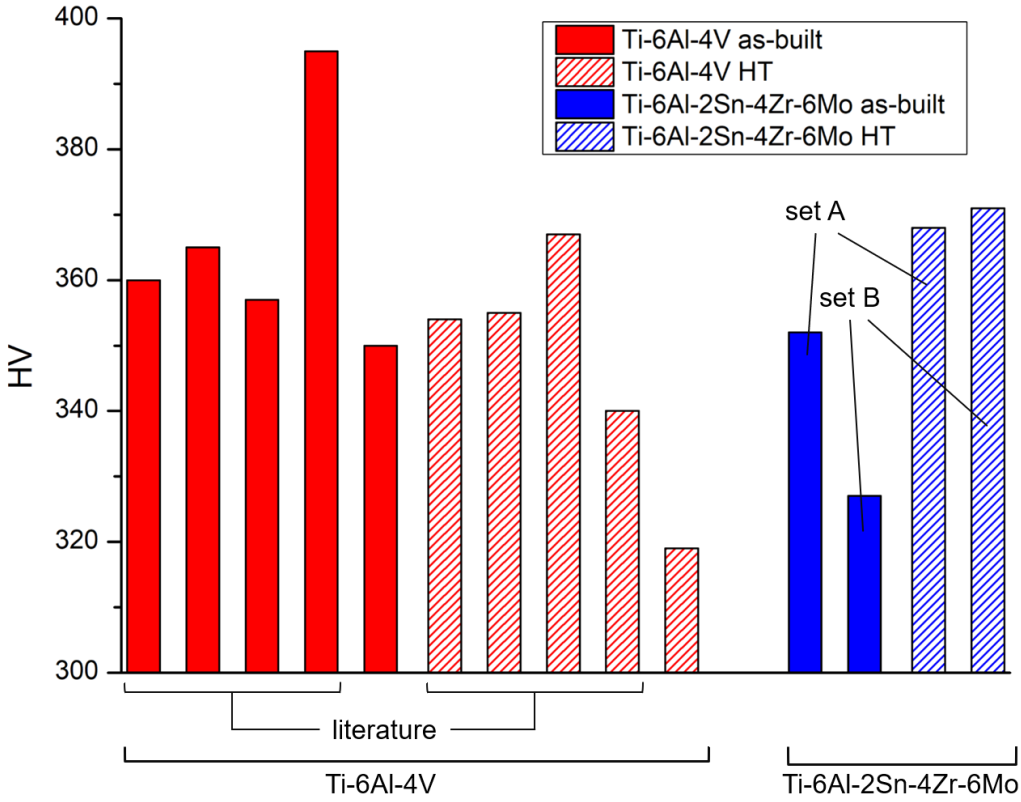


**Figure 115**: Vickers microhardness of the Ti-6Al-4V and Ti-6Al-2Sn-4Zr-6Mo alloys, both in the as-built and heat treated (HT) state. The self-obtained data are compared with several sources available in literature [95,229,250–254]

Concerning the Ti-6Al-4V alloy, the slightly detrimental effect of the heat treatment in terms of hardness was confirmed by the other data found in literature. However, the experimental results appeared quite lower in comparison. In fact, hardness values ranging from 357 to 395 HV were reported in literature for the as-built Ti-6Al-4V samples, whilst the experimental value obtained by the author was 350 HV. However, the comparison with the other works appeared more critical considering the post-processed samples. According to literature, the heat treated (800 °C, 2 h) Ti-6Al-4V samples were characterized by hardness values ranging from 340 up to 367 HV, consistently higher than 319 HV, value experimentally obtained by the author in this study. Such a significant difference might be related to multiple factors, for instance the different LPBF systems or process parameters used or even the furnaces adopted for the heat treatments. The latter is particularly important, because different systems can significantly affect the final microstructure of the material, even if the same heat treatment time and temperatures are set. For example, a furnace big in size can require a markedly

higher time to cool than a smaller one, thus influencing the cooling rate that the material undergoes. This phenomenon must be taken into consideration as all the samples were let cool inside the furnaces at the end of the heat treatments.

The as-built Ti-6Al-2Sn-4Zr-6Mo, produced with the highest productivity, provided lower hardness values then the as-built Ti-6Al-4V. On the other hand, if the most performing set of parameters is considered, a mean hardness value of 352 HV was obtained, appearing comparable with the results related to Ti-6Al-4V samples. Oppositely, after the heat treatment at 750 °C, hardness rose significantly to 368-371 HV allowing the Ti-6Al-2Sn-4Zr-6Mo alloy to assess to hardness values higher than that of Ti-6Al-4V, even in the as-built state, for most of the data found. This might be caused by the very fine α+β microstructure obtained during the heat treatment (Figure 114).

A similar comparative analysis with the data available in other works was conducted in order to study the tensile properties of the two alloys. In this case, since the data relative to the LPBF produced Ti-6Al-4V alloy are abundant, the experimental values obtained for the Ti-6Al-2Sn-4Zr-6Mo alloy were merely compared with the numbers found in literature [89,90,251,255,96,132,137–141,245], as provided in Figure 116, and no self-assessment of the tensile properties was conducted.

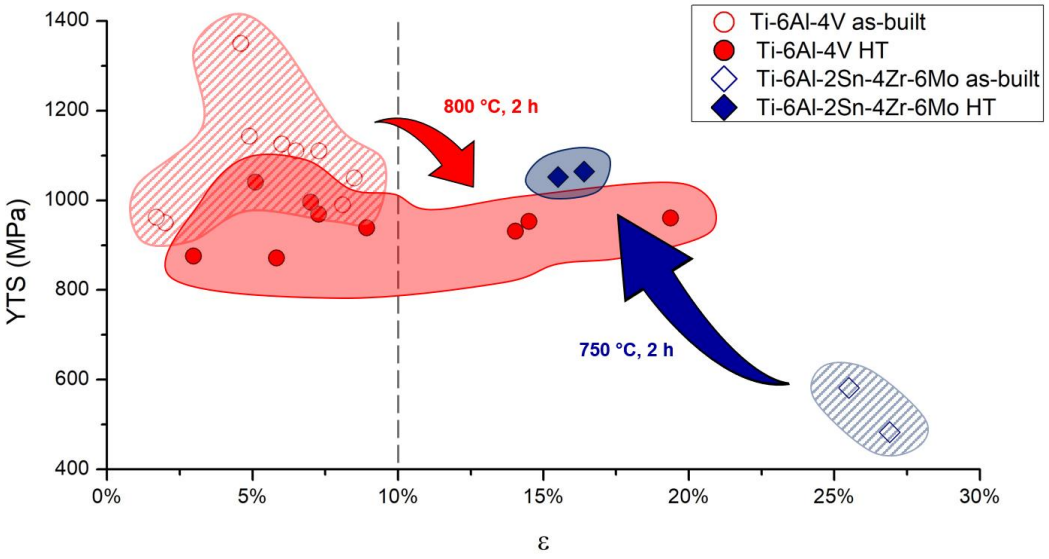


**Figure 116**: Comparison of the YTS and ε of the Ti-6Al-2Sn-4Zr-6Mo and Ti-6Al-4V alloys in the as-built and heat treated conditions. The dashed line represents the ductility minimum threshold as per ASTM-F2924. The data relative to the Ti-6Al-4V alloy were taken from several literature both for the as-built [89,90,96,132,137–141] and heat treated [141,245,251,255] conditions.

The Ti-6Al-4V alloy appeared characterized by markedly high strength values (from 962 to 1350 MPa) in the as-printed state, mainly due to the strengthening effect given by the α' needles ability to hinder dislocation motion. However, ductility appeared significantly low and no evidence of samples compliant with ASTM-F2924 (ε ≥ 10%) were found in this condition. The heat treatment was assessed to cause a decrease in YTS (871-1040 MPa) coupled with an average rise in ductility (best case at 19%). Instead, the Ti-6Al-2Sn-4Zr-6Mo alloy was

characterized by extremely low YTS values (<< 700 MPa) in the as-built condition, but its ductility (> 25%) was significantly high for a titanium alloy, mainly due to the effect of the α" martensite. After the post-processing heat treatment, ε decreased at values still > 15% and the minimum YTS evaluated was 1052 MPa. Therefore, the Ti-6Al-2Sn-4Zr-6Mo alloy provided unmatched YTS when compared with Ti-6Al-4V. Moreover, the closest values for the Ti-6Al-2Sn-4Zr-6Mo alloy were obtained for Ti-6Al-4V samples reported to have a rather low ductility (< 10%). If only the samples compliant with ASTM-F2924 were considered, the most promising YTS value related to the Ti-6Al-4V would have been 960 MPa. Hence, after the considered sub-β heat treatment, the Ti-6Al-2Sn-4Zr-6Mo alloy provided combinations of strength and ductility unreachable, by similar means, by the well-established workhorse Ti-6Al-4V alloy.

## *Conclusions*

The main goal of this comparative evaluation was to assess whether the mechanical properties, in particular strength and elongation, of the LPBF produced Ti-6Al-2Sn-4Zr-6Mo alloy, were superior to the ones of the Ti-6Al-4V alloy or not. This assessment is industrially relevant as the former material is usually involved in some specific applications in the race cars and aerospace industries, in which it is adopted mainly due to its higher mechanical resistance. However, since no data were available on the LPBF produced material in literature, a comparison of the mechanical properties between Ti-6Al-2Sn-4Zr-6Mo and Ti-6Al-4V produced by LPBF was also lacking. The main outcomes of this comparison can be summarized as follows:

- The microstructure of both materials in the as-built state is mostly formed by martensitic needles, which differ in terms of crystal structures, being α' (hexagonal) present in Ti-6Al-4V and α" (orthorhombic) in Ti-6Al-2Sn-4Zr-6Mo. Both microstructures were quite fine and characterized by needles markedly thinner than 1 μm on average.
- The heat treated samples of both alloys were characterized by lamellar α+β microstructures. The β phase content was markedly higher in Ti-6Al-2Sn-4Zr-6Mo, consistently with its higher $SI_{\beta}$. This alloy also provided significantly thinner α laths.
- The hardness and strength values of the Ti-6Al-2Sn-4Zr-6Mo alloy were definitely lower than the Ti-6Al-4V ones in the as-built state. However, after the post-processing heat treatment, the former material appeared more performing, grating unmatched combinations of YTS and ε.
- Since its tensile mechanical properties were superior than the ones of the Ti-6Al-4V alloy, the Ti-6Al-2Sn-4Zr-6Mo alloy proved to be a

viable alternative for industrial applications in which LPBF manufacturing technology is adopted.

# Chapter 4

# Conclusions

In this work, the microstructural and mechanical properties of different titanium alloys produced using several AM technologies were investigated and correlated. The studies presented in the first part of this thesis focused on understanding the main reasons why a certain thermal history, result of the manufacturing processes (DED, EBM) and/or heat treatments, resulted in the formation of certain phases, their morphology and their related impact on hardness and tensile properties. In the second part, the Ti-6Al-2Sn-4Zr-6Mo alloy was successfully manufactured for the first time using a LPBF system. Furthermore, its mechanical properties were assessed in comparison to the Ti-6Al-4V alloy. The aim of this analysis was to understand whether the superior performance of the Ti-6Al-2Sn-4Zr-6Mo alloy, in terms of mechanical resistance, would persist when switching from a conventional manufacturing process to LPBF.

The results were reported in the following order: the analysis of the DED produced Ti-6Al-4V, the analysis of the EBM produced Ti-6Al-4V, the comparison of the heat treated DED and EBM produced samples, the analysis of LPBF produced Ti-6Al-2Sn-4Zr-6Mo and its relative comparison with LPBF produced Ti-6Al-4V in terms of microstructures and mechanical properties. Therefore, the main results obtained are summarised accordingly.

### *DED Produced Ti-6Al-4V*

- The single scans approach proved to be a useful, cost and time efficient tool in order to obtain the suitable process window to process the Ti-6Al-4V alloy by DED. Through this methodology, the laser power values that provided insufficient melting of the powder (P = 100 W) and the combination of parameters that resulted in the impossibility to build fully dense 3D components (G/D > 1) were excluded. Moreover, a further optimization of the process was possible by evaluating the powder efficiency, which appeared maximized using high laser power values associated with intermediate-high scanning speeds.

- The comparative analysis of the samples built with and without switching on the additional shielding gas flow allowed to determine the importance of this system. In fact, when the additional Ar flow lacked, the resulting samples were characterized by hybrid α+β/α' microstructures. These were related to oxygen/nitrogen enrichment, which leads to cracks when manufacturing 3D components.
- A correlation between the process parameters and the microstructures was found. In particular, coarser martensitic microstructures were associated with lower LED values.
- An overall best combination was not found. In fact, the deposition process appeared quite stable and flexible for this material as several process parameters resulted acceptable. This results in the possibility to tailor the process according to the properties that needs to be emphasized (e.g. efficiency, ductility, etc.).
- The process environment (glovebox-like, additional shielding gas in open environment) had a great impact on the microstructure and mechanical properties of the samples analyzed. In particular, a sealed environment filled with an inert gas proved to be the only alternative to obtain crack-free large components. The use of the additional shielding gas resulted acceptable only for small components/reparations.
- The post-processing heat treatments influenced significantly the microstructures of the DED produced Ti-6Al-4V samples. Since super-β transus annealing heat treatments were conducted, all the samples provided a shift from a columnar to an equiaxed grain morphology. Notwithstanding that, the intrinsic anisotropy in grain width (increasing along Z) caused by the DED process influenced the post-treatment grains even if a complete recrystallization of the microstructures occurred. This was caused by the columnar grain boundaries, more concentrated in the bottom region of the sample, favoring the nucleation of new grains at $T > T_{\beta}$. Hence, a sort of "grain memory" effect was found.
- Allowing the samples to slowly cool down to room temperature after the annealing treatment did not prove to be a viable post-processing operation, as the resulting mechanical properties were rather low.

## *EBM of Ti-6Al-4V*

- The as-printed EBM samples were characterized by a mostly lamellar α+β microstructure. The α laths were found in different morphologies, depending on the area of the specimen considered. Other microstructural features were found, such as small lamellar colonies, $\alpha_{GB}$ and α'.
- Similarly to the DED produced samples, the super-β transus heat treatments provided an equiaxed grain morphology and a complete recrystallization of the microstructure. The phases present near room temperature were also mostly dependent on the cooling rate applied.

- Water quenching the samples at the end of the annealing heat treatment resulted the only viable alternative to improve the mechanical performances (YTS, UTS) on the samples analyzed, with respect to the as-built condition. However, a post-annealing ageing treatment was mandatory to recover most of the ductility loss caused by the martensite insurgence as a consequence of the water quench.
- In general, the ageing treatment improved the mechanical properties of all the heat treated samples, independently from the cooling rate applied.

### *Comparison of the Heat Treated DED and EBM Produced Samples*

- The application of the same recrystallization heat treatment allowed to obtain the same type of microstructure in DED and EBM produced samples, independently from the initial microstructure.
- The EBM produced samples were characterized by finer grains in the as-built state. This peculiarity was maintained in post-heat treatment samples. Hence, a "grain memory effect" was assessed also in this case.
- Overall, the mechanical properties (YTS, UTS, ε) of the EBM produced samples resulted higher than the DED produced ones, even if a complete recrystallization occurred and these were expected to be comparable.

### *LPBF of Ti-6Al-2Sn-4Zr-6Mo and Relative Comparison with Ti-6Al-4V*

- The overall most performing process parameters were determined using porosity minimization as a criterion. Among the combinations considered in this study, the ones providing the highest VED values appeared as the most performing for the reduction of residual pores in the Ti-6al-2Sn-4Zr-6Mo alloy. Moreover, the higher the VED the more the pores induced appeared spherical.
- The as-built microstructure was characterized by fine α" martensite needles. These were completely decomposed during a sub-β annealing at 750 °C for 2 h.
- The martensite present in the Ti-6Al-2Sn-4Zr-6Mo alloy had a significantly softening effect. Thus, the as-built samples provided low hardness and strength values coupled with an outstanding ductility.
- The heat treatments caused a significant rise in hardness and tensile properties. Plasticity was reduced, however it remained significantly high (> 15%). The mechanical properties resulted comparable/better when compared to those of materials produced by conventional processing. Therefore, this technology appeared very promising in order to achieve an optimal combination of strength and ductility.
- The mechanical properties of the LPBF produced Ti-6Al-4V alloy greatly differed from the Ti-6Al-2Sn-4Zr-6Mo ones, mostly due to the opposite

effects that α' and α" provided. In fact, the former appeared brittle, strong and hard, whilst the latter was ductile and soft in comparison.

- The heat treatments implied in both samples the formation of a lamellar α+β microstructure. The Ti-6Al-4V alloy was characterized by significantly larger α laths and a lower β phase content with respect to the Ti-6Al-2Sn-4Zr-6Mo alloy.
- After the heat treatment, the Ti-6Al-2Sn-4Zr-6Mo alloy provided unmatched combinations of strength and ductility over the Ti-6Al-4V one. Thus, the Ti-6Al-2Sn-4Zr-6Mo alloy can be considered to be a higher-strength substitute to Ti-6Al-4V, even if switching from a conventional to an innovative (LPBF) manufacturing technology.

# References


[1] A.A. Yaroshevsky, Abundances of chemical elements in the Earth's crust, Geochemistry Int. 44 (2006) 48–55. doi:10.1134/S001670290601006X.

[2] A.P. Vinogradov, Average contents of chemical elements in the principal types of igneous rocks of the earth's crust, Geochemistry. 7 (1962) 641–664.

[3] A.B. Ronov, A.A. Yaroshevskii, A.A. Migdisov, Chemical Structure of the Earth's Crust and Geochemical Balance of Major Elements, (1990).

[4] C. Leyens, M. Peters, Titanium and titanium alloys: fundamentals and applications, 2003.

[5] A. Russell, K.L. Lee, Structure-property relations in nonferrous metals, John Wiley & Sons, 2005.

[6] G. Lütjering, J.C. Williams, Titanium Book, 2007. doi:10.10007/978-3-540-71398-2.

[7] F.H. Froes, Titanium: Physical Metallurgy Processing and Application, 2015.

[8] Z. Jia, W. Zeng, Y. Zhang, C. Shi, B. Quan, J. Wu, The color changes and tensile properties of oxidized Ti-6A1-2Mo-1.5Cr-2Zr-2Sn-2Nb alloy, J. Alloys Compd. 640 (2015) 488–496. doi:10.1016/j.jallcom.2015.03.227.

[9] H.R. Ogden, R.I. Jaffee, The effects of carbon, oxygen and nitrogen on the mechanical properties of titanium and titanium alloys, 1955.

[10] B. Dutta, F.H. Froes, The Additive Manufacturing (AM) of titanium alloys, in: Elsevier (Ed.), Titan. Powder Metall., 2015: pp. 447–468.

[11] C. Veiga, J.P. Davim, A.J.R. Loureiro, Proprties and applications of titanium alloys, Rev. Adv. Mater. Sci. 32 (2012) s. 133-148.

[12] R.R. Boyer, An overview on the use of titanium in the aerospace industry, Mater. Sci. Eng. A. 213 (1996) 103–114.

[13] J.C. Williams, Titanium alloys: processing, properties, and applications, Encycl. Aerosp. Eng. (2010).

[14] M. Balazic, J. Kopac, M.J. Jackson, W. Ahmed, Titanium and titanium alloy applications in medicine, Int. J. Nano Biomater. 1 (2007) 3–34.

[15] C.N. Elias, J.H.C. Lima, R. Valiev, M.A. Meyers, Biomedical applications of titanium and its alloys, Jom. 60 (2008) 46–49.

[16] T. Majumdar, N. Eisenstein, J.E. Frith, S.C. Cox, N. Birbilis, Additive Manufacturing of Titanium Alloys for Orthopedic Applications: A Materials Science Viewpoint, Adv. Eng. Mater. 20 (2018). doi:10.1002/adem.201800172.

[17] J.C. Williams, A.F. Belov, Titanium and Titanium Alloys: Scientific and Technological Aspects., 1982.

[18] R. Pederson, The microstructures of Ti-6Al-4V and Ti-6Al-2Sn-4Zr-6Mo and their relationship to processing and properties, 2004. doi:ISSN 1402-1544 / ISRN LTU-DT--04/19--SE / NR 2004:19.
[19] A.K. Dutt, B. Gwalani, V. Tungala, M. Carl, R.S. Mishra, S.A. Tamirisakandala, M.L. Young, K.C. Cho, R.E. Brennan, A novel nano-particle strengthened titanium alloy with exceptional specific strength, Sci. Rep. 9 (2019) 1–9. doi:10.1038/s41598-019-48139-8.
[20] R. Boyer, G. Welsch, E.W. Collings, Materials properties handbook : titanium alloys, 1994.
[21] R.P. Kolli, A. Devaraj, A review of metastable beta titanium alloys, Metals (Basel). 8 (2018) 1–41. doi:10.3390/met8070506.
[22] P.J. Bania, Beta titanium alloys and their role in the titanium industry, Jom. 46 (1994) 16–19.
[23] M.J. Donachie, Titanium: a technical guide, ASM international, 2000.
[24] J. Yang, H. Yu, J. Yin, M. Gao, Z. Wang, X. Zeng, Formation and control of martensite in Ti-6Al-4V alloy produced by selective laser melting, Mater. Des. 108 (2016) 308–318. doi:https://doi.org/10.1016/j.matdes.2016.06.117.
[25] E. Salsi, M. Chiumenti, M. Cervera, Modeling of microstructure evolution of Ti6Al4V for additive manufacturing, Metals (Basel). 8 (2018). doi:10.3390/met8080633.
[26] A.K. Swarnakar, O. Van der Biest, B. Baufeld, Thermal expansion and lattice parameters of shaped metal deposited Ti–6Al–4V, J. Alloys Compd. 509 (2011) 2723–2728.
[27] J.C. Chesnutt, C.G. Rhodes, J.C. Williams, Relationship between mechanical properties, microstructure, and fracture topography in α+ β titanium alloys, in: Fractography—Microscopic Crack. Process., ASTM International, 1976.
[28] A. Gisario, M. Kazarian, F. Martina, M. Mehrpouya, Metal additive manufacturing in the commercial aviation industry: A review, J. Manuf. Syst. 53 (2019) 124–149. doi:10.1016/j.jmsy.2019.08.005.
[29] W.E. Frazier, Metal additive manufacturing: A review, J. Mater. Eng. Perform. 23 (2014) 1917–1928. doi:10.1007/s11665-014-0958-z.
[30] M. Yakout, M.A. Elbestawi, S.C. Veldhuis, A review of metal additive manufacturing technologies, Solid State Phenom. 278 SSP (2018) 1–14. doi:10.4028/www.scientific.net/SSP.278.1.
[31] N.R. Council, Accelerating technology transition: bridging the valley of death for materials and processes in defense systems, National Academies Press, 2004.
[32] T.D. Ngo, A. Kashani, G. Imbalzano, K.T.Q. Nguyen, D. Hui, Additive manufacturing (3D printing): A review of materials, methods, applications and challenges, Compos. Part B Eng. 143 (2018) 172–196. doi:10.1016/j.compositesb.2018.02.012.
[33] J.E. Barnes, W. Peter, C.A. Blue, Evaluation of low cost titanium alloy products, in: Mater. Sci. Forum, Trans Tech Publ, 2009: pp. 165–168.
[34] C. Beyer, Strategic implications of current trends in additive manufacturing, J. Manuf. Sci. Eng. 136 (2014).
[35] H. Shipley, D. McDonnell, M. Culleton, R. Coull, R. Lupoi, G. O'Donnell, D. Trimble, Optimisation of process parameters to address fundamental challenges during selective laser melting of Ti-6Al-4V: A review, Int. J.

Mach. Tools Manuf. 128 (2018) 1–20. doi:10.1016/j.ijmachtools.2018.01.003.
[36] J. Gardan, Additive manufacturing technologies: State of the art and trends, Int. J. Prod. Res. 54 (2016) 3118–3132. doi:10.1080/00207543.2015.1115909.
[37] M. Zenou, L. Grainger, Additive manufacturing of metallic materials, in: Addit. Manuf., Elsevier, 2018: pp. 53–103.
[38] M. Elahinia, N. Shayesteh Moghaddam, M. Taheri Andani, A. Amerinatanzi, B.A. Bimber, R.F. Hamilton, Fabrication of NiTi through additive manufacturing: A review, Prog. Mater. Sci. 83 (2016) 630–663. doi:10.1016/j.pmatsci.2016.08.001.
[39] R. Narayan, Rapid Prototyping of Biomaterials: Techniques in Additive Manufacturing, Woodhead Publishing, 2019.
[40] M. Koike, P. Greer, K. Owen, G. Lilly, L.E. Murr, S.M. Gaytan, E. Martinez, T. Okabe, Evaluation of titanium alloys fabricated using rapid prototyping technologies-electron beam melting and laser beam melting, Materials (Basel). 4 (2011) 1776–1792. doi:10.3390/ma4101776.
[41] S. Liu, Y.C. Shin, Additive manufacturing of Ti6Al4V alloy: A review, Mater. Des. 164 (2018) 8–12. doi:10.1016/j.matdes.2018.107552.
[42] M. Fousová, D. Vojtěch, K. Doubrava, M. Daniel, C.-F. Lin, Influence of inherent surface and internal defects on mechanical properties of additively manufactured Ti6Al4V alloy: Comparison between selective laser melting and electron beam melting, Materials (Basel). 11 (2018) 537.
[43] H.P. Tang, M. Qian, N. Liu, X.Z. Zhang, G.Y. Yang, J. Wang, Effect of powder reuse times on additive manufacturing of Ti-6Al-4V by selective electron beam melting, Jom. 67 (2015) 555–563. doi:10.1007/s11837-015-1300-4.
[44] J.M. Wilson, C. Piya, Y.C. Shin, F. Zhao, K. Ramani, Remanufacturing of turbine blades by laser direct deposition with its energy and environmental impact analysis, J. Clean. Prod. 80 (2014) 170–178. doi:10.1016/j.jclepro.2014.05.084.
[45] N. Li, S. Huang, G. Zhang, R. Qin, W. Liu, H. Xiong, G. Shi, J. Blackburn, Progress in additive manufacturing on new materials: A review, J. Mater. Sci. Technol. 35 (2019) 242–269. doi:10.1016/j.jmst.2018.09.002.
[46] G. Mathers, The welding of aluminium and its alloys, Woodhead publishing, 2002.
[47] K. Schmidtke, F. Palm, A. Hawkins, C. Emmelmann, Process and mechanical properties: applicability of a scandium modified Al-alloy for laser additive manufacturing, Phys. Procedia. 12 (2011) 369–374.
[48] H. Schwab, F. Palm, U. Kühn, J. Eckert, Microstructure and mechanical properties of the near-beta titanium alloy Ti-5553 processed by selective laser melting, Mater. Des. 105 (2016) 75–80.
[49] T. Marcu, M. Todea, I. Gligor, P. Berce, C. Popa, Effect of surface conditioning on the flowability of Ti6Al7Nb powder for selective laser melting applications, Appl. Surf. Sci. 258 (2012) 3276–3282.
[50] L.C. Zhang, D. Klemm, J. Eckert, Y.L. Hao, T.B. Sercombe, Manufacture by selective laser melting and mechanical behavior of a biomedical Ti–24Nb–4Zr–8Sn alloy, Scr. Mater. 65 (2011) 21–24.
[51] M. Speirs, J. Van Humbeeck, J. Schrooten, J. Luyten, J.-P. Kruth, The effect of pore geometry on the mechanical properties of selective laser

melted Ti-13Nb-13Zr scaffolds, Procedia Cirp. 5 (2013) 79–82.
[52] R.W. Bush, C.A. Brice, Elevated temperature characterization of electron beam freeform fabricated Ti-6Al-4V and dispersion strengthened Ti-8Al-1Er, Mater. Sci. Eng. A. 554 (2012) 12–21. doi:10.1016/j.msea.2012.05.083.
[53] S.M. Kelly, S.L. Kampe, Microstructural evolution in laser-deposited multilayer Ti-6Al-4V builds: Part II. Thermal Modeling, Metall. Mater. Trans. A Phys. Metall. Mater. Sci. 35 A (2004) 1869–1879. doi:10.1007/s11661-004-0095-7.
[54] S.G. Lambrakos, K.P. Cooper, An algorithm for inverse modeling of layer-by-layer deposition processes, J. Mater. Eng. Perform. 18 (2009) 221–230.
[55] L.E. Murr, E. Martinez, S.M. Gaytan, D.A. Ramirez, B.I. Machado, P.W. Shindo, J.L. Martinez, F. Medina, J. Wooten, D. Ciscel, Microstructural architecture, microstructures, and mechanical properties for a nickel-base superalloy fabricated by electron beam melting, Metall. Mater. Trans. A. 42 (2011) 3491–3508.
[56] J.H. Martin, B.D. Yahata, J.M. Hundley, J.A. Mayer, T.A. Schaedler, T.M. Pollock, 3D printing of high-strength aluminium alloys, Nature. 549 (2017) 365–369.
[57] D. Herzog, V. Seyda, E. Wycisk, C. Emmelmann, Additive manufacturing of metals, Acta Mater. 117 (2016) 371–392. doi:10.1016/j.actamat.2016.07.019.
[58] X. Gong, T. Anderson, K. Chou, Review on powder-based electron beam additive manufacturing Technology, Manuf. Rev. 1 (2014) 1–9. doi:10.1051/mfreview/2014001.
[59] L.C. Zhang, Y. Liu, S. Li, Y. Hao, Additive Manufacturing of Titanium Alloys by Electron Beam Melting: A Review, Adv. Eng. Mater. 20 (2018) 1–16. doi:10.1002/adem.201700842.
[60] X. Tan, Y. Kok, Y.J. Tan, M. Descoins, D. Mangelinck, S.B. Tor, K.F. Leong, C.K. Chua, Graded microstructure and mechanical properties of additive manufactured Ti-6Al-4V via electron beam melting, Acta Mater. 97 (2015) 1–16. doi:10.1016/j.actamat.2015.06.036.
[61] S.S. Al-Bermani, M.L. Blackmore, W. Zhang, I. Todd, The origin of microstructural diversity, texture, and mechanical properties in electron beam melted Ti-6Al-4V, Metall. Mater. Trans. A Phys. Metall. Mater. Sci. 41 (2010) 3422–3434. doi:10.1007/s11661-010-0397-x.
[62] A.H. Chern, P. Nandwana, T. Yuan, M.M. Kirka, R.R. Dehoff, P.K. Liaw, C.E. Duty, A review on the fatigue behavior of Ti-6Al-4V fabricated by electron beam melting additive manufacturing, Int. J. Fatigue. 119 (2019) 173–184. doi:10.1016/j.ijfatigue.2018.09.022.
[63] A.A. Antonysamy, J. Meyer, P.B. Prangnell, Effect of build geometry on the β-grain structure and texture in additive manufacture of Ti6Al4V by selective electron beam melting, Mater. Charact. 84 (2013) 153–168. doi:https://doi.org/10.1016/j.matchar.2013.07.012.
[64] H. Galarraga, D.A. Lados, R.R. Dehoff, M.M. Kirka, P. Nandwana, Effects of heat treatments on microstructure and properties of Ti-6Al-4V ELI alloy fabricated by electron beam melting (EBM), (n.d.).
[65] Y.J. Liu, S.J. Li, H.L. Wang, W.T. Hou, Y.L. Hao, R. Yang, T.B. Sercombe, L.C. Zhang, Microstructure, defects and mechanical behavior of beta-type titanium porous structures manufactured by electron beam

melting and selective laser melting, Acta Mater. 113 (2016) 56–67. doi:https://doi.org/10.1016/j.actamat.2016.04.029.

[66] S. Zhao, S.J. Li, W.T. Hou, Y.L. Hao, R. Yang, R.D.K. Misra, The influence of cell morphology on the compressive fatigue behavior of Ti-6Al-4V meshes fabricated by electron beam melting, J. Mech. Behav. Biomed. Mater. 59 (2016) 251–264. doi:https://doi.org/10.1016/j.jmbbm.2016.01.034.

[67] L.E. Murr, E. V. Esquivel, S.A. Quinones, S.M. Gaytan, M.I. Lopez, E.Y. Martinez, F. Medina, D.H. Hernandez, E. Martinez, J.L. Martinez, S.W. Stafford, D.K. Brown, T. Hoppe, W. Meyers, U. Lindhe, R.B. Wicker, Microstructures and mechanical properties of electron beam-rapid manufactured Ti-6Al-4V biomedical prototypes compared to wrought Ti-6Al-4V, Mater. Charact. 60 (2009) 96–105. doi:10.1016/j.matchar.2008.07.006.

[68] C. de Formanoir, S. Michotte, O. Rigo, L. Germain, S. Godet, Electron beam melted Ti-6Al-4V: Microstructure, texture and mechanical behavior of the as-built and heat-treated material, Mater. Sci. Eng. A. 652 (2016) 105–119. doi:10.1016/j.msea.2015.11.052.

[69] M. Svensson, U. Ackelid, A. Ab, Titanium alloys manufactured with electron beam melting mechanical and chemical properties, in: Proc. Mater. Process. Med. Devices Conf., ASM International, 2010: pp. 189–194.

[70] L. Facchini, E. Magalini, P. Robotti, A. Molinari, Microstructure and mechanical properties of Ti-6Al-4V produced by electron beam melting of pre-alloyed powders, Rapid Prototyp. J. 15 (2009) 171–178. doi:10.1108/13552540910960262.

[71] ASTM F2924-12, Standard Specification for Additive Manufacturing Titanium-6 Aluminum-4 Vanadium with Powder Bed Fusion, ASTM Int. i (2012) 1–9. doi:10.1520/F2924-14.2.

[72] M. Qian, W. Xu, M. Brandt, H.P. Tang, Additive manufacturing and postprocessing of Ti-6Al-4V for superior mechanical properties, MRS Bull. 41 (2016) 775–783. doi:10.1557/mrs.2016.215.

[73] S. Tammas-Williams, H. Zhao, F. Léonard, F. Derguti, I. Todd, P.B. Prangnell, XCT analysis of the influence of melt strategies on defect population in Ti–6Al–4V components manufactured by Selective Electron Beam Melting, Mater. Charact. 102 (2015) 47–61. doi:https://doi.org/10.1016/j.matchar.2015.02.008.

[74] P. Karimi, T. Raza, J. Andersson, L.-E. Svensson, Influence of laser exposure time and point distance on 75-µm-thick layer of selective laser melted Alloy 718, Int. J. Adv. Manuf. Technol. 94 (2018) 2199–2207.

[75] S.M. Gaytan, L.E. Murr, F. Medina, E. Martinez, M.I. Lopez, R.B. Wicker, Advanced metal powder based manufacturing of complex components by electron beam melting, Mater. Technol. 24 (2009) 180–190.

[76] Z. Xu, W. Wen, T. Zhai, Effects of Pore Position in Depth on Stress/Strain Concentration and Fatigue Crack Initiation, Metall. Mater. Trans. A. 43 (2012) 2763–2770. doi:10.1007/s11661-011-0947-x.

[77] V. Semak, A. Matsunawa, The role of recoil pressure in energy balance during laser materials processing, J. Phys. D. Appl. Phys. 30 (1997) 2541.

[78] S.K. Everton, P. Dickens, C. Tuck, B. Dutton, Identification of Sub-Surface Defects in Parts Produced by Additive Manufacturing, Using Laser Generated Ultrasound, Addit. Manuf. 3D Print. Res. Group, Univ.

Nottingham. (2016).
[79] J. Schwerdtfeger, P. Heinl, R.F. Singer, C. Körner, Auxetic cellular structures through selective electron-beam melting, Phys. Status Solidi. 247 (2010) 269–272.
[80] W.J. Sames, F.A. List, S. Pannala, R.R. Dehoff, S.S. Babu, The metallurgy and processing science of metal additive manufacturing, Int. Mater. Rev. 61 (2016) 315–360.
[81] D. Agius, K.I. Kourousis, C. Wallbrink, A review of the as-built SLM Ti-6Al-4V mechanical properties towards achieving fatigue resistant designs, Metals (Basel). 8 (2018). doi:10.3390/met8010075.
[82] D.K. Do, P. Li, The effect of laser energy input on the microstructure, physical and mechanical properties of Ti-6Al-4V alloys by selective laser melting, Virtual Phys. Prototyp. 11 (2016) 41–47. doi:10.1080/17452759.2016.1142215.
[83] J. Han, J. Yang, H. Yu, J. Yin, M. Gao, Z. Wang, X. Zeng, Microstructure and mechanical property of selective laser melted Ti6Al4V dependence on laser energy density, Rapid Prototyp. J. (2017).
[84] M. V. Pantawane, Y.H. Ho, S.S. Joshi, N.B. Dahotre, Computational Assessment of Thermokinetics and Associated Microstructural Evolution in Laser Powder Bed Fusion Manufacturing of Ti6Al4V Alloy, Sci. Rep. 10 (2020) 1–14. doi:10.1038/s41598-020-63281-4.
[85] J. Yang, J. Han, H. Yu, J. Yin, M. Gao, Z. Wang, X. Zeng, Role of molten pool mode on formability, microstructure and mechanical properties of selective laser melted Ti-6Al-4V alloy, Mater. Des. 110 (2016) 558–570. doi:https://doi.org/10.1016/j.matdes.2016.08.036.
[86] W. Xu, M. Brandt, S. Sun, J. Elambasseril, Q. Liu, K. Latham, K. Xia, M. Qian, Additive manufacturing of strong and ductile Ti-6Al-4V by selective laser melting via in situ martensite decomposition, Acta Mater. 85 (2015) 74–84. doi:10.1016/j.actamat.2014.11.028.
[87] W. Xu, S. Sun, J. Elambasseril, Q. Liu, M. Brandt, M. Qian, Ti-6Al-4V Additively Manufactured by Selective Laser Melting with Superior Mechanical Properties, JOM. 67 (2015) 668–673. doi:10.1007/s11837-015-1297-8.
[88] H. Ali, L. Ma, H. Ghadbeigi, K. Mumtaz, In-situ residual stress reduction, martensitic decomposition and mechanical properties enhancement through high temperature powder bed pre-heating of Selective Laser Melted Ti6Al4V, Mater. Sci. Eng. A. 695 (2017) 211–220. doi:https://doi.org/10.1016/j.msea.2017.04.033.
[89] B. Vrancken, L. Thijs, J.P. Kruth, J. Van Humbeeck, Heat treatment of Ti6Al4V produced by Selective Laser Melting: Microstructure and mechanical properties, J. Alloys Compd. 541 (2012) 177–185. doi:10.1016/j.jallcom.2012.07.022.
[90] C. Qiu, N.J.E.E. Adkins, M.M. Attallah, Microstructure and tensile properties of selectively laser-melted and of HIPed laser-melted Ti–6Al–4V, Mater. Sci. Eng. A. 578 (2013) 230–239. doi:https://doi.org/10.1016/j.msea.2013.04.099.
[91] M. Niinomi, Mechanical properties of biomedical titanium alloys, Mater. Sci. Eng. A. 243 (1998) 231–236.
[92] M. Geetha, A.K. Singh, R. Asokamani, A.K. Gogia, Ti based biomaterials, the ultimate choice for orthopaedic implants–a review, Prog. Mater. Sci. 54

(2009) 397–425.
[93] L.C. Zhang, H. Attar, M. Calin, J. Eckert, Review on manufacture by selective laser melting and properties of titanium based materials for biomedical applications, Mater. Technol. 31 (2016) 66–76. doi:10.1179/1753555715Y.0000000076.
[94] M. Simonelli, Y.Y. Tse, C. Tuck, Effect of the build orientation on the mechanical properties and fracture modes of SLM Ti–6Al–4V, Mater. Sci. Eng. A. 616 (2014) 1–11. doi:https://doi.org/10.1016/j.msea.2014.07.086.
[95] S.Q. Wu, Y.J. Lu, Y.L. Gan, T.T. Huang, C.Q. Zhao, J.J. Lin, S. Guo, J.X. Lin, Microstructural evolution and microhardness of a selective-laser-melted Ti–6Al–4V alloy after post heat treatments, J. Alloys Compd. 672 (2016) 643–652.
[96] T. Vilaro, C. Colin, J.D. Bartout, As-fabricated and heat-treated microstructures of the Ti-6Al-4V alloy processed by selective laser melting, Metall. Mater. Trans. A Phys. Metall. Mater. Sci. 42 (2011) 3190–3199. doi:10.1007/s11661-011-0731-y.
[97] L.M. Plaza, A.M. Irisarri, A. Gil-Negrete, Improvement of Ti-6Al-4V fracture thoughness by sub-transus heat treatment, Scr. Metall. 24 (1990) 1765–1769.
[98] H. Gong, K. Rafi, T. Starr, B. Stucker, The effects of processing parameters on defect regularity in Ti-6Al-4V parts fabricated by selective laser melting and electron beam melting, in: 24th Annu. Int. Solid Free. Fabr. Symp. Addit. Manuf. Conf. Austin, TX, 2013: pp. 424–439.
[99] B. Ferrar, L. Mullen, E. Jones, R. Stamp, C.J. Sutcliffe, Gas flow effects on selective laser melting (SLM) manufacturing performance, J. Mater. Process. Technol. 212 (2012) 355–364. doi:https://doi.org/10.1016/j.jmatprotec.2011.09.020.
[100] J.P. Kruth, L. Froyen, J. Van Vaerenbergh, P. Mercelis, M. Rombouts, B. Lauwers, Selective laser melting of iron-based powder, J. Mater. Process. Technol. 149 (2004) 616–622. doi:https://doi.org/10.1016/j.jmatprotec.2003.11.051.
[101] R. Morgan, C.J. Sutcliffe, W. O'neill, Density analysis of direct metal laser re-melted 316L stainless steel cubic primitives, J. Mater. Sci. 39 (2004) 1195–1205.
[102] J.Y.H. Fuh, Y.S. Choo, A.Y.C. Nee, L. Lu, K.C. Lee, Improvement of the UV curing process for the laser lithography technique, Mater. Des. 16 (1995) 23–32. doi:https://doi.org/10.1016/0261-3069(95)00007-L.
[103] A. Saboori, D. Gallo, S. Biamino, P. Fino, M. Lombardi, An Overview of Additive Manufacturing of Titanium Components by Directed Energy Deposition: Microstructure and Mechanical Properties, Appl. Sci. 7 (2017) 883. doi:10.3390/app7090883.
[104] L. Bian, S.M. Thompson, N. Shamsaei, Mechanical Properties and Microstructural Features of Direct Laser-Deposited Ti-6Al-4V, Jom. 67 (2015) 629–638. doi:10.1007/s11837-015-1308-9.
[105] N. Shamsaei, A. Yadollahi, L. Bian, S.M. Thompson, An overview of Direct Laser Deposition for additive manufacturing; Part II: Mechanical behavior, process parameter optimization and control, Addit. Manuf. 8 (2015) 12–35. doi:10.1016/j.addma.2015.07.002.
[106] S. Bontha, N.W. Klingbeil, P.A. Kobryn, H.L. Fraser, Thermal process maps for predicting solidification microstructure in laser fabrication of

thin-wall structures, J. Mater. Process. Technol. 178 (2006) 135–142. doi:10.1016/j.jmatprotec.2006.03.155.
[107] C. Selcuk, Laser metal deposition for powder metallurgy parts, Powder Metall. 54 (2011) 94–99.
[108] R. Vilar, Laser cladding, J. Laser Appl. 11 (1999) 64–79.
[109] C.M. Liu, X.J. Tian, H.B. Tang, H.M. Wang, Microstructural characterization of laser melting deposited Ti–5Al-5Mo–5V–1Cr–1Fe near β titanium alloy, J. Alloys Compd. 572 (2013) 17–24.
[110] T. Wang, Y.Y. Zhu, S.Q. Zhang, H.B. Tang, H.M. Wang, Grain morphology evolution behavior of titanium alloy components during laser melting deposition additive manufacturing, J. Alloys Compd. 632 (2015) 505–513.
[111] W. Hofmeister, M. Wert, J. Smugeresky, J.A. Philliber, M. Griffith, M. Ensz, Investigating solidification with the laser-engineered net shaping (LENSTM) process, Jom. 51 (1999) 1–6.
[112] A.M. Beese, B.E. Carroll, Review of Mechanical Properties of Ti-6Al-4V Made by Laser-Based Additive Manufacturing Using Powder Feedstock, Jom. 68 (2016) 724–734. doi:10.1007/s11837-015-1759-z.
[113] B. Baufeld, O. Van der Biest, R. Gault, Additive manufacturing of Ti-6Al-4V components by shaped metal deposition: Microstructure and mechanical properties, Mater. Des. 31 (2010) S106–S111. doi:10.1016/j.matdes.2009.11.032.
[114] S. Palanivel, A.K. Dutt, E.J. Faierson, R.S. Mishra, Spatially dependent properties in a laser additive manufactured Ti-6Al-4V component, Mater. Sci. Eng. A. 654 (2016) 39–52. doi:10.1016/j.msea.2015.12.021.
[115] J. Beuth, N. Klingbeil, The role of process variables in laser-based direct metal solid freeform fabrication, Jom. 53 (2001) 36–39. doi:10.1007/s11837-001-0067-y.
[116] P. Rangaswamy, M.L. Griffith, M.B. Prime, T.M. Holden, R.B. Rogge, J.M. Edwards, R.J. Sebring, Residual stresses in LENS® components using neutron diffraction and contour method, Mater. Sci. Eng. A. 399 (2005) 72–83.
[117] J. Mazumder, A. Schifferer, J. Choi, Direct materials deposition: designed macro and microstructure, Mater. Res. Innov. 3 (1999) 118–131. doi:10.1007/s100190050137.
[118] L. Wang, S.D. Felicelli, J.E. Craig, Experimental and numerical study of the LENS rapid fabrication process, J. Manuf. Sci. Eng. 131 (2009).
[119] W. Hofmeister, M. Griffith, Solidification in direct metal deposition by LENS processing, JOM. 53 (2001) 30–34. doi:10.1007/s11837-001-0066-z.
[120] T.M. Mower, M.J. Long, Mechanical behavior of additive manufactured, powder-bed laser-fused materials, Mater. Sci. Eng. A. 651 (2016) 198–213. doi:10.1016/j.msea.2015.10.068.
[121] J. Alcisto, A. Enriquez, H. Garcia, S. Hinkson, T. Steelman, E. Silverman, P. Valdovino, H. Gigerenzer, J. Foyos, J. Ogren, J. Dorey, K. Karg, T. McDonald, O.S. Es-Said, Tensile Properties and Microstructures of Laser-Formed Ti-6Al-4V, J. Mater. Eng. Perform. 20 (2011) 203–212. doi:10.1007/s11665-010-9670-9.
[122] Z. Liu, Z.-X. Qin, F. Liu, X. Lu, H.-M. Wang, The microstructure and mechanical behaviors of the Ti–6.5 Al–3.5 Mo–1.5 Zr–0.3 Si alloy produced by laser melting deposition, Mater. Charact. 97 (2014) 132–139.

[123] S. Wolff, T. Lee, E. Faierson, K. Ehmann, J. Cao, Anisotropic properties of directed energy deposition (DED)-processed Ti–6Al–4V, J. Manuf. Process. 24 (2016) 397–405. doi:10.1016/j.jmapro.2016.06.020.
[124] D. Barba, C. Alabort, Y.T. Tang, M.J. Viscasillas, R.C. Reed, E. Alabort, On the size and orientation effect in additive manufactured Ti-6Al-4V, Mater. Des. 186 (2020) 108235.
[125] S. Ghods, E. Schultz, C. Wisdom, R. Schur, R. Pahuja, A. Montelione, D. Arola, M. Ramulu, Electron beam additive manufacturing of Ti6Al4V: Evolution of powder morphology and part microstructure with powder reuse, Materialia. 9 (2020) 100631.
[126] N. Hrabe, T. Quinn, Effects of processing on microstructure and mechanical properties of a titanium alloy (Ti-6Al-4V) fabricated using electron beam melting (EBM), part 1: Distance from build plate and part size, Mater. Sci. Eng. A. 573 (2013) 264–270. doi:10.1016/j.msea.2013.02.064.
[127] P.A. Kobryn, S.L. Semiatin, Mechanical Properties of Laser-Deposited Ti-6Al-4V 179, in: 2001 Int. Solid Free. Fabr. Symp., 2001.
[128] C. Qiu, G.A. Ravi, C. Dance, A. Ranson, S. Dilworth, M.M. Attallah, Fabrication of large Ti-6Al-4V structures by direct laser deposition, J. Alloys Compd. 629 (2015) 351–361. doi:10.1016/j.jallcom.2014.12.234.
[129] B.E. Carroll, T.A. Palmer, A.M. Beese, Anisotropic tensile behavior of Ti-6Al-4V components fabricated with directed energy deposition additive manufacturing, Acta Mater. 87 (2015) 309–320. doi:10.1016/j.actamat.2014.12.054.
[130] Y. Zhai, H. Galarraga, D.A. Lados, Microstructure, static properties, and fatigue crack growth mechanisms in Ti-6Al-4V fabricated by additive manufacturing: LENS and EBM, Eng. Fail. Anal. 69 (2016) 3–14. doi:10.1016/j.engfailanal.2016.05.036.
[131] M.O. Sklyar, G.A. Turichin, O.G. Klimova, O.G. Zotov, I.K. Topalov, Microstructure of 316L stainless steel components produced by direct laser deposition, Steel Transl. 46 (2016) 883–887. doi:10.3103/S096709121612010X.
[132] H.K. Rafi, N. V. Karthik, H. Gong, T.L. Starr, B.E. Stucker, Microstructures and mechanical properties of Ti6Al4V parts fabricated by selective laser melting and electron beam melting, J. Mater. Eng. Perform. 22 (2013) 3872–3883. doi:10.1007/s11665-013-0658-0.
[133] E. Arrieta, M. Haque, J. Mireles, C. Stewart, C. Carrasco, R.B. Wicker, Mechanical Behavior of Differently Oriented Electron Beam Melting Ti–6Al–4V Components Using Digital Image Correlation, J. Eng. Mater. Technol. 141 (2019) 011004. doi:10.1115/1.4040553.
[134] H. Galarraga, R.J. Warren, D.A. Lados, R.R. Dehoff, M.M. Kirka, P. Nandwana, Effects of heat treatments on microstructure and properties of Ti-6Al-4V ELI alloy fabricated by electron beam melting (EBM), Mater. Sci. Eng. A. 685 (2017) 417–428. doi:10.1016/j.msea.2017.01.019.
[135] A. Mohammadhosseini, D. Fraser, S.H. Masood, M. Jahedi, Microstructure and mechanical properties of Ti-6Al-4V manufactured by electron beam melting process, Mater. Res. Innov. 17 (2013). doi:10.1179/1432891713Z.000000000302.
[136] A. Kirchner, B. Klöden, T. Weißgärber, B. Kieback, A. Schoberth, D. Greitemeier, S. Bagehorn, Mechanical properties of Ti-6Al-4V fabricated

by electron beam melting, in: Key Eng. Mater., Trans Tech Publ, 2016: pp. 235–240.
[137] L. Facchini, E. Magalini, P. Robotti, A. Molinari, S. Höges, K. Wissenbach, Ductility of a Ti-6Al-4V alloy produced by selective laser melting of prealloyed powders, Rapid Prototyp. J. 16 (2010) 450–459. doi:10.1108/13552541011083371.
[138] L.E. Murr, S.A. Quinones, S.M. Gaytan, M.I. Lopez, A. Rodela, E.Y. Martinez, D.H. Hernandez, E. Martinez, F. Medina, R.B. Wicker, Microstructure and mechanical behavior of Ti-6Al-4V produced by rapid-layer manufacturing, for biomedical applications, J. Mech. Behav. Biomed. Mater. 2 (2009) 20–32. doi:10.1016/j.jmbbm.2008.05.004.
[139] D.A. Hollander, M. Von Walter, T. Wirtz, R. Sellei, B. Schmidt-Rohlfing, O. Paar, H.J. Erli, Structural, mechanical and in vitro characterization of individually structured Ti-6Al-4V produced by direct laser forming, Biomaterials. 27 (2006) 955–963. doi:10.1016/j.biomaterials.2005.07.041.
[140] B. Vandenbroucke, J.P. Kruth, Selective laser melting of biocompatible metals for rapid manufacturing of medical parts, Rapid Prototyp. J. 13 (2007) 196–203. doi:10.1108/13552540710776142.
[141] S. Cao, Z. Chen, C.V.S. Lim, K. Yang, Q. Jia, T. Jarvis, D. Tomus, X. Wu, Defect, microstructure, and mechanical property of Ti-6Al-4V alloy fabricated by high-power selective laser melting, Jom. 69 (2017) 2684–2692. doi:10.1007/s11837-017-2581-6.
[142] F. Mazzucato, A. Aversa, R. Doglione, S. Biamino, A. Valente, M. Lombardi, Influence of Process Parameters and Deposition Strategy on Laser Metal Deposition of 316L Powder, Metals (Basel). 9 (2019) 1160. doi:https://doi.org/10.3390/met9111160.
[143] Q. Zhang, C. Yu, Y. Peng, Q. Peng, Quantification of the thickness of Widmanstatten α-laths in Ti alloys, 2012 5th Int. Congr. Image Signal Process. CISP 2012. (2012) 464–468. doi:10.1109/CISP.2012.6469866.
[144] G.F. Vander Voort, A. Roósz, Measurement of the interlamellar spacing of pearlite, Metallography. 17 (1984) 1–17. doi:10.1016/0026-0800(84)90002-8.
[145] A. INTERNATIONAL, Standard Test Methods for Determining Average Grain Size, Astm E112-10. (2010) 1–27. doi:10.1520/E0112-13.1.4.
[146] B.D. Cullity, S.R. Stock, Elements of X-Ray Diffraction, Addison-Wesley Publishing, 1956.
[147] E. ASTM, Standard test methods for tension testing of metallic materials, Annu. B. ASTM Stand. ASTM. (2001).
[148] E. Brandl, D. Greitemeier, Microstructure of additive layer manufactured Ti-6Al-4V after exceptional post heat treatments, Mater. Lett. 81 (2012) 84–87. doi:10.1016/j.matlet.2012.04.116.
[149] Y. Huang, M.B. Khamesee, E. Toyserkani, A new physics-based model for laser directed energy deposition (powder-fed additive manufacturing): From single-track to multi-track and multi-layer, Opt. Laser Technol. 109 (2019) 584–599. doi:10.1016/j.optlastec.2018.08.015.
[150] P.A. Kobryn, E.H. Moore, S.L. Semiatin, Effect of laser power and traverse speed on microstructure, porosity, and build height in laser-deposited Ti-6Al-4V, Scr. Mater. 43 (2000) 299–305. doi:10.1016/S1359-6462(00)00408-5.
[151] R. Cottam, M. Brandt, Laser cladding of Ti-6Al-4V powder on Ti-6Al-4V

substrate: Effect of laser cladding parameters on microstructure, Phys. Procedia. 12 (2011) 323–329. doi:10.1016/j.phpro.2011.03.041.
[152] R.M. Mahamood, E.T. Akinlabi, S. Akinlabi, Laser power and Scanning Speed Influence on the Mechanical Property of Laser Metal Deposited Titanium-Alloy, Lasers Manuf. Mater. Process. 2 (2015) 43–55. doi:10.1007/s40516-014-0003-y.
[153] L. Peng, Y. Taiping, L. Sheng, L. Dongsheng, H. Qianwu, X. Weihao, Z. Xiaoyan, Direct laser fabrication of nickel alloy samples, Int. J. Mach. Tools Manuf. 45 (2005) 1288–1294. doi:10.1016/j.ijmachtools.2005.01.014.
[154] A. Aversa, M. Moshiri, F. Calignano, D. Manfredi, S. Tusacciu, M. Busatto, M. Lai, M. Lombardi, M. Pavese, S. Biamino, A comparison of the laser powder interaction in laser powder bed fusion and direct energy deposition processes, Proc. Euro PM 2017 Int. Powder Metall. Congr. Exhib. (2017).
[155] J. Gockel, J. Beuth, Understanding Ti-6Al-4V microstructure control in additive manufacturing via process maps, 24th Int. SFF Symp. - An Addit. Manuf. Conf. SFF 2013. (2013) 666–674.
[156] C. Katinas, S. Liu, Y.C. Shin, Self-sufficient modeling of single track deposition of Ti-6Al-4V with the prediction of capture efficiency, J. Manuf. Sci. Eng. Trans. ASME. 141 (2019) 1–10. doi:10.1115/1.4041423.
[157] A. Carrozza, A. Aversa, F. Mazzucato, M. Lombardi, S. Biamino, A. Valente, P. Fino, An Innovative Approach on Directed Energy Deposition Optimization : A Study of the Process Environment's Influence on the Quality of Ti-6Al-4V Samples, Appl. Sci. 10 (2020).
[158] O.G. Klimova-Korsmik, G.A. Turichin, S.A. Shalnova, M.O. Gushchina, V. V. Cheverikin, Structure and properties of Ti-6Al-4V titanium alloy products obtained by direct laser deposition and subsequent heat treatment, J. Phys. Conf. Ser. 1109 (2018) 012061.
[159] M. Gharbi, P. Peyre, C. Gorny, M. Carin, S. Morville, P. Le Masson, D. Carron, R. Fabbro, Influence of various process conditions on surface finishes induced by the direct metal deposition laser technique on a Ti-6Al-4V alloy, J. Mater. Process. Technol. 213 (2013) 791–800. doi:10.1016/j.jmatprotec.2012.11.015.
[160] F. Mazzucato, A. Marchetti, A. Valente, Analysis of the Influence of Shielding and Carrier Gases on the DED Powder Deposition Efficiency for a New Deposition Nozzle Design Solution, Ind. Addit. Manuf. - Proc. Addit. Manuf. Prod. Appl. - AMPA2017. (2018) 59–69. doi:10.1007/978-3-319-66866-6_6.
[161] W. Peng, W. Zeng, Y. Zhang, C. Shi, B. Quan, J. Wu, The effect of colored titanium oxides on the color change on the surface of Ti-5Al-5Mo-5V-1Cr-1Fe alloy, J. Mater. Eng. Perform. 22 (2013) 2588–2593. doi:10.1007/s11665-013-0573-4.
[162] J. Alcisto, A. Enriquez, H. Garcia, S. Hinkson, M. Hahn, J. Foyos, J. Ogren, E.W. Lee, O.S. Es-Said, The effect of thermal history on the color of oxide layers in titanium 6242 alloy, Eng. Fail. Anal. 11 (2004) 811–816. doi:10.1016/j.engfailanal.2004.04.001.
[163] AWS-D17.1 (American Welding Society), 2001.
[164] E. Capello, B. Previtali, The influence of operator skills, process parameters and materials on clad shape in repair using laser cladding by

wire, J. Mater. Process. Technol. 174 (2006) 223–232. doi:10.1016/j.jmatprotec.2006.01.005.
[165] U. de Oliveira, V. Ocelík, J.T.M. De Hosson, Analysis of coaxial laser cladding processing conditions, Surf. Coatings Technol. 197 (2005) 127–136. doi:10.1016/j.surfcoat.2004.06.029.
[166] L. Yan, L. Hill, J.W. Newkirk, F. Liou, Investigation of Build Strategies for a Hybrid Manufacturing Process Progress on Ti-6Al-4V, Solid Free. Fabr. Symp. (2017) 1846–1852.
[167] S. Malinov, W. Sha, Z. Guo, Application of artificial neural network for prediction of time-temperature-transformation diagrams in titanium alloys, Mater. Sci. Eng. A. 283 (2000) 1–10. doi:10.1016/S0921-5093(00)00746-2.
[168] X. Xu, J. Ding, S. Ganguly, C. Diao, S. Williams, Oxide accumulation effects on wire + arc layer-by-layer additive manufacture process, J. Mater. Process. Technol. 252 (2018) 739–750. doi:10.1016/j.jmatprotec.2017.10.030.
[169] M. Yan, W. Xu, M.S. Dargusch, H.P. Tang, M. Brandt, M. Qian, Review of effect of oxygen on room temperature ductility of titanium and titanium alloys, Powder Metall. 57 (2014) 251–257. doi:10.1179/1743290114Y.0000000108.
[170] G.P. Dinda, L. Song, J. Mazumder, Fabrication of Ti-6Al-4V Scaffolds by Direct Metal Deposition, Metall. Mater. Trans. A. 39A (2008) 2914–2922. doi:10.1007/s11661-008-9634-y.
[171] B.A. Szost, S. Terzi, F. Martina, D. Boisselier, A. Prytuliak, T. Pirling, M. Hofmann, D.J. Jarvis, A comparative study of additive manufacturing techniques: Residual stress and microstructural analysis of CLAD and WAAM printed Ti-6Al-4V components, Mater. Des. 89 (2016) 559–567. doi:10.1016/j.matdes.2015.09.115.
[172] S. Gorsse, C. Hutchinson, M. Gouné, R. Banerjee, Additive manufacturing of metals: a brief review of the characteristic microstructures and properties of steels, Ti-6Al-4V and high-entropy alloys, Sci. Technol. Adv. Mater. 18 (2017) 584–610. doi:10.1080/14686996.2017.1361305.
[173] B. Wysocki, P. Maj, R. Sitek, J. Buhagiar, K.J. Kurzydłowski, W. Święszkowski, W. Świeszkowski, Laser and Electron Beam Additive Manufacturing Methods of Fabricating Titanium Bone Implants, Appl. Sci. 7 (2017) 657. doi:10.3390/app7070657.
[174] M. Nabhani, R. Shoja Razavi, M. Barekat, Corrosion study of laser cladded Ti-6Al-4V alloy in different corrosive environments, Eng. Fail. Anal. 97 (2019) 234–241. doi:10.1016/j.engfailanal.2019.01.023.
[175] M.R. Amaya-Vazquez, J.M. Sánchez-Amaya, Z. Boukha, F.J. Botana, Microstructure, microhardness and corrosion resistance of remelted TiG2 and Ti6Al4V by a high power diode laser, Corros. Sci. 56 (2012) 36–48. doi:10.1016/j.corsci.2011.11.006.
[176] J.M. Oh, B.G. Lee, S.W. Cho, S.W. Lee, G.S. Choi, J.W. Lim, Oxygen effects on the mechanical properties and lattice strain of Ti and Ti-6Al-4V, Met. Mater. Int. 17 (2011) 733–736. doi:10.1007/s12540-011-1006-2.
[177] R. Montanari, G. Costanza, M.E. Tata, C. Testani, Lattice expansion of Ti-6Al-4V by nitrogen and oxygen absorption, Mater. Charact. 59 (2008) 334–337. doi:10.1016/j.matchar.2006.12.014.
[178] Y. Kok, X. Tan, S.B. Tor, C.K. Chua, Fabrication and microstructural characterisation of additive manufactured Ti-6Al-4V parts by electron

beam melting: This paper reports that the microstructure and micro-hardness of an EMB part is thickness dependent, Virtual Phys. Prototyp. 10 (2015) 13–21. doi:10.1080/17452759.2015.1008643.

[179] A. Azarniya, X.G. Colera, M.J. Mirzaali, S. Sovizi, F. Bartolomeu, M. k. St Weglowski, W.W. Wits, C.Y. Yap, J. Ahn, G. Miranda, F.S. Silva, H.R. Madaah Hosseini, S. Ramakrishna, A.A. Zadpoor, Additive manufacturing of Ti–6Al–4V parts through laser metal deposition (LMD): Process, microstructure, and mechanical properties, J. Alloys Compd. 804 (2019) 163–191. doi:10.1016/j.jallcom.2019.04.255.

[180] K. Wei, Z. Wang, F. Li, H. Zhang, X. Zeng, Densification behavior, microstructure evolution, and mechanical performances of selective laser melted Ti-5Al-2.5Sn α titanium alloy: Effect of laser energy input, J. Alloys Compd. 774 (2019) 1024–1035. doi:10.1016/j.jallcom.2018.09.153.

[181] M. Bignon, E. Bertrand, F. Tancret, P.E.J. Rivera-Díaz-del-Castillo, Modelling martensitic transformation in titanium alloys: The influence of temperature and deformation, Materialia. 7 (2019) 100382. doi:10.1016/j.mtla.2019.100382.

[182] J. He, D. Li, W. Jiang, L. Ke, G. Qin, Y. Ye, Q. Qin, D. Qiu, The Martensitic Transformation and Mechanical Properties of Ti6Al4V Prepared via Selective Laser Melting, Materials (Basel). 12 (2019). doi:10.3390/ma12020321.

[183] D.A. Porter, K.E. Easterling, M.Y. Sherif, Phase transformations in metals and alloys, third edition, CRC press, 2009.

[184] P. Wollants, J.R. Roos, L. Delaey, Thermally- and stress-induced thermoelastic martensitic transformations in the reference frame of equilibrium thermodynamics, Prog. Mater. Sci. 37 (1993) 227–288. doi:10.1016/0079-6425(93)90005-6.

[185] W. Zhang, Y.M. Jin, A.G. Khachaturyan, Phase field microelasticity modeling of heterogeneous nucleation and growth in martensitic alloys, Acta Mater. 55 (2007) 565–574. doi:10.1016/j.actamat.2006.08.050.

[186] F.J. Gil, M.P. Ginebra, J.M. Manero, J.A. Planell, Formation of α-Widmanstätten structure: Effects of grain size and cooling rate on the Widmanstätten morphologies and on the mechanical properties in Ti6Al4V alloy, J. Alloys Compd. 329 (2001) 142–152. doi:10.1016/S0925-8388(01)01571-7.

[187] E.O. Hall, The deformation and ageing of mild steel: II Characteristics of the Lüders deformation, Proc. Phys. Soc. Sect. B. 64 (1951) 742–747. doi:10.1088/0370-1301/64/9/302.

[188] N.J. Petch, The Cleavage Strength of Polycrystals, J. Iron Steel Inst. 174 (1953) 25–28.

[189] W. Lu, Y. Shi, X. Li, Y. Lei, Correlation between tensile strength and hardness of electron beam welded TC4-DT joints, J. Mater. Eng. Perform. 22 (2013) 1694–1700. doi:10.1007/s11665-012-0469-8.

[190] E.J. Pavlina, C.J. Van Tyne, Correlation of Yield strength and Tensile strength with hardness for steels, J. Mater. Eng. Perform. 17 (2008) 888–893. doi:10.1007/s11665-008-9225-5.

[191] A. Ho, H. Zhao, J.W. Fellowes, F. Martina, A.E. Davis, P.B. Prangnell, On the origin of microstructural banding in Ti-6Al4V wire-arc based high deposition rate additive manufacturing, Acta Mater. 166 (2019) 306–323. doi:10.1016/j.actamat.2018.12.038.

[192] J. Alcisto, A. Enriquez, H. Garcia, S. Hinkson, T. Steelman, E. Silverman, P. Valdovino, H. Gigerenzer, J. Foyos, J. Ogren, J. Dorey, K. Karg, T. Mcdonald, O.S. Es-said, Tensile Properties and Microstructures of Laser-Formed Ti-6Al-4V, 20 (2011) 203–212.

[193] E. Dolgun, E. Zemlyakov, S. Shalnova, M. Gushchina, V. Promahov, The influence of heat treatment on the microstructure of products manufactured by direct laser deposition using titanium alloy Ti-6Al-4V, Mater. Today Proc. 30 (2020) 688–693. doi:https://doi.org/10.1016/j.matpr.2020.01.523.

[194] G. Suprobo, A.A. Ammar, N. Park, E.R. Baek, S. Kim, Thermal Decomposition of Massive Phase to Fine Lamellar α/β in Ti–6Al–4V Additively Manufactured Alloy by Directed Energy Deposition, Met. Mater. Int. 25 (2019) 1428–1435. doi:10.1007/s12540-019-00304-4.

[195] Y. Lu, H.B. Tang, Y.L. Fang, D. Liu, H.M. Wang, Microstructure evolution of sub-critical annealed laser deposited Ti–6Al–4V alloy, Mater. Des. 37 (2012) 56–63. doi:https://doi.org/10.1016/j.matdes.2011.12.016.

[196] H. Shao, Y. Zhao, P. Ge, W. Zeng, Influence of Cooling Rate and Aging on the Lamellar Microstructure and Fractography of TC21 Titanium Alloy, Metallogr. Microstruct. Anal. 2 (2013) 35–41. doi:10.1007/s13632-012-0055-3.

[197] G.T. Aleixo, E.S.N. Lopes, R. Contieri, A. Cremasco, C.R.M. Afonso, R. Caram, Effects of cooling rate and Sn addition on the microstructure of Ti-Nb-Sn alloys, in: Solid State Phenom., Trans Tech Publ, 2011: pp. 190–195.

[198] F.J. Gil, J.A. Planell, Growth order and activation energies for grain growth of Ti6Al4V alloy in ß phase, Scr. Metall. Mater. 25 (1991) 2843–2848. doi:https://doi.org/10.1016/0956-716X(91)90167-Y.

[199] H. Yu, W. Li, H. Zou, S. Li, T. Zhai, L. Liu, Study on non-isothermal transformation of Ti-6Al-4V in solution heating stage, Metals (Basel). 9 (2019). doi:10.3390/met9090968.

[200] J. Cho, Characterization of the α'-Martensite phase and its decomposition in Ti-6Al-4V additively manufactured by selective laser melting, RMIT University, 2018.

[201] C. Pirozzi, S. Franchitti, R. Borrelli, F. Caiazzo, V. Alfieri, P. Argenio, Study on the Factors Affecting the Mechanical Behavior of Electron Beam Melted Ti6Al4V, J. Mater. Eng. Perform. 26 (2017) 4491–4499. doi:10.1007/s11665-017-2894-1.

[202] M. Qian, W. Xu, M. Brandt, H.P. Tang, Additive manufacturing and postprocessing of Ti-6Al-4V for superior mechanical properties, MRS Bull. 41 (2016) 775–783. doi:10.1557/mrs.2016.215.

[203] S. Raghavan, M.L.S. Nai, P. Wang, W.J. Sin, T. Li, J. Wei, Heat treatment of electron beam melted (EBM) Ti-6Al-4V: microstructure to mechanical property correlations, Rapid Prototyp. J. 24 (2018) 774–783. doi:10.1108/RPJ-05-2016-0070.

[204] A.K. Syed, M. Awd, F. Walther, X. Zhang, Microstructure and mechanical properties of as-built and heat-treated electron beam melted Ti–6Al–4V, Mater. Sci. Technol. (United Kingdom). 35 (2019) 653–660. doi:10.1080/02670836.2019.1580434.

[205] Z. Li, C. Liu, B. Wang, C. Wang, Z. Wang, F. Yang, C. Gao, H. Liu, Y. Qin, J. Wang, Heat treatment effect on the mechanical properties, roughness and bone ingrowth capacity of 3D printing porous titanium

alloy, RSC Adv. 8 (2018) 12471–12483. doi:10.1039/c7ra13313h.
[206] L. Lizzul, M. Sorgato, R. Bertolini, A. Ghiotti, S. Bruschi, Influence of additive manufacturing-induced anisotropy on tool wear in end milling of Ti6Al4V, Tribol. Int. 146 (2020) 106200. doi:10.1016/j.triboint.2020.106200.
[207] A. Ataee, Y. Li, D. Fraser, G. Song, C. Wen, Anisotropic Ti-6Al-4V gyroid scaffolds manufactured by electron beam melting (EBM) for bone implant applications, Mater. Des. 137 (2018) 345–354. doi:10.1016/j.matdes.2017.10.040.
[208] A. Kirchner, B. Klöden, J. Luft, T. Weißgärber, B. Kieback, Process window for electron beam melting of Ti-6Al-4V, Powder Metall. 58 (2015) 246–249. doi:10.1179/0032589915Z.000000000244.
[209] Y. Chong, G. Deng, S. Gao, J. Yi, A. Shibata, N. Tsuji, Yielding nature and Hall-Petch relationships in Ti-6Al-4V alloy with fully equiaxed and bimodal microstructures, Scr. Mater. 172 (2019) 77–82.
[210] H. Galarraga, D.A. Lados, R.R. Dehoff, M.M. Kirka, P. Nandwana, Effects of the microstructure and porosity on properties of Ti-6Al-4V ELI alloy fabricated by electron beam melting (EBM), Addit. Manuf. 10 (2016) 47–57. doi:10.1016/j.addma.2016.02.003.
[211] I. Halevy, G. Zamir, M. Winterrose, G. Sanjit, C.R. Grandini, A. Moreno-Gobbi, Crystallographic structure of Ti-6Al-4V, Ti-HP and Ti-CP under high-pressure, J. Phys. Conf. Ser. 215 (2010) 2–11. doi:10.1088/1742-6596/215/1/012013.
[212] N. Velisavljevic, Titanium Alloys at Extreme Pressure Conditions, in: S. MacLeod (Ed.), IntechOpen, Rijeka, 2012: p. Ch. 4. doi:10.5772/36038.
[213] M. Motyka, A. Baran-Sadleja, J. Sieniawski, M. Wierzbinska, K. Gancarczyk, Decomposition of deformed α′(α″) martensitic phase in Ti–6Al–4V alloy, Mater. Sci. Technol. (United Kingdom). 35 (2019) 260–272. doi:10.1080/02670836.2018.1466418.
[214] K. Yang, J. Wang, L. Jia, G. Yang, H. Tang, Y. Li, Additive manufacturing of Ti-6Al-4V lattice structures with high structural integrity under large compressive deformation, J. Mater. Sci. Technol. 35 (2019) 303–308. doi:10.1016/j.jmst.2018.10.029.
[215] M.T. Jovanović, S. Tadić, S. Zec, Z. Mišković, I. Bobić, The effect of annealing temperatures and cooling rates on microstructure and mechanical properties of investment cast Ti–6Al–4V alloy, Mater. Des. 27 (2006) 192–199. doi:https://doi.org/10.1016/j.matdes.2004.10.017.
[216] S.S. Al-Bermani, M.L. Blackmore, W. Zhang, I. Todd, The Origin of Microstructural Diversity, Texture, and Mechanical Properties in Electron Beam Melted Ti-6Al-4V, Metall. Mater. Trans. A. 41 (2010) 3422–3434. doi:10.1007/s11661-010-0397-x.
[217] P.L. Blackwell, A. Wisbey, Laser-aided manufacturing technologies; their application to the near-net shape forming of a high-strength titanium alloy, J. Mater. Process. Technol. 170 (2005) 268–276. doi:10.1016/j.jmatprotec.2005.05.014.
[218] S. Birosca, J.Y. Buffiere, F.A. Garcia-Pastor, M. Karadge, L. Babout, M. Preuss, Three-dimensional characterization of fatigue cracks in Ti-6246 using X-ray tomography and electron backscatter diffraction, Acta Mater. 57 (2009) 5834–5847. doi:10.1016/j.actamat.2009.08.009.
[219] M.J. Donachie, A Guide to Engineering Selection of Titanium Alloys for

Design, in: Mech. Eng. Handb., Wiley Online Library, 2014: pp. 1–37.
[220] M.M. Attallah, S. Zabeen, R.J. Cernik, M. Preuss, Comparative determination of the α/β phase fraction in α+β-titanium alloys using X-ray diffraction and electron microscopy, Mater. Charact. 60 (2009) 1248–1256. doi:10.1016/j.matchar.2009.05.006.
[221] S. Bein, J. Bechet, Phase Transformation Kinetics and Mechanisms in Titanium Alloys Ti-6.2.4.6,β-CEZ and Ti-10.2.3, J. Phys. IV. 6 (1996).
[222] Y. Ito, Y. Moriguchi, N. Takashi, The Effect of Microstructures on Mechanical Properties of the β rich α-β Titanium alloy of Ti-6Al-2Sn-4Zr-6Mo, (1986) 1–8.
[223] M. Young, E. Levine, H. Margolin, Aging Behavior of Orthorhombic Martensite in Ti-6-2-4-6., Met. Trans. 5 (1974) 1891–1898. doi:10.1007/BF02644157.
[224] S. Neelakantan, P.E.J.J. Rivera-Díaz-del-Castillo, S. van der Zwaag, Prediction of the martensite start temperature for β titanium alloys as a function of composition, Scr. Mater. 60 (2009) 611–614. doi:10.1016/j.scriptamat.2008.12.034.
[225] R. Pederson, F. Niklasson, F. Skystedt, R. Warren, Microstructure and mechanical properties of friction-and electron-beam welded Ti–6Al–4V and Ti–6Al–2Sn–4Zr–6Mo, Mater. Sci. Eng. A. 552 (2012) 555–565.
[226] P. Åkerfeldt, M.L. Antti, R. Pederson, Influence of microstructure on mechanical properties of laser metal wire-deposited Ti-6Al-4V, Mater. Sci. Eng. A. 674 (2016) 428–437. doi:10.1016/j.msea.2016.07.038.
[227] Y. Guo, T. Jung, Y.L. Chiu, H. Li, S. Bray, P. Bowen, Microstructure and microhardness of Ti6246 linear friction weld, Mater. Sci. Eng. A. 562 (2013) 17–24. doi:10.1016/j.msea.2012.10.089.
[228] C.M. Cepeda-Jiménez, F. Potenza, E. Magalini, V. Luchin, A. Molinari, M.T. Pérez-Prado, Effect of energy density on the microstructure and texture evolution of Ti-6Al-4V manufactured by laser powder bed fusion, Mater. Charact. (2020) 110238.
[229] C. de Formanoir, U. Paggi, T. Colebrants, L. Thijs, G. Li, K. Vanmeensel, B. Van Hooreweder, Increasing the productivity of laser powder bed fusion: Influence of the hull-bulk strategy on part quality, microstructure and mechanical performance of ti-6al-4v, Addit. Manuf. 33 (2020) 101129. doi:10.1016/j.addma.2020.101129.
[230] S.E. Brika, M. Letenneur, C.A. Dion, V. Brailovski, Influence of particle morphology and size distribution on the powder flowability and laser powder bed fusion manufacturability of Ti-6Al-4V alloy, Addit. Manuf. 31 (2020) 100929.
[231] Y. Xiao, N. Dai, Y. Chen, J. Zhang, S.-W. Choi, On the microstructure and corrosion behaviors of selective laser melted CP-Ti and Ti-6Al-4V alloy in Hank's artificial body fluid, Mater. Res. Express. 6 (2019) 126521.
[232] A.W. Gebisa, H.G. Lemu, Additive manufacturing for the manufacture of gas turbine engine components: Literature review and future perspectives, Proc. ASME Turbo Expo. 6 (2018) 1–10. doi:10.1115/GT2018-76686.
[233] A.E. Wilson-Heid, Z. Wang, B. McCornac, A.M. Beese, Quantitative relationship between anisotropic strain to failure and grain morphology in additively manufactured Ti-6Al-4V, Mater. Sci. Eng. A. 706 (2017) 287–294. doi:10.1016/j.msea.2017.09.017.
[234] B. Shen, H. Li, S. Liu, J. Zou, S. Shen, Y. Wang, T. Zhang, D. Zhang, Y.

Chen, H. Qi, Influence of laser post-processing on pore evolution of Ti–6Al–4V alloy by laser powder bed fusion, J. Alloys Compd. 818 (2020) 152845. doi:10.1016/j.jallcom.2019.152845.

[235] ISO 9276-6:2008 Representation of results of particle size analysis — Part 6: Descriptive and quantitative representation of particle shape and morphology, (n.d.).

[236] P.A. Hooper, Melt pool temperature and cooling rates in laser powder bed fusion, Addit. Manuf. 22 (2018) 548–559. doi:10.1016/j.addma.2018.05.032.

[237] V. Thampy, A.Y. Fong, N.P. Calta, J. Wang, A.A. Martin, P.J. Depond, A.M. Kiss, G. Guss, Q. Xing, R.T. Ott, A. van Buuren, M.F. Toney, J.N. Weker, M.J. Kramer, M.J. Matthews, C.J. Tassone, K.H. Stone, Subsurface Cooling Rates and Microstructural Response during Laser Based Metal Additive Manufacturing, Sci. Rep. 10 (2020) 1–9. doi:10.1038/s41598-020-58598-z.

[238] Y. Li, L. Song, P. Xie, M. Cheng, H. Xiao, Enhancing hardness and wear performance of laser additive manufactured Ti6Al4V alloy through achieving ultrafine microstructure, Materials (Basel). 13 (2020) 15–18. doi:10.3390/ma13051210.

[239] C. Sauer, G. Lütjering, Influence of α layers at β grain boundaries on mechanical properties of Ti-alloys, Mater. Sci. Eng. A. 319–321 (2001) 393–397. doi:10.1016/S0921-5093(01)01018-8.

[240] P. Stella, I. Giovanetti, G. Masi, M. Leoni, A. Molinari, Microstructure and microhardness of heat-treated Ti-6Al-2Sn-4Zr-6Mo alloy, J. Alloys Compd. 567 (2013) 134–140. doi:10.1016/j.jallcom.2013.03.046.

[241] W. Sha, S. Malinov, Titanium alloys: modelling of microstructure, properties and applications, Elsevier, 2009.

[242] S. Hémery, P. Villechaise, Comparison of slip system activation in Ti-6Al-2Sn-4Zr-2Mo and Ti-6Al-2Sn-4Zr-6Mo under tensile, fatigue and dwell-fatigue loadings, Mater. Sci. Eng. A. 697 (2017) 177–183.

[243] R.B. Sparks, J.R. Long, Improved Manufacturing Methods for Producing High Integrity More Reliable Forgings, Technical Report AFML-TR-73-301, Air Force Materials Laboratory, Wright …, 1974.

[244] S.L. Semiatin, V. Seetharaman, I. Weiss, Hot working of titanium alloys - an overview, Adv. Sci. Technol. Titan. Alloy Process. (1996) 3–73.

[245] S. Cao, R. Chu, X. Zhou, K. Yang, Q. Jia, C.V.S. Lim, A. Huang, X. Wu, Role of martensite decomposition in tensile properties of selective laser melted Ti-6Al-4V, J. Alloys Compd. 744 (2018) 357–363.

[246] C. Kenel, D. Grolimund, X. Li, E. Panepucci, V.A. Samson, D.F. Sanchez, F. Marone, C. Leinenbach, In situ investigation of phase transformations in Ti-6Al-4V under additive manufacturing conditions combining laser melting and high-speed micro-X-ray diffraction, Sci. Rep. 7 (2017) 1–10.

[247] R.P. Elliott, Diffusion in titanium and titanium alloys, Armour Research Foundation Chicago, 1962.

[248] S.L. Semiatin, T.M. Brown, T.A. Goff, P.N. Fagin, D.R. Barker, R.E. Turner, J.M. Murry, J.D. Miller, F. Zhang, Diffusion coefficients for modeling the heat treatment of Ti-6Al-4V, Metall. Mater. Trans. A Phys. Metall. Mater. Sci. 35 A (2004) 3015–3018. doi:10.1007/s11661-004-0250-1.

[249] X. Tan, Y. Kok, W.Q. Toh, Y.J. Tan, M. Descoins, D. Mangelinck, S.B.

Tor, K.F. Leong, C.K. Chua, Revealing martensitic transformation and α/β interface evolution in electron beam melting three-dimensional-printed Ti-6Al-4V, Sci. Rep. 6 (2016) 1–10. doi:10.1038/srep26039.

[250] J. Haubrich, J. Gussone, P. Barriobero-Vila, P. Kürnsteiner, E.A. Jägle, D. Raabe, N. Schell, G. Requena, The role of lattice defects, element partitioning and intrinsic heat effects on the microstructure in selective laser melted Ti-6Al-4V, Acta Mater. 167 (2019) 136–148. doi:10.1016/j.actamat.2019.01.039.

[251] X. Yan, S. Yin, C. Chen, C. Huang, R. Bolot, R. Lupoi, M. Kuang, W. Ma, C. Coddet, H. Liao, Effect of heat treatment on the phase transformation and mechanical properties of Ti6Al4V fabricated by selective laser melting, J. Alloys Compd. 764 (2018) 1056–1071.

[252] M. Roudnicka, E.A. Tarquino, D. Vojtech, Choosing a Suitable Heat Treatment Regime for Stress-Relief and Microstructure Stabilization of Ti6Al4V Alloy 3D-Printed by SLM Method, in: Defect Diffus. Forum, Trans Tech Publ, 2020: pp. 11–18.

[253] G. Kasperovich, J. Hausmann, Improvement of fatigue resistance and ductility of TiAl6V4 processed by selective laser melting, J. Mater. Process. Technol. 220 (2015) 202–214.

[254] K. Dietrich, J. Diller, S. Dubiez-Le Goff, D. Bauer, P. Forêt, G. Witt, The influence of oxygen on the chemical composition and mechanical properties of Ti-6Al-4V during laser powder bed fusion (L-PBF), Addit. Manuf. 32 (2020) 100980.

[255] M. Thöne, S. Leuders, A. Riemer, T. Tröster, H.A. Richard, Influence of heat-treatment on Selective Laser Melting products–eg Ti6Al4V, in: Solid Free. Fabr. Symp. SFF, Austin Texas, 2012.